

Pumps running as turbines for energy recovery in water supply systems

THÈSE N° 9036 (2018)

PRÉSENTÉE LE 23 NOVEMBRE 2018

À L'ÉCOLE POLYTECHNIQUE FÉDÉRALE DE LAUSANNE
À LA FACULTÉ DES SCIENCES ET TECHNIQUES DE L'INGÉNIEUR
LABORATOIRE DE MACHINES HYDRAULIQUES

ET

À L'INSTITUTO SUPERIOR TÉCNICO (IST) DA UNIVERSIDADE DE LISBOA

PROGRAMME DOCTORAL EN ENERGIE
ET
DOUTORAMENTO EM ENGENHARIA CIVIL

POUR L'OBTENTION DU GRADE DE DOCTEUR ÈS SCIENCES (PhD)

PAR

João Nuno GOMES BORGA DELGADO

acceptée sur proposition du jury:

Prof. D. Dujic, président du jury
Prof. F. Avellan, Prof. D. I. Cameira Covas, directeurs de thèse
Dr Ph. Dupont, rapporteur
Dr B. Silva, rapporteur
Prof. J. Schiffmann, rapporteur



Suisse
2018

Sê todo em cada coisa. Põe quanto és
No mínimo que fazes.
— Ricardo Reis (Fernando Pessoa heteronim)

To my parents, Ana and João

Acknowledgements

I am sincerely grateful to both my thesis directors Professor François Avellan and Professor Dídía Covas. Thank you Professor François Avellan for providing me with the amazing opportunity to carry out my doctoral studies and be a member of the Laboratory for Hydraulic Machines. Your knowledge, trust and encouragement to achieve my best were essential to successfully complete this PhD. Thank you Professor Dídía Covas for trusting me at such a young age which allowed me entering in the world of research in Instituto Superior Técnico. Your scientific guidance and advice, constant support, ready availability and positive thinking were a driving force to finish this PhD.

I would like to thank my thesis jury members, Professor Drazen Dujic, Professor Jürg Schiffmann, Doctor Philippe Dupont and Doctor Bernardo Silva for spending their valuable time and patience reading my thesis and for challenging me with tough questions during my thesis defence. I also acknowledge your comments and suggestion during the defence.

This thesis was performed thanks to the generous financial support provided by the doctoral program H2Doc (PD/00206/2012) funded by the Portuguese Foundation for Science and Technology, by the European Commission's LIFE Program (LIFE14 ENV/PT/000508) and by the Laboratory for Hydraulic Machines of École Polytechnique Fédérale de Lausanne. I also acknowledge Grundfos for their equipment offer for pursuing my experimental tests.

I would like to acknowledge Doctor Loïc Andolfatto for his scientific advice, suggestions and support during my PhD. The final result of my thesis is greatly influenced by the discussions we had. I express my gratitude to Professor António Cardoso for urging my critical thinking during our many talks in the halls of IST. I also thank Professor Paulo Branco for receiving me as a host in the Laboratory of Electric Machines of IST. I am grateful to Professor Helena Ramos and Professor Rui Ferreira for sharing their laboratory equipment during my experiments.

I was lucky to find a great environment and teams in both the Laboratory for Hydraulic Machines (LMH) and in Instituto Superior Técnico (IST).

I would like to express my gratitude to all LMH staff. I acknowledge Doctor Mohamed Farhat for the many interesting scientific discussions. I express my deep gratitude to Henri-Pascal Mombelli and to George Crittin for sharing his tremendous knowledge about hydraulic test-rigs and instrumentation. I appreciate the time and effort spent by the test engineers group with special mention to Alberto Bullani and Ambrosio Acal Ganaza. I express my gratitude to Vincent Berruex, Alain Renaud and Philippe Faucherre for the assistance during the mechani-

Acknowledgements

cal design of my test-rig and for the numerous problem-solving ideas, as well as to Philippe Cerrutti for his technical support with software. A special thanks go to Isabelle Stoudmann Schmutz for all her administrative support, good mood and travelling tips. Finally, this document would not have been possible without the administrative support provided by Cécile Taverney at EDEY doctoral school and Sandra Roux at the registrar's office.

I would like to express my gratitude to all the IST staff. I acknowledge Pedro Sanches for helping me in the management of the laboratory activities. I also acknowledge João Pedro Caetano for the technical support provided and for constantly challenging me with difficult decision making. I express my gratitude to João Paulo for helping me with the experimental tests and for managing the test-rig while I was in Lausanne. I also want to appreciate Jóni Silva for helping me during my stay in the Laboratory for Electric Machines in IST. A special thanks go to Dulce Fernandes for her endless administrative support and fast problem-solving. Finally, I acknowledge the administrative support provided by Paula Marques at the Civil Engineering doctoral school and of Júlia Oliveira at the post-graduation area.

Life at LMH was much easier because of the wonderful people I have met here. A special thanks go to João, Elena and Outi. Thank you, João, for the helpful discussion and advice, but also for the every-day comical comparisons between Portuguese of Portugal and Portuguese of Brasil. Good luck with your doctoral thesis. Thank you, Elena, for being always available to help. Thank you, Outi, for your inspiring positivity. I am grateful to Andres, Arthur, Christian L., Cristhian V., Keita and Matthieu for welcoming me in LMH and introducing me *Great Escape* and *Étoile Blanche*. Also, I would like to thank Ali, Sebastian, Siamak and Alexis for the many coffee breaks, lunches and for the many absurd conversations. Good luck with your doctoral thesis. I would like also to thank Audrey, Ebrahim, Federico, Simon and Pascal for the memorable moments in LMH. Finally, I acknowledge the visiting members Chu, Masashi, Qin, Takashi, Vinod and Xiaoran for having brought a bit of their culture to LMH.

The journey in IST was much easier thanks to my colleagues and the great environment that they have provided. I acknowledge my office mates Ana Quaresma and Federica for the many hours spent in our tiny office. I am grateful for having met my H2Doc colleagues Ana Clara, Dora and Paloma for sharing great moments between Lisbon and Lausanne. A special thanks go to Ivan for the great friendship and for the amazing weekend in Madrid. Sorry for all the rice they feed you in IST. I am grateful for taking part in a great research team lead by Professor Dídia Covas, namely Alexandre, Aisha, David Ferras, David Figueiredo, João Paulo, Laura, Marta and Nuno. Thank you for all the discussions and ideas-sharing moments during this period. I would like also to acknowledge other research members, namely Ana Margarida, Daniel, Isabel, Maria João, Mariana, Mohsen, Moisés, Nuno B., Ricardo, Sebastián, Olga for contributing to a great work environment in IST.

To all my friends from Salvaterra de Magos, one sentence is nothing but shorting our long-lasting friendship. However, I am grateful: to André D., for your everlasting missing promises for breakfast after the *Sardinha Assada*; to André R., for our travels around Europe due to Sport Lisboa e Benfica matches; to Catarina C., for Martim and for the honour of being your wedding best man; to Catarina F., for being always available no matter the time and distance; to Cátia,

for your impressive and contagious joy; to Cláudia, for your nearly awkward but compelling honesty; to Inês, for your endless effort to keep up our friendship despite living 350 km apart; to João C., for your creativity in the kitchen and delivering next-level ideas to our dinners; to João L., for the amazing moments in Stockholm and the shared "pain" of making a PhD :); to Luís L., for being a great kid with a big soul; to Patrícia, for bringing me up in the most challenging moments; To Pedro D., for your bullseye observations and being an *ex-aequo* best flatmate ever; to Pedro S., for your delayed laughs and random discussions; to Rui S., for your nearly provocative but funny rhetoric; to Teresa, for your inspiring kindness and for being the other *ex-aequo* best flatmate ever; to Tiago, for your encouraging drive and positivity and for your immediate readiness for having dinner and beers.

I would like to express my gratitude to my friends from *IsB*, namely Diogo, Francisco, João C., João E, João M., Manuel, Romeu and Rui. Thank you for the many dinners, Cais do Sodrê beers, roasted suckling pig lunches and 580+ messages a day in WhatsApp. I will always remember the bachelor party of Manuel in Porto and I am actually looking forward to the next one. Who takes the lead? I want also to acknowledge Bruno David, Diogo E, Diogo R., Eddy, Hugo, João B. and Luís for the several after-work beers in *Cidália* and for the long dinners on Thursdays like if it was Friday. I hope our university bond remains for the future. Otherwise, how would we discuss complex subjects with the seriousness of an expert but with the accuracy of a tavern keeper? Also, I want to thank Samuel for the many weekends travelling, skiing and partying, which deeply facilitated my stay in Switzerland. Thank you for teaching me how to ski.

The journey in Lausanne would have been much more difficult without the support of José, Lurdes and their two amazing daughters Cátia and Patrícia. Thank you for welcoming me in Lausanne, for helping in whatever request I asked you and for the many dinners. You were and will continue to be, a true inspiration for me.

I am extremely grateful to my girlfriend, Ana. Everything I write here will fall short compared to the support you have provided me in my difficult moments and the great time we have spent together. Thank you for the countless hours we have spent on video calls and for the long weeks you have waited for me. You were a true driving force for the successful completion of this thesis. Thank you so much for everything!

Finally, I am grateful to my grandparents Adelaide, Antónia and João for showing me the positive change we can make in the world without even knowing how to read. Thank you Avó Adelaide for looking at me from up there. To my sister Joana, I am grateful for the countless advice, for the constant support and for providing me with the best gift I have had in these 4 years: my nephew Pedro Gil. I am also grateful to my brother-in-law Pedro for the great time and funny moments we had during this period. Last but not least, I am deeply thankful to my parents Ana and João for providing me with the best possible education, for never placing barriers in my creativity and objectives and for showing me that the concept of resilience achieves a whole new other magnitude when applied to you. This thesis is dedicated to you!

Lausanne, 06 November 2018

J. D.

Abstract

Pressurised water supply systems are infrastructures that offer a potential for energy recovery in locations where these systems operate with an excessive pressure. The integration of micro hydropower plants for energy recovery is a challenge, as these systems feature a significant daily discharge variation, which limits the domain of operation of these power plants.

Pumps running as turbines (PATs) are hydraulic machines suitable for this application, despite facing two major issues. Firstly, PATs are characterised by a sharp efficiency decrease when operating far from the best operating point. Secondly, the characteristic curves of the turbine mode are not provided by pump manufacturers, which hinders the implementation of PAT power plants.

The present thesis is based on the experimental investigation of the variable speed operation of centrifugal pumps used as turbines aiming at optimising the energy recovered. A new methodology is developed, firstly, to estimate the performance of the turbine mode (flow rate, specific energy, power and efficiency) and, secondly, to model the variable speed hill chart performance of PATs. The research procedure includes the experimental investigation of the characteristic curves of the PATs, the experimental investigation of the unstable phenomena experienced by the PATs and, finally, the development of an empirical model for predicting the PATs performance.

Firstly, the variable speed operation of PATs is experimentally investigated. Data are collected for three single-stage end-suction centrifugal pumps with different unit specific speed values to characterise the characteristic curves of the turbine mode and of the extended operation in the generating mode. Measurements of the water temperature, the discharge, the pressure, the torque and the rotational speed are performed to determine the hydraulic and the mechanical performance of these PATs.

Secondly, the pressure fluctuations developed during the part load and the full load operation of PATs are investigated. Data collected include the pressure measurements in the high and in the low pressure sections of the PAT and the high speed flow visualisation in the PAT draft tube. The spectral analysis of the pressure measurements and the image processing of the flow visualisation highlight the dynamics of a cavitation precessing vortex rope that develops in the PAT draft tube.

Thirdly, a new empirical model is developed to estimate the hydraulic and mechanical characteristic curve of PATs and to model the variable speed hill chart performance of the PAT. The methodology is based on the Hermite polynomial chaos expansion (PCE), which propagates the known characteristic curves obtained during the experimental tests, providing a continu-

Acknowledgements

ous surrogate function for predicting the characteristic curves of a given PAT, inside the range of unit specific speed values tested. The PCE is, afterwards, applied for modelling the variable speed hill chart performance of the PAT.

Obtained results provide an insight on the variable speed operation of PATs with respect to the turbine mode, the extended operation in the generating mode, the possibility of the development of pressure fluctuation instabilities and, finally, the modelling of the variable speed hill chart performance for a given PAT. The hill chart model is described by a continuous polynomial function, which can be used to optimise the design and the operation of PAT micro hydropower plants, aiming at maximising the energy recovered and at avoiding potential instabilities caused by the part load and the full load operation.

Keywords: Pumps running as turbines, variable speed operation, water supply systems, hydropower, performance prediction, hill chart modelling.

Résumé

Les réseaux de distribution d'eau sont des infrastructures qui offrent un potentiel de récupération d'énergie dans le cas où les conduites sont sous haute pression. L'intégration des microcentrales hydroélectriques dans ces réseaux pour récupérer l'énergie constitue un défi, car ils sont caractérisés par un débit variable et ce qui limite le domaine de fonctionnement de ces microcentrales.

Les pompes utilisées comme des turbines (PATs) sont des machines hydrauliques adaptées pour cette application, cependant elles doivent faire face à deux problèmes. Premièrement, les PATs sont caractérisées par une brusque baisse de rendement dans les modes de fonctionnement qui s'éloignent du rendement optimal. Deuxièmement, les courbes caractéristiques du fonctionnement en turbine ne sont pas fournies par les fabricants des pompes et ce qui fait obstacle à leur mise en œuvre.

La présente thèse s'appuie sur l'étude expérimentale du fonctionnement à vitesse variable des pompes centrifuges utilisées comme des turbines avec l'objectif d'optimiser l'énergie récupérée. Une méthodologie est développée d'une part pour estimer les performances du fonctionnement en turbine (le débit, l'énergie spécifique, la puissance et le rendement) et d'autre part pour la modélisation du fonctionnement à vitesse variable des PATs. La démarche suivie comprend l'étude expérimentale des courbes caractéristiques des PATs, l'étude expérimentale des phénomènes instables auxquelles sont soumises les PAT et, enfin, le développement d'une méthode de modélisation empirique permettant de prédire son fonctionnement.

Premièrement, le fonctionnement à vitesse variable des PATs est étudié expérimentalement. Les données sont collectées pour trois pompes centrifuges à un étage et à aspiration axiale avec différentes valeurs de vitesse spécifique pour caractériser les courbes caractéristiques du fonctionnement en turbine et son extension. Les mesures de la température de l'eau, du débit, de la pression, du couple et de la vitesse de rotation sont effectuées pour déterminer les performances hydrauliques et mécaniques de ces PATs.

Deuxièmement, les fluctuations de pression qui se développent pendant le fonctionnement en turbine à charge partielle ou à forte charge sont étudiées. L'étude expérimentale inclut des mesures de pression dans les sections à haute et basse pression et l'acquisition d'images à haute vitesse dans la section à basse pression. L'analyse spectrale des mesures de pression et les traitements d'images mettent en lumière la dynamique d'un vortex de cavitation animé d'un mouvement de précession qui se développe dans la section à basse pression de la PAT. Troisièmement, le développement d'un modèle empirique est réalisé pour estimer les courbes caractéristiques des PATs et modéliser la colline de rendements à vitesse variable de la PAT.

Acknowledgements

La méthodologie est basée sur la méthode du chaos polynomial, qui propage les courbes caractéristiques connues, obtenues lors d'essais expérimentaux, fournissant ainsi une fonction d'interpolation continue pour les prédire les courbes caractéristiques hydrauliques et mécaniques de la PAT, dans l'intervalle des valeurs de vitesse spécifiques testées. Cette méthode du chaos polynomial est également appliquée pour modéliser la colline de rendement de la PAT fonctionnant à vitesse variable.

Les résultats obtenus donnent un aperçu du fonctionnement à vitesse variable des PATs en ce qui concerne les performances en mode turbine et son extension, l'éventualité du développement d'instabilités et, enfin, la modélisation de la colline des rendements de la PAT. La modélisation du fonctionnement à vitesse variable fournit une fonction polynomiale continue, qui peut être utilisée pour optimiser la conception et le fonctionnement de la microcentrale hydroélectrique avec l'objectif de maximiser la récupération d'énergie et d'éviter les instabilités éventuelles causées par les fonctionnements à charge partielle et à forte charge.

Mots-clés : pompes utilisées comme des turbines, vitesse variable, réseaux de distribution d'eau, hydroélectricité, prédiction de performances, modéliser la colline des rendements.

Resumo

Os sistemas de abastecimento de água são infraestruturas que oferecem um potencial para recuperação de energia nos locais onde as suas condutas operam com um excesso de pressão. A integração de micro centrais hidroelétricas para recuperação de energia nos sistemas de abastecimento de água é um desafio, uma vez que estas infraestruturas são caracterizadas por um caudal variável, o que limita o domínio de operação destas micro centrais hidroelétricas. As bombas a funcionar como turbinas (PATs) são máquinas hidráulicas apropriadas para esta aplicação. No entanto, a sua utilização para este fim apresenta dois desafios. Em primeiro lugar, as PATs são caracterizadas por uma queda de rendimento acentuada quando estas operam longe do ponto de melhor eficiência. Em segundo lugar, as curvas características do funcionamento no modo de turbina não são fornecidas pelos fabricantes das bombas, dificultando o dimensionamento das micro centrais hidroelétricas.

A presente tese é baseada na investigação experimental de bombas centrífugas a funcionar como turbina com velocidade variável com o objetivo de otimizar a energia recuperada. É desenvolvida uma nova metodologia que permite não só prever as curvas características da operação em modo de turbina (caudal, energia específica, potência e eficiência), como também modelar a operação das PATs com velocidade variável. A metodologia seguida inclui a investigação experimental da operação das PATs com velocidade variável em regime estacionário, a investigação experimental de fenómenos de instabilidade a que as PATs estão sujeitas quando operam longe do ponto de melhor eficiência e, finalmente, o desenvolvimento de um método de modelação empírica para prever as curvas características em modo de turbina e modelar a colina de rendimentos da operação com velocidade variável em modo turbina.

Em primeiro lugar, a operação com velocidade variável é investigada experimentalmente. São testadas experimentalmente três bombas centrífugas de um andar e aspiração axial com diferentes valores de velocidade específica para determinar as suas curvas características em modo de turbina e nos quatro quadrantes de operação. São efetuadas medições de caudal, de pressão, da temperatura da água, do binário no eixo e da velocidade de rotação para caracterizar o desempenho hidráulico e mecânico das três PATs.

Em segundo lugar, as flutuações de pressão que se desenvolvem quando as PATs operam com carga parcial e em plena carga são investigadas. A investigação experimental inclui medições de pressão nas secções de alta e de baixa pressão da PAT e a visualização do escoamento na secção de baixa pressão da bomba através da aquisição de imagens a alta velocidade. A análise espectral das medições de pressão e o processamento das imagens adquiridas revela a

Acknowledgements

dinâmica de um vórtice de cavitação com um movimento de precessão que se desenvolve na secção de baixa pressão da PAT durante a operação em carga parcial.

Em terceiro lugar, é desenvolvido uma metodologia para estimar as curvas características do funcionamento das PATs e para modelar as suas colinas de rendimento da operação com velocidade variável destas máquinas no modo de turbina. A metodologia é baseada na teoria do caos polinomial que propaga as curvas características obtidos nos ensaios experimentais, disponibilizando uma função empírica contínua para prever as curvas características hidráulicas e mecânicas do funcionamento das PATs, dentro do intervalo de valores da velocidade específica das bombas testadas experimentalmente. A teoria do caos polinomial também é aplicada para modelar o diagrama em colina da bomba funcionar como turbina com velocidade variável.

Os resultados obtidos nesta tese fornecem um novo conhecimento da operação das PATs em relação ao seu desempenho em modo de turbina e da operação nos quatro quadrantes, à possibilidade de desenvolvimento de instabilidade e, finalmente, à modelação da colina de rendimento da operação com velocidade variável em modo turbina. A modelação desta colina de rendimento através da teoria do caos polinomial fornece uma função contínua que pode ser utilizada para otimizar a conceção e a operação de micro centrais hidroelétricas com o objetivo de maximizar a recuperação de energia e evitar as possíveis instabilidades causadas pela operação das PATs em carga parcial e em plena carga.

Palavras chave: Bombas a funcionar como turbina, velocidade variável, sistemas de abastecimento de água, energia hidroelétrica, previsão curvas características, modelação da colina de rendimentos.

Contents

Acknowledgements	v
Abstract (English/Français/Português)	ix
List of figures	xvi
List of tables	xxii
Nomenclature	xxv
1 Introduction	1
1.1 Research context	1
1.2 Literature review	2
1.2.1 Water supply systems	2
1.2.2 Pumps running as turbines	7
1.2.3 Gaps of knowledge	14
1.3 Thesis objective	15
1.4 Thesis structure	15
2 Experimental investigation	17
2.1 Introduction	18
2.2 Experimental setup	23
2.2.1 Test-rig and measurement equipment	23
2.2.2 Experimental tests performed	26
2.3 Results	29
2.3.1 Pump mode	29
2.3.2 Turbine mode	29
2.3.3 Extended operation	30
2.4 Discussion	39
2.4.1 Variable speed operation in turbine mode	39
2.4.2 Extended operation	42
2.5 Conclusions and perspectives	46
2.6 Appendix	47
2.6.1 Appendix A - BEP measurements of the pump mode	47
2.6.2 Appendix B - BEP measurements of the turbine mode	49

Contents

3	Pressure fluctuations in off-design operation	51
3.1	Introduction	52
3.2	Experimental setup	54
3.2.1	Test-rig and measurement equipment	54
3.2.2	Investigated operating points	57
3.3	Methodology	60
3.3.1	Pressure fluctuation and spectral analysis	60
3.3.2	Cavitation vortex rope image processing	61
3.4	Results and discussion	64
3.4.1	Preliminary analysis	64
3.4.2	Part load operation	65
3.4.3	Full load operation	71
3.5	Conclusion and future perspectives	73
4	PAT characteristic curves modelling and prediction	75
4.1	Introduction	76
4.2	Experimental data	79
4.3	Hermite polynomial chaos expansion modelling	83
4.3.1	General approach	83
4.3.2	Hermite polynomials basis	84
4.3.3	Identification of the surrogate function	86
4.4	Modelling of the surrogate functions	91
4.4.1	Identification of the truncated basis	91
4.4.2	Turbine mode surrogate functions	92
4.4.3	Extended operation surrogate functions	98
4.5	Hill chart modelling	100
4.6	Conclusions and future perspectives	101
5	Guidelines for modelling the PAT performance	105
5.1	Introduction	105
5.2	Guidelines	107
5.2.1	Performance prediction	107
5.2.2	Hill chart modelling	113
5.3	Surrogate functions parameters	118
6	Conclusion and outlook	123
6.1	Conclusion	123
6.2	Outlook	126
	Bibliography	129
	Curriculum Vitae	145

List of Figures

1.1	Trunk main system of the water utility <i>Águas do Algarve</i> , Portugal.	4
1.2	Water distribution network of Lisbon, Portugal. The different colours represent independent control areas of the network supplied by different service tanks. . .	5
1.3	Consumption pattern: (a) monthly variation; (b) weekly and seasonal variation. . .	6
1.4	Centrifugal pumps commonly used in drinking water applications. (a) Single-stage end-suction centrifugal pump, (b) in-line radially split centrifugal pump; (c) in-line single-stage centrifugal pump; (d) in-line multi-stage centrifugal pump. . .	8
1.5	Velocity triangles at the PAT high and low pressure sections for the BEP and for the part load and full load operating conditions.	9
2.1	Average head and discharge values available for energy recovery in water supply systems. The isolines represent the available hydraulic power.	18
2.2	Comparison between the scope of application of conventional hydropower turbines and the average operating conditions for energy recovery in WSS.	20
2.3	Comparison between PAT scope of operation and the average values of the head and discharge available for energy recovery in WSS	20
2.4	Schematic representation of the discharge time history in a water distribution network during one week. The dashed line represents the average discharge. Typically, the maximum discharge is higher by a factor of 3 or 4 than the minimum discharge.	21
2.5	Velocity triangles in the PAT high and low pressure sections for the part load operation, the best efficiency point and the full load operation.	21
2.6	Identification of the four-quadrants of operation.	22
2.7	Test-rig assembled for collecting the experimental investigation.	24
2.8	Measurement equipment setup.	25
2.9	Experimental results in the pumping mode of the $n_q = 23.1$ pump.	31
2.10	Experimental results in the pumping mode of the $n_q = 41.0$ pump.	32
2.11	Experimental results in the pumping mode of the $n_q = 67.3$ pump.	33
2.12	Experimental results in the turbine mode of the $n_q = 23.1$ pump.	34
2.13	Experimental results in the turbine mode of the $n_q = 41.0$ pump.	35
2.14	Experimental results in the turbine mode of the $n_q = 67.3$ pump.	36
2.15	Experimental results in the four-quadrants of the $n_q = 23.1$ pump.	37
2.16	Experimental results in the four-quadrants of the $n_q = 41.0$ pump.	37

List of Figures

2.17	Experimental results in the four-quadrants of the $n_q = 67.3$ pump.	38
2.18	Summary of the three PATs characteristic curves in generating mode. Variation of n_{ED} and η^T with respect to Q_{ED} . The colors of the markers refer to the rotational speed value, for instance as in Figure 2.14.	40
2.19	Visualisation of the cavitation vortex rope in the $n_q = 67.3$ PAT draft tube for the operation in part load conditions.	41
2.20	Effect of variable speed in the third and fourth quadrant of the $n_q = 23.1$ pump.	42
2.21	Effect of variable speed in the third and fourth quadrant of the $n_q = 41.0$ pump.	43
2.22	Effect of variable speed in the third and fourth quadrants of the $n_q = 67.3$ pump.	44
2.23	Total relative error of n_{ED} and Q_{ED} in the third and fourth quadrant of $n_q = 41.0$ pump.	45
3.1	Test-rig assembled for the experimental investigation. The high speed visualisation setup is shown in 4.	55
3.2	Measurement equipment and high speed camera setup.	56
3.3	Measured operating points of the stationary PAT performance in the turbine mode given by the variation of n_{ED} and η^T with respect to Q_{ED} . Details a to g indicate the Q_{ED} constant values used to define the operating points for investigating the pressure fluctuations.	59
3.4	PAT variable speed hill chart performance of E and η^T as a function of N and Q with the indication of the operating points for investigating the pressure fluctuations. The white line represents the best efficiency ridge line.	59
3.5	Flow chart of the image processing method for tracking the vortex. x represents the area of the white pattern of interest in the image to feature the vortex. This flow chart corresponds to methodology applied to each frame.	62
3.6	Image processing method example applied to the target area (corresponding to 100 px). (a) identification of the cavitation vortex edges; (b) application of the filter for the filling function.	63
3.7	Time history of the pressure coefficient measured in the low pressure section $C_{p,2}$ with respect to the runner revolutions. The operating points correspond to Q/Q_{BEP} values of 1.07, 0.93, 0.84 and 0.76 and $N = 2'400 \text{ min}^{-1}$ (thus, 1 rev = 0.025 s). The operating points are given for two constant back-pressure levels, defined by: (a) $\chi_{nD} = 10.0$; (b) $\chi_{nD} = 17.5$	65
3.8	Flow visualisation in the PAT draft tube for $N = 2'400 \text{ min}^{-1}$ and Q/Q_{BEP} values of 1.07, 0.93, 0.84 and 0.76. Each operating point is shown for two constant χ_{nD} values of 10.0 and 17.5.	66
3.9	Waterfall plot of the auto-spectrum density functions of the pressure coefficient at the low pressure side $G_{xx}(C_{p,2})$ for the operating points corresponding to $N = 2'400 \text{ min}^{-1}$ and Q/Q_{BEP} values of 1.07, 0.93, 0.84 and 0.76. Each waterfall plot correspond to a constant value of back-pressure defined by: (a) $\chi_{nD} = 10.0$; and (b) $\chi_{nD} = 17.5$	66

3.10	Image processing of the cavitation vortex rope precessing motion. The radial displacement of the vortex y is compared with six snapshots during one period of the precessing motion $T = 1/24.9 = 0.04$ s identified by the details (i) to (vi) in the time history chart. The operating point corresponds to $Q_{ED} = 0.376$, $N = 2'400 \text{ min}^{-1}$ and $\chi_{nD} = 17.5$	67
3.11	Analysis of the precessing frequency of the cavitation vortex rope for the operating points corresponding to $N = 3'000 \text{ min}^{-1}$: (a) influence of the relative discharge on the precessing frequency; (b) Influence of the Swirl number on the Strouhal number of the precessing vortex core. The colours of the scatter points in both charts are scaled by the Thoma number σ	68
3.12	Waterfall plot of the auto-spectrum density functions of the pressure coefficients: (a) in the high pressure section $G_{xx}(C_{p,1})$; and (b) in the low pressure section $G_{xx}(C_{p,2})$. Each chart shows the operating points shown corresponding to $N = 2'400 \text{ min}^{-1}$ and $Q_{ED} = 0.376$. All operating points are shown for χ_{nD} values of 10.0, 12.5, 15.0 and 17.5.	69
3.13	Identification of the synchronous frequency f_0 by the computation of the auto-spectrum density functions $G_{xx}(C_{p,1})$ and $G_{xx}(C_{p,2})$, coherence function C_{xy} and cross-spectrum density G_{xy} between $C_{p,1}$ and $C_{p,2}$. The frequency values $f_A = 0.68 \times n$ and $f_B = 1.00 \times n$ represent the f_0 values found for $\chi_{nD} = 10.0$ and $\chi_{nD} = 10.0$, respectively.	70
3.14	Influence of the local cavitation coefficient χ_{nD} on the cavitation vortex rope diameter D_{rope} and on the frequency values f_{PVC} , f_0 and f_1 identified in the flow visualisation image processing and in the spectral analysis of the pressure measurements.	71
3.15	Waterfall plot of the auto-spectrum density functions of the pressure coefficients: (a) in the high pressure section $G_{xx}(C_{p,1})$; and (b) in the low pressure section $G_{xx}(C_{p,2})$. Each chart shows the operating points shown corresponding to $N = 2'400 \text{ min}^{-1}$ and $Q/Q_{\text{BEP}} = 1.07$. All operating points are shown for χ_{nD} values of 10.0, 12.5, 15.0 and 17.5.	72
3.16	Waterfall plot of the auto-spectrum density functions of the pressure coefficients: (a) at the high pressure section $G_{xx}(C_{p,1})$; and (b) at the low pressure section $G_{xx}(C_{p,2})$. Each chart shows the operating points shown corresponding to $N = 2'100 \text{ min}^{-1}$ and $Q/Q_{\text{BEP}} = 1.17$. All operating points are shown for χ_{nD} values of 12.5, 15.0 and 17.5 and 20.0.	73
4.1	Four-quadrants of operation of a pump. Identification of the operating zones of interest for the PAT performance modelling in the extended operation in the generating mode, hereafter referred as <i>extended operation</i> . The zones of interest are Turbine (A), Turbine break (B) and Reverse pump (C), which correspond to the Quadrants of operation III and IV.	78

List of Figures

4.2	Turbine mode stationary performance of the three PATs experimentally tested described by the non-dimensional coefficients Q_{ED} , T_{ED} and P_{ED} with respect to n_{ED}	81
4.3	Extended operation performance of the three PATs described by the non-dimensional coefficients Q_{ED} , T_{ED} and P_{ED} with respect to n_{ED}	82
4.4	First 15 bivariate polynomials of the family He_p	86
4.5	Flow chart for the identification of the truncated basis for describing the surrogate function of a given variable of interest y with respect to the interpolation domain $\mathbf{x} = (x_1, x_2)$	89
4.6	Flow chart for computing the surrogate functions for the identified hydraulic and mechanical surrogate functions.	90
4.7	Application of the standardisation function $g(\mathbf{x})$ to a physical input data set: (a) measured data $\mathbf{x} = (n_{ED}, n_q)$; (b) standardised data $\mathbf{X} = (X_1, X_2)$. The convex hull is indicated by the blue area.	92
4.8	Metrics evaluation for determining the surrogate function $f_{QED}^T(n_{ED}, n_q)$ applied to the experimental data.	93
4.9	Comparison of the truncated basis cardinality for computing the surrogate function f_{QED}^T : (a) underfitted model; (b) chosen model; (c) overfitted model.	94
4.10	3D view of the identified surrogate functions for the propagation of the: (a) hydraulic and the (b) mechanical characteristic curves. The red mesh refers to the surrogate functions found for the collected experimental data f_{QED}^T and f_{PED}^T . The green mesh refers to the surrogate functions found for the literature data $f_{QED,B}^T$ and $f_{PED,B}^T$	94
4.11	Contour view of the identified surrogate functions for the propagation of the hydraulic and mechanical characteristic curves referent to the turbine mode. The red contours indicate the surrogate functions applied to the collected experimental data. The green contours indicate the evaluation of the surrogate functions applied to the literature data. (a.1) f_{QED}^T ; (b.1) f_{PED}^T ; (a.2) $f_{QED,B}^T$; (b.2) $f_{PED,B}^T$	95
4.12	Comparison between the experimental data, literature data and the results obtained from implementing the hydraulic surrogate functions regarding the turbine mode f_{QED}^T and $f_{QED,B}^T$ (see Table 4.3 for the nomenclature of the surrogate functions). PATs are identified by the n_q values (see Table 4.2). The scatter points refer to the experimental data and to the literature data for each PAT. The lines refer to the results obtained by the identified hydraulic surrogate functions.	96
4.13	Comparison between the experimental data, literature data and the results obtained from implementing the mechanical surrogate functions regarding the turbine mode f_{PED}^T and $f_{PED,B}^T$ (see Table 4.3 for the nomenclature of the surrogate functions). PATs are identified by the n_q values (see Table 4.2). The scatter points refer to the experimental data and to the literature data for each PAT. The lines refer to the results obtained by the identified mechanical surrogate functions.	97

4.14	3D view of the identified surrogate functions for the propagation of the (a) hydraulic and the (b) mechanical characteristic curves referent to the extended operation. The red mesh refers to the surrogate functions found for the experimental data f_{QED}^{EO} and f_{TED}^{EO}	98
4.15	Comparison between the experimental data and the results obtained from implementing the surrogate functions in the extended operation: (a) hydraulic surrogate function f_{QED}^{EO} ; (b) mechanical surrogate function f_{TED}^{EO} . PATs are identified by the n_q values (see Table 4.2). The scatter points refer to the experimental data for each PAT. The lines refer to the results obtained by the identified surrogate functions.	99
4.16	3D view of the adjustment of the surrogate functions for modelling the variable speed hill chart performance of the $n_q = 23.1$ PAT: (a) f_E^{HC} ; (b) f_η^{HC} . The red mesh surface indicate the identified surrogate functions, while the scatter dots indicate the experimental data collected.	102
4.17	Hill chart of the turbine mode performance of the PAT with $n_q = 23.1$. Specific hydraulic energy E and efficiency η variation as a function of the discharge Q and rotational speed N . The white line indicates the best efficiency ridge line. .	103
4.18	Hill chart of the turbine mode performance of the PAT with $n_q = 41.0$. Specific hydraulic energy E and efficiency η variation as a function of the discharge Q and rotational speed N . The white line indicates the best efficiency ridge line. .	103
4.19	Hill chart of the turbine mode performance of the PAT with $n_q = 67.3$. Specific hydraulic energy E and efficiency η variation as a function of the discharge Q and rotational speed N . The white line indicates the best efficiency ridge line. .	104
5.1	Flow chart diagram for modelling the PAT variable speed hill chart performance depending on the design stage of the power plant.	106
5.2	Illustration of the PAT performance prediction methodology for the case of a pump with $n_q^P = 50$ using the hydraulic surrogate function for the experimental data collected in Chapter 2.	106
5.3	Flow chart diagram for predicting the PAT characteristic curves. If predicting the extended operation, the computed value for the mechanical characteristic curve in Step 8 corresponds to T_{ED} and Step 10 is not performed.	112
5.4	Flow chart diagram for modelling the variable speed hill chart performance of the PAT. This flow chart is valid for one variable of interest y . Repeat the flow chart if more than one variable of interest is to be modelled.	117
5.5	Contour view of the identified surrogate functions for the propagation of the hydraulic and mechanical characteristic curves referent to the turbine mode using the experimental data collected (see Chapter 2). (a) f_{QED}^T ; (b) f_{PED}^T	119
5.6	Contour view of the identified surrogate functions for the propagation of the hydraulic and mechanical characteristic curves referent to the turbine mode using the literature data. (a) $f_{QED,B}^T$; and (b) $f_{PED,B}^T$	121

List of Figures

- 5.7 Contour view of the identified surrogate functions for the propagation of the hydraulic and mechanical characteristic curves referent to the extended operation using the experimental data collected (see Chapter 2). (a) f_{QED}^{EO} ; (b) f_{TED}^{EO} 122

List of Tables

1.1	Potential for energy recovery found in literature.	3
2.1	Breakdown of minimum and maximum values of head and discharge for energy recovery per infrastructure.	19
2.2	Quadrants and operating modes definitions used for the experimental investigation.	23
2.3	Measurement equipment characteristics.	25
2.4	Rated characteristics in pump mode of the tested centrifugal pumps.	26
2.5	Maximum efficiency values measured in pump and turbine mode.	30
2.6	BEP measurements for the three tested pumps in the pump mode for absolute N values between $1'500 \text{ min}^{-1}$ and $2'920 \text{ min}^{-1}$. Values inside parentheses indicate the total relative errors.	47
2.7	BEP measurements for the three tested pumps in the pump mode for absolute N values between $1'500 \text{ min}^{-1}$ and $2'920 \text{ min}^{-1}$. Values inside parentheses indicate the total relative errors. Note: * BEP not measured due to discharge limitations in the test-rig.	48
2.8	BEP measurements for the three tested pumps in the pump mode for absolute N values between $1'500 \text{ min}^{-1}$ and $2'920 \text{ min}^{-1}$. Values inside parentheses indicate the total relative errors.	48
2.9	BEP measurements for the three tested pumps in the turbine mode for absolute N values between $1'500 \text{ min}^{-1}$ and $3'000 \text{ min}^{-1}$. Values inside parentheses indicate the total relative errors.	49
2.10	BEP measurements for the three tested pumps in the turbine mode for absolute N values between $1'500 \text{ min}^{-1}$ and $3'000 \text{ min}^{-1}$. Values inside parentheses indicate the total relative errors. Note: * BEP not measured due to discharge limitations in the test-rig.	50
2.11	BEP measurements for the three tested pumps in the turbine mode for absolute N values between $1'500 \text{ min}^{-1}$ and $3'000 \text{ min}^{-1}$. Values inside parentheses indicate the total relative errors.	50
3.1	Measurement equipment characteristics.	55
3.2	Measured operating points for investigating the pressure fluctuations.	60

List of Tables

4.1	Domain of application of empirical formulations for predicting the PAT characteristic curves.	79
4.2	Rated characteristics in the pumping mode of the PATs used in this research. . .	80
4.3	Surrogate functions for the prediction and modelling of the PAT performance. . .	91
4.4	Characteristics and metrics values of the surrogate functions used for modelling the hydraulic and the mechanical characteristic curves in the turbine mode. Note that Q_{ED} and P_{ED} are dimensionless.	93
4.5	Characteristics and metrics values of the identified surrogate functions for modelling the propagation of the hydraulic and mechanical characteristic curves in the extended operation. Note that Q_{ED} and T_{ED} are dimensionless.	98
4.6	Characteristics and metrics values of the surrogate functions for modelling the variable speed hill chart performance of the PATs experimentally tested. Results of the metrics of the surrogate functions referring to E are in $\text{J} \cdot \text{kg}^{-1}$, while the ones referring to η^T are in %.	100
5.1	Surrogate functions identified for the prediction PAT performance	118
5.2	Values of the coefficient a , b and c and the average values μ_1 and μ_2 for the definition of the standardisation function $g(\mathbf{x})$	118
5.3	Values of the index p_{\max} and the corresponding truncated basis Ψ	119
5.4	Values of the weighting coefficients λ for the computation of the surrogate functions defined in Table 5.1.	120

Nomenclature

Acronyms

BEP	Best Efficiency Point
CFD	Computational Fluid Dynamics
EPFL	École Polytechnique Fédérale de Lausanne
IEC	International Electrotechnical Commission
IST	Instituto Superior Técnico
LMH	Laboratoire de Machine Hydraulique
PAT	Pump running As Turbine
PATs	Pumps running As Turbines
PCE	Polynomial Chaos Expansion
PVC	Precessing Vortex Core
PRV	Pressure Reducing Valve
RMS	Root Mean Square
VSD	Variable Speed Drive
WDN	Water Distribution Network
WSS	Water Supply System
WTP	Water Treatment Plant

Superscripts

FQ	Four-quadrants of operation
EO	Extended operation of the generating mode
HC	Hill chart
RMS	Root mean square
P	Pump mode
T	Turbine mode

Subscripts

1	High pressure section of the PAT
2	Low pressure section of the PAT
abs	Absolute
amb	Ambient
ED	IEC factor
el	Electric
g	Global
h	Hydraulic
R	Rated conditions
ref	Reference section
rope	Cavitation vortex rope
t	Total
va	vapour

Latin letters

C	Absolute flow velocity	$(\text{m}\cdot\text{s}^{-1})$
C_m	Meridional velocity component	$(\text{m}\cdot\text{s}^{-1})$
C_u	Circumferential (azimuthal) velocity component	$(\text{m}\cdot\text{s}^{-1})$
C_{xy}	Coherence	(-)
D	Diameter	(m)
E	Specific hydraulic energy	$(\text{J}\cdot\text{kg}^{-1})$
f	Frequency	(Hz)
f_0	Fundamental frequency	(Hz)
G_{xx}	Auto-spectrum density	(-)
G_{xy}	Cross-spectrum density	(-)
g	Gravity acceleration	$(\text{m}\cdot\text{s}^{-2})$
H	Head	(m)
He	Hermite polynomial	(-)
J	Pump moment of inertia	$(\text{kg}\cdot\text{m}^{-2})$
N	Rotational speed	(min^{-1})
$NPSE$	Net Positive Suction Energy	$(\text{J}\cdot\text{kg}^{-1})$
n	Rotating frequency	(Hz)
P	Shaft power	(W)
P_{sup}	Active supplied electric power	(W)
p	Pressure	(Pa)
Q	Discharge	$(\text{m}^3\cdot\text{s}^{-1})$
Q_{sup}	Reactive supplied electric power	(VAr)
R^2	Coefficient of determination	(-)
T	Shaft torque	$(\text{N}\cdot\text{m})$

t	Time	(s)
U	Rotating velocity	(m·s ⁻¹)
W	Relative flow velocity	(m·s ⁻¹)
z	Elevation	(m)

Greek letters

α	Absolute flow angle	(rad)
β	Relative flow angle	(rad)
Δp_1	Differential pressure between the high and the low pressure sections	(Pa)
Δp_2	Differential pressure between the low pressure section and the reference level	(Pa)
η	Efficiency	(-)
λ	Weighting coefficient	(-)
ρ	water density	(kg·m ⁻³)
σ	Thoma number	(-)
θ	Water temperature	(°C)
Ψ	Truncated basis of the surrogate function	(-)
ω	Angular velocity	(rad·s ⁻¹)

Dimensionless number

C_p	Pressure coefficient	(-)
Fr	Froude number	(-)
n_{ED}	IEC speed factor	(-)
n_q	Unit specific speed	(-)
Re	Reynolds number	(-)
P_{ED}	IEC power factor	(-)
Q_{ED}	IEC discharge factor	(-)
S	Swirl number	(-)
St	Strouhal number	(-)
T_{ED}	IEC torque factor	(-)
χ_{nD}	Local cavitation coefficient	(-)

Sets of Numbers

\mathbb{N}	Set of natural numbers	(-)
\mathbb{R}	Set of real numbers	(-)

1 Introduction

1.1 Research context

Documents, such as the as the Directive 2009/28/EC [1] with the 20/20/20 objectives or the World energy issues monitor report [2], point innovation in renewables energies and energy efficiency improvement as priority actions for the future. Energy recovery from existing water supply systems (WSS) targets both objectives, as it: (i) increases the infrastructures energy efficiency, by exploiting locally available resources [3]; and (ii) simultaneously leads to energy savings and increased revenue for the water utility during the infrastructure lifetime by producing renewable hydroelectric energy [4]. The integration of micro hydropower plants in WSS requires fewer construction works and has lower environmental impacts compared to conventional power plants [5], as the installation of these power plants only require minimum adaptation works in the existing infrastructure.

There are several water infrastructures where the recovery of the excess energy is possible, namely in: (i) pressurised drinking water systems [6]; (ii) wastewater systems [7]; (iii) irrigation networks [8]; (iv) runoff collection schemes [9]; desalination plants [10]; (v) district heating [11]; and (vi) cooling systems of deep mines [12]. This thesis work targets the challenges arising from recovering energy in pressurised drinking water systems.

Pressurised water supply systems are frequently operated with excess pressure, leading water utilities to implement pressure management strategies, aiming at reducing water leakage, at decreasing pipe ruptures and at improving the level of service [13]. Most pressure management strategies consist of the installation of pressure reduction or flow control devices, which dissipate the excess pressure by creating a local energy loss. Thus, the opportunity arises for the substitution of the aforementioned devices by micro hydropower plants, which simultaneously reduce the excess pressure in the water infrastructures while recovering energy. The installation of these power plants for energy recovery must comply with the water utilities main objective [14], which is to supply drinking water to consumers with adequate pressure and in sufficient quantity in both normal operation and emergency situations.

Pumps running as turbines (PATs¹) are pointed as cost-effective solutions for equipping power plants in WSS, where the installation of conventional hydropower units is usually unaffordable [15]. This is mainly motivated by the small available hydraulic power for recovery, which is generally in the order of magnitude of kilowatts. PATs are industrially made pumps, in which the flow is reversed through the machine. Consequently, instead of converting mechanical shaft power into hydraulic power of the fluid (normal pump operation), the PAT uses the excess energy in the fluid and converts it into mechanical shaft power, which is then used to drive a generator for electric energy production.

PATs are not specifically designed and engineered for energy production and, therefore, two main challenges need to be addressed [16]: (i) the difficulty in accurately predicting the turbine mode characteristic curves of the pump, as this information is usually not provided by pump manufacturers; and (ii) the improvement of the low efficiency when the PAT operates far from the best operating point, which is caused by the absence of an inlet flow control component (e.g., guide vanes of a Francis turbine). The latter challenge is especially relevant, as WSS are characterised by a daily discharge variation driven by the consumer's demand. The variable speed operation of PATs is suggested as an operating strategy suitable for controlling the discharge at the PAT inlet, resulting in a higher operating efficiency of the PAT micro hydropower plant [17]. However, this PAT variable speed control for energy recovery in WSS still requires further investigation.

In this context, the current research work addresses both the PAT characteristic curves prediction and the use of variable speed operation for increasing the PAT efficiency when operating under variable discharge conditions. The following Section 1.2 aims at: (i) summarising the main opportunities and challenges for energy recovery in pressurised drinking WSS (see Section 1.2.1); (ii) reviewing the research literature about PATs, which focuses on the turbine mode characteristic curves prediction and on the operating strategies for maximising the efficiency under the variable discharge (see Section 1.2.2); and (iii) identifying the gaps of knowledge which ground the research motivation of this thesis (see Section 1.2.3).

1.2 Literature review

1.2.1 Water supply systems

Pressurised drinking water supply systems may be divided into two sub-systems: trunk mains and water distribution networks. The characteristics of each system, both concerning the processes of water supply and of energy recovery, are distinct. Independently of the sub-system, the potential locations for energy recovery are defined as the sites where the flow is conveyed with an excessive pressure, not required for the effective downstream water supply.

The quantification of the available potential for energy recovery is one of the main challenges

¹For notation simplicity: (i) PAT refer to the single version of the acronym – pump running as turbine; (ii) PATs refer to the plural version of the acronym – pumps running as turbines

for the correct assessment of hydropower availability in a WSS. Examples of methodologies for screening and assessing the potential for energy recovery at a planning stage can be found in [18, 19]. Statistics of energy recovery potential in WSS in different regions made available in the literature are presented in Table 1.1. Despite smaller, if compared to conventional hydropower plants, the statistic values presented in Table 1.1 show a significant untapped potential for energy recovery in WSS.

Table 1.1 – Potential for energy recovery found in literature.

Reference	Location	Potential power (MW) or energy (GWh/year)
Choulot et al. [14]	Switzerland	20 MW
Gallagher et al. [19]	Wales and Ireland	18 GWh/year
Zakkour et al. [20]	United Kingdom	17 MW
Loots et al. [21]	Tshwane, South Africa	10 GWh/year
Soffia et al. [22]	Piemont, Italy	21 MW to 31 MW

The following sections describe in detail the characteristics and the opportunities for energy recovery in trunk mains and in water distribution networks.

Trunk mains

Trunk mains feature large diameter pipe systems (typically higher than 0.3 m) used for conveying bulk (or treated) water between pond reservoirs and water treatment plants (WTP), between WTP and service tanks, or between service tanks. Usually, a trunk main does not have service connections to the consumers [23]. Trunk mains convey water by means of gravity or pumping systems. Only the gravity-fed pipes are suitable for energy recovery, as pumping systems are designed for minimum energy consumption. An example of a trunk main system is shown in Figure 1.1. This trunk main system comprises two WTP, which supply multiple delivery points and service tanks using both pumping and gravity-fed pipes. Each gravity-fed trunk main supplies several service tanks. Thus, the difference of the elevation of the longitudinal pipeline profile and the service tanks water free surface level may create favourable conditions for energy recovery.

Locations for energy recovery in trunk mains are at the inlet of: (i) break-pressure tanks; (ii) service tanks; and (iii) water treatment plants. Break-pressure tanks are usually installed in trunk mains with significant variations in the elevation of the pipeline profile. Break-pressure tanks consist of water tanks at atmospheric pressure installed specifically for dissipating the excessive pressure in the trunk main [25]. Service tanks are installed between the trunk mains and the water distribution network. The service tanks main objectives are: (i) providing storage capacity by buffering the constant discharge supply from the trunk main and the variable consumer demand from the water distribution network [26]; (ii) guaranteeing the minimum pressure level at downstream the tank; and (iii) providing reliability in case of an emergency event (e.g., firefighting) [27]. Service tanks supplied by gravity-fed trunk mains are equipped with flow control valves at the tank inlet for controlling the discharge depending

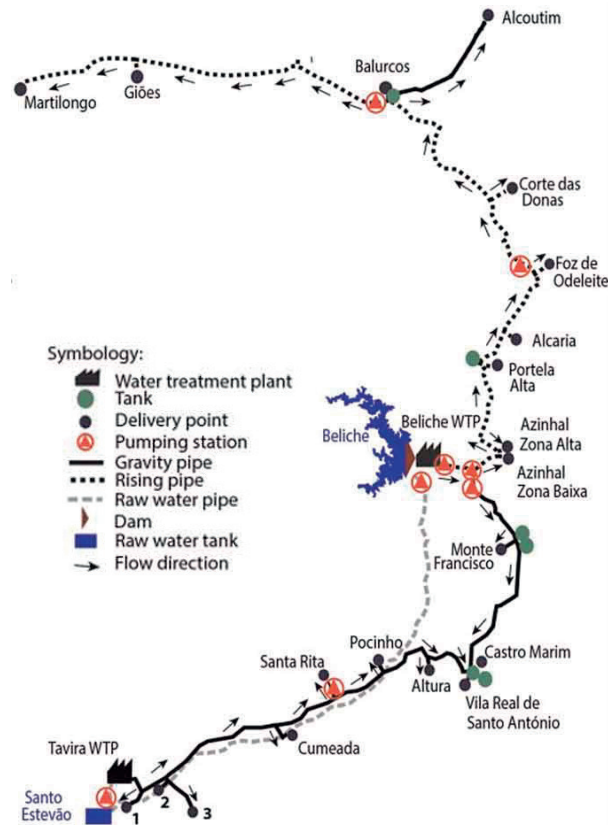


Figure 1.1 – Trunk main system of the water utility *Águas do Algarve*, Portugal. Adapted from [24].

on the maximum and minimum levels of the service tank and for dissipating the excessive pressure of the flow. Similarly to service tanks, water treatment plants are also provided with flow control valves at the inlet of the treatment process lines. The existence of the storage in the break-pressure tanks, service tanks and water treatment plants allows these infrastructures to operate with fairly uniform discharge throughout the day [28].

The main difficulty in installing micro hydropower plants for energy recovery in the aforementioned locations is the small back-pressure at downstream of the energy recovery scheme, as water is at the atmospheric pressure in the tanks. Such low back-pressure may induce cavitation in the turbines, for certain operating discharge and head values. The careful assessment of the site installation conditions and the cavitation occurrence is necessary to mitigate future operational problems and the accelerated degradation of the turbine. Also, the turbines should be installed in a bypass to the inlet flow control valves, for guaranteeing the normal water supply during maintenance operations or in the case of emergency situations.

Statistics of the average head and discharge values for energy recovery in trunk mains can be found in [29–34]. Examples of installed PAT micro hydropower plants for energy recovery in trunk mains are reported in [35–38].

Water distribution networks

Water distribution networks are infrastructures composed of pressurised branched and/or grid pipe networks for distributing drinking water to the consumers. Pipe diameters range from 0.08 m to 0.30 m, despite some regional WSS having higher diameters [23]. The water distribution network of Lisbon is presented in Figure 1.2. The network is composed of both branched and grid pipe networks. The different colours represent independent operating areas featuring different elevation range and supplied by different service tanks.

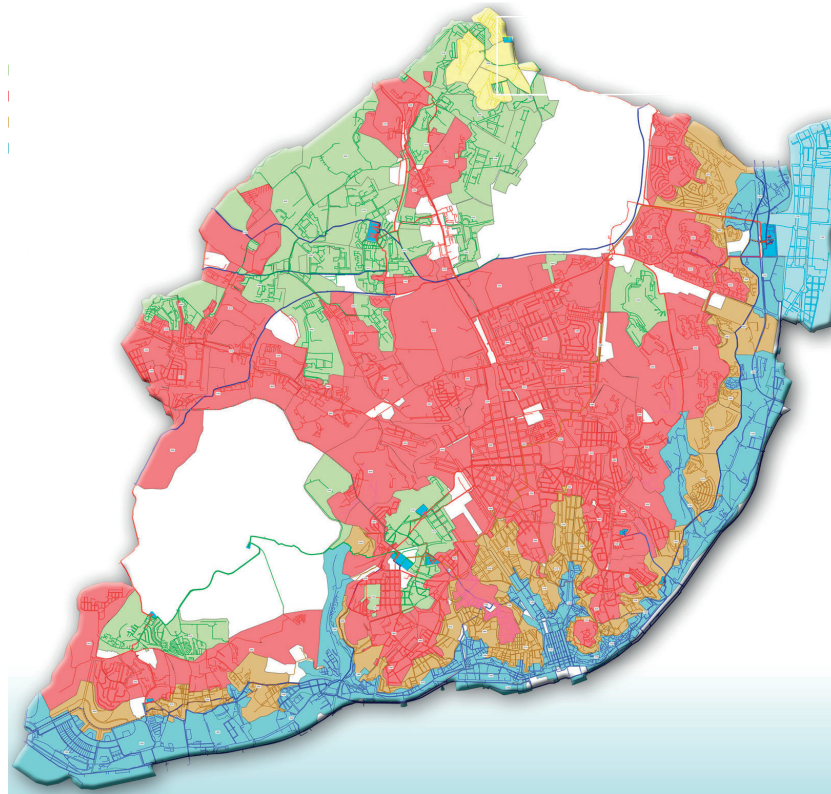


Figure 1.2 – Water distribution network of Lisbon, Portugal. The different colours represent independent control areas of the network supplied by different service tanks. Retrieved online from [39].

Water leakage through damaged pipes is a major concern for water utilities due to economic and environmental reasons. Water leakage can reach up to 50% of the total water supplied [40], leading water utilities to deploy pressure management strategies [41] to minimise the excessive pressure, which is directly related to the water leakage volume [42]. These strategies are defined aiming at guaranteeing a minimum service pressure, (e.g. for Switzerland [43]) for the adequate water supply to the consumers, as well as the maximum service pressure that minimises the water leakage in the pipe network.

The installation of pressure reducing valves (PRV) creating different pressure management areas in water distribution networks are the most commonly used method for pressure man-

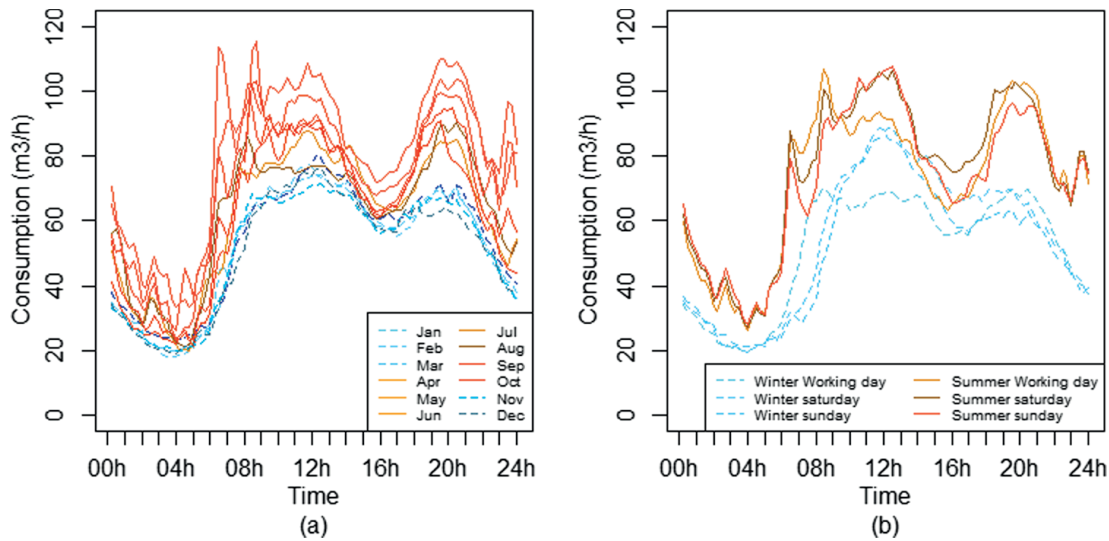


Figure 1.3 – Demand-driven patterns: (a) seasonal; (b) work-days. Retrieved from [47].

agement [44] and the most cost-effective measure for reducing leakage levels. PRV reduce the pressure by throttling the flow, which dissipates the excessive energy. The set-point of the dissipated pressure is selected for guaranteeing the minimum service pressure in all network nodes at downstream the PRV. The opportunity for energy recovery in water distribution networks is, thus, in the replacement of the existing PRV by micro hydropower plants that can simultaneously control the pressure in the network while recovering part of the excessive energy. A straightforward approach to estimate an interval of minimum and maximum recoverable pressure values is presented in [45]. This interval is a function of the location and the elevation of the PAT power plant, the head losses in the network, and the maximum and minimum service pressure values in the network. Note that the pressure interval is significantly affected by the consumption variation in the network.

One of the main challenges for operating a power plant in a water distribution network is the daily demand variation, which strongly affects the operation of the power plant. Demand patterns depend on several factors, such as socio-demography, temperature, seasonality, and day of the week, amongst others [46]. An example of daily discharge pattern in a Portuguese water distribution network is presented in Figure 1.3 [47]. Data provided in this figure show that, for this case, the maximum discharge in the network is approximately 5 times higher than the minimum discharge and that there is also a significant difference in the average consumption during winter and summer seasons.

Apart from the direct replacement of existing PRV by hydraulic turbines, research has been conducted on the optimisation of the water distribution network for minimising the water leakage and for maximising the energy recovered. The aim is at finding additional locations for installing energy recovery power plants and the corresponding values of installed power. Fontana et al. [48] applied Genetic Algorithms for minimising water leakage and further

designed a power plant depending on the recoverable pressure and discharge pattern. Giugni et al. [49] compared several optimisation functions combining the savings from water leakage reduction and the revenue from energy recovery. Corcoran et al. [50] compared the use of genetic algorithms, non-linear programming and mixed integer non-linear programming for combined energy recovery and water leakage reduction. Samora et al. [51] used an optimisation algorithm based on the simulated annealing to identify the optimal locations for energy recovery. All previous authors use the EPANET software [52] for modelling the water distribution network. De Marchis et al. [53] suggest the use of dynamic simulations based on the method of characteristics for modelling water infrastructures. General conclusions from these research works are that the micro hydropower plants are effective at controlling the pressure in all nodes of the network and at reducing the water leakage, which is one of the main objectives of water utilities. The additional revenue from the energy generation is an advantage for the utility since it rationalises the resources of the infrastructure by locally producing renewable energy. Conclusions reported in the literature point to small pay-back periods of the investment, in the range of 3 to 8 years, depending on the constraints considered by the different authors. These short pay-back periods are highly influenced by the small civil works required, when using existing buildings and infrastructures, in comparison to mini hydropower plants where additional construction is required for the water diversion structures, penstock and powerhouse.

Statistics regarding the average head and discharge values available for energy recovery in water distribution networks can be found in [37, 54, 55]. A PAT micro hydropower plant for energy recovery in a water distribution network installed in a bypass to a PRV is reported in [56]. Despite the PAT being installed in a bypass to the PRV, the range of power values recovered by the PAT is between 0.7 kW and 7 kW. This significant power variation is caused by the discharge variation in the water distribution network, which strongly decreases the PAT efficiency. This subject is discussed in detail in the following section.

1.2.2 Pumps running as turbines

The large range of pump applications across different industries lead manufacturers to develop different types of pumps. Pumps can be classified, for instance by the type of operating principle (centrifugal, side channel, positive displacement pumps), the direction of the flow in the impeller (radial, semi-axial and axial flow), the type of design (e.g., single-stage, multistage, end-suction, in-line, single-entry, double-entry), the pumped medium (e.g, drinking water, sewage, pulp, oil) [57]. The main types of centrifugal pumps commonly used in drinking water applications are depicted in Figure 1.4.

Main advantages of PATs are related to the industrial-scale production [59], namely (i) the low initial cost (ii) the availability for a broad range of head and flow values; (iii) the availability in a significant number of standard sizes; (iv) the short delivery time; and (v) the easy availability of spare parts such as seals and bearings. Moreover, the easy installation, operation

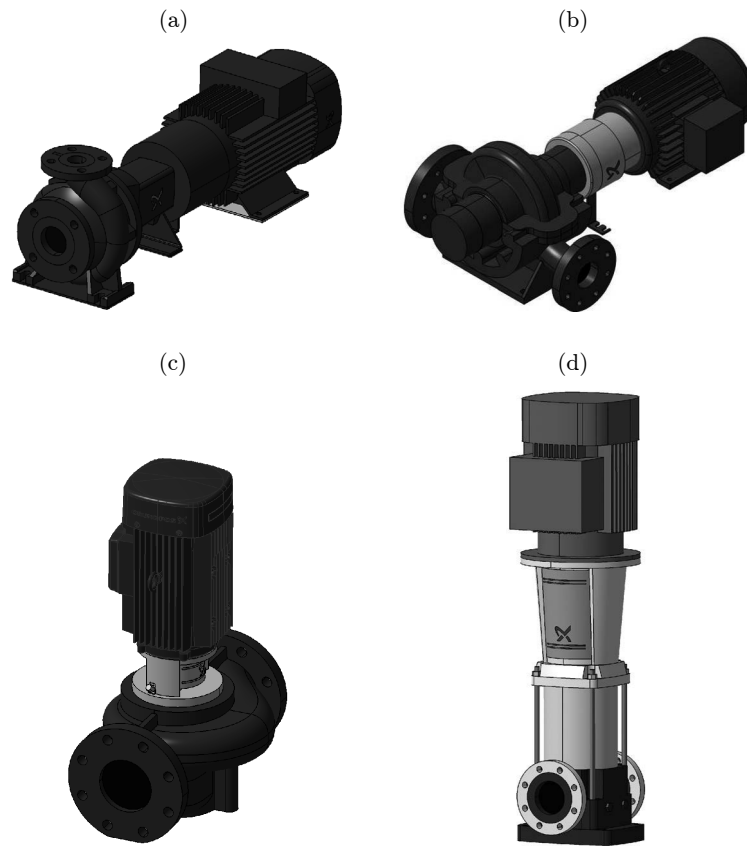


Figure 1.4 – Centrifugal pumps commonly used in drinking water applications. (a) Single-stage end-suction centrifugal pump, (b) in-line radially split centrifugal pump; (c) in-line single-stage centrifugal pump; (d) in-line multi-stage centrifugal pump. Drawings retrieved online from [58].

and maintenance, compared to conventional hydropower units, as well as the possibility of delivering power from 1 kW up to hundreds of kilowatts [60], make PATs cost-effective solutions for micro hydropower applications. Furthermore, pumps are usually supplied with an asynchronous motor, which can be used as an induction generator [61], reducing further the capital expenditure.

The comparison of the operating features between the turbine mode and the pump mode can be summarised, according to [62], as follows: (i) the best efficiency is approximately the same, or it can be slightly higher in the turbine mode, depending on the size of the machine; (ii) the Best Efficiency Point (BEP) is located at a higher discharge and head values in the turbine mode; (iii) the shaft power is, thus, larger in the turbine mode; (iv) the efficiency curve in full load drops slower in the turbine mode compared to the pump mode; and (v) the lower susceptibility to cavitation of the turbine mode.

The effective use of PAT micro hydropower plants for energy recovery in WSS still faces two

major issues: (i) the difficulty of obtaining the turbine mode characteristic curves in the full range of operation; and (ii) the sharp efficiency decrease when operating far from the BEP. Both of these issues arise from the fact that PATs are not specifically designed and engineered for energy generation. The turbine mode characteristic curves are usually not provided by pump manufacturers. For this reason, several researchers have developed methodologies for predicting the PAT characteristic curves, usually based on information provided by pump manufacturers, such as the rated values of the pump. These methodologies still fall short in the prediction accuracy. The efficiency decrease when the PAT is operating far from the BEP is caused by the absence of an inlet flow control component (e.g., Francis turbines guide vanes). Industrial pumps are usually designed to operate at nominal conditions, this is, at the best operating point, which does not require flow control component. This sharp efficiency decrease can be explained by the velocity triangles at the PAT high and low pressure sections, as illustrated in Figure 1.5.

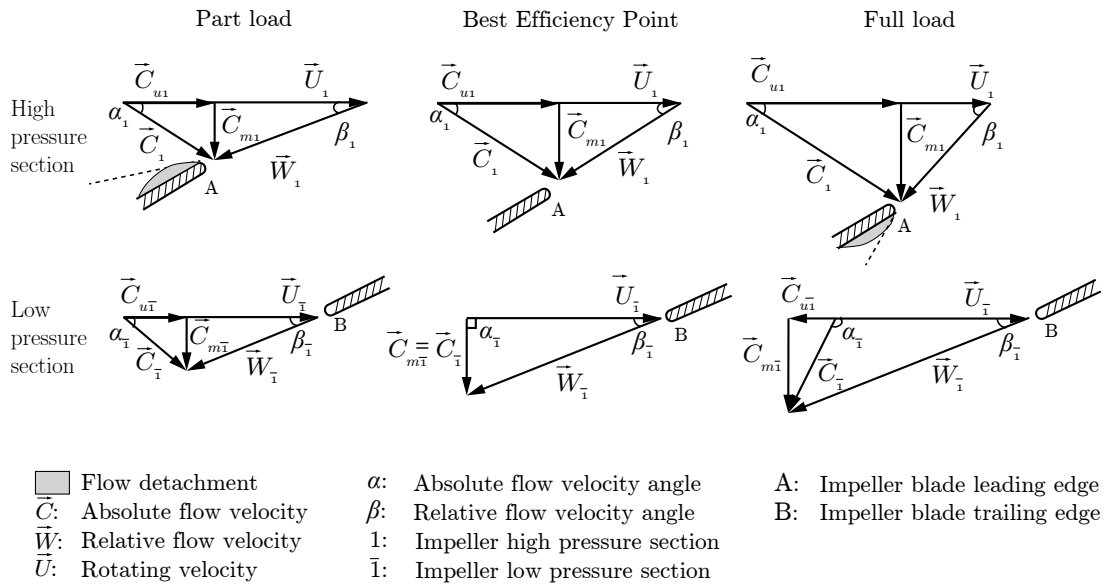


Figure 1.5 – Velocity triangles at the PAT high and low pressure sections for the BEP and for the part load and full load operating conditions.

At the BEP, the volute casing of the PAT is capable of fairly distributing the flow to the impeller, resulting into minimum power losses. As a consequence, the relative flow velocity angle at the PAT impeller high pressure reference section β_1 is coincident with the impeller blades leading edge angle. Also, at the PAT low pressure reference section, the absolute flow velocity \vec{C}_1 is axial at the PAT outlet, which corresponds to an angle $\beta_1 = 90^\circ$. The previous conditions correspond to the best operating point of the machine, this is, when the losses during the power flow are minimum.

As the discharge varies, and the PAT operates in off-design conditions, the previous conditions are not guaranteed. At the PAT high pressure reference section, since the absolute flow velocity angle α_1 is imposed by the volute casing geometry, the discharge variation induces changes

the relative flow angle in the impeller high pressure reference section β_1 . This change in β_1 results in flow detachments in the pressure side and in the suction side of the blades leading edge for the part load and the full load operation, respectively. The rounding of the impeller blades leading edge is suggested for mitigating the extent of the flow incidence [63, 64].

At the PAT low pressure reference section, the operation far from the BEP creates a tangential flow component $C_u \neq 0$, as the relative velocity flow angle in the PAT low pressure section $\beta_{\bar{1}}$ is fixed by the impeller blades trailing edge angle. This tangential component induces a swirling flow in the PAT draft tube in the same direction of rotation and in the reverse direction of rotation of the PAT impeller for the part load and full load conditions, respectively. The effects of operating in the off-design conditions are discussed in detail in the following section.

The following two sections aim at reviewing the main research literature respective to these two challenges: the turbine mode characteristic curves prediction and the efficiency decrease under variable discharge operation. The operation with variable speed control is also justified for mitigating the efficiency decrease when operating under variable discharge.

Characteristic curves prediction

The methodologies for predicting the turbine mode characteristic curves can be divided into four main groups: (i) expedite formulas; (ii) theoretical formulations; (iii) computational fluid dynamics numerical simulations; and (iv) empirical formulations based on experimental data. The following paragraphs summarise each of the aforementioned groups.

Expedite formulas [65–74] aim at estimating the head and discharge values corresponding to the BEP in the turbine mode. The computation of these values relies on the use of expedite formulations based on the pump efficiency or on the unit specific speed value of the machine. A summary of these formulations can be found in [16]. Despite these formulas offering a very expedite way of assessing the BEP in turbine mode, several authors report dissimilar accuracies, with deviations generally than 20% [75]. It can not be expected that the same equations would apply to pumps with different unit specific speed values, though both machines have the same efficiency values.

Theoretical formulations provide more reliable predictions compared to expedite formulas. These formulations require, however, data regarding the full pump geometry, which is a considerable drawback as this information is not usually provided by pump manufacturers. Derakhshan and Nourbakhsh [76] propose the computation of the BEP in turbine mode based on an *area ratio* method, which provided an underestimation of the discharge, head, power and efficiency with a maximum deviation of 5.25% when compared with experimental data. Huang et al. [77] describe a formulation based on the principle of characteristic matching between rotor and volute, with a reported deviation between model results and experimental data in the range of $\pm 5\%$. Gülich [57] estimates the full characteristic curves in the turbine mode based on the computation of the theoretical specific hydraulic energy (Euler equation)

and on the computation of the hydraulic, leakage, disk friction and mechanical losses. The model considers a calculation of more than 30 equations and the knowledge of internal geometric parameters, making it hard to apply in practice. Also, the uncertainty of some of the equations for computing the losses is in the range of $\pm 5\%$, reducing the accuracy of the turbine mode characteristic curves prediction. Barbarelli et al. [78] describe a methodology very similar to [57]. The main advantage is the estimation of the geometry of the pump (geometry model) based on information provided by pump manufacturers when the full geometry of the pump is not available. However, predictions have fallen short when the geometry model is used combined with the prediction model, with deviations in the range of $\pm 21\%$.

Similarly to theoretical formulations, computational fluid dynamics (CFD) numerical simulations require data about the full geometry of the PAT. CFD numerical results generally overestimate the full characteristic curves, which is attributed to geometry simplifications and to underestimation of disk friction, mechanical losses in bearings and seals and to leakage losses in balancing holes [76, 79–81]. Yet, CFD numerical simulations allow investigating subjects such as the losses distribution in the PAT [82], geometry modifications [83], flow distribution in the impeller [84, 85], swirling flow at the PAT outlet [86] and unsteady axial and radial load fluctuations [87]. The last two subjects are analysed in higher detail in the following section.

The higher accuracy in the prediction of the turbine mode characteristic curves is provided by the empirical formulations based on experimental data. These formulations aim at predicting the full characteristic curves in the turbine mode, instead of only determining the head and discharge values corresponding to the BEP. Also, the required input data are provided by pump manufacturers, such as the rated values of the pump mode and pump geometry data, such as the values of the impeller diameter. The empirical nature of these formulations restricts their application only to the domain of operation for which the experimental data used for defining the empirical formulations have been collected. This domain of operation is usually defined by the type of pumps (e.g., end-suction centrifugal pumps, in-line multi-stage pump) and by the corresponding interval of unit specific speed values.

Singh and Nestmann [88, 89] propose a methodology based on the specific speed-specific diameter plots [90]. Authors report deviations in the prediction of the BEP in the range of $\pm 4\%$, although the predictions have fallen short in the part load operating region. A similar approach using the same specific speed-specific diameter plots is presented in [91]. Derakhshan and Nourbakhsh [92] estimate the turbine mode characteristic curves using quadratic and cubic polynomial equations, respectively for the characteristic curves of the head and the power, with respect to the discharge. This formulation [92] seems to be widely accepted by the research community due to their simplicity and having been tested by different authors [93–95]. Despite providing acceptable results, authors consistently readjust the empirical coefficients originally found in [92], which indicate that the simple use of polynomial equations is very susceptible to the change of the sample of PATs used. Fecarotta et al. [96] suggest a methodology based on the modified affinity laws of turbomachines, which seem to provide lower accuracy in

the part load and full load operating zones. Rossi and Renzi [97] suggest the use of artificial neural networks for predicting the turbine mode characteristic curves, which seems to be of non-trivial application. Barbarelli et al. [98] also use polynomial equations for predicting the turbine mode characteristic curves. These authors [98] provide a straightforward approach for sizing and selecting a PAT for installing in a given location in a WSS, based on the average values of head and discharge measured in the WSS.

The experimental formulations usually provide lower accuracy at describing the PAT performance in the part load and in the full load of operation. The determination of the full characteristic curves (i.e., BEP, part load and full load) is of the utmost importance, as design engineers need to minimise the impact of the efficiency decrease caused by the operation under variable discharge. For this reason, PAT hydropower plant developers usually test the machines before the on-site installation, as in [38, 56]. Experimental methods are the most reliable for determining hydraulic turbomachines performance. Moreover, standardised procedures, such as the ones outlined in the IEC60193:1999 [99] and in the ISO9906:2012 [100] allow the determination of the turbomachine performance, where the previous formulations lack in accuracy. These standards present indications for the development of precise test-rigs and procedures for accurately measuring hydraulic and mechanical parameters, as well as acquiring and processing data, both in the steady and unsteady state. The final design should be performed with precise data about the PAT characteristic curves aiming at avoiding operational issues during the lifetime of the power plant.

As a final note, to the author knowledge, no methodology was found for estimating the PAT characteristic curves in the extended operation of the generating mode. These characteristic curves are of the utmost importance for modelling the hydraulic transients in hydropower plants [101]. The extended operation in the generating mode can be described by the IEC non-dimensional factors [99] or by the Suter parameters [102]. These characteristic curves provide the information about the rotational speed, the discharge, the head and the torque, when the PAT experiences abnormal operating conditions, for instance, when there is a sudden load rejection of the generator. Research literature suggests that, if no data are available for these characteristic curves for the PAT to be installed in the micro hydropower plants, design engineers may use data available for a PAT with closest unit specific speed value [103]. However, this assumption may overlook the real performance of the machine and introduce significant errors in the analysis of the hydraulic transients.

Operation under variable discharge

As referred before, one of the major drawbacks of the PAT performance is the efficiency decrease when operating under variable discharge, which is caused by the absence of an inlet flow control component. The efficiency decrease with respect to the relative discharge variation is higher in part load operation than in the full load operation. The efficiency decrease in off-design operation is a major setback for the energy recovery in WSS, as the discharge variability is one of the main WSS features. Multiple operating strategies are proposed to

mitigate this PAT feature disadvantage and to increase the overall efficiency of the power plants. All strategies have their advantages and drawbacks. The choice of the best measure depends on the specific operating conditions and should be analysed independently for every specific case.

Orchard and Klos [15] and Power et al. [104] proposes the use of multiple PATs installed in parallel and operating with constant rotational speed. The operation of a set of pumps requires only minimal control and the operational settings of the power plant can be changed with minimum costs. Pumps are brought into and out of service as a function of available discharge at the inlet of the power plant.

Carravetta et al. [105] suggest a hydraulic control based on the installation of the PAT in series with a control valve and in parallel with a bypass flow regulation valve. When the available head is higher than the head drop produced by the PAT, the control valve dissipates the remaining pressure, while the bypass regulating valve opens when the discharge is greater than the maximum flow of the PAT. This strategy allows operating the PAT mostly near the BEP, being the drawback the recovery of only part of the available energy. A real-time control for this kind of operation is provided in [106]. Carravetta et al. [17] propose a variable speed control to accommodate the discharge fluctuations, allowing an increase of the instantaneous efficiency under variable flow. The speed is automatically adjusted, increasing or decreasing the impeller rotating frequency, according to the discharge variation. Main advantage is the efficiency increase when operating in off-design conditions. The previous strategies (hydraulic vs. electric control) were compared in a water distribution network case study based on three parameters: capability, flexibility and reliability [107]. Authors suggest the use of combined hydraulic and electric control for providing a better overall operating performance of the PAT power plant.

Finally, the use of a custom-made spiral case with inlet flow control is suggested in [108]. The spiral case distributor provides a better flow distribution to the impeller when operating in off-design conditions. Chapallaz [36] presents guidelines for the design of a spiral case and distributor with guide vanes. The major drawback of this approach is the need to customise the PAT, resulting in a capital cost increase.

Apart from the strong efficiency decrease when the PAT operates far from the BEP, numerical simulations suggest the occurrence of severe load fluctuations when operating with variable discharge conditions. These fluctuations are mainly caused during the full load operation due to the interaction of the impeller blades leading edge and the volute tongue [87]. As the impeller blades pass near the volute tongue, the static pressure field is locally affected, which induce high unsteady radial load fluctuations in the impeller. Such load increase may reduce the lifetime of the PAT mechanical components. Numerical results presented in [109] suggest that the amplitude of the unsteady fluctuations is affected by the radial clearance between the impeller blade tip and the volute tongue. Also, CFD numerical simulations [86] report the development of a swirling flow at the PAT draft tube which may lead to the development of a

cavitation vortex flow. Swirling cavitation flows in pipes are associated with the development of severe pressure fluctuations [110]. This kind of phenomenon has been heavily investigated in Francis turbines used in large hydropower plants. Research literature indicates the existence of large pressure fluctuations developed both in the part load [111, 112] and in the full load of operation [113, 114]. However, no research has been found on this subject for the off-design operation of PATs. Not only the operation instabilities caused by the pressure fluctuations may lead to the PAT lifetime reduction, but the amplitude of the developed pressure fluctuations may be incompatible with the adequate supply of water to the consumers.

Summing up, the variable speed control of PATs seems to be a promising solution for addressing the operational challenges of recovering energy under the variable discharge conditions of WSS. This type of control may provide conditions for achieving a higher energy yield while avoiding the onset of operation instabilities caused by the part load or by the full load operation of these hydraulic machines.

1.2.3 Gaps of knowledge

Based on the literature review described in Sections 1.2.1 and 1.2.2 several gaps of knowledge and topics that require further investigation are identified. These gaps of knowledge support the motivation for the development of this research work.

Statistics of the average head and discharge values available for energy recovery in WSS is spread in the literature. A collection of these statistics and the comparison with the scope of operation of different types of turbines is required to identify the most appropriate machines for each location for energy recovery in WSS.

The PAT variable speed control has been proposed to increase the efficiency when operating under variable discharge conditions. However, few experimental research has been conducted on variable speed operation of PATs. Also, the PAT extended operation in the generating mode has been barely addressed.

CFD numerical simulations point to the onset of significant operation instabilities during the part load and the full load operation of the PAT. The existence of a swirling flow at the PAT draft tube may lead to the development of a cavitation vortex rope if the stationary back-pressure is too low. This cavitation flow induces severe pressure fluctuations in Francis turbines. However, no research is found for PATs. The occurrence of significant pressure fluctuations may be incompatible with the adequate water supply.

Existing methodologies for predicting the turbine mode characteristic curves of pumps lack accuracy, especially for describing the part load and the full load operating conditions. Also, no methodology is known for estimating the PAT characteristic curves in the extended operation in the generating mode.

1.3 Thesis objective

The main objective of this research work is the experimental investigation and the prediction of the variable speed performance of pumps running as turbines. The variable speed operation is investigated to determine if this operating strategy is suitable for maximising the energy recovered by PAT power plants under the variable discharge conditions of water supply systems. The variable speed control may also be used to prevent the operation of the PAT far from the best operating point avoiding, thus, the occurrence of eventual operation instabilities. This main objective is addressed by three research contributions.

The first contribution is the enlightenment of the variable speed performance feature of pumps operating in the turbine mode and in the extended operation of the generating mode. The goal is to understand if the variable speed control is suitable for improving the PAT operating performance under the variable discharge conditions of WSS. This is achieved by an extensive experimental investigation carried out for collecting data for the turbine mode and for the extended operation in the generating mode.

The second contribution aims at investigating the operation instabilities caused during the PAT operation in off-design conditions. This contribution focuses on the unsteady pressure fluctuations which are measured in the high and in the low pressure sections when the PAT operates in part load and in full load. This contribution seeks to identify the areas where such pressure fluctuations occur and the physical mechanisms underlying this phenomenon.

The third contribution of this research work is the development of a new methodology for predicting the characteristic curves of the PAT in the turbine mode and in the extended operation in the generating mode, using the data collected during the first contribution. This methodology aims at improving the accuracy of predictions for the turbine mode in the part load and in the full load operating zones. Also, the same methodology is used to model the variable speed efficiency hill chart of a given PAT.

This research work is based on an extensive experimental investigation for addressing the first and second research contributions. The data collected in the experimental investigation are used to develop the prediction methodology. This investigation solely focuses on the hydraulic and mechanical properties of the PAT operation. The discussion of the performance and the control of the generator parameters are out of the scope of the current research.

1.4 Thesis structure

The present research work is a collection of manuscripts submitted for peer-review international journals. The following chapters address the research contributions described above and present practical guidelines for the application of the methodology developed for predicting and modelling the PAT performance.

Chapter 1. Introduction

In **Chapter 2**, it is presented the experimental investigation carried out for collecting data to characterise the performance characteristic curves of the turbine mode and the extended operation in the generating mode. Three end-suction single-stage centrifugal pumps with different unit specific speed values are tested. The description of the test-rig designed, engineered and assembled for this research work is performed in this Chapter. The comparison between the average values of head and discharge for energy recovery in WSS and the scope of application of different turbines is carried out in the introduction of this Chapter, aiming at justifying the range of unit specific speed values of the PATs tested in this thesis.

In **Chapter 3**, the off-design operation of the PAT with the higher unit specific speed value is investigated. The investigation focuses on the unsteady pressure fluctuations which arise when the machine is operated far from the best operating point. Experimental data of the dynamic pressure at the high and at the low pressure sections of the PAT and the flow visualisation at the PAT draft are collected to characterise the cavitation vortex rope developed during the off-design operation. The investigation focuses both on the part load and on the full load operation.

In **Chapter 4**, the new methodology for predicting the PAT characteristic curves in the turbine mode and in the extended operation of the generating mode is presented. The methodology defines surrogate functions to propagate the hydraulic and mechanical characteristic curves in-between of the tested unit specific speed values of the PATs tested in Chapter 2. Also, this chapter describes the modelling of the variable speed efficiency hill chart of the PAT.

Finally, in **Chapter 5**, practical stepwise guidelines are provided for applying the methodology for predicting and modelling the PAT variable speed characteristic curves. The guidelines provide the tools for modelling: (i) the prediction of the turbine mode performance; (ii) the prediction of the extended operation in the generating mode; and (iii) the variable speed efficiency hill chart of the PAT.

Chapters 2, 3 and 4 are the collection of three independent research papers submitted to international peer-review scientific journals, which may contain repeated equations and similar figures. The references that support each manuscript are cited by order of appearance in this thesis and are all presented at the end of this document (see Page 129). Details of each research paper are presented at the beginning of each Chapter.

2 Experimental investigation

This chapter corresponds to the research paper:

J. Delgado, D.I.C. Covas and F. Avellan (2018), *Variable speed operation of centrifugal pumps running as turbines. Experimental investigation*. Submitted to Renewable Energy, Elsevier.

Author contribution: The author designed the test-rig, assembled the measurement setup and developed the data acquisition system. He performed the measurements and the data analysis.

Abstract

Pumps running as turbines (PAT) are pointed out as a suitable solution for energy recovery in pressurised water supply systems (WSS). However, these hydraulic machines feature low efficiency under variable discharge operation due to the lack of an inlet flow control component. The variable speed operation is an approach for controlling the discharge at the PAT inlet. This research work presents the experimental investigation of the PAT performance with variable speed, focusing on the turbine mode and the extended operation mode. Three single-stage end-suction centrifugal pumps with different unit specific speed values are experimentally tested. Turbine mode test results show that the variable speed control allows broadening the operating range of the PAT and also increasing the efficiency when the PAT is operated far from the best efficiency point. Extended operation results show that these hydraulic machines do not feature the instability region near the runaway conditions, the so-called the “s-curve”. Outcomes of this experimental investigation provide the required insights for establishing the design specifications of variable speed PAT micro hydropower plants, aiming at maximizing the energy recovered in pressurised water supply systems.

Keywords: Pumps running as turbines, variable speed, energy recovery, turbine mode, four-quadrants, experimental tests.

2.1 Introduction

Pressurised water supply systems (WSS) have a significant potential for energy recovery [3, 25]. Locations for energy recovery in these systems are defined as the sites where the flow is conveyed with an excessive pressure, not required for the effective downstream water supply. The scope of the average head and discharge values available for energy recovery in WSS is broad and infrastructure dependent, as illustrated in Figure 2.1. Data in this figure are clustered into five types of WSS, namely in: (i) irrigation networks, (ii) inlet of water treatment plants; (iii) inlet of storage tanks or break-pressure tanks, in trunks mains; (iv) pressure reducing valves in water distribution networks; and (v) outlet of wastewater treatment plants [24, 29–35, 37, 38, 54, 55, 115–120].

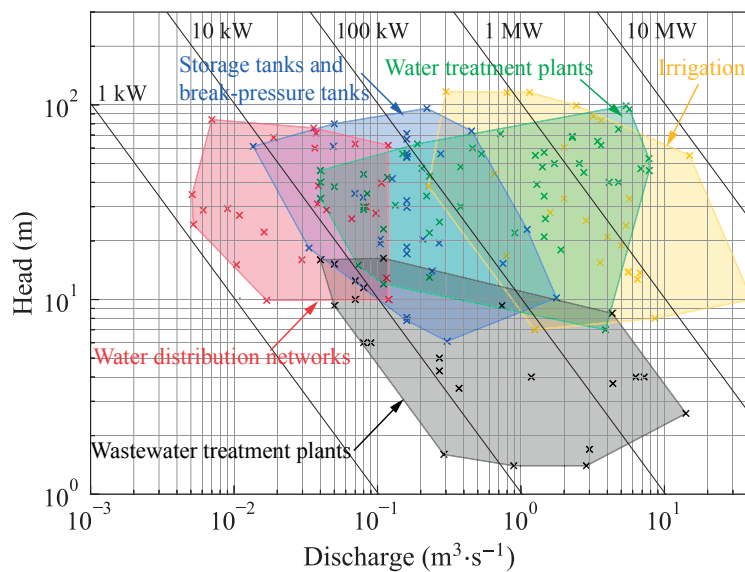


Figure 2.1 – Average head and discharge values available for energy recovery in water supply systems. The isolines represent the available hydraulic power.

The operating range breakdown of the available discharge Q , head H and hydraulic power P_h values, for each type of WSS is detailed in Table 2.1. Irrigation infrastructures feature the highest discharge values as agriculture is more water-intensive than drinking water supply [121]. Differences between water distribution networks, storage tanks and water treatment plants are justified by the water supply chain. Water treatment plants convey water to several storage tanks, while these supply several district meter areas, where pressure reducing valves (PRV) are usually installed. The head values in the above-mentioned infrastructures have the same order of magnitude, while wastewater treatment plants feature lower values for this parameter.

The orders of magnitude of WSS operating conditions are smaller compared to conventional hydropower plants. As an example, approximately 85% of the sites represented in Figure 2.1 have an available hydraulic power lower than 1 MW. In fact, the average head and discharge

Table 2.1 – Breakdown of minimum and maximum values of head and discharge for energy recovery per infrastructure.

Location	Q ($\text{m}^3 \cdot \text{s}^{-1}$)		H (m)		P_h (kW)	
	min	max	min	max	min	max
Irrigation networks	0.230	40.0	7.0	120	85	8'100
Water treatment plants (inlet)	0.040	7.8	6.0	100	11	5'300
Storage tanks (inlet)	0.015	1.8	6.0	100	6	325
Water distribution networks (PRV)	0.005	0.12	10.0	85	1	75
Wastewater treatment plants (outlet)	0.040	14.0	1.5	16	5	360

values found for energy recovery in WSS (Figure 2.1) are not matched by custom-made hydropower units scope of application, as illustrated in Figure 2.2. Therefore, the deployment of energy recovery systems in these infrastructures is relying on hydraulic machines that can cover such operating conditions. The unit specific speed n_q represented in Figure 2.2 is defined by Equation (2.1). The computation of this parameter considers values of the rotational speed between 500 min^{-1} and $3'000 \text{ min}^{-1}$, and the use of several units in parallel, depending on the discharge.

$$n_q = N \frac{Q^{\frac{1}{2}}}{H^{\frac{3}{4}}} \quad (2.1)$$

where N is the rotational speed in (min^{-1}), Q is the discharge in ($\text{m}^3 \cdot \text{s}^{-1}$), and H is the head in (m). Note that n_q is unit dependent.

Pumps running as turbines (PAT) are pointed as a cost-effective solution for energy recovery in WSS [123], among other turbines [124–130]. The use of PATs for energy recovery in WSS has been extensively investigated in topics such as turbine mode prediction, control strategies and performance enhancement, for instance in [48, 49, 92, 94, 96, 106, 131–134]. Main advantages are the small capital investment, the immediate availability in a wide range of head and discharge, and the considerable efficiency at the best efficiency point (BEP) [59]. Indeed, the PATs range of application covers most of the WSS average operating conditions, as illustrated in Figure 2.3. Yet, PATs feature a low efficiency in off-design operation. This is, when the discharge is smaller or higher than the value at the BEP, the so-called part load and full load operation conditions, respectively. A PAT power plant installed in a WSS is surely bound to experience off-design operation, as one of WSS main characteristic is the daily discharge variations, as illustrated in Figure 2.4, which is caused by the consumer-driven demand [19, 47].

The efficiency decrease when operating in off-design conditions is a result of the absence of a discharge regulation component (e.g., guide vanes in Francis turbines). When the discharge deviates from the value at the BEP, the impeller blades leading edge experience flow detachment in the pressure side and suction side of the impeller blades leading edge, respectively for

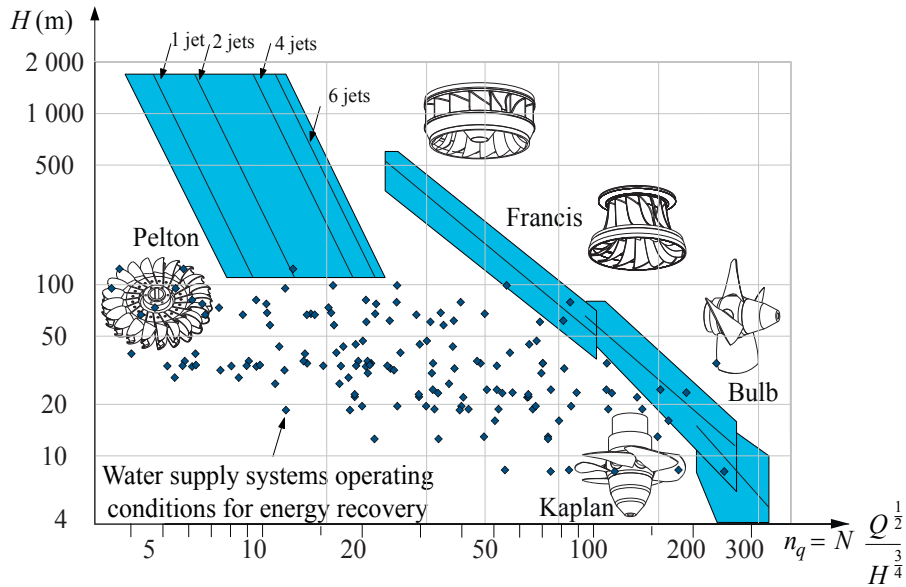


Figure 2.2 – Comparison between the scope of application of conventional hydropower turbines [122] and the average operating conditions for energy recovery in WSS.

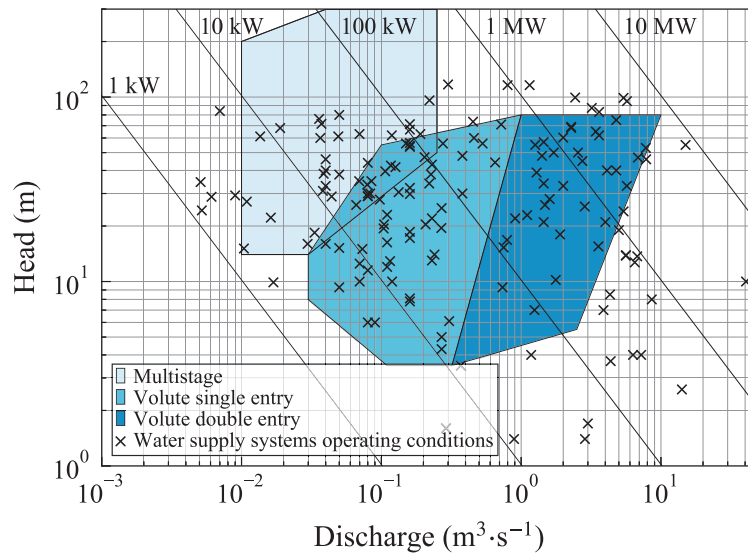


Figure 2.3 – Comparison between PAT range of operation [135] and the potential for energy recovery in WSS. The isolines represent the available hydraulic power.

the part load and the full load operation (see Figure 2.5). The tip rounding of the blades leading edge is suggested to mitigate this problem [63, 64]. Furthermore, a swirling flow is developed at the impeller low pressure section (i.e., $C_{u,1} \neq 0$) in the same and inverse runner rotation direction, for part load and full load, respectively. Both these occurrences may decrease the PAT efficiency.

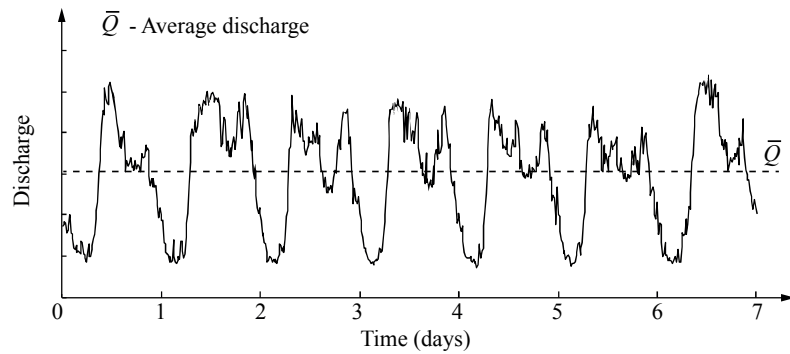


Figure 2.4 – Schematic representation of the discharge time history in a water distribution network during one week. The dashed line represents the average discharge. Typically, the maximum discharge is higher by a factor of 3 or 4 than the minimum discharge.

The variable speed control is pointed as a strategy to increase the efficiency and the energy yield under variable discharge operation [17]. The rotational speed control allows adjusting the velocity triangles at the PAT high and low pressure sections, as illustrated in Figure 2.5. Research findings of PAT variable speed operation are inconsistent. Jain et al. [136] suggest that the maximum efficiency decreases with increasing rotational speed. These results are contradicted by the results shown in [38]. Therefore, this topic still requires further research.

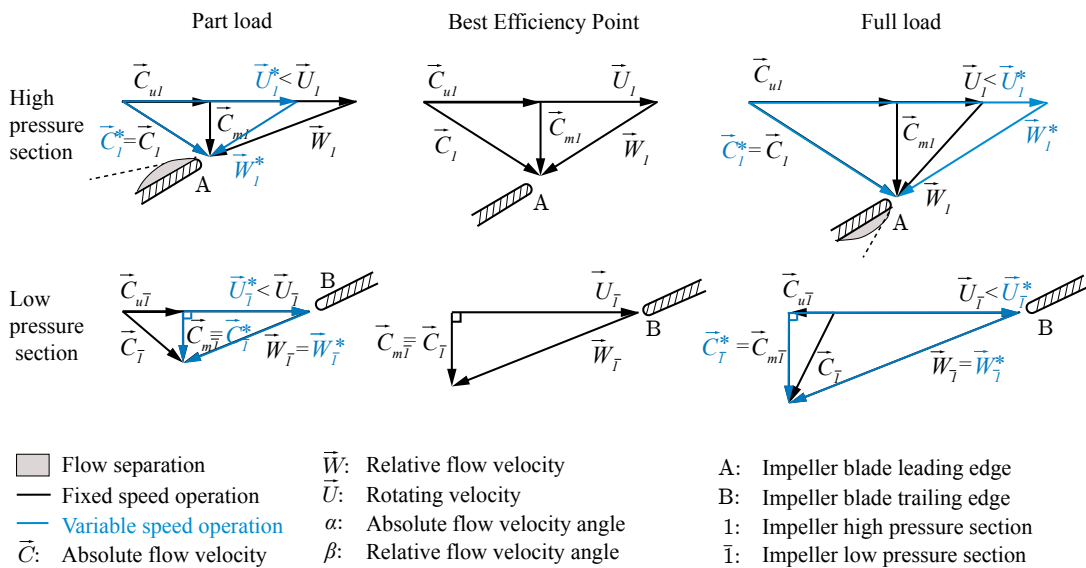


Figure 2.5 – Velocity triangles in the PAT high and low pressure sections for the part load operation, the best efficiency point and the full load operation.

The hydropower plants installed in WSS need to maintain the safety and the adequate water supply [14] both in regular (e.g., start-up) and in the case of emergency operation (e.g., generator sudden load rejection). The dynamics of the power plant are represented by the Equation (2.2), which describes the inertial effect of the rotating masses, and by the pump

Chapter 2. Experimental investigation

characteristic curves in the four-quadrants of operation. The latter describes the interaction between the specific hydraulic energy $E = gH$, being H the head, the discharge Q , the torque T , and the runner rotating frequency n . The four-quadrants characteristic curves (see Figure 2.6 and Table 2.2) are described by the variation of the IEC factors of discharge Q_{ED} , and torque T_{ED} with respect to the IEC speed factor n_{ED} , which are defined Equation (2.3) [99].

$$J \frac{d\omega}{dt} = T + T_{el} \quad (2.2)$$

$$\begin{aligned} n_{ED} &= \frac{nD}{\sqrt{E}} \\ Q_{ED} &= \frac{Q}{D^2 \sqrt{E}} \\ T_{ED} &= \frac{T}{\rho_1 D^3 E} \end{aligned} \quad (2.3)$$

where J is the pump moment of inertia, ω is the angular speed and T_{el} is the electric resisting torque. D is the reference diameter and ρ_1 is the water density in the high pressure reference section of the PAT.

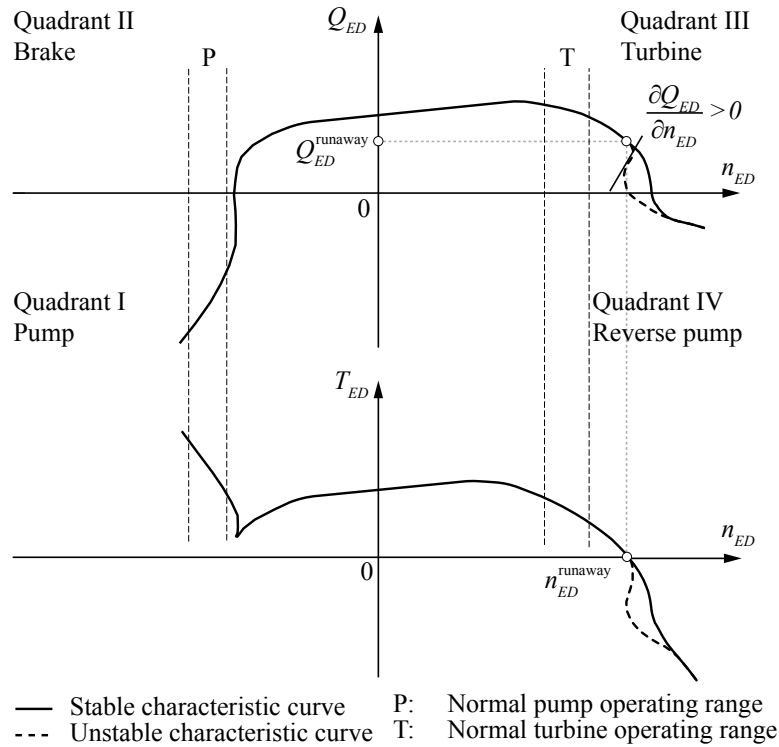


Figure 2.6 – Identification of the four-quadrants of operation.

Table 2.2 – Quadrants and operating modes definitions used for the experimental investigation.

ID	Quadrant	Q	N	T	Mode
1	Pump	-	-	+	Pump
1/2	-	0	-	+	Zero discharge
2	Brake	+	-	+	Pump-brake
		+	+	+	Turbine
3	Turbine	+	+	0	Runaway
		+	+	-	Turbine-brake
3/4	-	0	+	-	Zero discharge
4	Reverse pump	-	+	-	Reverse pump

The extended operation of custom-made Francis reversible pump-turbines often features an unstable characteristic curve near the runaway operating point defined by $\partial Q_{ED}/\partial n_{ED} \geq 0$ (see Figure 2.6). This unstable characteristic curve is frequently observed in low specific speed reversible pump-turbines [101]. This unstable feature may induce the constant shift between the turbine and the reverse pump quadrants, creating vibration and noise [137]. PATs are also likely to feature this unstable characteristic curve, as pump-turbines impellers are mostly designed for the pumping mode. Yet, no research was found about this topic on PATs.

This research paper aims at gathering the stationary performance data required for the specifications development of variable speed PAT power plants for energy recovery in WSS. A new experimental facility is designed, engineered and assembled for testing reaction hydraulic machines, both in the pumping and in the generating mode. The experimental investigation is performed in three end-suction single-stage centrifugal pumps with different n_q values. The description of the test-rig and the experimental procedure are outlined in Section 2.2. The collected experimental results of the pump, the turbine and the extended operation modes are presented in Section 2.3. These results are later discussed in Section 2.4, focusing on the variable speed characteristics. Finally, the main conclusions and future perspectives are outlined in Section 2.5.

2.2 Experimental setup

2.2.1 Test-rig and measurement equipment

The experimental investigation is carried out in a new test-rig assembled in the Laboratory of Hydraulics and Environment at Instituto Superior Técnico, Universidade de Lisboa. The test-rig consists of a reversible closed-loop steel-pipe facility (Figure 2.7). Two feed pumps, installed at a lower level, provide the hydraulic power to the test-rig. Each pump, with a rated power of 15 kW, delivers a maximum discharge and pressure of $24 \text{ l} \cdot \text{s}^{-1}$ and 8 bar, respectively. The discharge supplied to the PATs is controlled using two variable speed drives (VSD). The feed pumps are provided with a bypass for flow circulation in both directions. The maximum installed pumping power allows operating the test-rig up to $40 \text{ l} \cdot \text{s}^{-1}$.

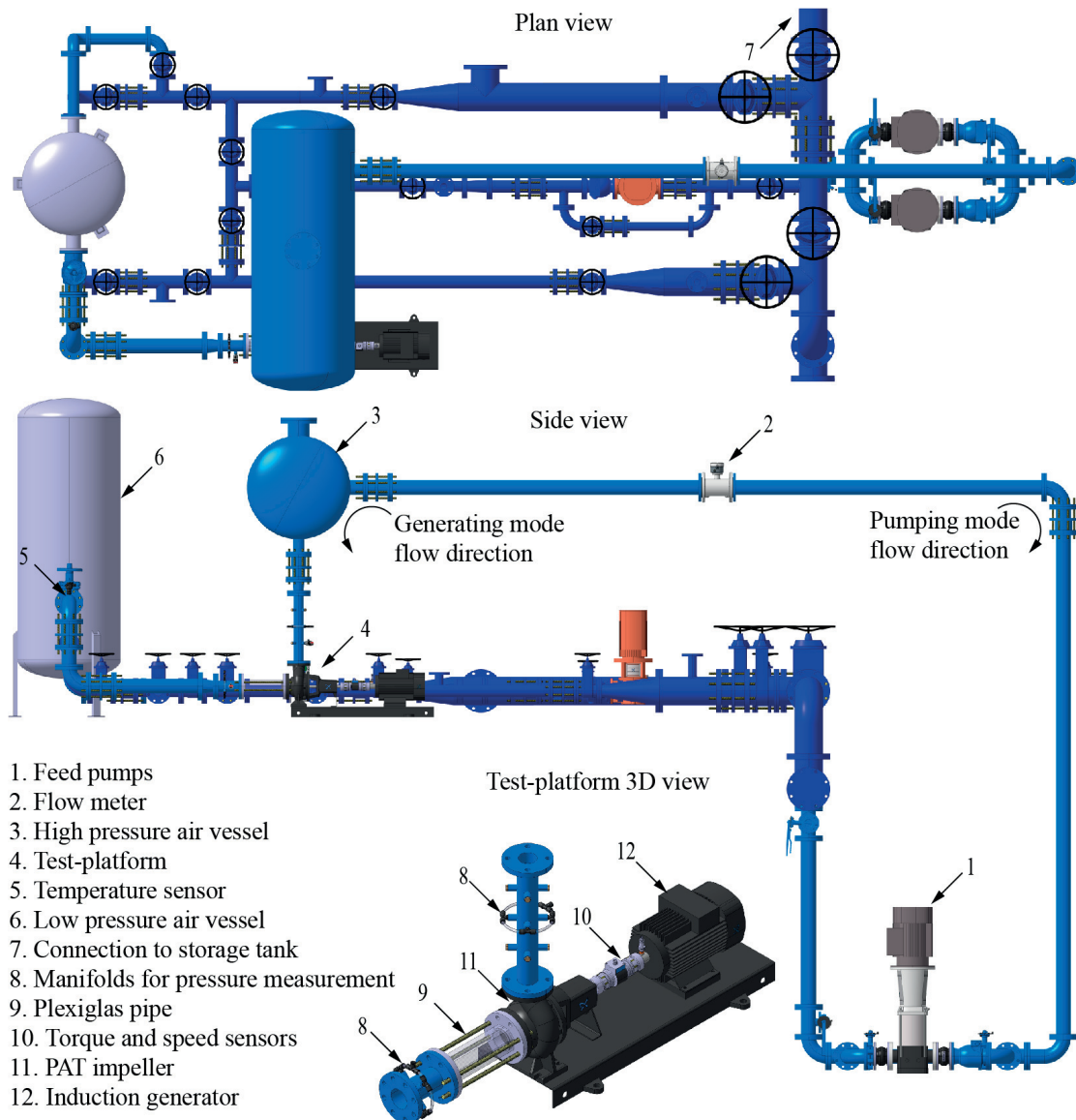


Figure 2.7 – Test-rig assembled for collecting the experimental investigation.

A 1 m³ pressure vessel, installed at the PAT high pressure side, provides flow stabilisation and a uniform velocity profile at the PAT inlet. The test-rig allows investigating differently sized hydraulic machines. The PATs rotational speed is fully regulated between 300 min⁻¹ and 3'000 min⁻¹ using a 15 kW four-quadrant VSD. The original induction motors are used as asynchronous generators. A 350 mm straight transparent Plexiglas pipe is installed in the PAT low pressure section to allow detecting the occurrence of cavitation in the draft tube.

A second 1 m³ pressure vessel, installed at the PAT low pressure side, is used to create different back-pressure levels. Both vessels are equipped with valves for admission and release of compressed air. The low pressure vessel and the feed pumps are connected by three pipes,

Table 2.3 – Measurement equipment characteristics.

ID	Measurement	Range	Units	Accuracy
Q	Discharge	0 – 0.04	$\text{m}^3 \cdot \text{s}^{-1}$	0.40% of span
Δp_1	Differential pressure 1	0 – 7.5	bar	0.14% of span
Δp_2	Differential pressure 2	-0.2 – 2.1	bar	0.14% of span
T	Torque	-50 – 50	N·m	0.30% of upper limit
n	Runner rotating frequency	0 – 50	s^{-1}	0.20% of span
θ	Temperature	0 – 100	$^{\circ}\text{C}$	0.30% of span
P_{sup}	Active power	-10 – 10	kW	0.50% of upper limit
Q_{sup}	Reactive power	-10 – 10	kVAr	2.00% of upper limit

installed in parallel, equipped with isolation valves to allow operating the pipes in different configurations. The test-rig is supplied with water from a 40 m³ storage tank.

The test-rig is equipped with instrumentation for measuring the PATs hydraulic, mechanical and electrical parameters. The location and characteristics of the measurement equipment are shown in Figure 2.8 and in Table 2.3, respectively. Measurements are simultaneously acquired using a data acquisition hardware (NI cDAQ9178) from National Instruments™, connected to a computer. The acquisition hardware is equipped for both voltage (NI 9205) and current (NI 9203) analogue inputs. Moreover, it also generates voltage analogue outputs (NI 9269) for controlling the three VSD. The data acquisition and control software controls the three VSD, as well as acquires, processes, logs and visualises the measurement data in real-time.

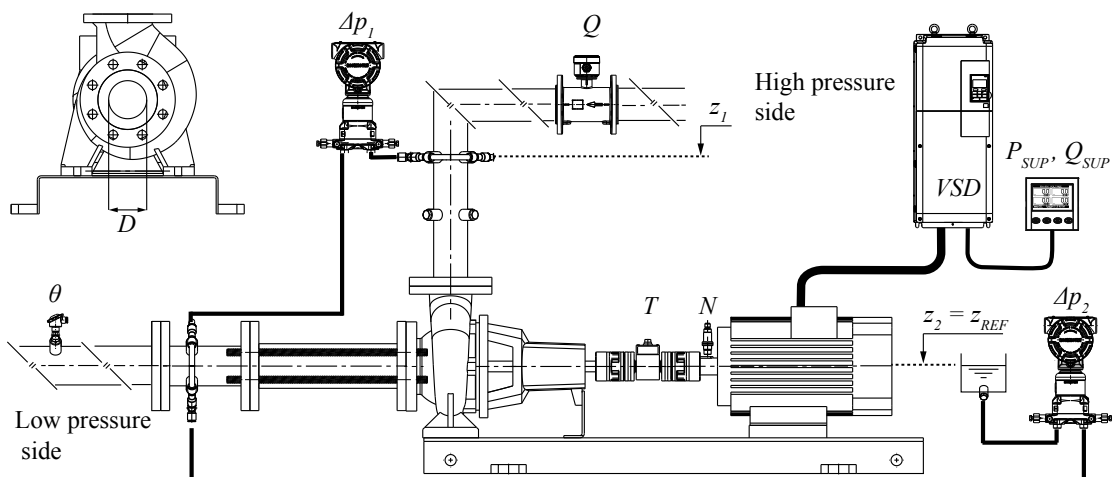


Figure 2.8 – Measurement equipment setup.

Chapter 2. Experimental investigation

Table 2.4 – Rated characteristics in pump mode of the tested centrifugal pumps.

Pump ID	N_R^P (min ⁻¹)	Q_R^P (l·s ⁻¹)	H_R^P (m)	P_R^P (kW) ⁽¹⁾	n_q (SI)	D (mm) ⁽²⁾
NK40-160/158	2'910	10.9	31.1	5.0	23.1	65
NK40-125/127	2'900	13.0	16.2	2.8	41.0	65
NK65-125/127	2'910	29.8	14.6	5.5	67.3	80

⁽¹⁾ Shaft power corresponding to the rated operating point

⁽²⁾ Diameter of the low pressure section of the volute

2.2.2 Experimental tests performed

The experimental investigation is performed in three single-stage end-suction centrifugal pumps with closed impeller and single volute. The three pumps are characterised by different n_q values. The rated characteristics in pumping mode are outlined in Table 2.4, namely: the discharge Q_R^P , the head H_R^P , the rotational speed N_R^P , the shaft power P_R^P , the unit specific speed n_q , and the reference diameter D , which is considered as the value at the pump low pressure flange internal section (see Figure 2.8).

The specific hydraulic energy E is defined by:

$$E = \frac{p_{\text{abs},1} - p_{\text{abs},2}}{\bar{\rho}} + \frac{C_1^2 - C_2^2}{2} + g(z_1 - z_2) \quad (2.4)$$

where p_{abs} is the absolute pressure, C is the flow velocity, g is the gravity acceleration, z is the elevation, and $\bar{\rho} = (\rho_1 + \rho_2)/2$ is the average water density, which is a function of the pressure and temperature [99]. Subscripts 1 and 2 refer to the high and low pressure measurement sections, respectively. According to the measurement setup of Figure 2.8, E is determined by Equation (2.5).

$$E = \frac{\Delta p_1}{\rho_2} + \frac{C_1^2 - C_2^2}{2} \quad (2.5)$$

The hydraulic and mechanical shaft power, P_h and P are given by Equations (2.6) and (2.7), respectively. The active and reactive electric power P_{sup} and Q_{sup} , respectively, are directly measured using a digital power analyser.

$$P_h = \rho_1 Q E \quad (2.6)$$

$$P = 2\pi n T \quad (2.7)$$

where n is runner rotational speed (n and N refer to the the same parameter, though the units are Hz and min^{-1} , respectively).

Finally, the mechanical, electrical and global efficiency η , η_{el} and η_g , respectively, are given by Equation (2.8). Superscripts P and T refer to the pump and to the turbine mode, respectively. The torque sensor is assembled between the PAT shaft and the induction generator. The digital power analyser is installed between the electric grid and the regenerative VSD. Therefore, the mechanical efficiency η , takes into account the power losses associated with leakage flow, disk friction, specific energy losses in the volute and impeller and bearing and seals friction [57]. The electric efficiency η_{el} accounts the losses in the induction generator, namely the stator iron losses, the stator and rotor copper losses [61], and the VSD losses.

$$\left\{ \begin{array}{l} \text{Pump mode : } \eta^{\text{P}} = \frac{P_h}{P}; \eta_{\text{el}}^{\text{P}} = \frac{P}{P_{\text{sup}}}; \eta_g^{\text{P}} = \frac{P_h}{P_{\text{sup}}} \\ \text{Turbine mode : } \eta^{\text{T}} = \frac{P}{P_h}; \eta_{\text{el}}^{\text{T}} = \frac{P_{\text{sup}}}{P}; \eta_g^{\text{T}} = \frac{P_{\text{sup}}}{P_h} \end{array} \right. \quad (2.8)$$

Measurements are performed under cavitation-free conditions, being the cavitation occurrence controlled by direct observation in the transparent Plexiglas pipe installed at the low pressure side of the PAT. The Net Positive Suction Energy $NPSE$ is defined by:

$$NPSE = \frac{p_{\text{abs},2} - p_{\text{va}}}{\rho_2} + \frac{C_2^2}{2} + g(z_{\text{ref}} - z_2) \quad (2.9)$$

where p_{va} is the vapour pressure, which is a function of the temperature θ [99], and z_{ref} is the reference elevation of the PAT. According to the measurement setup of Figure 2.8, the $NPSE$ is computed by [99]:

$$NPSE = \frac{\Delta p_2 + p_{\text{amb}} - p_{\text{va}}}{\rho_2} + \frac{C_2^2}{2} \quad (2.10)$$

Chapter 2. Experimental investigation

where p_{amb} is the ambient pressure at the test-rig location. Consequently, the Thoma Number σ is defined by Equation (2.11).

$$\sigma = \frac{NPSE}{E} \quad (2.11)$$

The systematic relative error $f_{X,s}$, of a given variable X is computed for every measured operating point by Equation (2.12). Consequently, the total relative error is given by Equation (2.13). This calculation considers a conservatively estimated random error $f_{X,r} = 0.1\%$. Finally, the propagated total relative error of a given parameter is determined based on the root mean square of all the total relative errors of its dependent variables [99].

$$f_{X,s} = \frac{e_{X,s}}{\bar{X}} \quad (2.12)$$

$$f_{X,t} = \sqrt{f_{X,s}^2 + f_{X,r}^2} \quad (2.13)$$

The experimental tests aim at obtaining the variable speed characteristic curves of the three centrifugal pumps in the pump mode, in the turbine mode and in the four-quadrants of operation. Each measurement is performed under stationary discharge conditions. Each operating point is collected with a sampling frequency of 5'000 Hz during a 20 s time window. Measurements average and standard deviation values are recorded. The temperature variation does not exceed 2 °C during each test.

The pump mode and the turbine mode are both investigated for constant N values ranging from 600 min^{-1} to 3'000 min^{-1} with steps of 300 min^{-1} . In the pump mode, the discharge is gradually increased between each measured operating point, using a discharge control valve installed in the low pressure pipes. The bypass to the feed pumps is open to allow flow circulation in the pumping mode flow direction (see Figure 2.7). In turbine mode, the discharge and the specific energy at the PAT high pressure reference section are controlled using the VSD of the feed pumps. Measurements of the turbine mode are performed for the operating points with positive torque values.

The extended operation experimental tests aim at retrieving the $n_{ED} - Q_{ED}$ and the $n_{ED} - T_{ED}$ characteristic curves for the four-quadrants of operation showed in Table 2.2. The first quadrant is measured during the pump mode tests. The second quadrant is obtained starting at zero discharge. The feed pumps gradually supply the discharge in the generating mode flow direction (see Figure 2.7), while the PAT impeller is rotating in the pump rotational speed direction. Measurements for higher values of q_{ED} are limited by the vibrations in the test-rig.

The third quadrant is measured starting at full load conditions and gradually reducing the supplied specific hydraulic energy to the PAT high pressure section. Near runaway operating point, the PAT performance becomes unstable. The additional head loss created by a bypass in the low pressure pipes stabilises the operation of the PAT [138]. As the machine reaches zero discharge conditions, the bypass to the feed pumps is opened to allow measuring the operating points in the fourth quadrant.

2.3 Results

2.3.1 Pump mode

Experimental tests in the pump mode aim at collecting data for further comparison with the turbine mode. Experimental results described by the characteristic curves of E , T , P and η^P with respect to Q , collected for the pump mode of the pumps with n_q values of 23.1, 41.0 and 67.3 are given in Figures 2.9, 2.10 and 2.11, respectively. The measured operating points corresponding to the BEP in the pump mode are given in Section 2.6.1.

The maximum power of the tested centrifugal pumps prevented to perform measurements for $Q > 26.0 \text{ l} \cdot \text{s}^{-1}$ (see Figure 2.11). The measured values of η^P are lower compared to the efficiency values provided by the original pump manufacturer, despite being within the tolerance band of the supplier (Grade 3B of the ISO9906:2012 [100]).

2.3.2 Turbine mode

Experimental results described by the characteristic curves of E , T , P and η^T , with respect to Q , collected for the turbine mode of the pumps with n_q values of 23.1, 41.0 and 67.3 are given in Figures 2.12, 2.13 and 2.14, respectively. The measured operating points corresponding to the BEP in the turbine mode are provided in Section 2.6.2. The maximum power of the feed pumps prevented to perform measurements for $Q > 40.0 \text{ l} \cdot \text{s}^{-1}$.

The BEP in the turbine mode feature higher values of E and Q than the BEP in the pump mode (see Section 2.6). The efficiency values at the BEP in both operating modes have approximately the same values, as shown in Table 2.5, which is in agreement with results reported in the literature.

The variable speed operation broadens the operating range of the PATs. Firstly, it increases the efficiency when the PAT operates far from the best operating point. For instance, the efficiency of the $n_q = 67.3$ PAT is $\eta^T = 36.2\%$ and $\eta^T = 69.1\%$, for $3'000 \text{ min}^{-1}$ and $1'800 \text{ min}^{-1}$, respectively, when operating at a discharge of $Q = 25.0 \text{ l} \cdot \text{s}^{-1}$ (Figure 2.14). Such efficiency increase by reducing the rotational speed results in a higher power yield from $P = 1.25 \text{ kW}$ to $P = 1.75 \text{ kW}$ (38.5% increase). Secondly, the rotational speed control broadens the operation range of E . For instance, the $n_q = 23.1$ PAT only operates at $E \leq 245 \text{ J} \cdot \text{kg}^{-1}$ if the machine runs for $N \leq 3'000 \text{ min}^{-1}$ (see Figure 2.12).

Table 2.5 – Maximum efficiency values measured in pump and turbine mode.

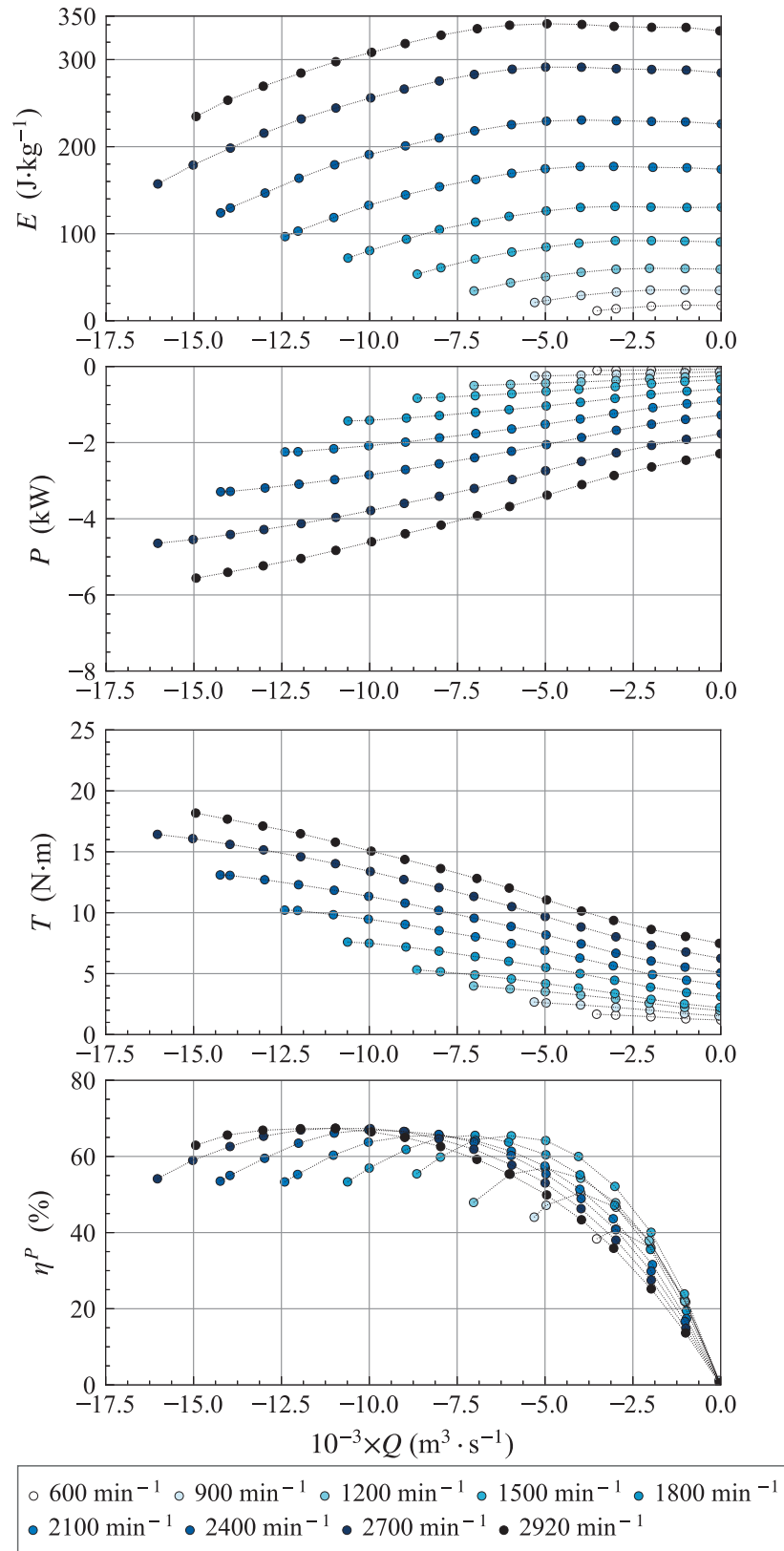
n_q (SI)	η_{\max}^P (%)	η_{\max}^T (%)	$\Delta\eta_{\max}$ (%)
23.1	67.4	72.3	4.9%
41.0	67.7	69.2	1.5%
67.3	73.5	70.7*	-**

* Maximum efficiency not measured due to discharge limitations in the test-rig.

** Comparison not meaningful as η_{\max}^T value in turbine mode for this PAT is not measured.

2.3.3 Extended operation

Experimental results of the four-quadrants of operation for the pumps with n_q values of 23.1, 41.0 and 67.3 are presented in Figures 2.15, 2.16 and 2.17, respectively. The four-quadrants characteristic curves presented in these figures are given by the variation of Q_{ED} and T_{ED} , with respect to n_{ED} . Also, the speed and the discharge factors values of the runaway operating point, n_{ED}^{runaway} and Q_{ED}^{runaway} respectively, are provided in these figures. These experimental data refer to the PATs performance with $N = 2'100 \text{ min}^{-1}$. The shape of the $n_{ED} - Q_{ED}$ and the $n_{ED} - T_{ED}$ characteristic curves are similar for all pumps. None of the PATs feature the unstable characteristic curve defined by $\partial Q_{ED} / \partial n_{ED} \geq 0$ near the runaway operating point. Both n_{ED}^{runaway} and Q_{ED}^{runaway} values increase with increasing unit specific speed.

Figure 2.9 – Experimental results in the pumping mode of the $n_q = 23.1$ pump.

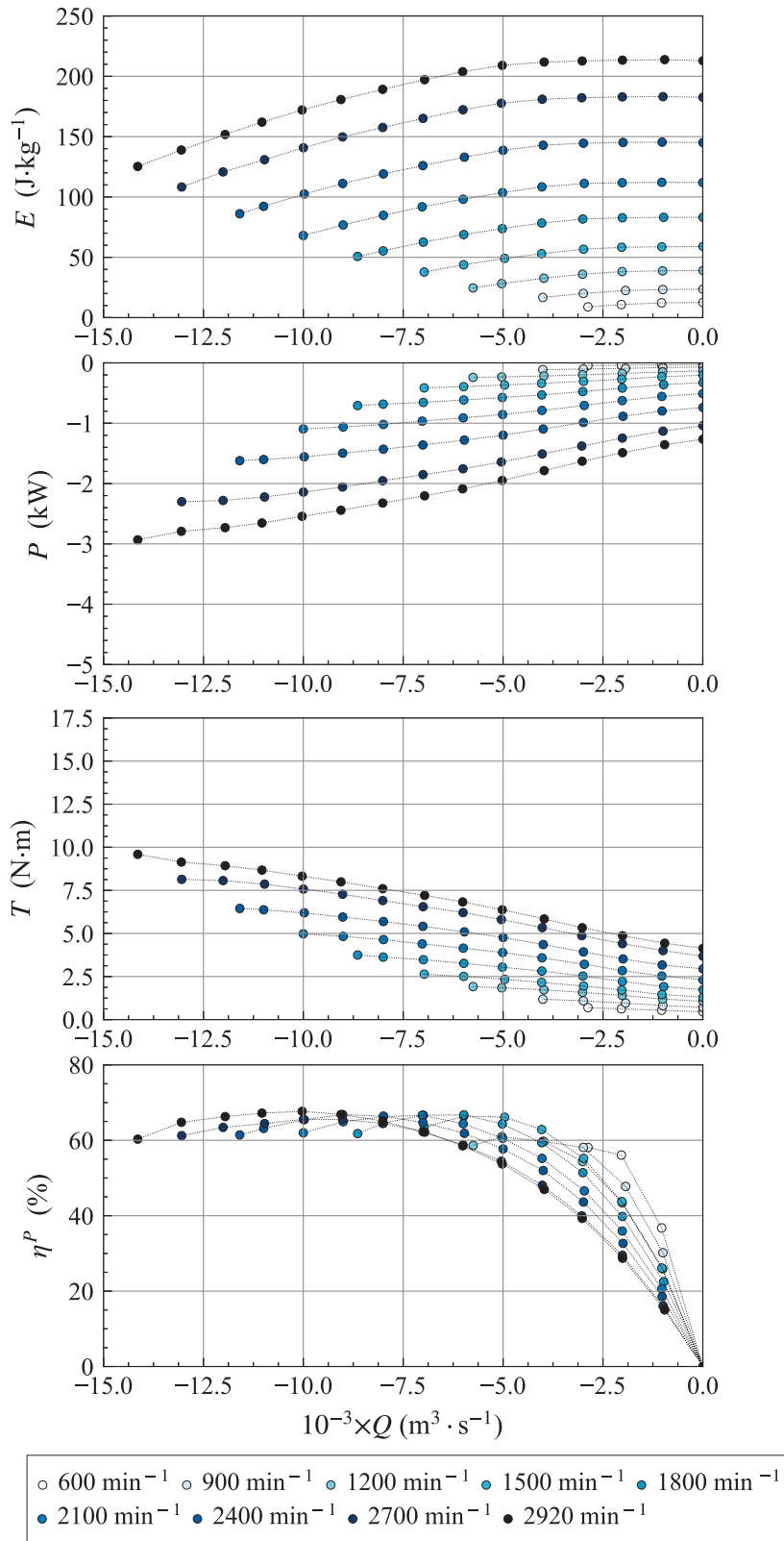
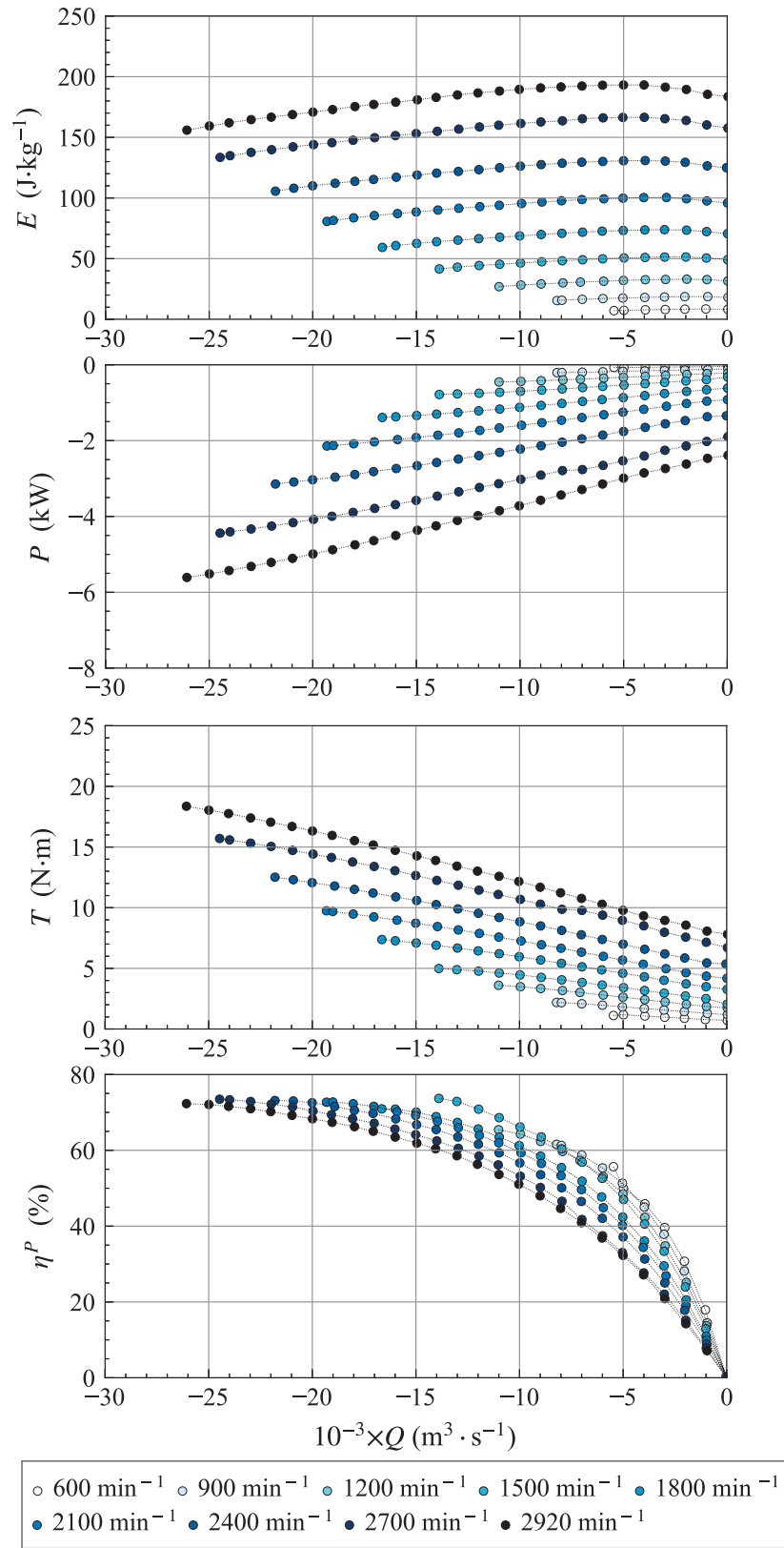


Figure 2.10 – Experimental results in the pumping mode of the $n_q = 41.0$ pump.

Figure 2.11 – Experimental results in the pumping mode of the $n_q = 67.3$ pump.

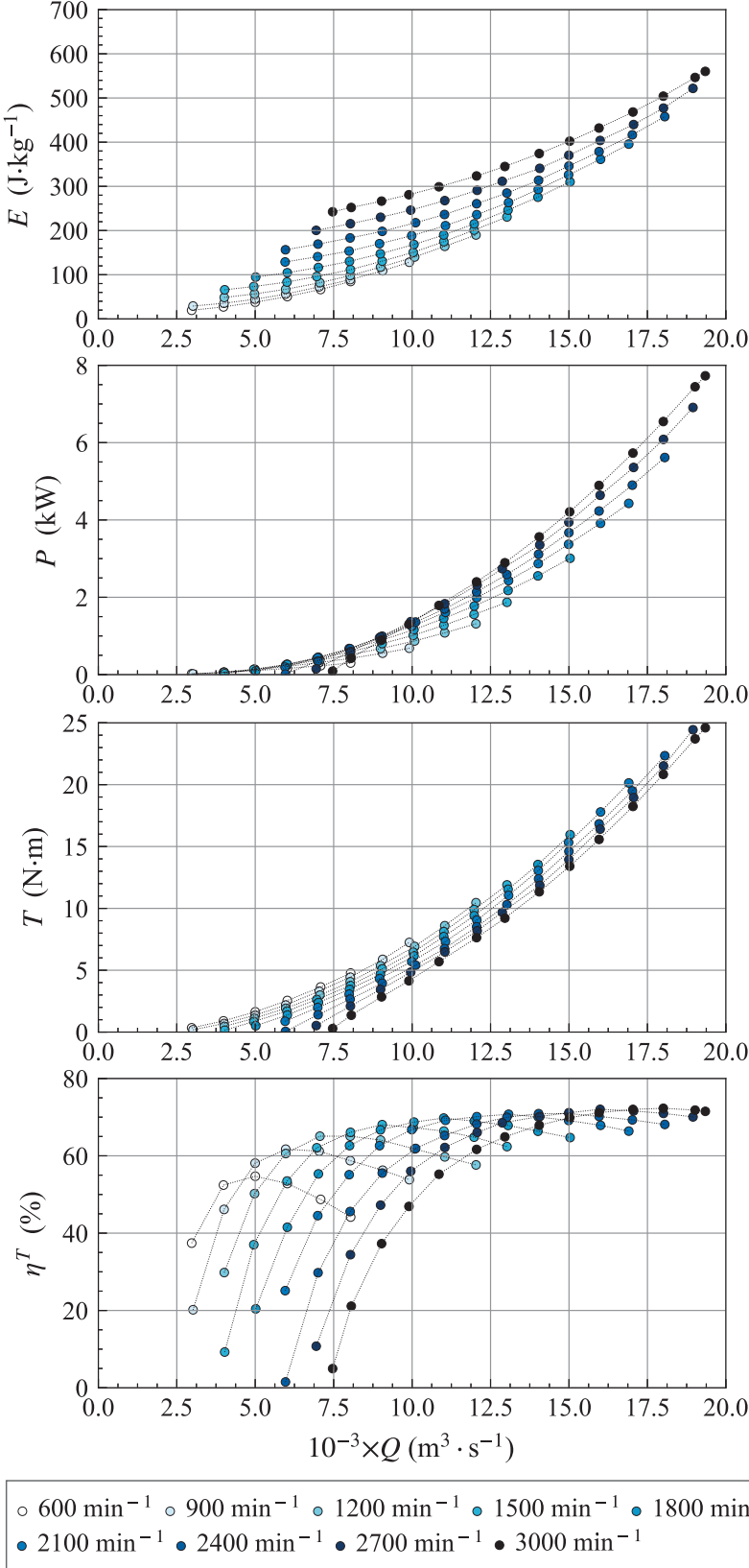
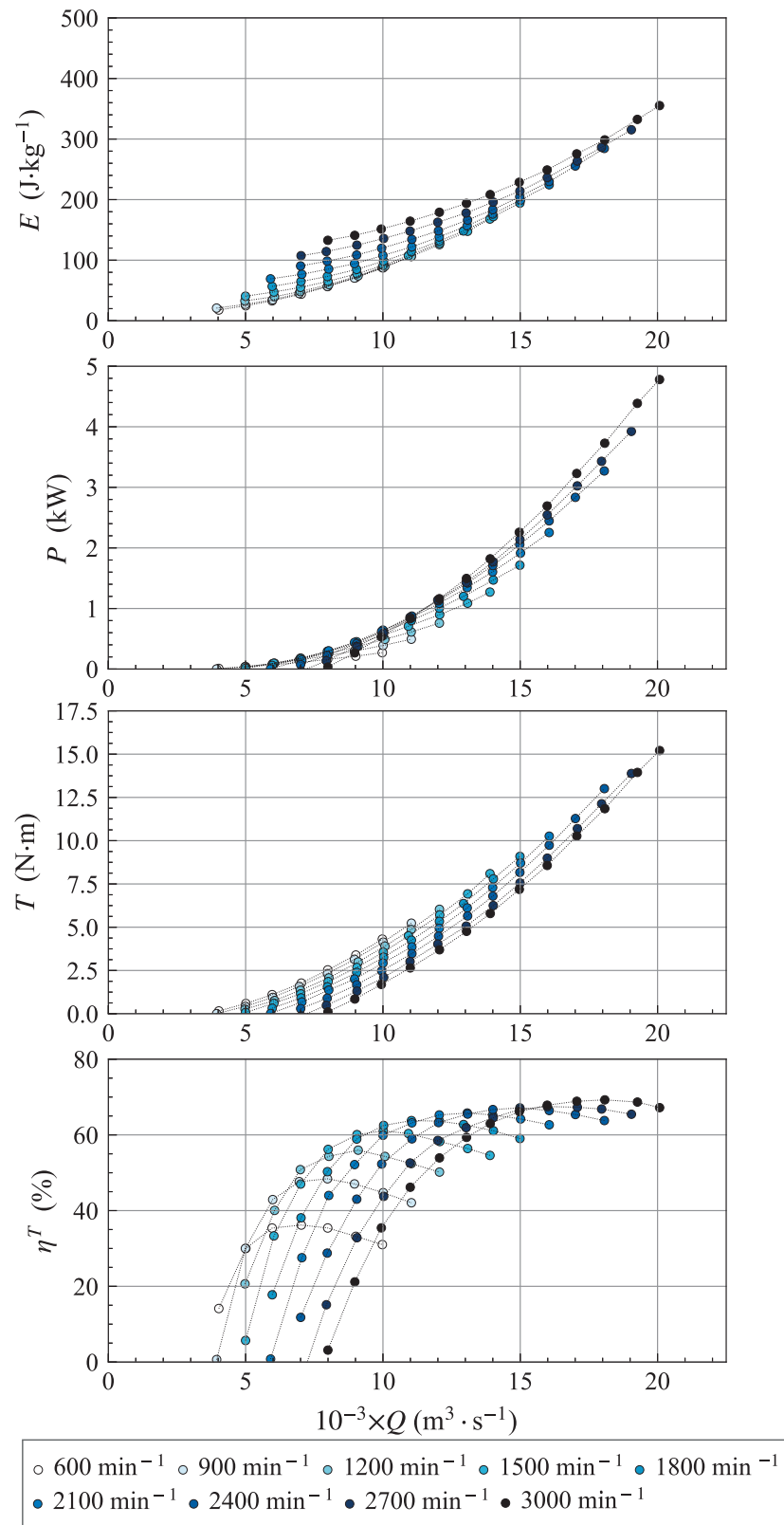
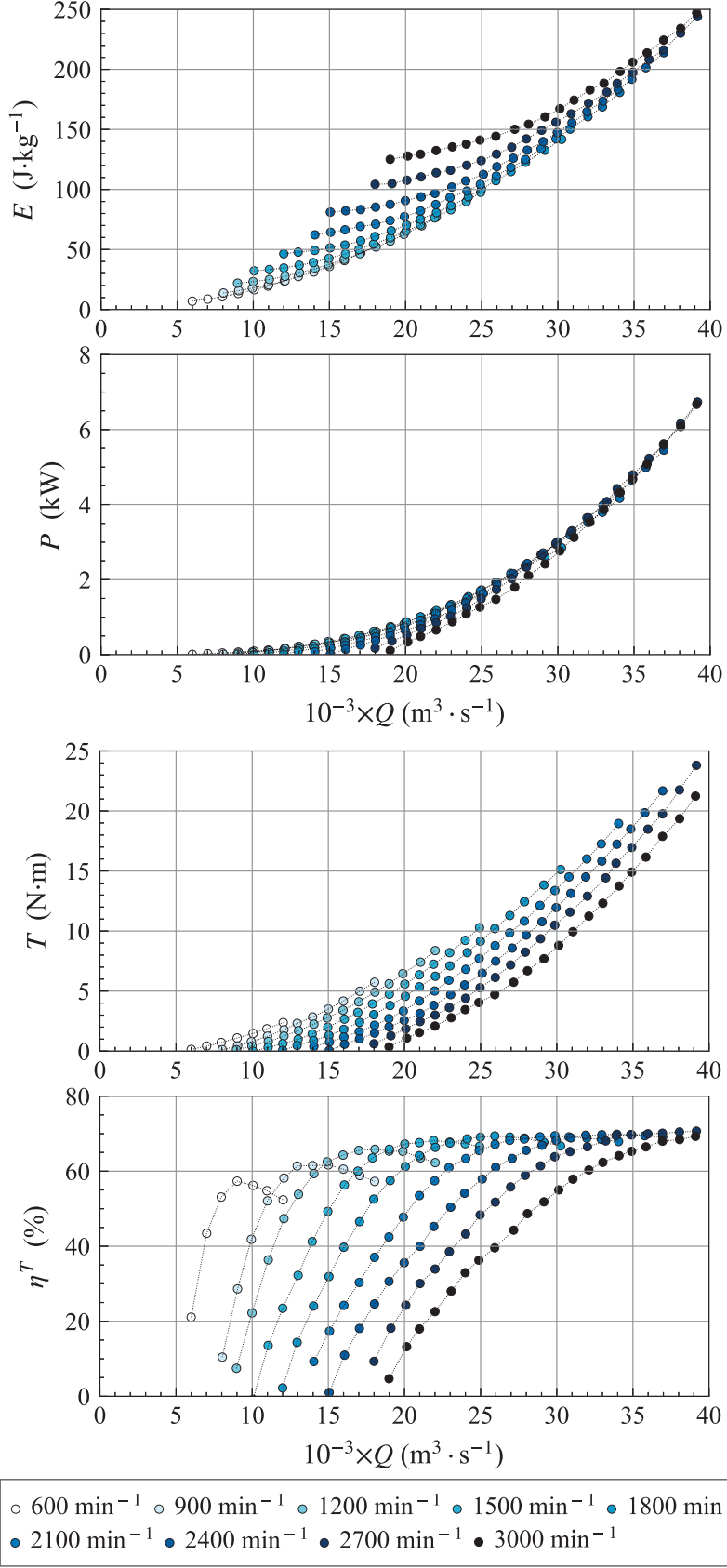
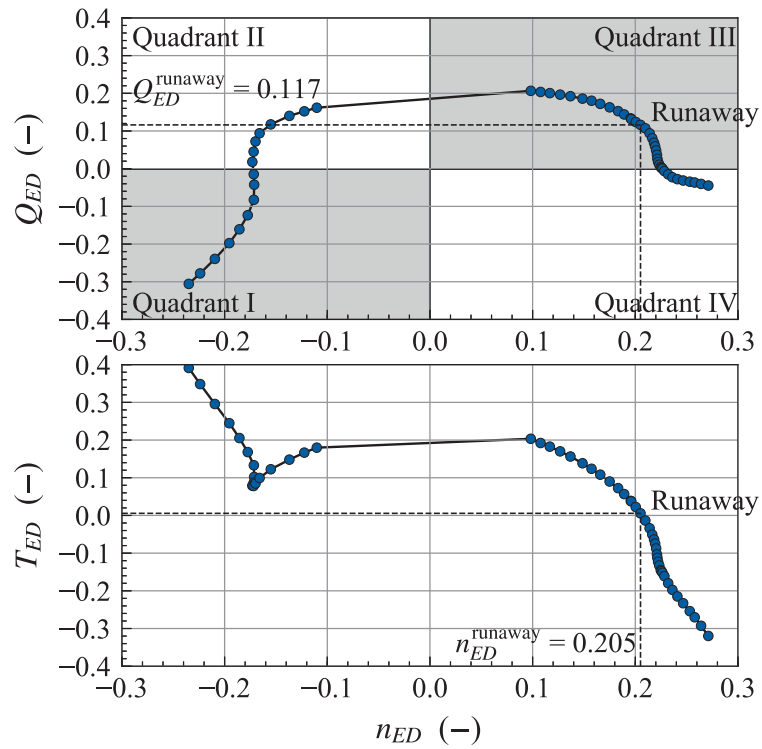
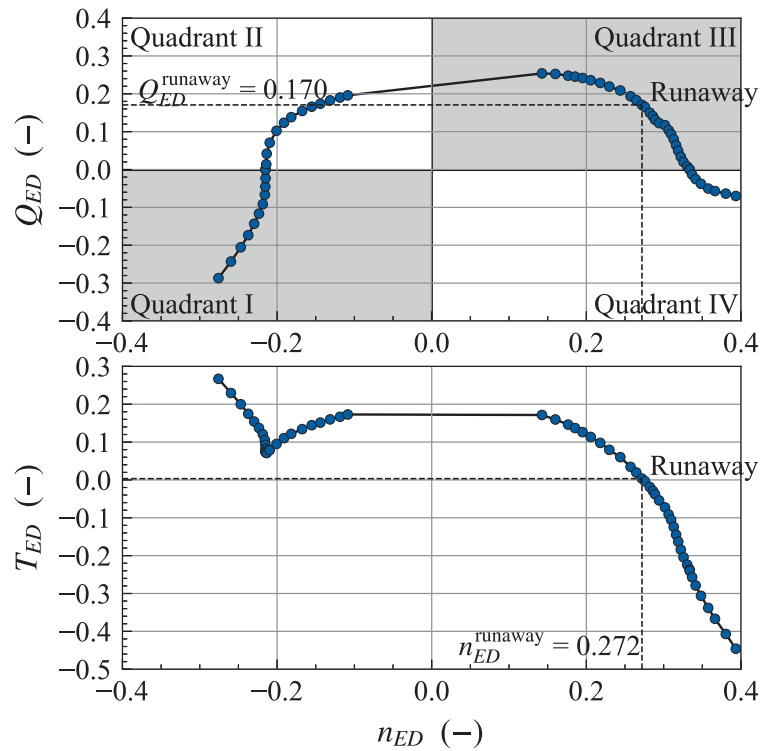


Figure 2.12 – Experimental results in the turbine mode of the $n_q = 23.1$ pump.

Figure 2.13 – Experimental results in the turbine mode of the $n_q = 41.0$ pump.



36 Figure 2.14 – Experimental results in the turbine mode of the $n_q = 67.3$ pump.

Figure 2.15 – Experimental results in the four-quadrants of the $n_q = 23.1$ pump.Figure 2.16 – Experimental results in the four-quadrants of the $n_q = 41.0$ pump.

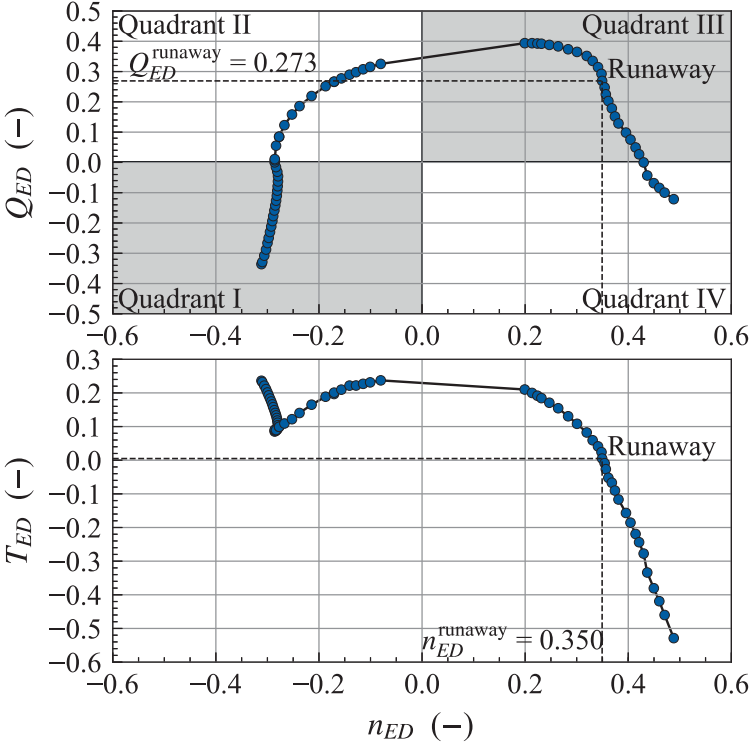


Figure 2.17 – Experimental results in the four-quadrants of the $n_q = 67.3$ pump.

2.4 Discussion

2.4.1 Variable speed operation in turbine mode

The variable speed operation in the turbine mode allows increasing the range of operation in both the discharge and the specific energy operating domain while increasing the efficiency. The stationary performance in the turbine mode of the three PATs is summarised in Figure 2.18. Data in this figure make apparent that, for each PAT, the maximum efficiency increases with increasing speed and is achieved for a constant value of the discharge factor. These discharge factor values corresponding to the maximum efficiency $Q_{ED}^{\eta_{max}}$ are provided in the Figure 2.18, for each tested PAT. The variable speed PAT performance is given by constant $Q_{ED} - n_{ED}$ characteristic curves. However, for $N = 600 \text{ min}^{-1}$ and $N = 900 \text{ min}^{-1}$ these curves are slightly deviated. This deviation could be explained by the Reynolds effects, as the discharge is reduced for these rotational speed values.

Furthermore, the efficiency significantly drops in the off-design operation if the PAT is operated with constant rotational speed. The efficiency decrease is sharper with decreasing values of n_q in the part load operation, whilst this efficiency decrease is more pronounced in full load operation with increasing values of n_q . As previously referred, the sharp efficiency decrease is related to the impeller blades leading edge flow incidence and the swirling flow at the PAT draft tube. In fact, this swirling flow is observed during the part load operation, as illustrated in Figure 2.19, if the stationary back-pressure value allows the development of a cavitation flow. The flow visualisations for this cavitation flow are shown for the the $n_q = 67.3$ PAT with similar back-pressure conditions, defined by $\sigma = 2.0$.

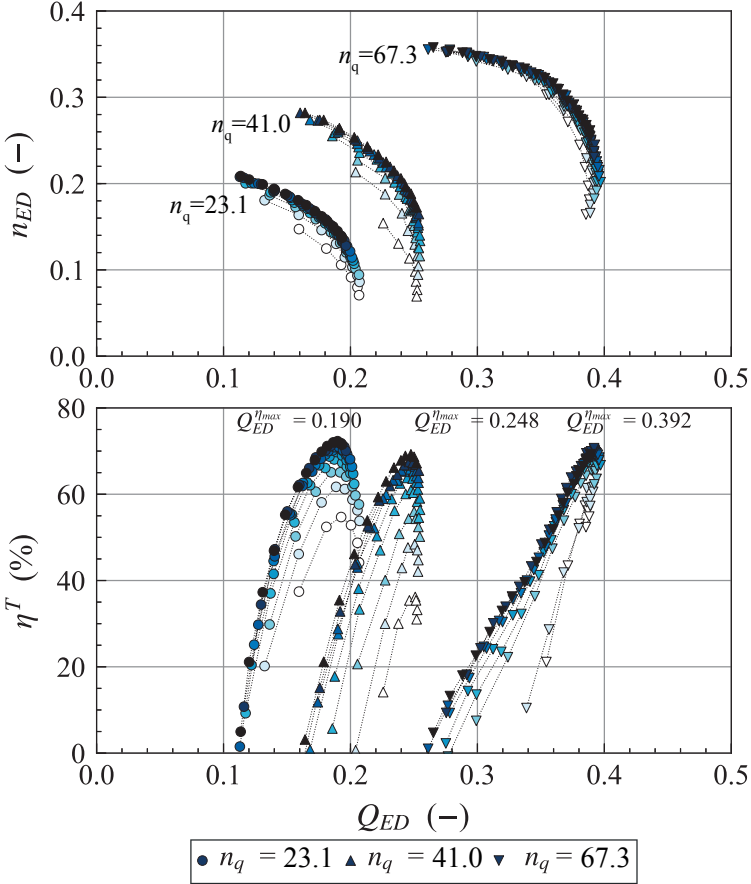
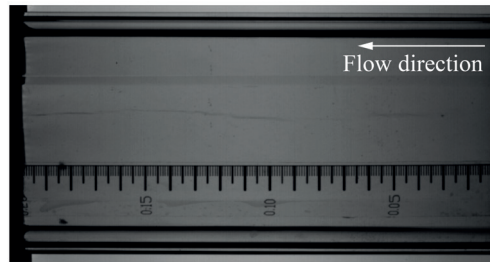
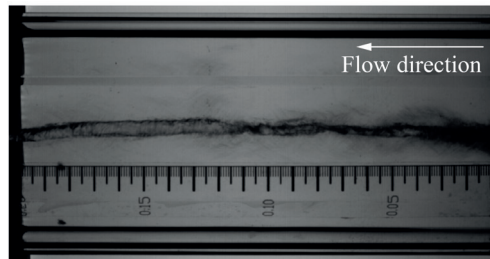


Figure 2.18 – Summary of the three PATs characteristic curves in generating mode. Variation of n_{ED} and η^T with respect to Q_{ED} . The colors of the markers refer to the rotational speed value, for instance as in Figure 2.14.

$$Q = 0.039 \text{ m}^3\cdot\text{s}^{-1}, N = 3000 \text{ min}^{-1}, \sigma = 2.0$$



$$Q = 0.030 \text{ m}^3\cdot\text{s}^{-1}, N = 3000 \text{ min}^{-1}, \sigma = 2.0$$



$$Q = 0.027 \text{ m}^3\cdot\text{s}^{-1}, N = 3000 \text{ min}^{-1}, \sigma = 2.0$$

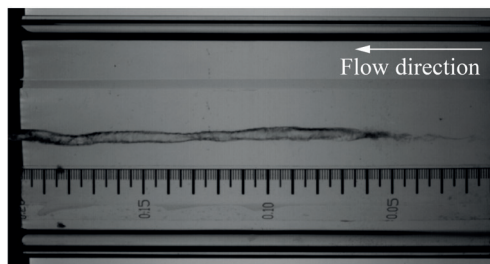


Figure 2.19 – Visualisation of the cavitation vortex rope in the $n_q = 67.3$ PAT draft tube for the operation in part load conditions.

2.4.2 Extended operation

Collected data for the variable speed operation in the third and fourth quadrants (i.e, the extended operation in the generating mode) are presented in Figures 2.20, 2.21 and 2.22, for the PATs with n_q values of 23.1, 41.0 and 67.3, respectively. Measurements are performed for constant N values ranging from $1'500 \text{ min}^{-1}$ to $3'000 \text{ min}^{-1}$. Similarly to the turbine mode, the PATs extended operation performance are given by constant $n_{ED} - Q_{ED}$ and $n_{ED} - T_{ED}$ characteristic curves, except for the $n_q = 41.0$ PAT. The analysis of the relative total errors of the n_{ED} and Q_{ED} parameters for this PAT, given in in Figure 2.23, makes apparent that the leftward deviation of the extended operation curves is not within the computed total error bands. Further measurements should be performed to determine if this deviation is caused by an error during the measurement collection for this pump. Nevertheless, the unstable feature of $\partial Q_{ED} / \partial n_{ED} \geq 0$ is not observed for any of the pumps.

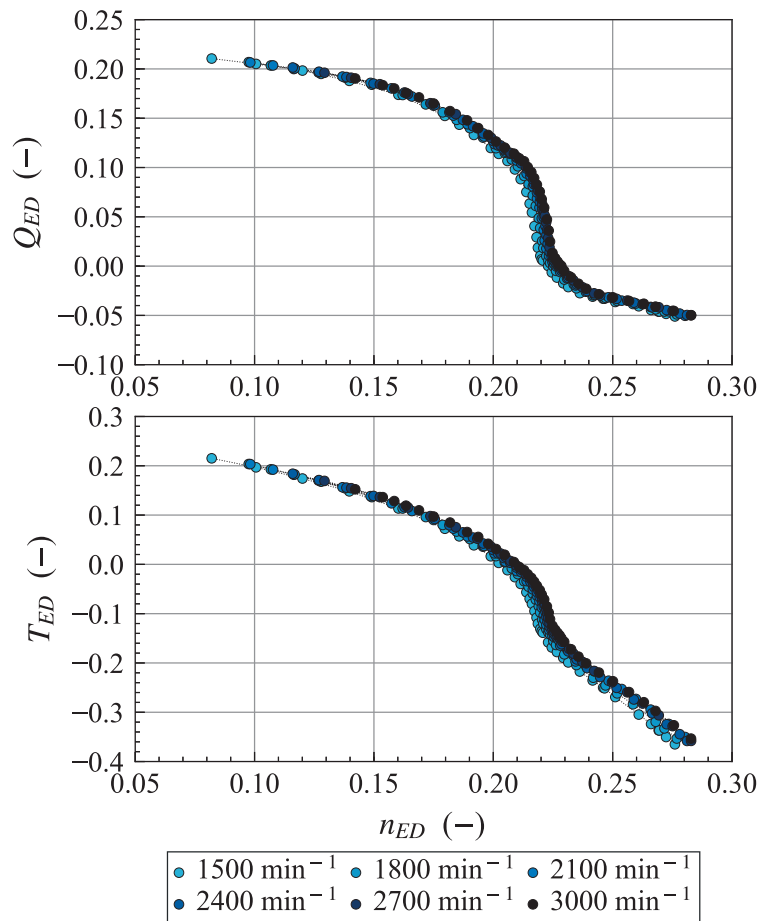


Figure 2.20 – Effect of variable speed in the third and fourth quadrant of the $n_q = 23.1$ pump.

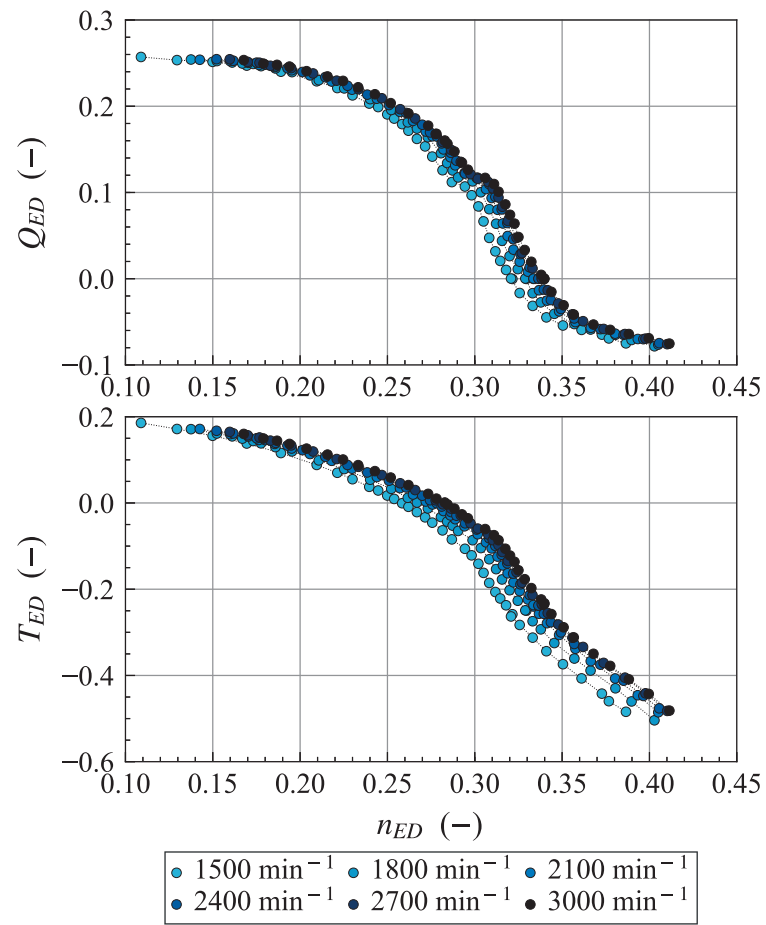


Figure 2.21 – Effect of variable speed in the third and fourth quadrant of the $n_q = 41.0$ pump.

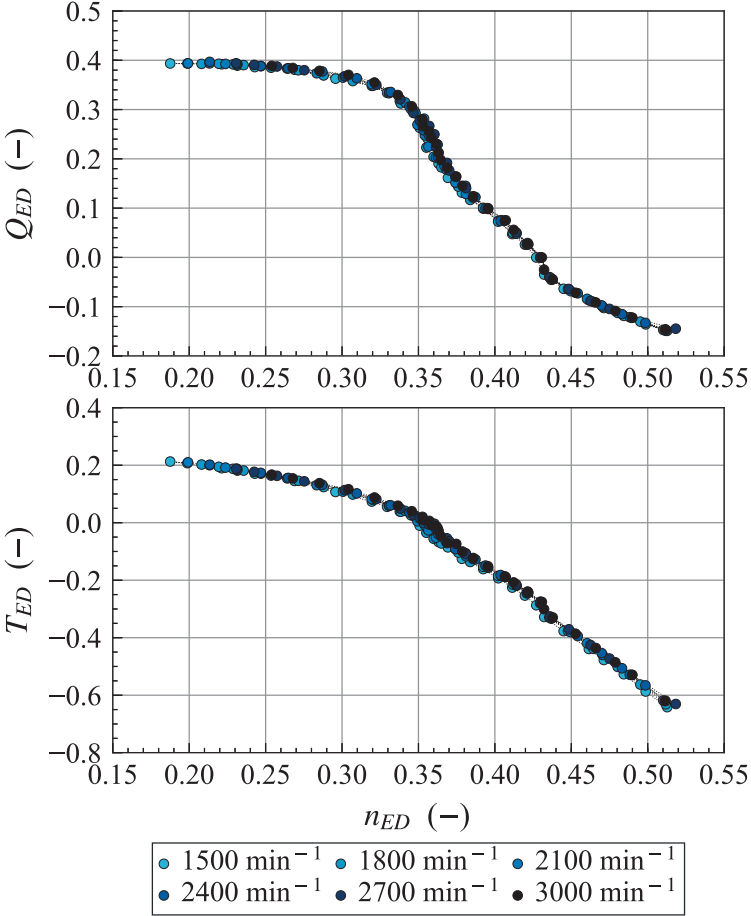


Figure 2.22 – Effect of variable speed in the third and fourth quadrants of the $n_q = 67.3$ pump.

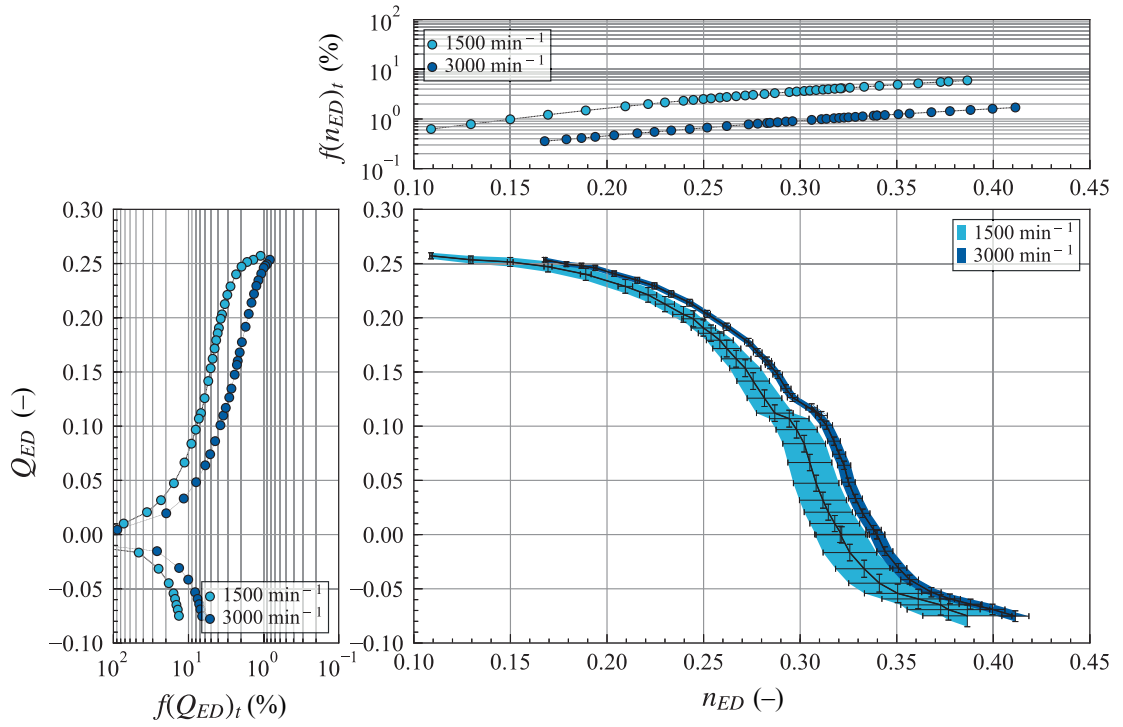


Figure 2.23 – Total relative error of n_{ED} and Q_{ED} in the third and fourth quadrant of $n_q = 41.0$ pump.

2.5 Conclusions and perspectives

This research work presents the experimental investigation of the stationary performance of variable speed PAT operation. The experimental tests are performed in three single-stage end-suction centrifugal pumps with different n_q values, focusing on the turbine mode and the extended operation performance.

Measurements collected allow concluding that the variable speed operation is suitable for increasing the operating efficiency of PATs under the variable discharge conditions of WSS. Also, the variable speed operation allows broadening the specific energy (or head) and discharge operating range. This operating range broadening is particularly relevant if the PAT is installed in a WSS where the pressure is dynamically controlled [45, 139], for optimal management of the water supply system. The maximum efficiency in the turbine mode is equal or higher as the efficiency in the pump mode. Also, the maximum efficiency is obtained for constant Q_{ED} values, independently of the rotational speed set-point. The collected data for the extended operation make apparent that the tested PATs do not feature the unstable characteristic curves described by $\partial Q_{ED}/\partial n_{ED} \geq 0$ near the runaway operating point.

The obtained results are currently being applied for the development of empirical models for describing the variable speed performance of this type of PATs, under the range of n_q values tested. These empirical models could be used for: (i) analysing the energy yield of the PAT system; (ii) provide the specifications for the start-up and shut-down manoeuvres; or (iii) assess the hydraulic transient effects in the micro hydropower system due to emergency operation. This will allow comparing the effectiveness of different system layouts and operating strategies, which is still an open research topic.

2.6 Appendix

2.6.1 Appendix A - BEP measurements of the pump mode

Table 2.6 – BEP measurements for the three tested pumps in the pump mode for absolute N values between $1'500 \text{ min}^{-1}$ and $2'920 \text{ min}^{-1}$. Values inside parentheses indicate the total relative errors.

Pump ID	N (min^{-1})	Q ($\text{l} \cdot \text{s}^{-1}$)	E ($\text{J} \cdot \text{kg}^{-1}$)
$n_q = 23.1$	$-1'500$ ($\pm 0.4\%$)	-6.0 ($\pm 2.7\%$)	79.0 ($\pm 1.3\%$)
	$-1'800$ ($\pm 0.3\%$)	-7.0 ($\pm 2.3\%$)	113.3 ($\pm 0.9\%$)
	$-2'099$ ($\pm 0.3\%$)	-8.0 ($\pm 2.0\%$)	154.0 ($\pm 0.7\%$)
	$-2'398$ ($\pm 0.3\%$)	-10.0 ($\pm 1.6\%$)	191.0 ($\pm 0.6\%$)
	$-2'700$ ($\pm 0.2\%$)	-10.0 ($\pm 1.6\%$)	256.0 ($\pm 0.4\%$)
	$-2'922$ ($\pm 0.2\%$)	-11.0 ($\pm 1.5\%$)	297.6 ($\pm 0.4\%$)
$n_q = 41.0$	$-1'500$ ($\pm 0.4\%$)	-6.0 ($\pm 2.7\%$)	43.8 ($\pm 2.4\%$)
	$-1'800$ ($\pm 0.3\%$)	-6.0 ($\pm 2.7\%$)	68.8 ($\pm 1.5\%$)
	$-2'099$ ($\pm 0.3\%$)	-7.0 ($\pm 2.3\%$)	91.9 ($\pm 1.2\%$)
	$-2'400$ ($\pm 0.2\%$)	-9.0 ($\pm 1.8\%$)	111.2 ($\pm 1.0\%$)
	$-2'700$ ($\pm 0.2\%$)	-10.0 ($\pm 1.6\%$)	140.8 ($\pm 0.8\%$)
	$-2'918$ ($\pm 0.2\%$)	-10.0 ($\pm 1.6\%$)	172.1 ($\pm 0.6\%$)
$n_q = 67.3$	$-1'499$ ($\pm 0.4\%$)	-13.9 ($\pm 1.2\%$)	41.6 ($\pm 2.5\%$)
	$-1'799$ ($\pm 0.3\%$)	-16.6 ($\pm 1.0\%$)	59.3 ($\pm 1.8\%$)
	$-2'099$ ($\pm 0.3\%$)	-19.3 ($\pm 0.8\%$)	80.7 ($\pm 1.3\%$)
	$-2'399$ ($\pm 0.3\%$)	-21.8 ($\pm 0.7\%$)	105.6 ($\pm 1.0\%$)
	$-2'699$ ($\pm 0.2\%$)	-24.5 ($\pm 0.7\%$)	133.5 ($\pm 0.8\%$)
	$-2'918$ ($\pm 0.2\%$)	-26.1 ($\pm 0.6\%$)	155.9 ($\pm 0.7\%$)

Chapter 2. Experimental investigation

Table 2.7 – BEP measurements for the three tested pumps in the pump mode for absolute N values between $1'500 \text{ min}^{-1}$ and $2'920 \text{ min}^{-1}$. Values inside parentheses indicate the total relative errors. Note: * BEP not measured due to discharge limitations in the test-rig.

Pump ID	N (min^{-1})	T ($\text{N}\cdot\text{m}$)	P (kW)	η^P (%)
$n_q = 23.1$	$-1'500$ ($\pm 0.4\%$)	4.6 ($\pm 3.3\%$)	-0.7 ($\pm 3.3\%$)	65.4 ($\pm 4.5\%$)
	$-1'800$ ($\pm 0.3\%$)	6.4 ($\pm 2.3\%$)	-1.2 ($\pm 2.4\%$)	65.5 ($\pm 3.4\%$)
	$-2'099$ ($\pm 0.3\%$)	8.5 ($\pm 1.8\%$)	-1.9 ($\pm 1.8\%$)	65.7 ($\pm 2.8\%$)
	$-2'398$ ($\pm 0.3\%$)	11.3 ($\pm 1.3\%$)	-2.8 ($\pm 1.3\%$)	67.0 ($\pm 2.2\%$)
	$-2'700$ ($\pm 0.2\%$)	13.4 ($\pm 1.1\%$)	-3.8 ($\pm 1.1\%$)	67.3 ($\pm 2.0\%$)
	$-2'922$ ($\pm 0.2\%$)	15.8 ($\pm 1.0\%$)	-4.8 ($\pm 1.0\%$)	67.4 ($\pm 1.8\%$)
$n_q = 41.0$	$-1'500$ ($\pm 0.4\%$)	2.5 ($\pm 6.0\%$)	-0.4 ($\pm 6.0\%$)	66.4 ($\pm 7.0\%$)
	$-1'800$ ($\pm 0.3\%$)	3.3 ($\pm 4.6\%$)	-0.6 ($\pm 4.6\%$)	66.7 ($\pm 5.5\%$)
	$-2'099$ ($\pm 0.3\%$)	4.4 ($\pm 3.4\%$)	-1.0 ($\pm 3.4\%$)	66.6 ($\pm 4.3\%$)
	$-2'400$ ($\pm 0.2\%$)	6.0 ($\pm 2.5\%$)	-1.5 ($\pm 2.5\%$)	66.8 ($\pm 3.2\%$)
	$-2'700$ ($\pm 0.2\%$)	7.6 ($\pm 2.0\%$)	-2.1 ($\pm 2.0\%$)	65.6 ($\pm 2.7\%$)
	$-2'918$ ($\pm 0.2\%$)	8.3 ($\pm 1.8\%$)	-2.5 ($\pm 1.8\%$)	67.7 ($\pm 2.5\%$)
$n_q = 67.3$	$-1'499$ ($\pm 0.4\%$)	5.0 ($\pm 3.0\%$)	-0.8 ($\pm 3.0\%$)	70.7 ($\pm 4.1\%$)
	$-1'799$ ($\pm 0.3\%$)	7.4 ($\pm 2.0\%$)	-1.4 ($\pm 2.1\%$)	70.9 ($\pm 2.9\%$)
	$-2'099$ ($\pm 0.3\%$)	9.7 ($\pm 1.5\%$)	-2.1 ($\pm 1.6\%$)	72.7 ($\pm 2.2\%$)
	$-2'399$ ($\pm 0.3\%$)	12.5 ($\pm 1.2\%$)	-3.1 ($\pm 1.2\%$)	73.1 ($\pm 1.7\%$)
	$-2'699$ ($\pm 0.2\%$)	15.7 ($\pm 1.0\%$)	-4.4 ($\pm 1.0\%$)	73.5 ($\pm 1.4\%$)*
	$-2'918$ ($\pm 0.2\%$)	18.4 ($\pm 0.8\%$)	-5.6 ($\pm 0.8\%$)	72.3 ($\pm 1.2\%$)*

Table 2.8 – BEP measurements for the three tested pumps in the pump mode for absolute N values between $1'500 \text{ min}^{-1}$ and $2'920 \text{ min}^{-1}$. Values inside parentheses indicate the total relative errors.

Pump ID	N (min^{-1})	n_{ED} (-)	Q_{ED} (-)	T_{ED} (-)
$n_q = 23.1$	$-1'500$ ($\pm 0.4\%$)	-0.18 ($\pm 1.4\%$)	-0.16 ($\pm 3.0\%$)	0.21 ($\pm 3.5\%$)
	$-1'800$ ($\pm 0.3\%$)	-0.18 ($\pm 1.0\%$)	-0.16 ($\pm 2.5\%$)	0.21 ($\pm 2.5\%$)
	$-2'099$ ($\pm 0.3\%$)	-0.18 ($\pm 0.7\%$)	-0.15 ($\pm 2.1\%$)	0.20 ($\pm 1.9\%$)
	$-2'398$ ($\pm 0.3\%$)	-0.19 ($\pm 0.6\%$)	-0.17 ($\pm 1.7\%$)	0.22 ($\pm 1.4\%$)
	$-2'700$ ($\pm 0.2\%$)	-0.18 ($\pm 0.5\%$)	-0.15 ($\pm 1.7\%$)	0.19 ($\pm 1.2\%$)
	$-2'922$ ($\pm 0.2\%$)	-0.18 ($\pm 0.4\%$)	-0.15 ($\pm 1.5\%$)	0.19 ($\pm 1.0\%$)
$n_q = 41.0$	$-1'500$ ($\pm 0.4\%$)	-0.25 ($\pm 2.4\%$)	-0.21 ($\pm 3.6\%$)	0.21 ($\pm 6.4\%$)
	$-1'800$ ($\pm 0.3\%$)	-0.24 ($\pm 1.6\%$)	-0.17 ($\pm 3.1\%$)	0.17 ($\pm 4.8\%$)
	$-2'099$ ($\pm 0.3\%$)	-0.24 ($\pm 1.2\%$)	-0.18 ($\pm 2.6\%$)	0.18 ($\pm 3.6\%$)
	$-2'400$ ($\pm 0.2\%$)	-0.25 ($\pm 1.0\%$)	-0.20 ($\pm 2.0\%$)	0.20 ($\pm 2.7\%$)
	$-2'700$ ($\pm 0.2\%$)	-0.25 ($\pm 0.8\%$)	-0.20 ($\pm 1.8\%$)	0.20 ($\pm 2.1\%$)
	$-2'918$ ($\pm 0.2\%$)	-0.24 ($\pm 0.7\%$)	-0.19 ($\pm 1.7\%$)	0.18 ($\pm 1.9\%$)
$n_q = 67.3$	$-1'499$ ($\pm 0.4\%$)	-0.31 ($\pm 2.6\%$)	-0.34 ($\pm 2.8\%$)	0.26 ($\pm 3.9\%$)
	$-1'799$ ($\pm 0.3\%$)	-0.31 ($\pm 1.8\%$)	-0.34 ($\pm 2.0\%$)	0.24 ($\pm 2.7\%$)
	$-2'099$ ($\pm 0.3\%$)	-0.31 ($\pm 1.3\%$)	-0.34 ($\pm 1.5\%$)	0.24 ($\pm 2.0\%$)
	$-2'399$ ($\pm 0.3\%$)	-0.31 ($\pm 1.0\%$)	-0.33 ($\pm 1.2\%$)	0.23 ($\pm 1.6\%$)
	$-2'699$ ($\pm 0.2\%$)	-0.31 ($\pm 0.8\%$)	-0.33 ($\pm 1.0\%$)	0.23 ($\pm 1.2\%$)
	$-2'918$ ($\pm 0.2\%$)	-0.31 ($\pm 0.7\%$)	-0.33 ($\pm 0.9\%$)	0.23 ($\pm 1.1\%$)

2.6.2 Appendix B - BEP measurements of the turbine mode

Table 2.9 – BEP measurements for the three tested pumps in the turbine mode for absolute N values between $1'500 \text{ min}^{-1}$ and $3'000 \text{ min}^{-1}$. Values inside parentheses indicate the total relative errors.

Pump ID	$N \text{ (min}^{-1}\text{)}$	$Q \text{ (l}\cdot\text{s}^{-1}\text{)}$	$E \text{ (J}\cdot\text{kg}^{-1}\text{)}$
$n_q = 23.1$	1'500 ($\pm 0.4\%$)	9.0 ($\pm 1.8\%$)	130.8 ($\pm 0.8\%$)
	1'800 ($\pm 0.3\%$)	11.0 ($\pm 1.5\%$)	189.9 ($\pm 0.6\%$)
	2'100 ($\pm 0.3\%$)	13.1 ($\pm 1.2\%$)	263.5 ($\pm 0.4\%$)
	2'400 ($\pm 0.2\%$)	15.0 ($\pm 1.1\%$)	346.0 ($\pm 0.3\%$)
	2'701 ($\pm 0.2\%$)	16.0 ($\pm 1.0\%$)	403.8 ($\pm 0.3\%$)
	3'001 ($\pm 0.2\%$)	18.0 ($\pm 0.9\%$)	504.1 ($\pm 0.2\%$)
$n_q = 41.0$	1'499 ($\pm 0.4\%$)	10.0 ($\pm 1.6\%$)	91.5 ($\pm 1.2\%$)
	1'800 ($\pm 0.3\%$)	11.0 ($\pm 1.4\%$)	114.1 ($\pm 0.9\%$)
	2'100 ($\pm 0.3\%$)	13.1 ($\pm 1.2\%$)	156.8 ($\pm 0.7\%$)
	2'402 ($\pm 0.2\%$)	15.0 ($\pm 1.1\%$)	204.7 ($\pm 0.5\%$)
	2'703 ($\pm 0.2\%$)	16.0 ($\pm 1.0\%$)	236.4 ($\pm 0.5\%$)
	3'005 ($\pm 0.2\%$)	18.1 ($\pm 0.9\%$)	298.6 ($\pm 0.4\%$)
$n_q = 67.3$	1'500 ($\pm 0.4\%$)	21.9 ($\pm 0.7\%$)	76.3 ($\pm 1.4\%$)
	1'801 ($\pm 0.3\%$)	25.9 ($\pm 0.6\%$)	107.3 ($\pm 1.0\%$)
	2'100 ($\pm 0.3\%$)	29.9 ($\pm 0.5\%$)	142.2 ($\pm 0.7\%$)
	2'401 ($\pm 0.2\%$)	33.9 ($\pm 0.5\%$)	183.2 ($\pm 0.6\%$)
	2'701 ($\pm 0.2\%$)	39.2 ($\pm 0.4\%$)	243.9 ($\pm 0.4\%$)
	3'000 ($\pm 0.2\%$)	39.1 ($\pm 0.4\%$)	247.0 ($\pm 0.4\%$)

Chapter 2. Experimental investigation

Table 2.10 – BEP measurements for the three tested pumps in the turbine mode for absolute N values between $1'500 \text{ min}^{-1}$ and $3'000 \text{ min}^{-1}$. Values inside parentheses indicate the total relative errors. Note: * BEP not measured due to discharge limitations in the test-rig.

Pump ID	N (min^{-1})	T ($\text{N}\cdot\text{m}$)	P (kW)	η^T (%)
$n_q = 23.1$	$1'500$ ($\pm 0.4\%$)	5.1 ($\pm 2.9\%$)	0.8 ($\pm 0.1\%$)	68.1 ($\pm 3.5\%$)
	$1'800$ ($\pm 0.3\%$)	7.7 ($\pm 1.9\%$)	1.5 ($\pm 0.2\%$)	69.8 ($\pm 2.5\%$)
	$2'100$ ($\pm 0.3\%$)	11.1 ($\pm 1.4\%$)	2.4 ($\pm 0.2\%$)	70.7 ($\pm 1.9\%$)
	$2'400$ ($\pm 0.2\%$)	14.6 ($\pm 1.0\%$)	3.7 ($\pm 0.2\%$)	70.9 ($\pm 1.5\%$)
	$2'701$ ($\pm 0.2\%$)	16.4 ($\pm 0.9\%$)	4.6 ($\pm 0.2\%$)	72.0 ($\pm 1.4\%$)
	$3'001$ ($\pm 0.2\%$)	20.8 ($\pm 0.7\%$)	6.5 ($\pm 0.3\%$)	72.3 ($\pm 1.2\%$)
$n_q = 41.0$	$1'499$ ($\pm 0.4\%$)	3.6 ($\pm 4.2\%$)	0.6 ($\pm 0.1\%$)	61.1 ($\pm 4.7\%$)
	$1'800$ ($\pm 0.3\%$)	4.2 ($\pm 3.5\%$)	0.8 ($\pm 0.1\%$)	63.8 ($\pm 3.9\%$)
	$2'100$ ($\pm 0.3\%$)	6.1 ($\pm 2.5\%$)	1.3 ($\pm 0.1\%$)	65.8 ($\pm 2.8\%$)
	$2'402$ ($\pm 0.2\%$)	8.2 ($\pm 1.8\%$)	2.1 ($\pm 0.1\%$)	67.1 ($\pm 2.2\%$)
	$2'703$ ($\pm 0.2\%$)	9.0 ($\pm 1.7\%$)	2.5 ($\pm 0.1\%$)	67.5 ($\pm 2.0\%$)
	$3'005$ ($\pm 0.2\%$)	11.8 ($\pm 1.3\%$)	3.7 ($\pm 0.2\%$)	69.2 ($\pm 1.6\%$)
$n_q = 67.3$	1500 ($\pm 0.4\%$)	7.2 ($\pm 2.1\%$)	1.1 ($\pm 0.2\%$)	68.2 ($\pm 2.6\%$)
	$1'801$ ($\pm 0.3\%$)	10.2 ($\pm 1.5\%$)	1.9 ($\pm 0.2\%$)	69.4 ($\pm 1.9\%$)
	$2'100$ ($\pm 0.3\%$)	13.4 ($\pm 1.1\%$)	2.9 ($\pm 0.3\%$)	69.4 ($\pm 1.5\%$)
	$2'401$ ($\pm 0.2\%$)	17.2 ($\pm 0.9\%$)	4.3 ($\pm 0.3\%$)	69.8 ($\pm 1.2\%$)
	$2'701$ ($\pm 0.2\%$)	23.8 ($\pm 0.6\%$)	6.7 ($\pm 0.4\%$)	70.7 ($\pm 0.9\%$)*
	$3'000$ ($\pm 0.2\%$)	21.2 ($\pm 0.7\%$)	6.7 ($\pm 0.3\%$)	69.3 ($\pm 0.9\%$)*

Table 2.11 – BEP measurements for the three tested pumps in the turbine mode for absolute N values between $1'500 \text{ min}^{-1}$ and $3'000 \text{ min}^{-1}$. Values inside parentheses indicate the total relative errors.

Pump ID	N (min^{-1})	n_{ED} (-)	Q_{ED} (-)	T_{ED} (-)
$n_q = 23.1$	$1'500$ ($\pm 0.4\%$)	0.14 ($\pm 0.9\%$)	0.19 ($\pm 1.9\%$)	0.14 ($\pm 3.0\%$)
	$1'800$ ($\pm 0.3\%$)	0.14 ($\pm 0.7\%$)	0.19 ($\pm 1.6\%$)	0.15 ($\pm 2.0\%$)
	$2'100$ ($\pm 0.3\%$)	0.14 ($\pm 0.5\%$)	0.19 ($\pm 1.3\%$)	0.15 ($\pm 1.4\%$)
	$2'400$ ($\pm 0.2\%$)	0.14 ($\pm 0.4\%$)	0.19 ($\pm 1.1\%$)	0.15 ($\pm 1.1\%$)
	$2'701$ ($\pm 0.2\%$)	0.15 ($\pm 0.4\%$)	0.19 ($\pm 1.0\%$)	0.15 ($\pm 1.0\%$)
	$3'001$ ($\pm 0.2\%$)	0.14 ($\pm 0.3\%$)	0.19 ($\pm 0.9\%$)	0.15 ($\pm 0.8\%$)
$n_q = 41.0$	$1'499$ ($\pm 0.4\%$)	0.17 ($\pm 1.2\%$)	0.25 ($\pm 2.0\%$)	0.14 ($\pm 4.4\%$)
	$1'800$ ($\pm 0.3\%$)	0.18 ($\pm 1.0\%$)	0.24 ($\pm 1.7\%$)	0.14 ($\pm 3.7\%$)
	$2'100$ ($\pm 0.3\%$)	0.18 ($\pm 0.7\%$)	0.25 ($\pm 1.4\%$)	0.14 ($\pm 2.5\%$)
	$2'402$ ($\pm 0.2\%$)	0.18 ($\pm 0.6\%$)	0.25 ($\pm 1.2\%$)	0.15 ($\pm 1.9\%$)
	$2'703$ ($\pm 0.2\%$)	0.19 ($\pm 0.5\%$)	0.25 ($\pm 1.1\%$)	0.14 ($\pm 1.7\%$)
	$3'005$ ($\pm 0.2\%$)	0.19 ($\pm 0.4\%$)	0.25 ($\pm 1.0\%$)	0.14 ($\pm 1.3\%$)
$n_q = 67.3$	$1'500$ ($\pm 0.4\%$)	0.23 ($\pm 1.4\%$)	0.39 ($\pm 1.6\%$)	0.19 ($\pm 2.5\%$)
	$1'801$ ($\pm 0.3\%$)	0.23 ($\pm 1.0\%$)	0.39 ($\pm 1.2\%$)	0.19 ($\pm 1.8\%$)
	$2'100$ ($\pm 0.3\%$)	0.23 ($\pm 0.8\%$)	0.39 ($\pm 0.9\%$)	0.18 ($\pm 1.3\%$)
	$2'401$ ($\pm 0.2\%$)	0.24 ($\pm 0.6\%$)	0.39 ($\pm 0.7\%$)	0.18 ($\pm 1.0\%$)
	$2'701$ ($\pm 0.2\%$)	0.23 ($\pm 0.5\%$)	0.39 ($\pm 0.6\%$)	0.19 ($\pm 0.8\%$)
	$3'000$ ($\pm 0.2\%$)	0.25 ($\pm 0.5\%$)	0.39 ($\pm 0.6\%$)	0.17 ($\pm 0.8\%$)

3 Pressure fluctuations in off-design operation

This chapter corresponds to the research paper:

J. Delgado, E. Vagnoni, D.I.C. Covas and F. Avellan (2018), *Experimental evidence of pressure fluctuations during off-design operation of a centrifugal pump running as turbine*. Submitted to Renewable Energy, Elsevier.

Author contribution: The author performed the experiments, the pressure data analysis and the comparison between the image processing data analysis and the pressure measurements.

Abstract

Pumps running as turbines (PAT) are suitable hydraulic machines for energy recovery in water supply systems (WSS). The reduced efficiency far from the best efficiency point (BEP), coupled with the daily discharge variation of WSS requires a flow control strategy aiming at improving the PAT performance. This control strategy is defined to guarantee the PAT operation in a discharge range near BEP. Severe pressure fluctuations may be developed if the PAT is operated in off-design conditions (i.e., far from the BEP). This paper presents the experimental investigation carried out for characterising the pressure fluctuations developed during the part load and the full load operation of a single-stage centrifugal PAT. Dynamic pressure measurements and the flow visualisation in the PAT draft tube are performed to investigate the pressure fluctuations in the part load and in the full load operating conditions. The fluctuations in the part load are caused by a cavitation vortex rope, which is developed in the PAT draft tube. The pressure fluctuations during the full load operation are strongly dependent on the back-pressure values. Obtained results show that, for this PAT, the operation should be limited to a range of 85% to 100% of the discharge at the BEP, to avoid the onset of pressure fluctuations.

Keywords: Pumps running as turbines, off-design operation, pressure fluctuation, vortex rope cavitation, image processing.

3.1 Introduction

The use of pumps running as turbines (PATs) for energy recovery in pressurised water supply systems (WSS) is an investigation subject that has engaged the hydropower research community in the past years. This rising interest stems from the replacement of existing pressure dissipation devices (e.g., pressure reducing valves and control valves at the inlet of storage tanks [19, 29, 134]) by energy recovery systems. Thus, an opportunity arises for the development of micro hydropower plants that can simultaneously control the pressure in the WSS, while efficiently recovering energy. The installation of such power plants needs to comply with the requirements for maintaining the adequate water supply to the population [14].

PATs are pointed as a low-cost alternative to custom-made turbines, as these hydraulic machines feature high efficiency near the best efficiency point (BEP) and are immediately available for a wide range of discharge and head values [59]. However, the absence of a component for the inlet flow control components results into sharp efficiency decrease in off-design operation [140]. This corresponds to the operating conditions where the discharge is lower or higher than the value at the BEP, the part load and the full load operating conditions, respectively. Such limitation is especially relevant in WSS, as these systems are characterised by a daily discharge variation [47], hindering the PAT operation at constant discharge near the BEP.

The operation of several units in parallel or the inlet discharge control using a hydraulic bypass are examples of typical strategies used to increase the overall efficiency of a PAT hydropower plant [15, 106]. These strategies rely on a flow rate control setup, generally through the operation of several valves, where the discharge is distributed so that every PAT of the power plant operates near the BEP. The control settings for these operation strategies are usually defined taking into account the PAT performance characteristics, neglecting eventual instabilities caused by the off-design operation.

CFD numerical simulations evidence the development of complex flows inside the PAT, when the machine is operated far from the BEP [86, 87]. Firstly, a flow detachment has been observed at the pressure side and the suction side of the impellers blade leading edges¹, respectively for the part load and the full load conditions. Secondly, the interaction between the impeller blades and the volute tongue induces an asymmetric pressure field, which triggers an unsteady radial load in the impeller, with a frequency value corresponding to the blade passing frequency. This unsteady component can achieve values up to 50% of the stationary load for the full load operation. Finally, authors [86, 87] report a tangential flow velocity component in the PAT draft tube. This tangential flow component induces a swirling flow in the same and in the opposite runner rotating direction, respectively for the part load and the full load operation. If the stationary pressure in the PAT draft tube is too low, a cavitation swirling flow is

developed. This cavitation flow is associated with the development of strong pressure fluctuations [141], which are reported both for straight and diffuser draft tubes [110]. Jain et al. [142] reported the increase of vibrations caused by the PAT operation with cavitation in the draft tube, volute and bearings. However, the development of pressure fluctuations in PATs is an issue that, to the authors' knowledge, has never been addressed.

The development of pressure fluctuations induced by the off-design operation has been extensively investigated in Francis turbines, as the integration of intermittent renewable energy sources in the electrical network requires a higher flexibility in the operation of hydropower plants for the electric grid stabilisation [143, 144]. Two examples of unstable flows are due to the part load and full load vortex ropes that are developed in the turbine draft tube [145]. Note that, like Francis turbines, PATs are radial flow reaction hydraulic machines.

During the part load operation, the flow at the turbine outlet features a helical cavitation vortex rope with a precessing motion between 0.2 to 0.4 times the runner rotating frequency [146]. The interaction between the vortex precessing motion and the draft tube elbow triggers a pressure fluctuation characterised by a convective and by a synchronous components [147]. The convective nature component, which is only observed in the draft tube, is created by the rotation of the pressure field with the vortex core precession and is quasi-independent on the back-pressure level [111]. The synchronous component propagates through the entire hydraulic system and, its amplitude is associated with the response of the system to the pressure excitation source [148]. The growth of a vapour cavity vortex rope decreases the wave speed at the draft tube, which reduces the hydraulic system eigenfrequencies [149]. Such decrease may lead to resonance onset if the eigenfrequency of the hydraulic system matches the precession frequency of the cavitation vortex rope, which may onset dangerous pressure fluctuations. Favrel et al. [112] present a methodology for predicting the operating conditions where resonance occurs based on the Swirl number at the turbine runner outlet.

During the full load operation, the Francis turbine features an axisymmetric cavitation vortex rope, which plays a key role in the development of severe self-sustained pressure fluctuations [113]. This cavitation flow induces the periodic fluctuations of parameters such as the pressure, the torque, the shaft power, the flow swirl number in the turbine outlet, and the vortex rope volume [114]. The dependence of the periodic fluctuations on the back-pressure levels and, consequently, on the vapour volume, suggests that the system self-excites at its eigenfrequencies [150]. The physical mechanisms governing

¹Note that the impeller blades leading edge change between the operation in the pump and in the turbine mode, as it depends on the direction of the flow. This publication discusses the turbine mode. Therefore, the impeller blades leading edge refer to the edges of the impeller high pressure section.

the development of the pressure fluctuations are still an on-going research topic.

There is a lack of research about the development of pressure fluctuations during the operation of PATs in off-design conditions. This research paper aims at providing additional insights into this phenomenon based on an experimental research. The main objective is the investigation of characteristics of the pressure fluctuations developed in the part load and in the full load operation and the identification of the operating regions where these pressure fluctuations occur. For this purpose, dynamic pressure measurements at both sides of the PAT and the high speed flow visualisation in the PAT draft tube are performed. The experimental setup and the investigated operating points are outlined in Section 3.2. The procedures for analysing the pressure measurements and the methodology developed for the image processing applied to the flow visualisation in the PAT draft tube are presented in Section 3.3. Obtained results are presented and discussed in Section 3.4. Finally, the main conclusions and the future perspectives are outlined in Section 3.5.

3.2 Experimental setup

3.2.1 Test-rig and measurement equipment

The experimental investigation is performed in the closed loop test-rig of the Laboratory of Hydraulics and Environment at Instituto Superior Técnico, Universidade de Lisboa (Figure 3.1). Two feed pumps, installed at a lower level, supply the required hydraulic power to the tested PAT. Each feed pump is equipped with a variable speed drive (VSD) to control the discharge at the PAT high pressure section. The maximum pumping power (2×15 kW) allows operating the test-rig up to $40 \text{ l} \cdot \text{s}^{-1}$. The PAT is installed between two pressure vessels in the upper-level of the test-rig. The high pressure vessel aims at damping the flow oscillation, caused by the feed pumps, for providing stable flow conditions to the PAT high pressure section. The low pressure vessel is used to control the PAT back-pressure level using compressed air. The PAT is equipped with a 350 mm length Plexiglas straight pipe assembled at the machine low pressure side for flow visualisation. The rotational speed of the PAT is controlled by a four-quadrants VSD.

The test-rig is equipped with a data acquisition system for measuring the PAT stationary performance, capturing the dynamic pressure at both sides of the PAT and to perform the high speed flow visualisation in the PAT draft tube. The location and the characteristics of the measurement equipment are given in Figure 3.2 and Table 3.1, respectively.

The stationary data acquisition system is used to measure, in a preliminary stage, the determine the PAT variable speed efficiency hill chart. The measured hydraulic

3.2. Experimental setup

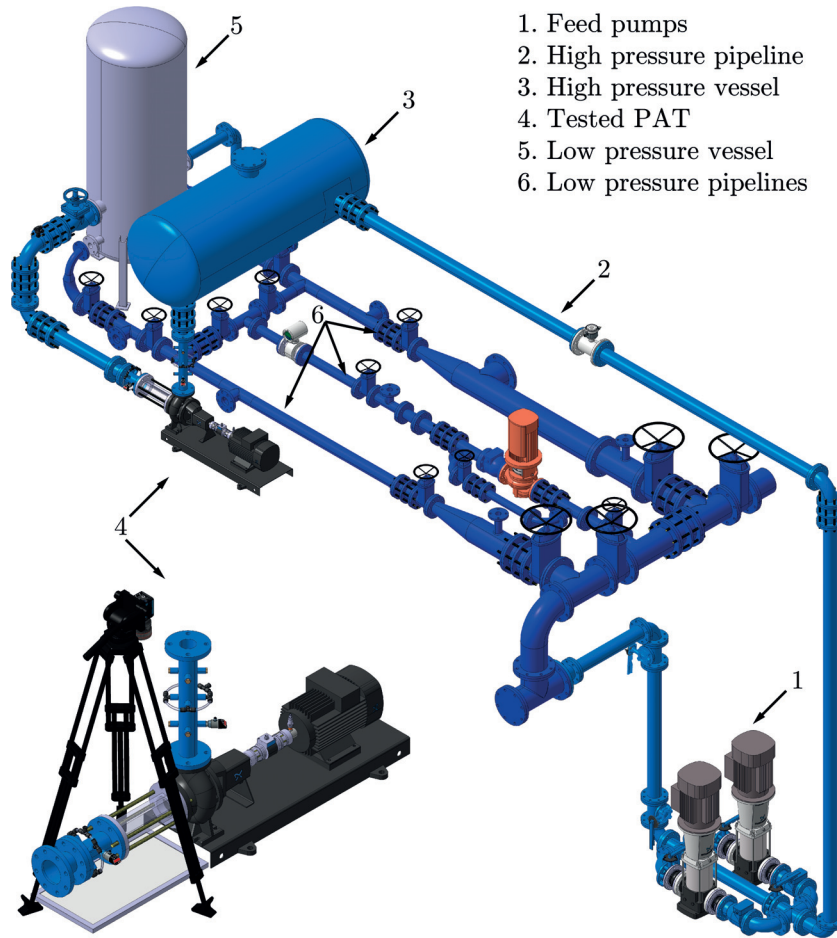


Figure 3.1 – Test-rig assembled for the experimental investigation. The high speed visualisation setup is shown in 4.

Table 3.1 – Measurement equipment characteristics.

ID	Measurement	Range	Units	Accuracy
Q	Discharge	0 – 0.04	$\text{m}^3 \cdot \text{s}^{-1}$	0.40% of span
Δp_1	Differential pressure 1	0 – 7.5	bar	0.14% of span
Δp_2	Differential pressure 2	-0.2 – 2.1	bar	0.14% of span
T	Torque	-50 – 50	N·m	0.30% of upper limit
n	Runner rotating frequency	0 – 50	s^{-1}	0.20% of span
θ	Temperature	0 – 100	$^{\circ}\text{C}$	0.30% of span
P_{sup}	Active power	-10 – 10	kW	0.50% of upper limit
Q_{sup}	Reactive power	-10 – 10	kVAr	2.00% of upper limit
p_1	Gauge pressure 1	0 – 6.0	bar	1.00% of span
p_2	Gauge pressure 2	0 – 2.5	bar	1.00% of span

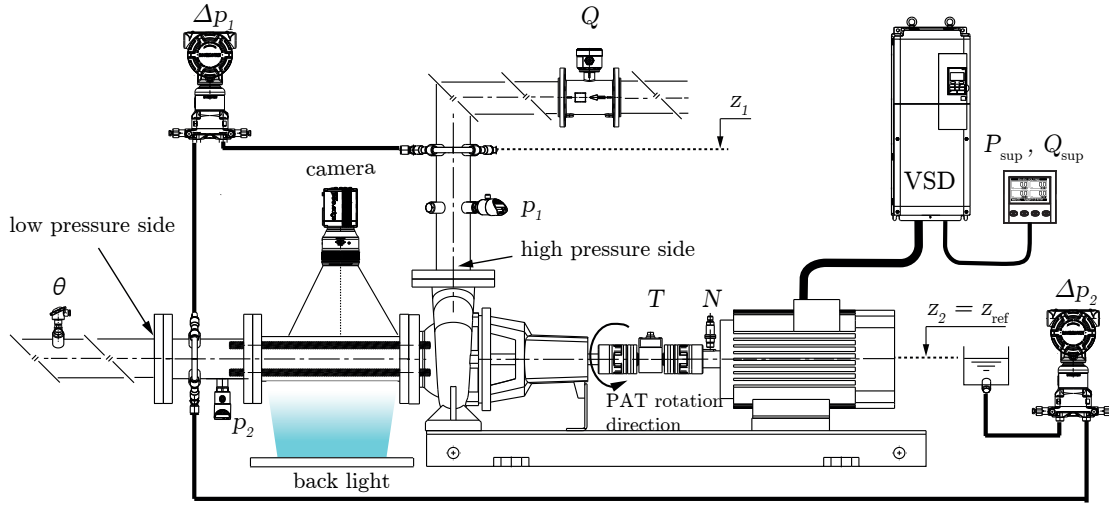


Figure 3.2 – Measurement equipment and high speed camera setup.

parameters are the discharge Q , the water temperature θ and two differential pressure measurements Δp_1 and Δp_2 . The mechanical performance is determined by measuring the torque T and the runner rotating frequency n . Finally, the supplied active and reactive electric power P_{sup} and Q_{sup} , respectively, are monitored for controlling the PAT operating point. Data are acquired simultaneously with a sampling frequency of 5'000 Hz during a 20 s time window. Average and standard deviation values are registered for the computation of the PAT stationary performance.

Two gauge pressure transducers are installed for measuring the dynamic pressure in the high and in the low pressure sections of the PAT, p_1 and p_2 , respectively. The first sensor is installed at $2 \times D_1$ of the PAT inlet. The transducer installed at the low pressure section is located at $5.5 \times D_2$ of the PAT outlet (see Figure 3.2). D_1 and D_2 represent the diameters of the PAT volute flanges at the high and low pressure sections, respectively. The pressure data acquisition is performed at 5'000 Hz during 10 s.

The flow visualisation is carried out using a high speed camera (Microtron EoSens 3CL equipped with a Sigma 24-70 mm lens) assembled above the Plexiglas pipe (see Figure 3.1). The camera provides a resolution of 800 pixels \times 400 pixels, representing a window of 0.2 m \times 0.1 m. On the opposite side of the Plexiglas pipe, a LED backlight is installed for increasing the contrast between the water and the vapour phases. The backlight consists of a panel with dimensions of 0.6 m \times 0.3 m and an illuminance of 10'200 $\text{lm} \cdot \text{m}^{-2}$. The acquisition is performed synchronously with the pressure measurements with a sampling frequency of 1'000 Hz during 10 s.

3.2.2 Investigated operating points

The experimental investigation is carried out in a single-stage end-suction centrifugal pump with a unit specific speed of $n_q = N \times (Q^{1/2}/H^{3/4}) = 67.3$, where N is the rotational speed in min^{-1} , Q is the discharge in $\text{m}^3 \cdot \text{s}^{-1}$ and H is the head in m. The previous value is calculated based on the rated rotational speed, discharge and head in pump mode, namely $N_R^P = 2'910 \text{ min}^{-1}$, $Q_R^P = 0.03 \text{ m}^3 \cdot \text{s}^{-1}$ and $H_R^P = 14.6 \text{ m}$. The impeller features 6 blades. Preliminary measurements are carried out for characterising PAT performance hill chart. The specific hydraulic energy E is defined by Equation (3.1). However, according to the measurement setup given in Figure 3.2, this parameter can be computed by Equation (3.2) [99]. Accordingly, the efficiency in the turbine mode η^T , defined by the ratio between the shaft power P and the hydraulic power P_h , is given by Equation (3.3).

$$E = \frac{p_{\text{abs},1} - p_{\text{abs},2}}{(\rho_1 + \rho_2)/2} + \frac{C_1^2 - C_2^2}{2} + g(z_1 - z_2) \quad (3.1)$$

$$E = \frac{\Delta p_1}{\rho_2} + \frac{C_1^2 - C_2^2}{2} \quad (3.2)$$

$$\eta^T = \frac{P}{P_h} = \frac{2\pi nT}{\rho_1 Q E} \quad (3.3)$$

where p_{abs} is the absolute pressure, C is the average flow velocity, z is the elevation and ρ is the water density, which is computed based on the pressure and the water temperature [99]. Subscripts 1 and 2 refer to the high pressure and low pressure measurement sections, respectively.

The performance of the PAT can be represented by the non-dimensional IEC factors of speed and discharge, n_{ED} , Q_{ED} , respectively, which are defined by [99]:

$$\begin{aligned} n_{ED} &= \frac{nD}{\sqrt{E}} \\ Q_{ED} &= \frac{Q}{D^2 \sqrt{E}} \end{aligned} \quad (3.4)$$

where $D = 0.08 \text{ m}$ is the reference diameter defined by the value at the pump low pressure flange internal diameter.

Chapter 3. Pressure fluctuations in off-design operation

The net positive suction energy $NPSE$ is defined by Equation (3.5). However, according to the measurement setup of Figure 3.2, $NPSE$ is determined by Equation (3.6) [99].

$$NPSE = \frac{p_{\text{abs},1} - p_{\text{va}}}{\rho_2} + \frac{C_2^2}{2} - g(z_{\text{ref}} - z_2) \quad (3.5)$$

$$NPSE = \frac{\Delta p_2 + p_{\text{amb}} - p_{\text{va}}}{\rho_2} + \frac{C_2^2}{2} \quad (3.6)$$

where p_{va} is the vapour pressure, which is a function of the temperature θ [99], p_{amb} is the ambient pressure, and z_{ref} is the elevation at the pump reference section (shaft elevation). Accordingly, the PAT cavitation conditions are monitored using both the Thoma number σ , and the local cavitation coefficient χ_{nD} , which are defined by Equations (3.7) and (3.8), respectively. The local cavitation coefficient χ_{nD} describes similar cavitation characteristics for different values of the rotational speed.

$$\sigma = \frac{NPSE}{E} \quad (3.7)$$

$$\chi_{nD} = \frac{p_2 - p_{\text{va}}}{\rho_2 n^2 D^2} \quad (3.8)$$

The operating points measured for determining the PAT stationary performance in the turbine mode are shown in Figure 3.3. These operating points are given by the variation of the n_{ED} and the η^T as a function of Q_{ED} . Measurements are performed for constant N values between $1'500 \text{ min}^{-1}$ and $3'000 \text{ min}^{-1}$, with steps of 300 min^{-1} . Results in this figure show that the BEP is achieved for a $Q_{ED}^{\text{BEP}} = 0.392$, for all N values, being the maximum efficiency $\eta_{\text{BEP}}^T = 70.8\%$. The variable speed efficiency hill chart of this PAT, which is illustrated in Figure 3.4 shows the isolines of the specific energy E and of the efficiency η^T with respect to the discharge Q and the rotational speed N .

This hill chart makes evident the existence of a best efficiency ridge line, which separates the operation zones in the part load and in the full load conditions. The part load operation zones are obtained for discharge values lower than the discharge in the best efficiency ridge line, for every value of rotational speed; while the full load operation zones are found for discharge values higher than the discharge values corresponding to the best efficiency ridge line, for each rotational speed value.

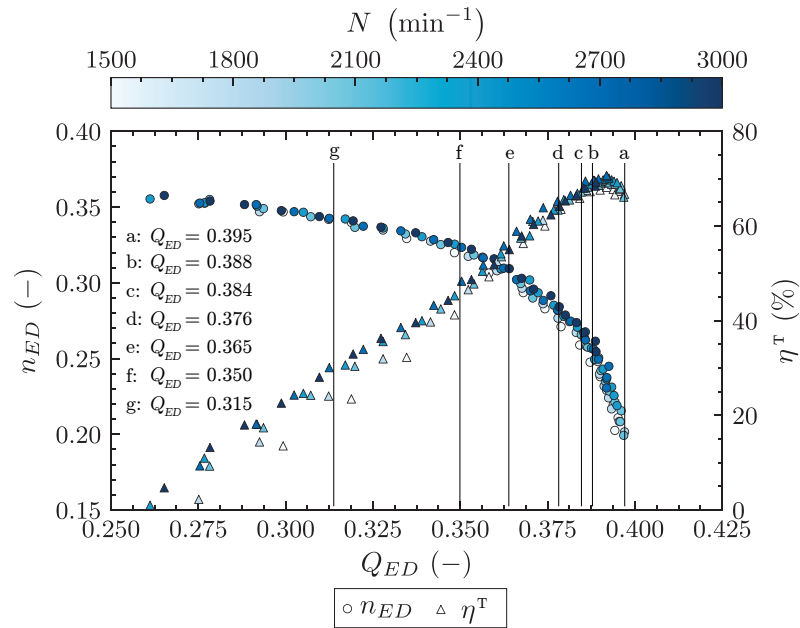


Figure 3.3 – Measured operating points of the stationary PAT performance in the turbine mode given by the variation of n_{ED} and η^T with respect to Q_{ED} . Details a to g indicate the Q_{ED} constant values used to define the operating points for investigating the pressure fluctuations.

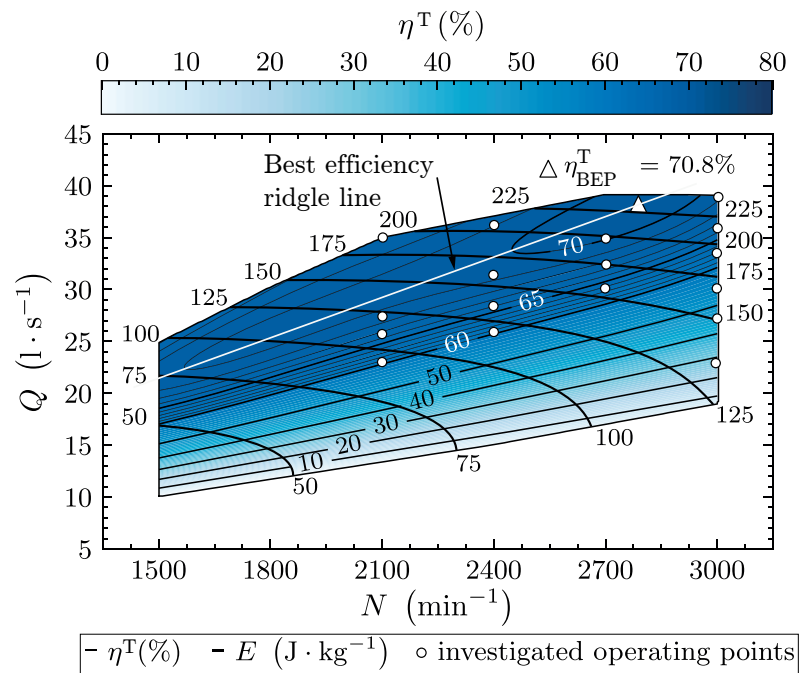


Figure 3.4 – PAT variable speed hill chart performance of E and η^T as a function of N and Q with the indication of the operating points for investigating the pressure fluctuations. The white line represents the best efficiency ridge line.

Chapter 3. Pressure fluctuations in off-design operation

Table 3.2 – Measured operating points for investigating the pressure fluctuations.

N (min^{-1})	Q_{ED} (-)	χ_{nD} (-)	Tests
3'000	0.388, 0.384, 0.376, 0.365 ⁽²⁾ , 0.350 ⁽²⁾ , 0.315 ⁽²⁾	7.5, 10.0, 12.5, 14.0 ⁽³⁾	24 tests
2'700	0.388, 0.384, 0.376	7.5, 10.0, 12.5, 15.0	12 tests
2'400	0.395 ⁽¹⁾ , 0.388, 0.384, 0.376	10.0, 12.5, 15.0, 17.5	16 tests
2'100	0.395 ⁽¹⁾ , 0.388, 0.384, 0.376	10.0, 12.5, 15.0, 17.5	16 tests

⁽¹⁾ Full load operating points

⁽²⁾ Deep part load operating points

⁽³⁾ Maximum back-pressure for this rotational speed due to sensor range.

The selected operating points for characterising the pressure fluctuations aim at mapping the part load and the full load operating conditions with relative efficiency values with respect to the BEP $\eta^T/\eta_{\text{BEP}}^T > 85\%$. These operating points are shown in Figure 3.4. The operating points are selected based on constant Q_{ED} values, which are indicated in Figure 3.3, for different rotational speed values.

The full load operating conditions, corresponding to $Q_{ED} = 0.395$ are only investigated for $N = 2'100 \text{ min}^{-1}$ and $N = 2'400 \text{ min}^{-1}$ due to discharge limitations in the test-rig. The part load conditions are measured for N values between $2'100 \text{ min}^{-1}$ and $3'000 \text{ min}^{-1}$ with constant Q_{ED} values of 0.388, 0.384 and 0.376. Furthermore, the deep part load region is captured for $N = 3'000 \text{ min}^{-1}$ and Q_{ED} values of 0.365, 0.350 and 0.315, for validating the image processing method for tracking the cavitation vortex precessing motion, which is described in Section 3.3.2.

Each operating point is investigated for four back-pressure levels, given by constant χ_{nD} values. The minimum χ_{nD} value is limited by the atmospheric pressure in the low pressure vessel (see Figure 3.1). Overall, the experimental investigation consists of 68 operating points, as summarised in Table 3.2.

3.3 Methodology

3.3.1 Pressure fluctuation and spectral analysis

The dynamic pressure measurements at a given section i are described by the non-dimensional pressure coefficient with respect to the specific hydraulic energy, $C_{p,i}$, as defined in Equation (3.9). This parameter is used to normalise all pressure variations with respect to E .

$$C_{p,i} = \frac{p_i - \bar{p}_i}{\rho_i E} \quad (3.9)$$

where \bar{p}_i is the average pressure at section i , and $i = 1$ or 2 refer to the high and low pressure sections, respectively (see Figure 3.2).

The spectral analysis of the measurements is performed. The auto-spectral density function $G_{xx}(X)$ of a given measurement X is computed based on the Welch method using a Hanning window [151]. The signal is sub-divided into 10 time histories, each with 5'000 samples (corresponding to 1 s per window) with 25% overlap for avoiding leakage. The corresponding resolution of the spectral analysis is 1 Hz. The cross-spectral density and coherence functions, G_{xy} and C_{xy} , respectively, are computed using the same window, to investigate the energy transfer between the high and the low pressure sections of the PAT [152].

3.3.2 Cavitation vortex rope image processing

An image processing method is developed to determine the precession of the cavitation vortex rope, as summarised in the flow chart of Figure 3.5. This method is a particle tracking based technique implemented in Python using the open source library scikit-image for the vortex core detection [153] and the library trackpy for tracking the vortex core position [154]. Applications similar to this method can be found in [155, 156].

The images are trimmed and filtered using an adaptive Gaussian thresholding filter [157] to identify the edge of the vortex in contrast with the bright background, as shown in Figure 3.6. The analysed target area of the vortex (cropped image of 100 px) should be small enough to ensure that the velocity field of the vortex is homogeneous along the considered length. A filling function [158] is applied to guarantee the homogeneity of the internal white area of the vortex in contrast to the homogeneous black background (Figure 3.6). The vortex corresponds to the area that satisfies the condition $A_{\min} < x < A_{\max}$, where A_{\min} and A_{\max} are the lower and upper bounds of the areas range corresponding to the cavitation vortex in the image. These values are tuned for each operating point based on the distribution of the areas of the identified white patterns. The lower bound is fixed to avoid that the algorithm erroneously considers more than one pattern, in case the filtering separates the vortex into two or more parts. The upper bound allows discarding errors due to the filling function.

The successive positions of the vortex center of mass in each frame are linked so that the radial displacement and the velocity of the vortex are computed. The precessing frequency of the cavitation vortex rope f_{PVC} is the value corresponding to the maximum amplitude observed by the auto-spectrum density function of the tangential velocity or radial displacement time history.

Finally, the methodology is validated by comparing the Strouhal number of the pre-

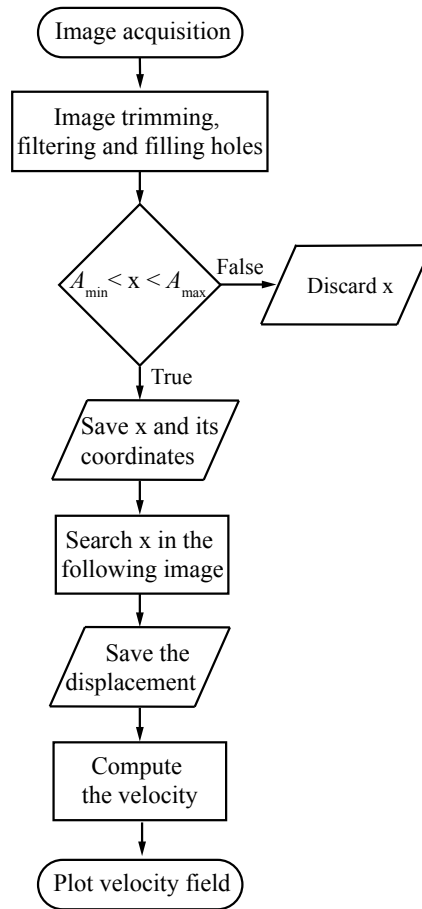


Figure 3.5 – Flow chart of the image processing method for tracking the vortex. x represents the area of the white pattern of interest in the image to feature the vortex. This flow chart corresponds to methodology applied to each frame.

cessing frequency St_{PVC} , defined by Equation (3.10), and the Swirl number at the PAT draft tube S , defined by the ratio between the axial flux of angular momentum and the axial flux of axial momentum [159], as defined in Equation (3.11).

$$St_{PVC} = \frac{f_{PVC} D^3}{Q} \quad (3.10)$$

$$S = \frac{\int_0^R C_m \cdot C_u \cdot r^2 \cdot dr}{R \int_0^R C_m^2 \cdot r \cdot dr} \quad (3.11)$$

where C_m and C_u are the time-averaged axial and tangential flow velocity components

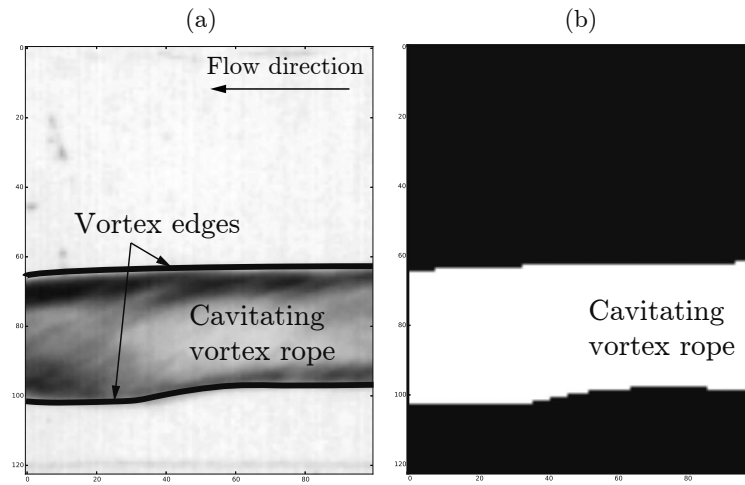


Figure 3.6 – Image processing method example applied to the target area (corresponding to 100 px). (a) identification of the cavitation vortex edges; (b) application of the filter for the filling function.

and R is the radius of the section. The experimental setup does not allow measuring the time history of C_m and C_u . Thus, the Swirl number is estimated by the analytical formula given in Equation (3.12) [112].

$$S = n_{ED} \frac{\pi^2}{8} \left(\frac{1}{Q_{ED}} - \frac{1}{Q_{ED}^{S=0}} \right) \quad (3.12)$$

where $Q_{ED}^{S=0}$ is the discharge factor corresponding to the swirl-free flow conditions, which is assumed to be $Q_{ED}^{S=0} = 0.392$, which correspond to the BEP.

The method described in Figure 3.5 is also used to record the time history of the vortex diameter, except that the successive images are not cropped. The diameter at each column of pixels D_j is given by the sum of the white pixels at the respective column. Thus, the diameter of the cavitation vortex rope D_{rope} is assumed to be the average value of the measured diameters in all columns of pixels, namely:

$$D_{rope} = \frac{1}{n} \sum_{j=0}^n D_j \quad (3.13)$$

3.4 Results and discussion

3.4.1 Preliminary analysis

The pressure fluctuations developed during off-design operation are significantly influenced by the relative discharge Q/Q_{BEP} and the back-pressure χ_{nD} , as illustrated in Figure 3.7. Data shown in this figure refer to the pressure coefficient $C_{p,2}$ time history with respect to the runner revolutions. The operating points are described by $N = 2'400 \text{ min}^{-1}$, with Q_{ED} values of 0.395, 0.388, 0.384, and 0.376 (which refer to Q/Q_{BEP} values of 1.07, 0.93, 0.84 and 0.76, respectively). Each operating point is shown for χ_{nD} values of 10.0 and 17.5. The root mean square (RMS) of the pressure coefficient, given by Equation (3.14), are also indicated in Figure 3.7. The corresponding flow visualisation in the PAT draft tube and the auto-spectrum density function of the pressure coefficient at the PAT outlet $G_{xx}(C_{p,2})$, for each operating point shown in Figure 3.7 are presented in Figures 3.8 and 3.9, respectively.

$$C_{p,2}^{\text{RMS}} = \sqrt{\frac{1}{N_{\text{samples}} - 1} \sum_{j=1}^{N_{\text{samples}}} (C_{p,2})^2} \quad (3.14)$$

where N_{samples} is the total number of samples.

The full load operation features, for the minimum back-pressure value $\chi_{nD} = 10.0$, the highest pressure fluctuation amplitude, with the main frequency values in the range of 1.8 to 2.5 times the runner frequency. This amplitude is significantly reduced by increasing the back-pressure (see Figure 3.9). The operating point with the highest amplitude corresponds to the onset of spontaneous mass flows of vapour bubbles in the PAT draft tube. This vapour is likely to arise from the flow separation in the impeller blades leading edge, though experimental data do not allow drawing a clear conclusion. This vapour flow is not observed for higher back-pressure values (see Figure 3.8), which could be related to the decrease of the pressure fluctuation amplitude.

The pressure fluctuation amplitude is significantly reduced for the Q/Q_{BEP} values of 0.93 and 0.84. The C_p^{RMS} values are approximately constant for the two operating points. The flow visualisation evidences a slight development of a cavitation vortex rope for the operating point corresponding to $Q/Q_{\text{BEP}} = 0.84$ and $\chi_{nD} = 10.0$, though there is no surge evidence in the pressure fluctuation amplitude. As a final note, the pressure fluctuation induced by the operation with a 7% discharge deviation from the BEP is more severe in the full load compared to the part load operation.

As the discharge decreases, the vortex rope increases in size, as shown in Figure 3.8.

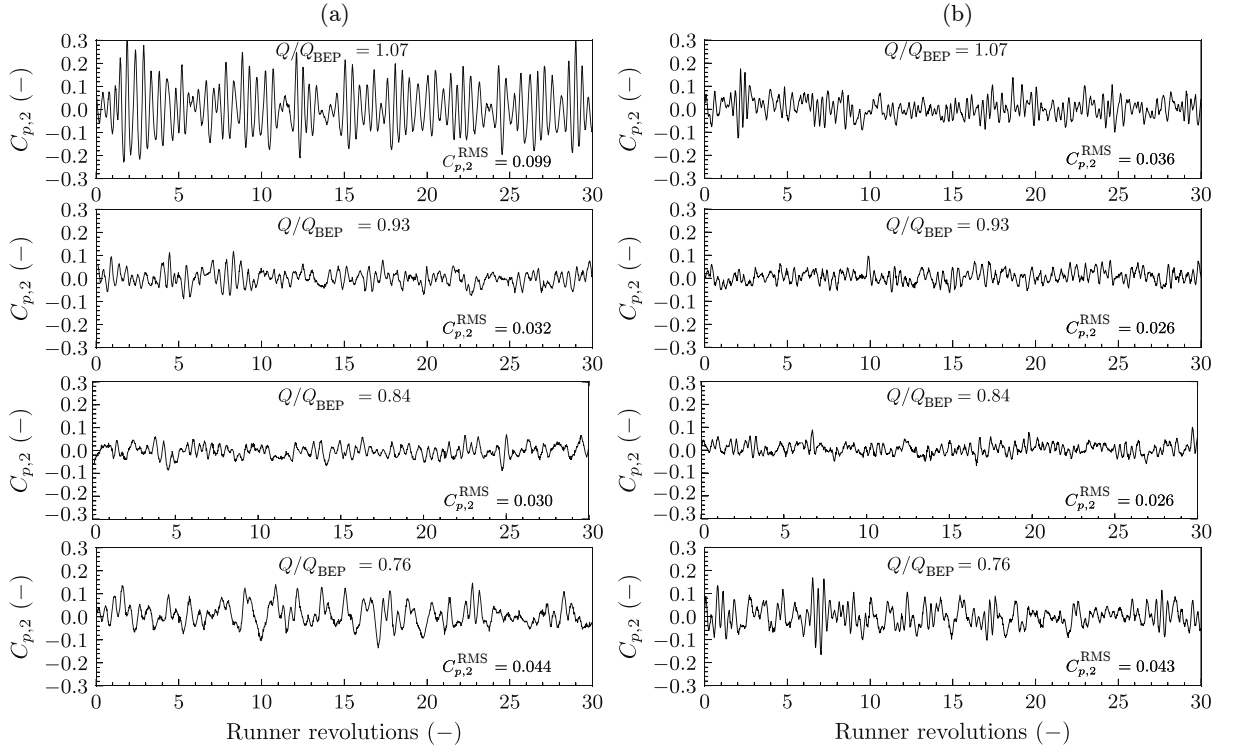


Figure 3.7 – Time history of the pressure coefficient measured in the low pressure section $C_{p,2}$ with respect to the runner revolutions. The operating points correspond to Q/Q_{BEP} values of 1.07, 0.93, 0.84 and 0.76 and $N = 2'400 \text{ min}^{-1}$ (thus, 1 rev = 0.025 s). The operating points are given for two constant back-pressure levels, defined by: (a) $\chi_{nD} = 10.0$; (b) $\chi_{nD} = 17.5$.

Firstly, this operating point, corresponding to $Q/Q_{\text{BEP}} = 0.76$ features a higher pressure fluctuation amplitude compared to the operating points $Q/Q_{\text{BEP}} = 0.93$ and $Q/Q_{\text{BEP}} = 0.84$. Secondly, the spectral analysis makes apparent a frequency component for values lower than the runner rotating frequency, and a second contribution in the range of 2 to 4 times the runner rotating frequency. Thirdly, the corresponding amplitude seems to be unaffected by the back-pressure. Finally, the flow visualisation in the PAT draft tube (Figure 3.8) evidences that the cavitation vortex rope diameter increases with decreasing back-pressure value.

3.4.2 Part load operation

Cavitation vortex rope

The image processing method for tracking the cavitation vortex radial displacement is illustrated in Figure 3.10, for the operating point described by $Q_{ED} = 0.376$, $N = 2'400 \text{ min}^{-1}$ and $\chi_{nD} = 17.5$. Data shown in this figure present the time history of the radial displacement and the corresponding auto-spectrum density function.

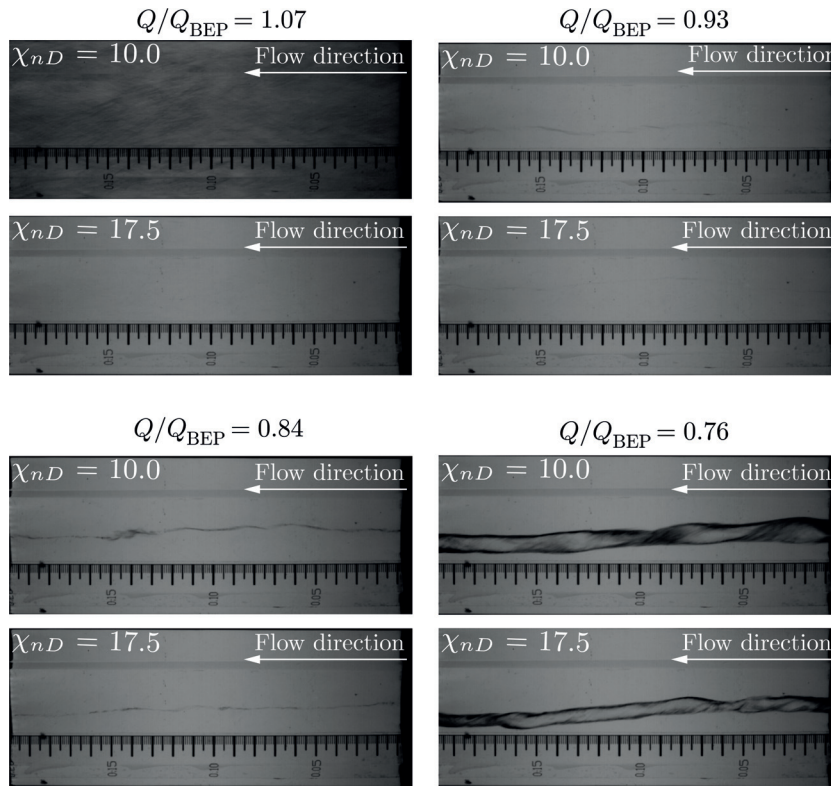


Figure 3.8 – Flow visualisation in the PAT draft tube for $N = 2'400 \text{ min}^{-1}$ and Q/Q_{BEP} values of 1.07, 0.93, 0.84 and 0.76. Each operating point is shown for two constant χ_{nD} values of 10.0 and 17.5.

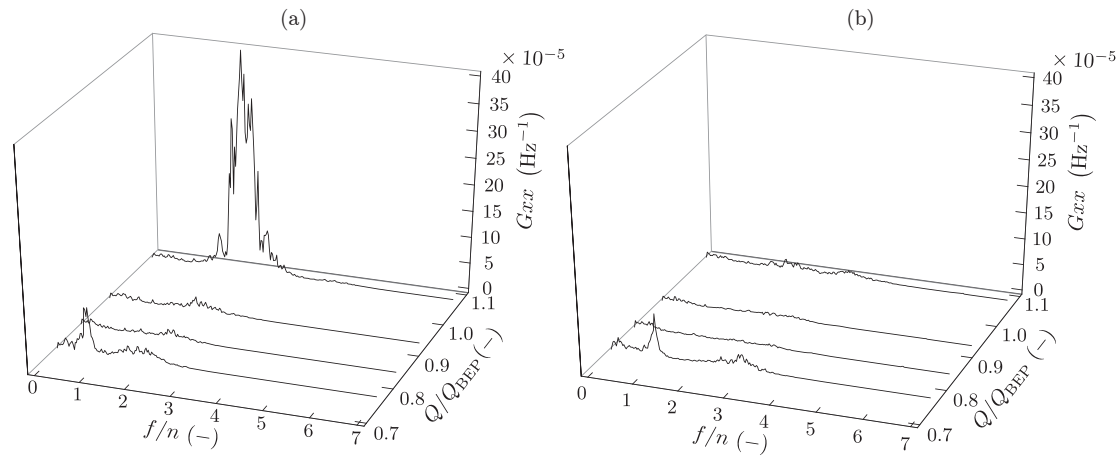


Figure 3.9 – Waterfall plot of the auto-spectrum density functions of the pressure coefficient at the low pressure side $G_{xx}(C_{p,2})$ for the operating points corresponding to $N = 2'400 \text{ min}^{-1}$ and Q/Q_{BEP} values of 1.07, 0.93, 0.84 and 0.76. Each waterfall plot correspond to a constant value of back-pressure defined by: (a) $\chi_{nD} = 10.0$; and (b) $\chi_{nD} = 17.5$.

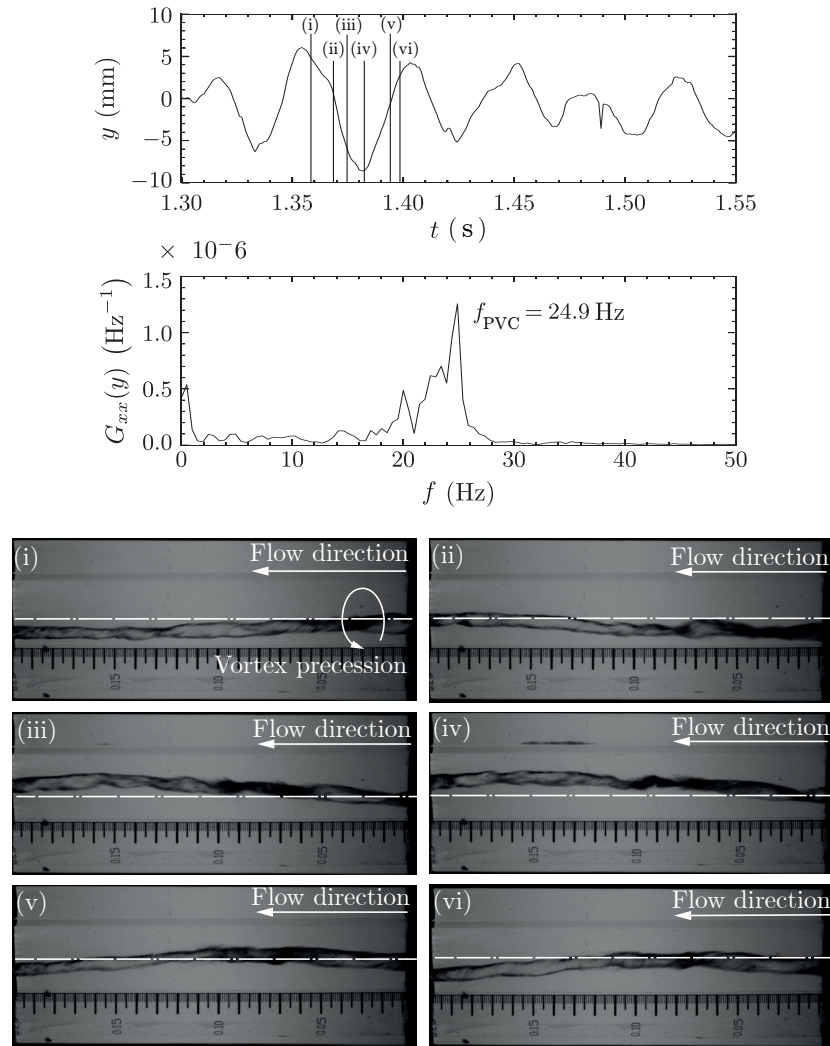


Figure 3.10 – Image processing of the cavitation vortex rope precessing motion. The radial displacement of the vortex y is compared with six snapshots during one period of the precessing motion $T = 1/24.9 = 0.04$ s identified by the details (i) to (vi) in the time history chart. The operating point corresponds to $Q_{ED} = 0.376$, $N = 2'400 \text{ min}^{-1}$ and $\chi_{nD} = 17.5$.

The comparison between the vortex displacement time history and the flow visualisation, during one rotation period, makes apparent that the method is capable of tracking the vortex centre of mass inside the target area (see details (i) to (vi) in Figure 3.10). The frequency corresponding to the maximum amplitude observed in the auto-spectrum density function corresponds to the precessing frequency of the cavitation vortex rope f_{PVC} . The wide band of frequency values near the f_{PVC} value of the auto-spectrum density functions given by the image processing method is explained by the limitations on the precise identification of the vortex edges, leading to small deviations between the real and the identified measured position of the vortex centre of mass, for each frame

This procedure is repeated for the operating points of $Q_{ED} \leq 0.376$ and $N = 3'000 \text{ min}^{-1}$. Results for these operating points are summarised in Figure 3.11. The precessing frequency f_{PVC} increases linearly by decreasing the relative discharge Q/Q_{BEP} . The Strouhal number of the precessing frequency St_{PVC} increases linearly with increasing swirl number S . Similar outcomes are reported in [112] for a swirling flow at the outlet of a Francis turbine during the part load operation, which validates the capability of the image processing method to identify f_{PVC} . The dispersion of the results shown in Figure 3.11 is caused by: (i) the uncertainty associated with the tracking method; (ii) the Thoma number σ variation; and (iii) the influence of the Froude number $Fr = \sqrt{E/(gD)}$, which cannot be kept constant.

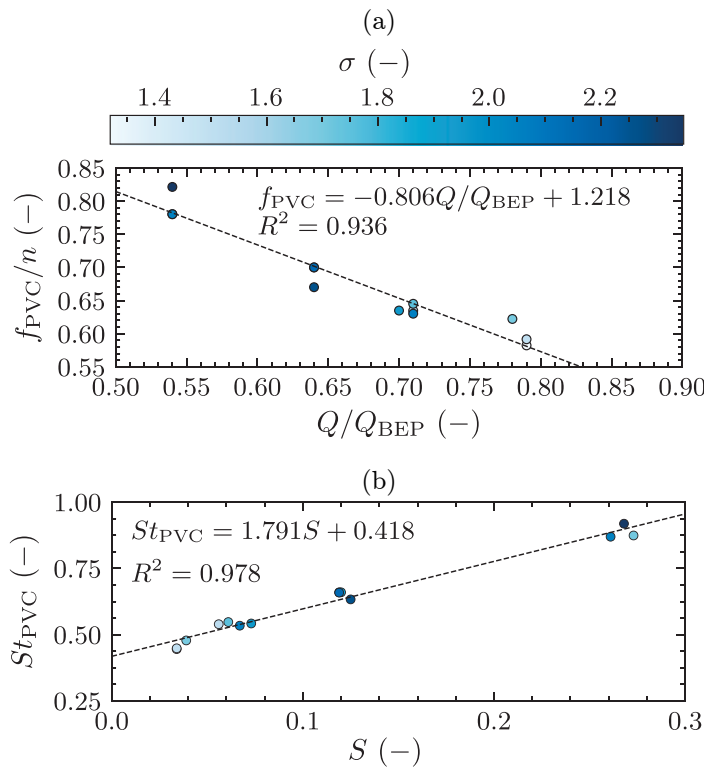


Figure 3.11 – Analysis of the precessing frequency of the cavitation vortex rope for the operating points corresponding to $N = 3'000 \text{ min}^{-1}$: (a) influence of the relative discharge on the precessing frequency; (b) Influence of the Swirl number on the Strouhal number of the precessing vortex core. The colours of the scatter points in both charts are scaled by the Thoma number σ .

As a final remark, this image processing method is used for the identification of the vortex precessing motion, as the measurement setup is not provided with two pressure transducers installed in the same measurement section and separated by 90° . This setup allows computing the phase difference between two spectral signals, for instance as in [111], and provide more accurate results.

Spectral analysis of pressure measurements

The auto-spectrum density functions of the pressure coefficients at the high and low pressure sections, $G_{xx}(C_{p,1})$ and $G_{xx}(C_{p,2})$ for the operating points given by $Q_{ED} = 0.376$, $N = 2'400 \text{ min}^{-1}$ and χ_{nD} values of 10.0, 12.5, 15.0 and 17.5 show three different contributions to the pressure fluctuation, as presented in Figure 3.12. The first component, f_0 (see detail 1 in Figure 3.12) is of synchronous nature, which propagates through the entire hydraulic circuit. This feature is observed by the coherence function between the p_1 and p_2 measurements, which are given in Figure 3.13 for the χ_{nD} values of 10.0 and 17.5.

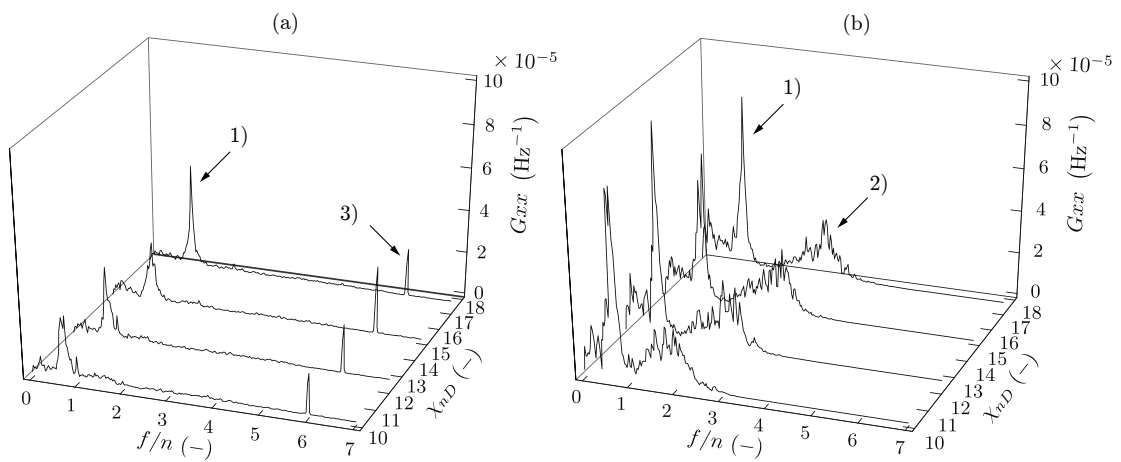


Figure 3.12 – Waterfall plot of the auto-spectrum density functions of the pressure coefficients: (a) in the high pressure section $G_{xx}(C_{p,1})$; and (b) in the low pressure section $G_{xx}(C_{p,2})$. Each chart shows the operating points shown corresponding to $N = 2'400 \text{ min}^{-1}$ and $Q_{ED} = 0.376$. All operating points are shown for χ_{nD} values of 10.0, 12.5, 15.0 and 17.5.

The second component f_1 (see detail 2 in Figure 3.12) is usually observed in upper part load regimes. This component is only detected in the low pressure side of the PAT and depends on the back-pressure, which could be explained by the reflection of the pressure waves in the low pressure vessel. The back-pressure increase is created by the admission of compressed air in the vessel, which increases the vessel capacitance²[101]. Such increase results in a higher frequency of the pressure wave vibration. Nevertheless, the collected data are not enough to draw additional conclusions and further research is required.

Finally, the third contribution (see detail 3 in Figure 3.12) corresponds to the blade passing frequency, as the PAT impeller is composed of 6 blades. This component, which is observed in all operating points, is caused by the interaction between the

²The capacitance of an air pressure vessel is defined by $C_{PV} = V_g / (h_g n_g)$, being V_g and h_g the volume and the head of the gas inside the vessel, respectively, and n_g the coefficient of the polytropic gas equation (see pp. 89 in [101]).

volute tongue and the impeller blades leading edge. This frequency component is only observed in the PAT high pressure measurement section.

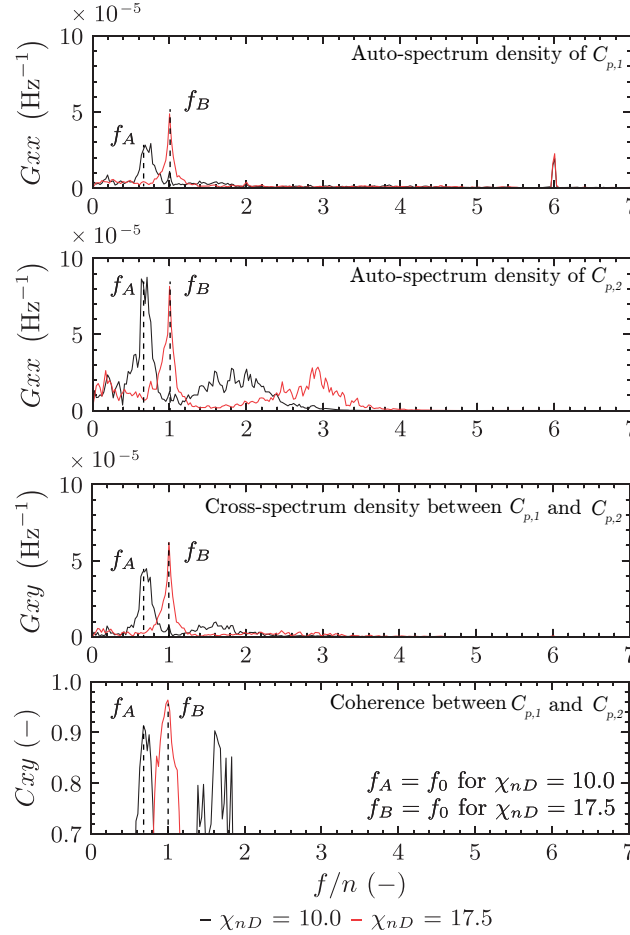


Figure 3.13 – Identification of the synchronous frequency f_0 by the computation of the auto-spectrum density functions $G_{xx}(C_{p,1})$ and $G_{xx}(C_{p,2})$, coherence function C_{xy} and cross-spectrum density G_{xy} between $C_{p,1}$ and $C_{p,2}$. The frequency values $f_A = 0.68 \times n$ and $f_B = 1.00 \times n$ represent the f_0 values found for $\chi_{nD} = 10.0$ and $\chi_{nD} = 17.5$, respectively.

The influence of local cavitation coefficient on the average vortex rope diameter D_{rope} and on the observed frequency values, f_{PVC} , f_0 and f_1 , for the operating points presented in Figure 3.12, is summarised in Figure 3.14. The f_{PVC} values are approximately constant regardless of the local cavitation coefficient. In contrast, the f_0 and f_1 values increase quasi-linearly with the increase of the local cavitation coefficient. The reduction of D_{rope} and the propagation of the pressure waves to the upstream side of the PAT confirm that f_0 can be identified as one of the eigenfrequencies of the hydraulic system. The decrease of the vapour volume leads to an increase in the wave speed of the pipe at the PAT downstream, which increases the value of the eigenfrequencies of the system [149].

The hypothesis on the nature of the f_1 fluctuations requires further validation, as the collected data are not sufficient to corroborate this conclusion. Additional data collected between the PAT low pressure section and the pressure vessel, together with the eigenfrequency analysis of the hydraulic system are required for validating this hypothesis.

The vortex precessing frequency is not detected in the pressure measurement spectral analysis. This could be justified by the location of the pressure measurement section ($L = 5.5 \times D_2$ downstream the PAT outlet), whose distance is significantly higher than in the experimental setups in [110, 112]. It is worth to notice that this pressure fluctuation component is of convective nature, and therefore, is quickly dissipated in the hydraulic system.

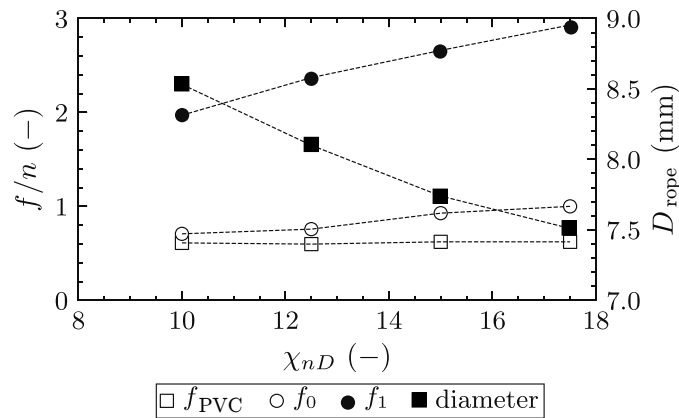


Figure 3.14 – Influence of the local cavitation coefficient χ_{nD} on the cavitation vortex rope diameter D_{rope} and on the frequency values f_{PVC} , f_0 and f_1 identified in the flow visualisation image processing and in the spectral analysis of the pressure measurements.

3.4.3 Full load operation

The auto-spectrum density functions $G_{xx}(C_{p,1})$ and $G_{xx}(C_{p,2})$ for the full load operating conditions with respect to $N = 2'400 \text{ min}^{-1}$ and $N = 2'100 \text{ min}^{-1}$ are presented in Figures 3.15 and 3.16, respectively. Despite the two operating points refer to $Q_{ED} = 0.395$, the Q/Q_{BEP} values correspond to 1.07 and 1.17, respectively for the N values aforementioned.

Contrarily to the part load operation, the full load operating conditions only show the contribution to the pressure fluctuation for $f \geq 2 \times n$. At the PAT low pressure side, the measured frequency values are in the range of 2 to 4 times the runner rotating frequency, where the maximum frequency is increasing with the increase of back-pressure. Moreover, the maximum amplitude is significantly reduced, as the back-pressure increases.

Chapter 3. Pressure fluctuations in off-design operation

On the high pressure side of the PAT, the observed frequency values are in the range of 2 to 6 times the runner rotating frequency, where the maximum amplitude is observed at higher frequency values, compared to the spectral analysis of the measurements in the low pressure section. The amplitude of the pressure fluctuations is hardly affected by the back-pressure parameter χ_{nD} .

The non-coincidence of the frequency ranges at both sides of the PAT suggests that the pressure fluctuations measured in the full load operation are not related with the excitation of the hydraulic system eigenfrequencies. Thus, the physical mechanisms of the pressure fluctuations measured on each side of the PAT seem to be of a different nature. This subject requires further investigation as the collected data do not allow drawing further conclusions.

Finally, the pressure fluctuation contribution corresponding to the blade passing frequency at the PAT high pressure measurement section is significantly amplified by increasing the relative discharge. This fluctuation is due to the interaction between the blade passing frequency and the volute tongue. The amplitude increase at this frequency due to the relative discharge increase is related to the higher discontinuity in the static pressure field near the volute tongue, which is also identified in the numerical simulations in [86].

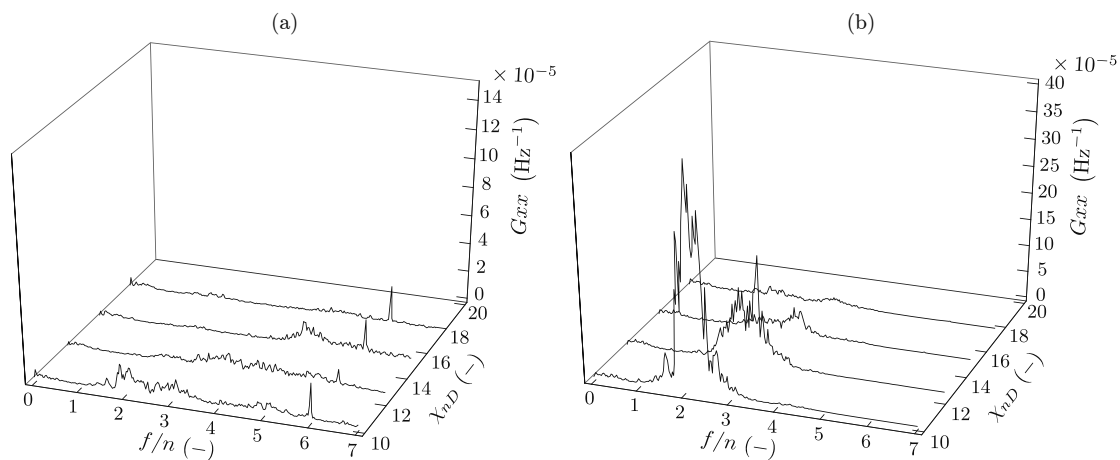


Figure 3.15 – Waterfall plot of the auto-spectrum density functions of the pressure coefficients: (a) in the high pressure section $G_{xx}(C_{p,1})$; and (b) in the low pressure section $G_{xx}(C_{p,2})$. Each chart shows the operating points shown corresponding to $N = 2'400 \text{ min}^{-1}$ and $Q/Q_{\text{BEP}} = 1.07$. All operating points are shown for χ_{nD} values of 10.0, 12.5, 15.0 and 17.5.

As a final remark, the axisymmetric cavitation vortex rope, observed in Francis turbines for full load operating conditions, with self-sustained periodic fluctuations associated with the hydraulic system eigenfrequencies, is not observed in this investigation. This could be due to the high values of back-pressure used in the experimental tests, as the occurrence of atmospheric pressure in the low pressure vessel prevented

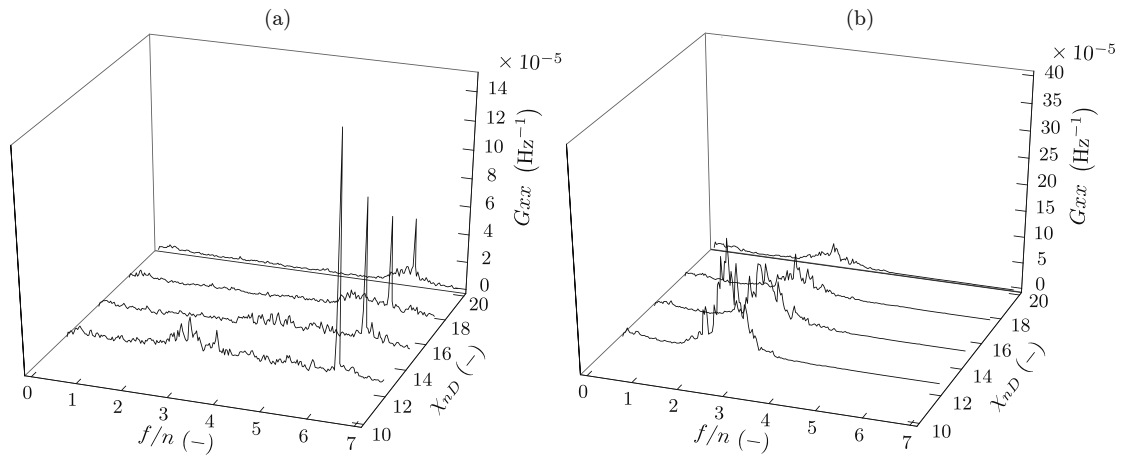


Figure 3.16 – Waterfall plot of the auto-spectrum density functions of the pressure coefficients: (a) at the high pressure section $G_{xx}(C_{p,1})$; and (b) at the low pressure section $G_{xx}(C_{p,2})$. Each chart shows the operating points shown corresponding to $N = 2'100 \text{ min}^{-1}$ and $Q/Q_{\text{BEP}} = 1.17$. All operating points are shown for χ_{nD} values of 12.5, 15.0 and 17.5 and 20.0.

to further decrease the back-pressure levels. Further investigation is required to assess if this phenomenon is exclusive to Francis turbines, or if it is solely by the swirling flow at the radial machine outlet. Note that the physical mechanisms that onset such oscillation are not fully understood yet and authors suggest further investigation [114].

3.5 Conclusion and future perspectives

This research aims at raising awareness about the development of pressure fluctuations during the off-design operation of PATs. The experimental tests focuses on the operating range with relative efficiency values of $\eta^T/\eta_{\text{BEP}}^T \geq 85\%$. Obtained results show that despite the high values of the relative efficiency, severe pressure fluctuations are measured in the high and in the low pressure sections of the tested PAT, both for the part load and the full load operating conditions.

The tested PAT features a cavitation vortex rope for the part load operation conditions $Q/Q_{\text{BEP}} \leq 84\%$. Other PATs may, however, present different values of the relative discharge for the development of this cavitation vortex rope. This cavitation flow onsets a synchronous pressure fluctuation, in a frequency range lower than the runner rotating frequency, which propagates throughout the entire test-rig, and is related with the excitation of the hydraulic system at one of its eigenfrequency values. A second pressure fluctuation is identified only in the PAT low pressure side. However, the mechanisms underlying this fluctuating component are not identified. The dependence on the back-pressure level suggests that this is related to the hydraulic system, however, further investigation is required.

Chapter 3. Pressure fluctuations in off-design operation

The pressure fluctuations in the full load operating conditions feature a frequency in the range of 2 to 4 times the runner rotating frequency at the PAT low pressure side. This fluctuation is associated with the hydraulic system, as it is dependent on the back-pressure level. Furthermore, the pressure fluctuations due to the interaction between the impeller blades and the volute tongue are significantly amplified with the increase of the relative discharge, corroborating previous results from CFD numerical simulations [86].

The characteristics of the pressure fluctuations during the part load and the full load operation are significantly different, where the latter can achieve strong amplitudes if the back-pressure value is not enough to sustain the pressure fluctuations. Note that the operation with a deviation of 7% with respect to the relative discharge, produced more severe pressure fluctuations at full load, than at part load operation (see Figure 3.7). Consequently, the results presented in this experimental research, together with the unsteady fluctuating radial forces identified by other authors evidence that the operation at full load conditions should be avoided. The matching between the frequency values of the precessing vortex rope and the eigenfrequency of the system, during the part load operation, may lead to the onset of system resonance, which represents a risk for the stability of the hydraulic system.

The results presented in this publication are a starting point for the investigation of the operation instabilities caused by the PAT operating off-design conditions. Note that the occurrence of these unsteady instabilities affect the load at which the hydraulic system and the PAT are subjected during the lifetime of the infrastructure. This load may have a direct impact on the reduction of the service life of the micro hydropower plant. The range of pressure fluctuations observed during this research indicates that this PAT should be operated in a discharge range of 85% to 100% with respect to the value referent to its BEP, for each rotational speed value. This discharge range is, however, dependent on the PAT investigated, stressing that further research is required on this subject. The achieved results show that the definition of the control settings for the flow regulation in a PAT micro hydropower plant needs to take into account the constraints related with both the machine performance (i.e., energy generation) and the stability issues (i.e., loads in the systems) of the PAT operation.

4 PAT characteristic curves modelling and prediction

This chapter corresponds to the manuscript:

J. Delgado, L. Andolfatto, D.I.C. Covas and F. Avellan (2018), *Pumps running as turbines: from performance prediction to hill chart modelling using the Hermite polynomial chaos expansion*. Submitted to Energy Conversion and Management, Elsevier.

Author contribution: The author collected the experimental data, developed and implemented the methodology for the prediction and modelling of the PAT performance.

Abstract

The accurate prediction of the characteristic curves of a pump running as turbine (PAT) still remains an issue that bottlenecks the design of PAT hydropower plants. Existing methodologies for the turbine mode prediction still do not provide reliable accuracy, especially for the part load and the full load operation. Also, no methodology is known for predicting the extended operation of a PAT, which is required for the analysis of the hydraulic transients in the power plant. This paper presents an empirical model for predicting the turbine mode performance and the extended operation. This methodology is based on the Hermite polynomial chaos expansion (PCE), which defines continuous surrogate functions based on known characteristic curves of PATs measured in test-rigs. The defined surrogate functions are later used for predicting the PAT performance. Finally, the same PCE technique is used to model the variable speed hill chart of a given PAT. The major advantage of using the PCE to model the PAT hill chart is its description by a continuous function composed of the summation of polynomial terms, which can be used for optimising PAT micro hydropower plant layout and control settings aiming at maximising the power plant efficiency.

Keywords: Pumps running as turbines, hydropower, turbine mode prediction, hill chart modelling, variable speed operation, polynomial chaos expansion.

4.1 Introduction

Pumps running as turbines (PATs) are hydraulic machines used for micro hydropower applications such as the energy recovery in pressurised water supply systems [123, 134, 160] or the rural electrification of remote areas [161–163]. The low capital investment, the immediate availability in several standardised sizes for a wide range of head and discharge values and the possibility of using the original induction motor as an asynchronous generator make PATs a cost-effective alternative to custom-made turbines for micro hydropower applications [59, 136].

The selection of the proper PAT to install in a given power plant is still a major challenge [16], as the turbine mode performance is not provided by pump manufacturers. The best efficiency point (BEP) in the turbine mode is found for higher values of head and discharge than the BEP in pump mode, while the maximum efficiency in both modes has approximately the same value [140]. The shape of the PAT characteristic curves in the entire operating range in turbine mode is, usually, dependent on the unit specific speed parameter [89]. The knowledge of the turbine full operating range is of the utmost importance for the development of the control strategies [106, 107] and for the assessment of project economic feasibility [45, 48], as PATs efficiency is highly affected when the machine operates under variable discharge conditions. Currently, existing methodologies still lack accuracy, especially in the description of the part load and in the full load operation. PATs are usually tested in laboratory conditions prior to on-site installation [38, 56].

The most accurate turbine mode performance predictions have been achieved by empirical formulations based on extensive sets of experimental data. These formulations use as input the pump rated characteristics provided by manufacturers. The application of this empirical formulations is limited, however, to the type of pumps (e.g., end-suction or in-line centrifugal pumps) and the range of values of the unit specific speed parameter for which the formulations were developed. This parameter provides information about the impeller shape, where small values refer to radial flow PATs, while high values refer to axial-flow PATs. The unit specific speed parameter n_q (or n_s depending on the parameter definition) is defined by:

$$\begin{aligned} n_q &= N \frac{Q^{\frac{1}{2}}}{H^{\frac{3}{4}}} \\ n_s &= N \frac{P^{\frac{1}{2}}}{H^{\frac{5}{4}}} \end{aligned} \tag{4.1}$$

where N is the rotational speed, Q is the discharge, H is the head and P is the shaft

power. As the parameters n_q and n_s are unit dependent, the parameters N , Q , H and P should be described in (min^{-1}), ($\text{m}^3 \cdot \text{s}^{-1}$), (m) and (kW), respectively.

Empirical formulations found in literature are based on the following methods: (i) specific speed-specific diameter charts [88, 91]; (ii) polynomial equations (generally quadratic and/or cubic polynomials) [92–94, 98, 164]; (iii) modified turbomachine affinity laws [96]; and (iv) artificial neural networks [97]. A summary of the domain of application of the empirical formulations (i.e., type of pumps and respective unit specific speed values) found in literature is provided in Table 4.1.

Empirical formulations still feature considerable deviations between predictions and actual performance. For instance, see results in [94], when applying the formulation described in [92]). Causes for the lack of repeatability in accuracy are still not clear. Authors in [88] suggest different designs of the pumps and different manufacturers as the main factors. However, other factors may play a key role, such as the setup used for collecting measurements, the uncertainty of the measurement equipment, the adequate PAT installation, the occurrence of cavitation, among others. Also, empirical formulations usually consider the same regression coefficients for the entire range of n_q values (see Table 4.1). Such fact neglects the influence of the unit specific speed in the shape of the characteristic curves, which may result in unsatisfactory descriptions of the PAT performance in the part load and full load operating zones.

The analysis of the hydraulic transients in a PAT power plant generated by both normal operating manoeuvres or by emergency events [101] relies on the knowledge of the PAT characteristic curves in the extended operation in generating mode. In this research, the extended operation in generating mode includes the quadrants of operation III and IV of a pump (see Figure 4.1), which, hereafter, are referred to as the *extended operation* for nomenclature simplicity. The extended operation characteristic curves shown in Figure 4.1 are described by the IEC factors of speed, discharge and torque, n_{ED} , Q_{ED} and T_{ED} , respectively [99]. These characteristic curves are also dependent on the unit specific speed of the PAT. To the authors knowledge, there is no formulation for predicting PAT performance in this extended operation mode. The modelling of the PAT performance during a hydraulic transient event is, usually, performed by assuming the extended operation characteristic curves of a pump with the closest value of unit specific speed, if the actual performance of the installed PAT is not available. However, this assumption should be used with caution, as it may introduce errors during the analysis of the hydraulic transients.

This research paper aims at providing a new methodology for predicting the PAT turbine mode and the extended operation characteristic curves for a given value of interest of unit specific speed. The core of the methodology is grounded in the bivariate Hermite polynomial chaos expansion (PCE), which is used to define continuous surro-

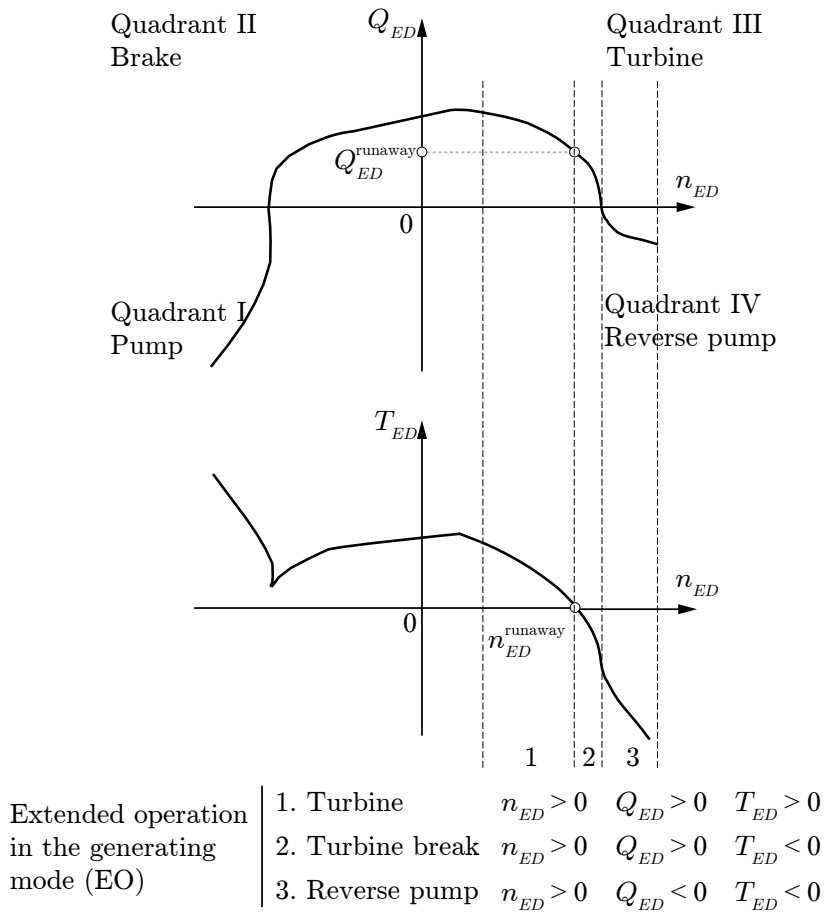


Figure 4.1 – Four-quadrants of operation of a pump. Identification of the operating zones of interest for the PAT performance modelling in the extended operation in the generating mode, hereafter referred as *extended operation*. The zones of interest are Turbine (A), Turbine break (B) and Reverse pump (C), which correspond to the Quadrants of operation III and IV.

gate functions. These surrogate functions propagate the known characteristic curves of the PAT inside a closed-bound interval corresponding to the unit specific speed values experimentally investigated. The obtained functions are later used to estimate the performance of a given PAT, using as input data the rated values in the pumping mode and the impeller diameter. The same PCE technique is also applied to model the variable speed hill chart of a given PAT. The modelling of the PAT hill chart may be carried out by using the characteristic curves provided by the surrogate functions found for the turbine mode, or by using data acquired in laboratory conditions.

The application of the methodology for the PAT characteristic curves prediction is shown for the experimental data collected for three end-suction single-stage centrifugal pumps in both the turbine mode and in the extended operation. The methodology is also validated using data published in the literature. Collected data and published

Table 4.1 – Domain of application of empirical formulations for predicting the PAT characteristic curves.

Reference	Type of pumps	Range of application
Singh and Nestmann [88]	13 end-suction single-stage centrifugal pumps	$n_q = 14.6 - 79.1$
Tan and Engeda [91]	4 pumps whose type is not detailed.	$n_q = 30.7 - 80.4$
Derakhshan and Nourbakhsh [92]	7 end-suction single-stage centrifugal pumps	$n_q = 14.6 - 55.6$
Naldi et al. [93]	2 end-suction multi-stage centrifugal pumps, 3 submersible multi-stage with vertical axis pumps and 2 end-suction single-stage centrifugal pumps	$n_q = 10.2 - 19.6$
Pugliese et al. [94]	1 in-line multi-stage centrifugal pump and 1 end-suction single-stage centrifugal pump	$n_q = 26.6 - 37.8$
Barbarelli et al. [98]	12 end-suction single-stage centrifugal pumps	$n_q = 9.1 - 64.1$
Novara and McNabola [164]	113 pumps comprising radial end-suction, semi-axial and axial pumps	–
Fecarotta et al. [96]	6 submersible semi-axial single-stage pumps	$n_s = 120 - 162$
Rossi and Renzi [97]	Data from multiple literature references (see [165])	–

data are presented in Section 4.2. The methodology for the PAT performance prediction and the Hermite polynomial chaos expansion are presented in Section 4.3. The application of the methodology for predicting the turbine mode and the extended operation performance is shown in Section 4.4. Section 4.5 presents the modelling of the variable speed hill chart using the PCE technique. Finally, conclusions and future perspectives are drawn in Section 4.6.

4.2 Experimental data

Experimental data are collected to measure the turbine mode characteristic curves and the extended operation characteristic curves of three end-suction single-stage centrifugal pumps. The three pumps feature unit specific speed n_q values of 23.1, 41.0 and 67.3, respectively. Additionally, the methodology is also tested using the data reported in literature [98] and the corresponding diameter values reported in [78]. Authors provide regression coefficients, which are used to build the characteristic curves of the PATs in the turbine mode. No data is available in the literature for the extended operation. The rated values for the pumps experimentally tested and for the

Chapter 4. PAT characteristic curves modelling and prediction

Table 4.2 – Rated characteristics in the pumping mode of the PATs used in this research.

Pump ID	n_q^P (SI)	N_R^P (min^{-1})	Q_R^P ($\text{l}\cdot\text{s}^{-1}$)	H_R^P (m)	P_R^P (kW)	D (mm) ⁽¹⁾
NK40-160/158	23.1	2'910	10.9	31.1	5.0	158
NK40-125/127	41.0	2'900	13.0	16.2	2.8	127
NK65-125/127	67.3	2'910	29.8	14.6	5.5	127
KSB40-335	9.1	1'450	7.4	33.0	5.4	330
KSB40-250	12.8	1'450	7.0	20.0	2.5	260
KSB50-160	28.7	1'450	9.7	8.5	1.2	174
KSB80-220	30.3	1'450	24.2	14.5	4.6	219
KSB80-200	34.1	1'450	23.2	12.1	3.8	198
KSB100-160	64.1	1'200	35.0	5.3	2.3	185

⁽¹⁾ D refers to the impeller diameter at the high pressure reference section.

pumps reported in literature [78, 98] are presented in Table 4.2.

In this research, pumps are identified by the n_q computed using the rated values in the pumping mode. Note that the n_q values referent to the turbine mode best operating point can only be computed after the prediction of the turbine mode characteristic curves has been performed.

The experimental investigation for collecting the data is performed in the closed-loop test-rig of Instituto Superior Técnico in the University of Lisbon, Portugal. The description of the experimental facility and the measurement equipment can be found in [166]. The characteristic curves measured for the turbine mode and for the extended operation are presented in Figures 4.2 and 4.3, respectively. Data presented in these figures is collected for values of rotational speed N between $2'100 \text{ min}^{-1}$ and $3'000 \text{ min}^{-1}$ with steps of 300 min^{-1} . All measurements are performed under stationary conditions. The turbine mode characteristic curves cover the part load, the BEP and the full load operating range of the three PATs. The extended operation characteristic curves describe the turbine mode, the turbine break and the reverse pump operating zones (see Figure 4.1).

The characteristic curves presented in these figures are described by the variation of Q_{ED} , T_{ED} and P_{ED} , with respect to n_{ED} , being these parameters defined in Equation (4.2) [99]. The IEC factors provide the condensed information regarding the runner rotating frequency n , the discharge Q , the specific hydraulic energy $E = gH$

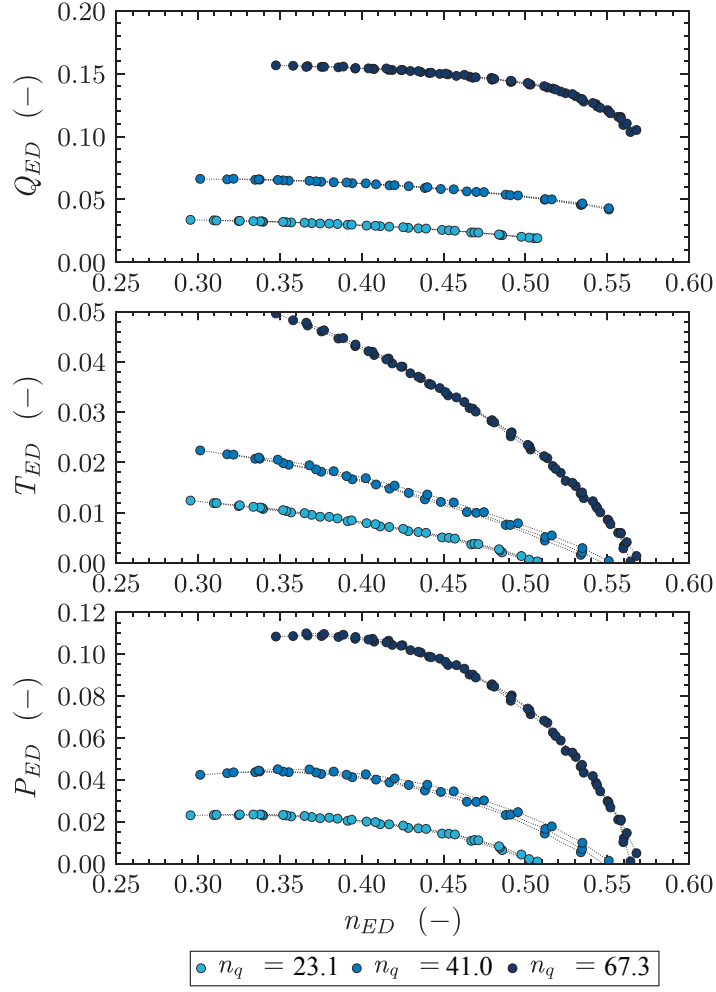


Figure 4.2 – Turbine mode stationary performance of the three PATs experimentally tested described by the non-dimensional coefficients Q_{ED} , T_{ED} and P_{ED} with respect to n_{ED} .

(being g the gravity acceleration and H the head), the shaft torque T and the power P .

$$\begin{aligned}
 n_{ED} &= \frac{nD}{\sqrt{E}} \\
 Q_{ED} &= \frac{Q}{D^2\sqrt{E}} \\
 T_{ED} &= \frac{T}{\rho D^3E} \\
 P_{ED} &= \frac{P}{\rho D^2\sqrt{E}^3}
 \end{aligned} \tag{4.2}$$

where ρ is the water density.

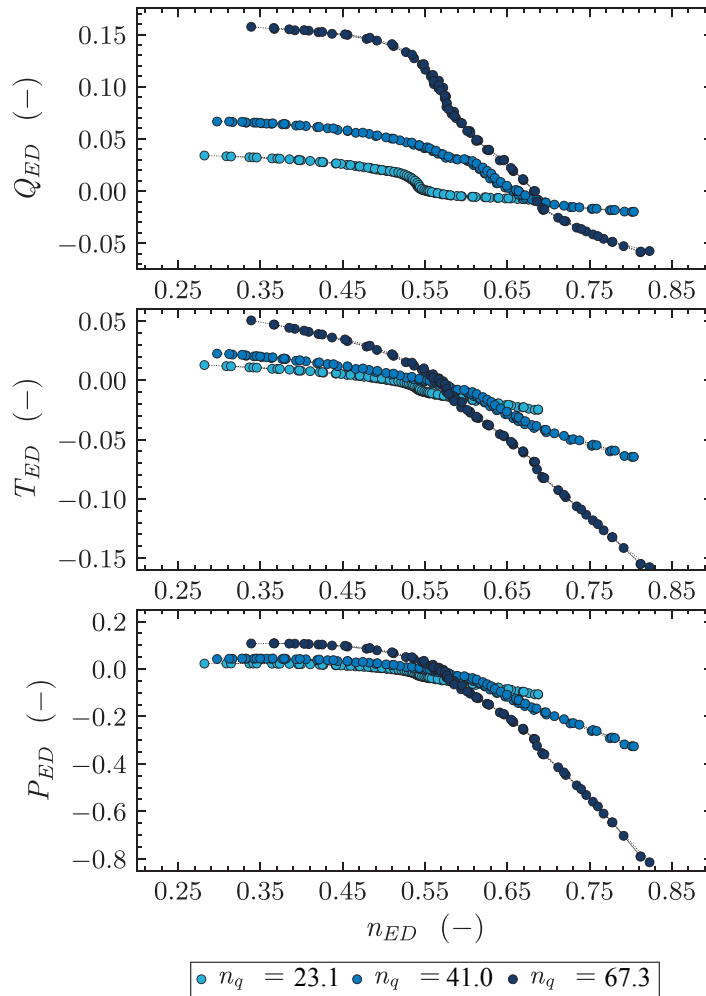


Figure 4.3 – Extended operation performance of the three PATs described by the non-dimensional coefficients Q_{ED} , T_{ED} and P_{ED} with respect to n_{ED} .

The IEC factors allow describing the variable speed performance data using a single characteristic curve. Collected data confirms that the unit specific speed value of the machine plays a key role in the shape of the characteristic curves, both in the turbine and in the extended operation modes. Such fact undermines the hypothesis of considering constant coefficients for describing the performance of different PATs in a given range of unit specific speed values. The same conclusion can be withdrawn from data presented in [89].

4.3 Hermite polynomial chaos expansion modelling

4.3.1 General approach

The prediction of the PAT performance aims at providing the functional means to estimate the hydraulic and mechanical characteristic curves inside a given range of unit specific speed values. A hypothesis for the turbine mode performance consists of propagating the characteristic curves of Q_{ED} and P_{ED} with respect to n_{ED} , in between of the tested unit specific speed values. Such hypothesis consists of the establishment of the empirical bivariate surrogate function $f_{Q_{ED}}^T(n_{ED}, n_q) = Q_{ED}$ and the function $f_{P_{ED}}^T(n_{ED}, n_q) = P_{ED}$, for the hydraulic and mechanical characteristic curves in the turbine, respectively. Similarly, for the extended operation performance, the methodology is based on finding the $f_{Q_{ED}}^{EO}(n_{ED}, n_q) = Q_{ED}$ and the $f_{T_{ED}}^{EO}(n_{ED}, n_q) = T_{ED}$ surrogate functions, for the hydraulic and mechanical characteristic curves, respectively. The T_{ED} parameter is selected instead of the one of P_{ED} for the extended operation, as the modelling of hydraulic transient events usually consider the $T_{ED} - n_{ED}$ characteristic curve for modelling the PAT behaviour during a hydraulic transient event in the power plant.

The Stone-Weierstrass theorem states that there is a surrogate polynomial function f^* , which approximates as closely as possible a continuous real function f defined on a bounded closed interval of real numbers [167]. Though the functional form of f is not known, it is assumed that the collected experimental data provide points that realize f . This surrogate function f^* is computed using the polynomial chaos expansion (PCE) [168], defined by:

$$f^* = \sum_k^{\infty} \lambda_k \text{He}_k \quad (4.3)$$

where λ_k are the weighting coefficients and He_k are the bivariate Hermite polynomials.

The bivariate Hermite polynomials are used as a functional basis for the polynomial expansion. Examples of this method applied to hydraulic machines can be found in [169, 170]. The polynomial basis can only be made of a finite set of polynomials, as there are only a limited number of experimental observations. The establishment of the surrogate functions consists of finding both the most appropriate truncated basis of polynomials Ψ and the corresponding weighting coefficients λ_k . The determination of Ψ and λ_k aims at minimising the error between observations and predictions (i.e., avoid underfitting) and at guaranteeing the realistic behaviour of the surrogate functions (i.e., avoid overfitting). Underfitting issues are characterised by large deviations between measured data y and the response of the surrogate function y^* . Overfitting

issues are associated with a surrogate function which exhibits unrealistic oscillations in the function operating domain, despite providing reduced deviations between y and y^* .

The definition of the bivariate Hermite polynomials is presented in Section 4.3.2, while the computation of the coefficients λ_k of the truncated basis is shown in Section 4.3.3. This step takes into account the computation of several fitting metrics, aiming at avoiding the aforementioned issues of underfitting or overfitting.

4.3.2 Hermite polynomials basis

The bivariate Hermite polynomials $\text{He}_{n,m}$, with indexes $n, m \in \mathbb{N}$ and $m \in [[2, n + 1]]$, being \mathbb{N} the set of natural numbers, are recursively defined by Equation (4.4) and by the boundary conditions given in Equation (4.5).

$$\begin{cases} \text{He}_{n+1,1} = a_n \cdot X_1 \cdot \text{He}_{n,1} + c_n \cdot \text{He}_{n-1,1} \\ \text{He}_{n+1,m} = \text{He}_{m-1,m} \cdot \text{He}_{n-m+2,1} \\ \text{He}_{n+1,n+2} = a_n \cdot X_2 \cdot \text{He}_{n,n+1} + c_n \cdot \text{He}_{n-1,n} \end{cases} \quad (4.4)$$

$$\begin{cases} \text{He}_{0,1} = 1 \\ \text{He}_{1,1} = X_1 \\ \text{He}_{1,2} = X_2 \end{cases} \quad (4.5)$$

where a_n and c_n are coefficients computed for each polynomial, which depend on the index $n \in \mathbb{N}$ and are defined in Equation (4.6). $X_1 \sim \mathcal{N}(0, 1)$ and $X_2 \sim \mathcal{N}(0, 1)$ are two input independent Gaussian random variables. For notation simplicity, the two input variables are gathered inside the vector $\mathbf{X} = (X_1, X_2)$. The Hermite polynomials are hereafter referred as He_p with $p \in \mathbb{N}$, using the index change of Equation (4.7).

$$\begin{cases} a_n = \sqrt{\frac{1}{n+1}} \\ c_n = -\sqrt{\frac{n}{n+1}} \end{cases} \quad (4.6)$$

$$p = \frac{n(n+1)}{2} + m - 1 \quad (4.7)$$

4.3. Hermite polynomial chaos expansion modelling

The Hermite polynomials family He_p form a complete basis of functions inside the Hilbert space that are orthogonal with respect to the scalar product defined by:

$$\langle \text{He}_A, \text{He}_B \rangle = \int_{\mathbb{R}^2} \text{He}_A(\mathbf{X}) \cdot \text{He}_B(\mathbf{X}) \cdot p(\mathbf{X}) d\mathbf{X} \quad (4.8)$$

where \mathbb{R} is the set of real numbers, $\text{He}_A(\mathbf{X})$ and $\text{He}_B(\mathbf{X})$ are any polynomial of the He_p family and $p(\mathbf{X})$ is the standardised bivariate probability density function defined by Equation (4.9). The graphical representation of the first 15 polynomials of the family He_p is depicted in Figure 4.4. Both indexes representations are shown in the figure, though only the p notation is used hereafter.

$$p(\mathbf{X}) = \frac{1}{2\pi} \exp\left(-\frac{\mathbf{X}^2}{2}\right) \quad (4.9)$$

The input data vector $\mathbf{x} = (x_1, x_2)$ collected during the experimental tests is usually not suitable for the Hermite PCE modelling. The polynomials He_p are only orthogonal with respect to the standardised bivariate normal probability density function. Thus, the standardisation function $g(\mathbf{x})$, defined in Equation (4.10), is applied to the physical input data. The coefficients a , b and c of $g(\mathbf{x})$ are computed by Equations (4.11), (4.12) and (4.13). The first equation guarantees the average values $\bar{X}_1 = 0$ and $\bar{X}_2 = 0$. The second equation ensures the standard variation $\sigma_{X_1} = 1$. The solution of the system of equations of Equation (4.13) satisfies the standard variation $\sigma_{X_2} = 1$ and the covariance $\text{cov}(X_1, X_2) = 0$.

$$g: \begin{cases} \mathbb{R}^2 & \mapsto & \mathbb{R}^2 \\ \mathbf{x} & \mapsto & \mathbf{X} = \begin{pmatrix} a & 0 \\ b & c \end{pmatrix} \cdot (\mathbf{x} - \boldsymbol{\mu}) \end{cases} \quad (4.10)$$

$$\boldsymbol{\mu} = \frac{1}{N} \sum_{j=1}^N {}^{(j)}\mathbf{x} \quad (4.11)$$

$$a = \sqrt{\frac{1}{\frac{1}{N-1} \sum_{j=1}^N ({}^{(j)}x_1 - \mu_1)^2}} \quad (4.12)$$

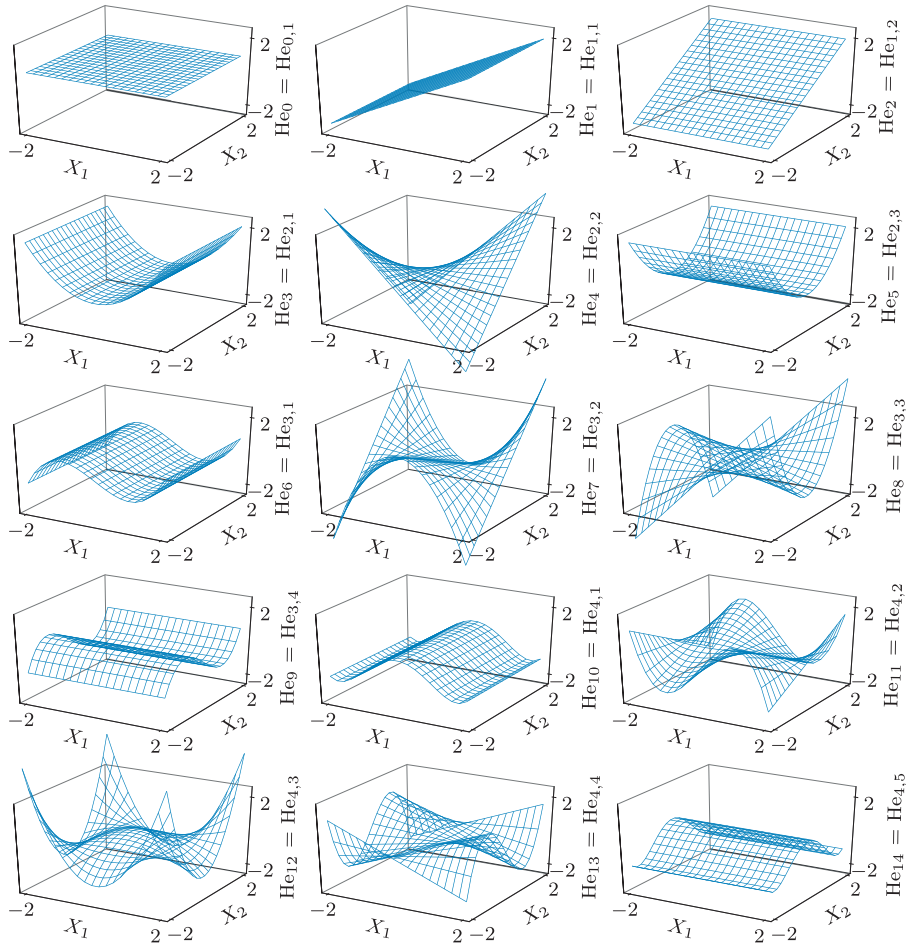


Figure 4.4 – First 15 bivariate polynomials of the family He_p . Adapted from [170].

$$\begin{cases} \frac{1}{N-1} \sum_{j=1}^N \left[b \binom{j}{1} x_1 - \mu_1 + c \binom{j}{2} x_2 - \mu_2 \right]^2 = 1 \\ \sum_{j=1}^N \binom{j}{1} X_1 \cdot \left[b \binom{j}{1} x_1 - \mu_1 + c \binom{j}{2} x_2 - \mu_2 \right] = 0 \end{cases} \quad (4.13)$$

4.3.3 Identification of the surrogate function

Considering a given truncated basis of Hermite polynomials selected *a priori* and defined by $\Psi = \{He_0, He_1, \dots, He_{p_{\max}}\}$, the response of the surrogate function y^* is defined by Equation (4.14). The weighting coefficients λ_k are computed based on minimising the mean-squared error $1/N_s \sum_{i=1}^{N_s} (y - y^*)^2$. The solution to this problem is given by the least-square solution as in Equation (4.15) [171]. This solution is only valid for an overdetermined system of equations such that $N_s > p_{\max}$, where N_s is the

total number of measurement samples and p_{\max} is the index of the maximum order polynomial of the family He_p of the truncated basis Ψ . This p_{\max} index also defines the cardinality of the truncated basis.

$$\mathbf{y}^* = f^*(\mathbf{x}) = \sum_{k \in \Psi} \lambda_k \cdot \text{He}_k(g(\mathbf{x})) \quad (4.14)$$

$$\boldsymbol{\lambda} = [\lambda_0 \quad \lambda_1 \quad \cdots \quad \lambda_{p_{\max}}]^\top = \left(\mathbf{He}(\mathbf{X})^\top \mathbf{He}(\mathbf{X}) \right)^{-1} \mathbf{He}(\mathbf{X})^\top \mathbf{y} \quad (4.15)$$

where $\boldsymbol{\lambda} \in \mathbb{R}^{p_{\max} \times 1}$ is the vector of the weighting coefficients, $\mathbf{He} \in \mathbb{R}^{N_s \times p_{\max}}$ is the matrix of the Hermite polynomials evaluated in the domain of \mathbf{X} defined in Equation (4.16) and $\mathbf{y} \in \mathbb{R}^{N_s \times 1}$ is the vector of the measured points defined in Equation (4.17). The superscript $(k) \in [[1, N_s]]$ refer to the number of the measurement samples.

$$\mathbf{He}(\mathbf{X}) = \begin{bmatrix} \text{He}_0^{(1)}(\mathbf{X}) & \text{He}_1^{(1)}(\mathbf{X}) & \cdots & \text{He}_{p_{\max}}^{(1)}(\mathbf{X}) \\ \text{He}_0^{(2)}(\mathbf{X}) & \text{He}_1^{(2)}(\mathbf{X}) & \cdots & \text{He}_{p_{\max}}^{(2)}(\mathbf{X}) \\ \vdots & \vdots & \ddots & \vdots \\ \text{He}_0^{(N_s)}(\mathbf{X}) & \text{He}_1^{(N_s)}(\mathbf{X}) & \cdots & \text{He}_{p_{\max}}^{(N_s)}(\mathbf{X}) \end{bmatrix} \quad (4.16)$$

$$\mathbf{y} = [{}^{(1)}y \quad {}^{(2)}y \quad \cdots \quad {}^{(N_s)}y]^\top \quad (4.17)$$

In this research, the truncated basis contains all polynomials between the index $p = 0$ up to p_{\max} . Sparse solutions are not taken into account (i.e., values of $\lambda_k = 0$). The choice of the truncated basis is performed by comparing several fitting metrics computed for the different candidate models. Metrics used are the maximum absolute error (Max. AE), the mean absolute error (Mean AE), the standard deviation of the error σ_e (see Equation 4.18), the determination coefficient R^2 (see Equation 4.19) and the Akaike Information Criterion (AIC) [172]. The latter estimates the maximum likelihood of a given model obtained using the least squares estimation and is penalised by the number of model parameters aiming at finding overfitted models (see Equation 4.20). The AIC metric is further corrected (AIC_c) according to Equation (4.21) to account for the number of parameters with respect to the existing number of samples [173]. As the results given by the AIC metric are dependent on the measurement samples, the absolute values of this metric do not provide relevant information. Results of the candidate models are further re-scaled with respect to the model with the minimum

AIC_c value, namely $AIC_{c,s} = AIC_c - AIC_{c,min}$.

$$\sigma_e(y, y^*) = \sqrt{\frac{1}{N_s} \sum_{i=1}^{N_s} (y_i - y_i^*)^2} \quad (4.18)$$

$$R^2(y, y^*) = 1 - \frac{\sum_{i=1}^{N_s} (y_i - y_i^*)^2}{\sum_{i=1}^{N_s} (y_i - \bar{y})^2} \quad (4.19)$$

$$AIC(y, y^*) = N_s (\log \sigma_e^2) + 2p_{max} \quad (4.20)$$

$$AIC_c(y, y^*) = AIC + \frac{2p_{max}(p_{max} + 1)}{N_s - p_{max} - 1} \quad (4.21)$$

The choice of the truncated basis Ψ for describing the surrogate function is performed by plotting the previous metrics with respect to the maximum index of the Hermite polynomial basis p_{max} . Best models should minimize both the maximum absolute error, the average absolute error, the standard deviation of the error and the AIC_{c,s} while maximizing the R^2 value. The final model is selected and plotted to analyse if underfitting or overfitting have occurred. This process is further illustrated in the application of the methodology.

The flow chart for identifying the surrogate function truncated basis and the corresponding weighting coefficients for a given measured quantity y is presented in Figure 4.5. The initial value of $p_{max} = 2$ is to take into account all polynomials from the boundary condition (see Equation 4.5) in the first iteration. The maximum value of $p_{max} = 100$ may be increased, though this value is found suitable for this research, as the p_{max} values for the different surrogate functions analysed in the next Sections vary between 10 and 35.

Considering that the truncated basis has been identified, the empirical surrogate functions for the propagation of the hydraulic and mechanical characteristic curves are computed based on the flow chart presented in Fig. 4.6. The input data are: (i) the variable used for defining the interpolating domain $\mathbf{x} = (x_1, x_2)$, which for the prediction methodology are $\mathbf{x}(n_{ED}, n_q)$; (ii) the values of the coefficients a , b and c and $\boldsymbol{\mu}$ of

4.3. Hermite polynomial chaos expansion modelling

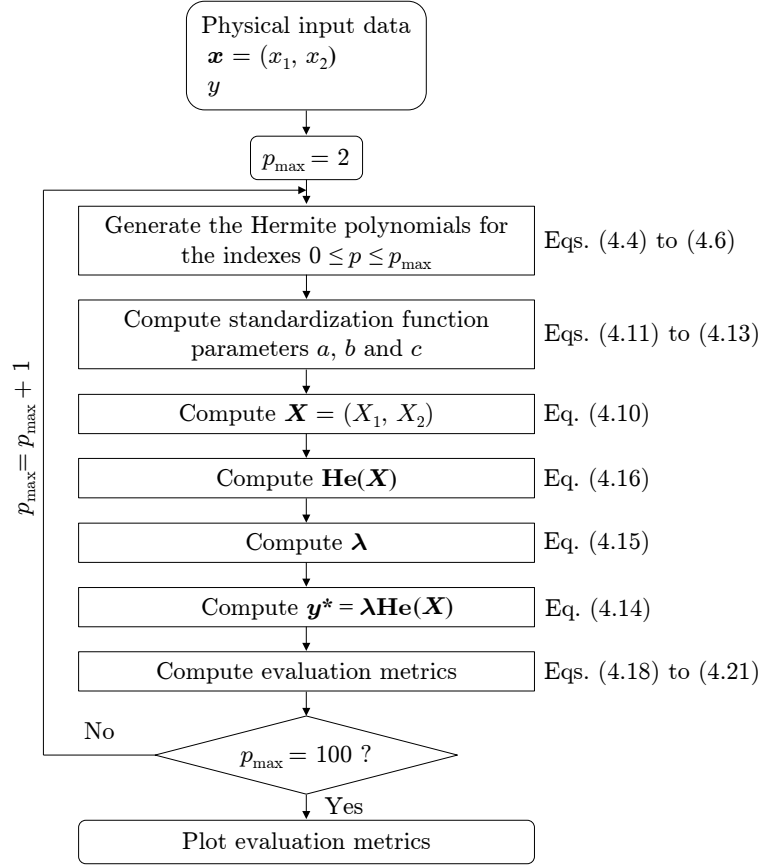


Figure 4.5 – Flow chart for the identification of the truncated basis for describing the surrogate function of a given variable of interest y with respect to the interpolation domain $\mathbf{x} = (x_1, x_2)$.

the standardisation function $g(x)$; (iii) the truncated basis defined by the $p_{\max,1}$ and the $p_{\max,2}$ values and the corresponding vectors of the weighting coefficients λ_1 and λ_2 , for the hydraulic and mechanical characteristic curves, respectively.

The identified surrogate functions allow computing the hydraulic and mechanical characteristic curves by using as input data the value of the unit specific speed for a given PAT of interest for the prediction, and the range of n_{ED} for which the characteristic curves are to be computed. This step is revisited in the following section.

In the case of the turbine mode, the parameters of E , Q and η^T can be compute from the $n_{ED} - Q_{ED}$ and the $n_{ED} - T_{ED}$ characteristic curves by using the Equation (4.22)

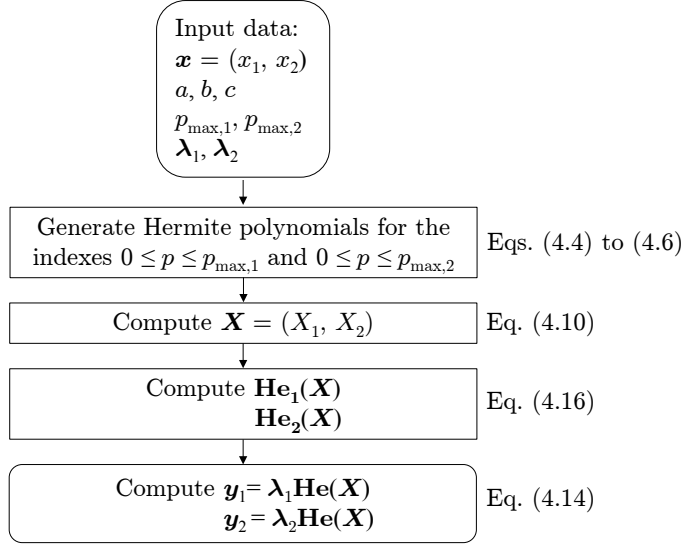


Figure 4.6 – Flow chart for computing the surrogate functions for the identified hydraulic and mechanical surrogate functions.

for a given value of the runner rotating frequency n .

$$\begin{aligned}
 E &= \frac{n^2 D^2}{n_{ED}^2} \\
 Q &= n D^3 \frac{Q_{ED}}{n_{ED}} \\
 \eta^T &= \frac{P_{ED}}{Q_{ED}}
 \end{aligned} \tag{4.22}$$

The variable speed hill chart performance of the PAT regarding defined by the variation of E and η^T with respect to N and Q can now be computed using the procedures described in Figures 4.5 and 4.6, using as input data $\mathbf{x} = (N, Q)$ for the variables of interest $y = E$ and $y = \eta^T$. This variable speed hill chart of the PAT can be computed using the turbine mode prediction results provided by the surrogate functions or by using precise performance data of a PAT, given by a pump manufacturer or acquired in laboratory conditions.

The identification of the truncated basis for a given surrogate function is illustrated in Section 4.4.1. The identification of the surrogate functions for the prediction of the turbine mode and for the extended operation are presented in Sections 4.4.2 and 4.4.3, respectively. Finally, the modelling of the variable speed performance hill chart is presented in Section 4.5. The summary of the surrogate functions for the prediction of the turbine mode performance, the prediction of the extended operation and the

modelling of the performance hill chart is given in Table 4.3.

Table 4.3 – Surrogate functions for the prediction and modelling of the PAT performance.

Operating mode	Surrogate function	Dataset	Operating domain	Variable of interest	Section
Turbine mode (T)	f_{QED}^T	Exp. data	$\mathbf{x} = (n_{ED}, n_q)$	$y = Q_{ED}$	4.4.2
	f_{PED}^T	Exp. data	$\mathbf{x} = (n_{ED}, n_q)$	$y = P_{ED}$	4.4.2
	$f_{QED,B}^T$	Lit. data	$\mathbf{x} = (n_{ED}, n_q)$	$y = Q_{ED}$	4.4.2
	$f_{PED,B}^T$	Lit. data	$\mathbf{x} = (n_{ED}, n_q)$	$y = P_{ED}$	4.4.2
Extended operation (EO)	f_{QED}^{EO}	Exp. data	$\mathbf{x} = (n_{ED}, n_q)$	$y = Q_{ED}$	4.4.3
	f_{TED}^{EO}	Exp. data	$\mathbf{x} = (n_{ED}, n_q)$	$y = T_{ED}$	4.4.3
Hill chart performance (HC)	f_E^{HC}	$n_q = 23.1$	$\mathbf{x} = (N, Q)$	$y = E$	4.5
	f_η^{HC}	$n_q = 23.1$	$\mathbf{x} = (N, Q)$	$y = \eta^T$	4.5
	f_E^{HC}	$n_q = 41.0$	$\mathbf{x} = (N, Q)$	$y = E$	4.5
	f_η^{HC}	$n_q = 41.0$	$\mathbf{x} = (N, Q)$	$y = \eta^T$	4.5
	f_E^{HC}	$n_q = 67.3$	$\mathbf{x} = (N, Q)$	$y = E$	4.5
	f_η^{HC}	$n_q = 67.3$	$\mathbf{x} = (N, Q)$	$y = \eta^T$	4.5

4.4 Modelling of the surrogate functions

4.4.1 Identification of the truncated basis

The application of the methodology described in the flow chart of Figure 4.5 is illustrated for the definition of the hydraulic surrogate function f_{QED}^T using the experimental data collected. The data transformation given by the standardisation function $g(x)$ is illustrated in Figure 4.7. The evaluation of the surrogate function is only performed inside the convex hull of the input data, as shown in Figure 4.7, for avoiding issues related with extrapolated data.

The comparison of the values computed for the metrics of different candidate models to describe the surrogate function $f_{QED}^T(n_{ED}, n_q)$ is illustrated in Figure 4.8. The use of truncated basis with $p_{\max} > 24$ does not provide a decrease in the errors between the measured data and the evaluation of the surrogate function. Also, the $AIC_{c,s}$ criteria starts to increase for truncated basis with $p_{\max} > 24$, which indicates possible overfitting.

The comparison between an underfitted model, the chosen model and an overfitted model is illustrated in Figure 4.9. These models correspond to p_{\max} values of 5, 24 and 40, respectively. The underfitted model does not represent the collected experimental data. The overfitted model shows that despite the slight decrease of the maximum, average and the standard deviation of the error of the predictions (Figure 4.8), the

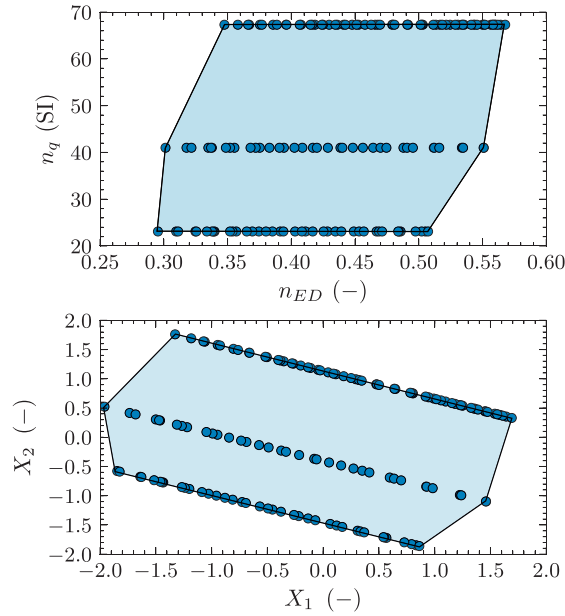


Figure 4.7 – Application of the standardisation function $g(\mathbf{x})$ to a physical input data set: (a) measured data $\mathbf{x} = (n_{ED}, n_q)$; (b) standardised data $\mathbf{X} = (X_1, X_2)$. The convex hull is indicated by the blue area.

model provides significant oscillations in-between of the tested unit specific speed values. The chosen model, in this example, corresponds to the one with the minimum $AIC_{c,s}$ value. This is not a mandatory criterion as the model corresponding to the $AIC_{c,s}$ value may often feature overfitting issues. A truncated basis with lower cardinality should be selected, considering the trade-off between the model accuracy and the expected likelihood of the surrogate function.

4.4.2 Turbine mode surrogate functions

The identification of the empirical surrogate functions for the propagation of the hydraulic and mechanical characteristic curves for the turbine mode prediction is performed separately for the collected experimental data and for the Barbarelli et al. [98] data (referred hereafter as literature data). The preliminary analysis of the data from both manufacturers indicates that there is no clear trend between the PATs of the two datasets, introducing higher deviation between the surrogate functions results and the actual performance of the PATs. This trend is, however, easily observed independently between the pumps of each dataset.

The truncated basis and the values computed for the fitting metrics regarding the identified surrogate functions are indicated in Table 4.4. The corresponding surrogate functions are illustrated in Figure 4.10 using a three dimensional view and, in Figure

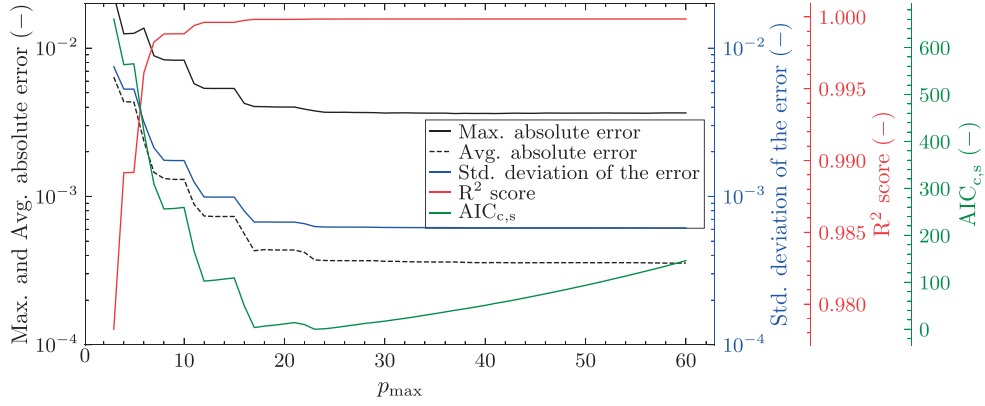


Figure 4.8 – Metrics evaluation for determining the surrogate function $f_{QED}^T(n_{ED}, n_q)$ applied to the experimental data.

4.11 using a contour view. The notation for the surrogate functions for the different datasets and variables of interest are indicated in Table 4.3.

The change of the trends of the surrogate functions surface with respect to the variation of the unit specific speed illustrated in Figures 4.10 and 4.11 show that the hypothesis of different regression coefficients for describing the hydraulic and mechanical characteristic curves, with respect to different values of the unit specific speed is correctly modelled using the bivariate Hermite PCE methodology. In fact, the recursive definition of the Hermite polynomials (Equation 4.4) implies that the interpolation coefficients are modified, depending on the n_q and consequently the X_2 values.

Table 4.4 – Characteristics and metrics values of the surrogate functions used for modelling the hydraulic and the mechanical characteristic curves in the turbine mode. Note that Q_{ED} and P_{ED} are dimensionless.

Parameter	f_{QED}^T	f_{PED}^T	$f_{QED,B}^T$	$f_{PED,B}^T$
p_{max}	23	17	18	18
Max. AE $\times 10^{-3}$ (-)	3.64	7.47	6.52	3.86
Mean AE $\times 10^{-3}$ (-)	0.04	0.87	0.58	0.67
$\sigma_e \times 10^{-3}$ (-)	0.64	1.40	0.96	1.02
R^2 (-)	0.999	0.998	0.999	0.998

Results presented in Figures 4.10 and 4.11 clearly show that the propagation of the characteristic curves between the two different datasets is not trivial. Firstly, the range of operation of PATs with similar values of unit specific speed n_q is different (i.e., different n_{ED} values for PATs with similar n_q value). Secondly, for the same n_q values, the surrogate functions found for the literature data provide higher values for both the Q_{ED} and the P_{ED} parameters. Nevertheless, the identified surrogate functions have

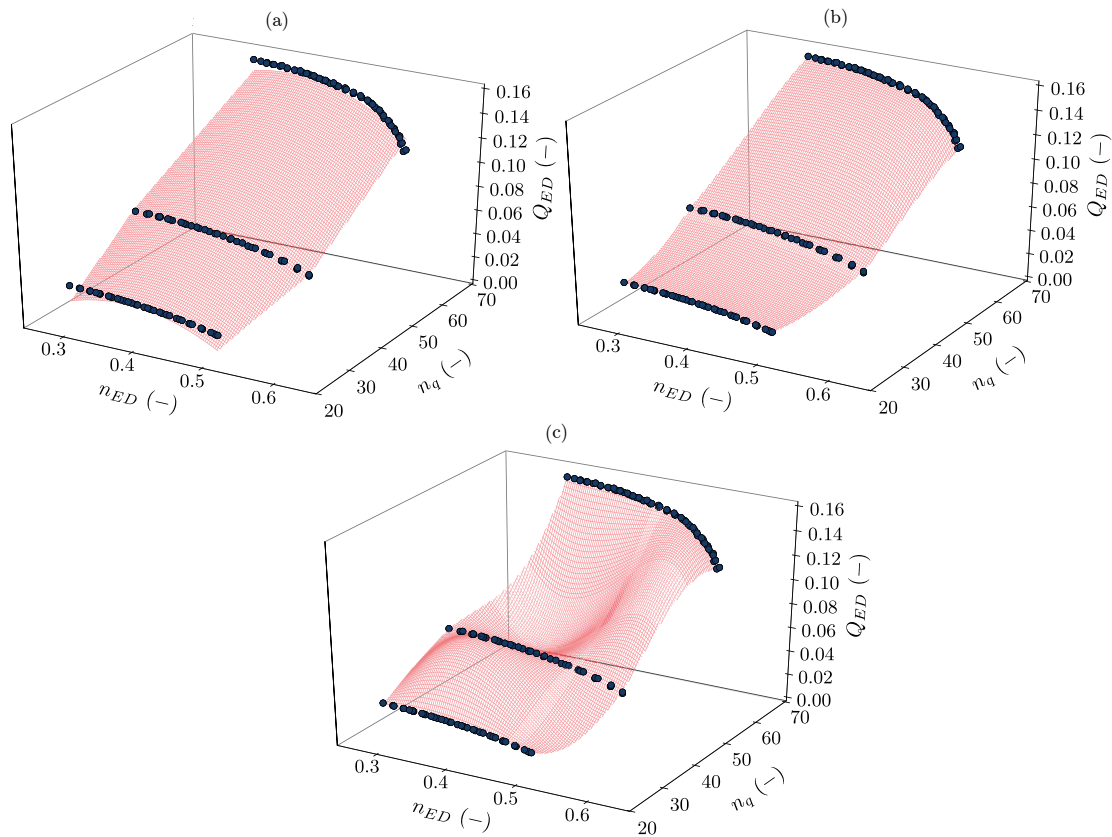


Figure 4.9 – Comparison of the truncated basis cardinality for computing the surrogate function f_{QED}^T : (a) underfitted model; (b) chosen model; (c) overfitted model.

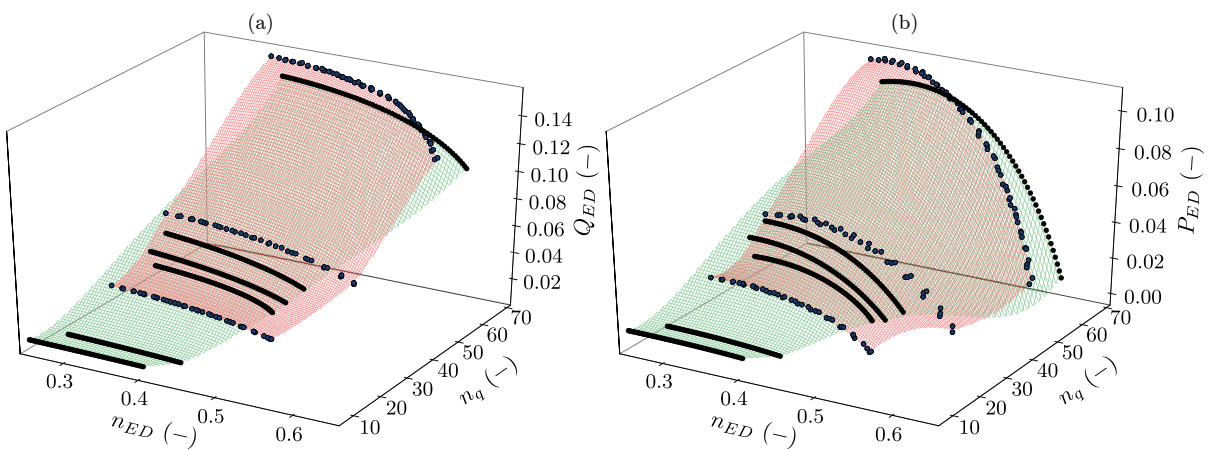


Figure 4.10 – 3D view of the identified surrogate functions for the propagation of the: (a) hydraulic and the (b) mechanical characteristic curves. The red mesh refers to the surrogate functions found for the collected experimental data f_{QED}^T and f_{PED}^T . The green mesh refers to the surrogate functions found for the literature data $f_{QED,B}^T$ and $f_{PED,B}^T$.

4.4. Modelling of the surrogate functions

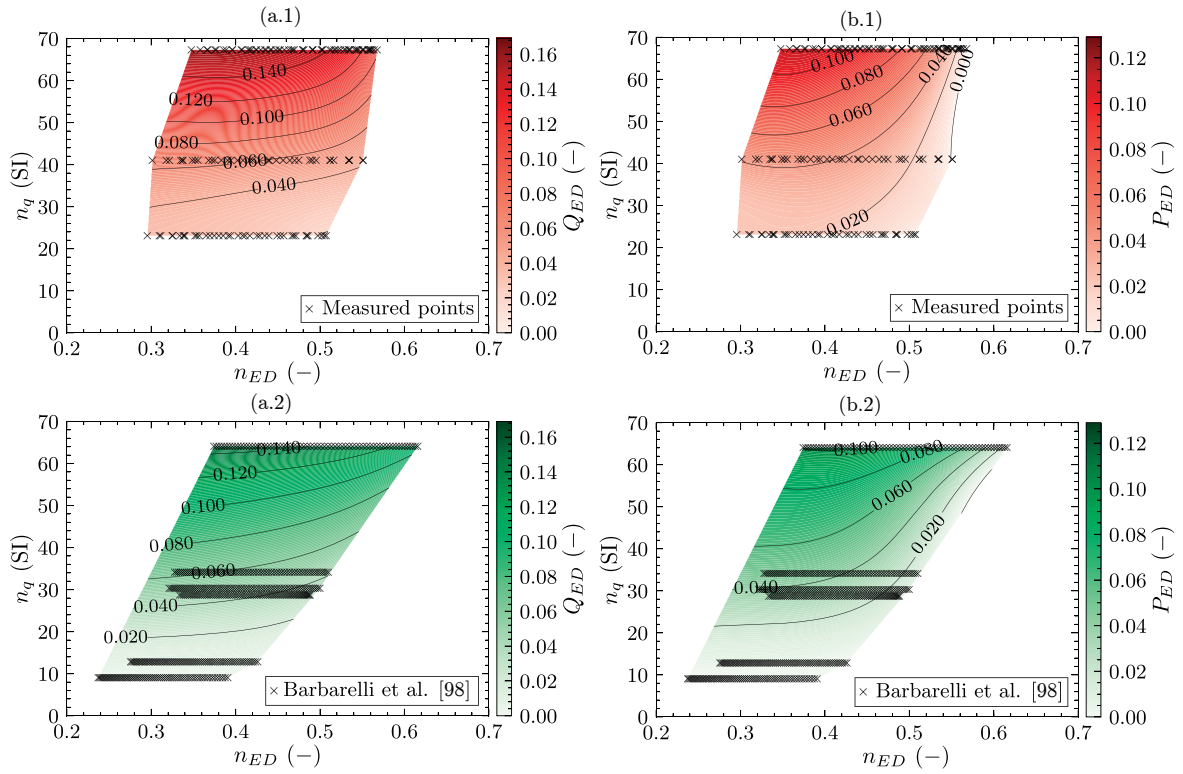


Figure 4.11 – Contour view of the identified surrogate functions for the propagation of the hydraulic and mechanical characteristic curves referent to the turbine mode. The red contours indicate the surrogate functions applied to the collected experimental data. The green contours indicate the evaluation of the surrogate functions applied to the literature data. (a.1) f_{QED}^T ; (b.1) f_{PED}^T ; (a.2) $f_{QED,B}^T$; (b.2) $f_{PED,B}^T$.

approximately the same trend and shape, which is clearly observed by the comparison of the isolines depicted in Figure 4.11.

The hypothesis of pumps of the same type from different manufacturers and with the same rated conditions featuring the same characteristic curves is likely to be far-fetched. Manufacturers may use different component designs (e.g., impeller, volute, bearings) and/or materials, even for pumps with the same rated values. Such differences may affect the performance in the turbine mode. Therefore, the application of this formulation for predicting the turbine mode performance (as well as the other available formulations) should be restricted to pumps of the same type and of the same manufacturer, whenever possible. This restriction aims at minimising the errors between the predictions made by the surrogate functions and the actual performance of the PATs.

Finally, the comparison of the evaluation of the surrogate functions with the original data from both datasets for the hydraulic and mechanical characteristic curves is

presented in Figures 4.12 and 4.13, respectively. Results presented in these figures are computed using the procedure presented in Figure 4.6, The PCE methodology is capable of accurately describing the propagation of the characteristic curves in the entire domain of interpolation. The major difference is observed for the PAT with $n_q = 9.1$ of the literature data. Results are only misfit in the part load operating region. The possible causes of this higher inaccuracy are discussed in Section 4.4.3.

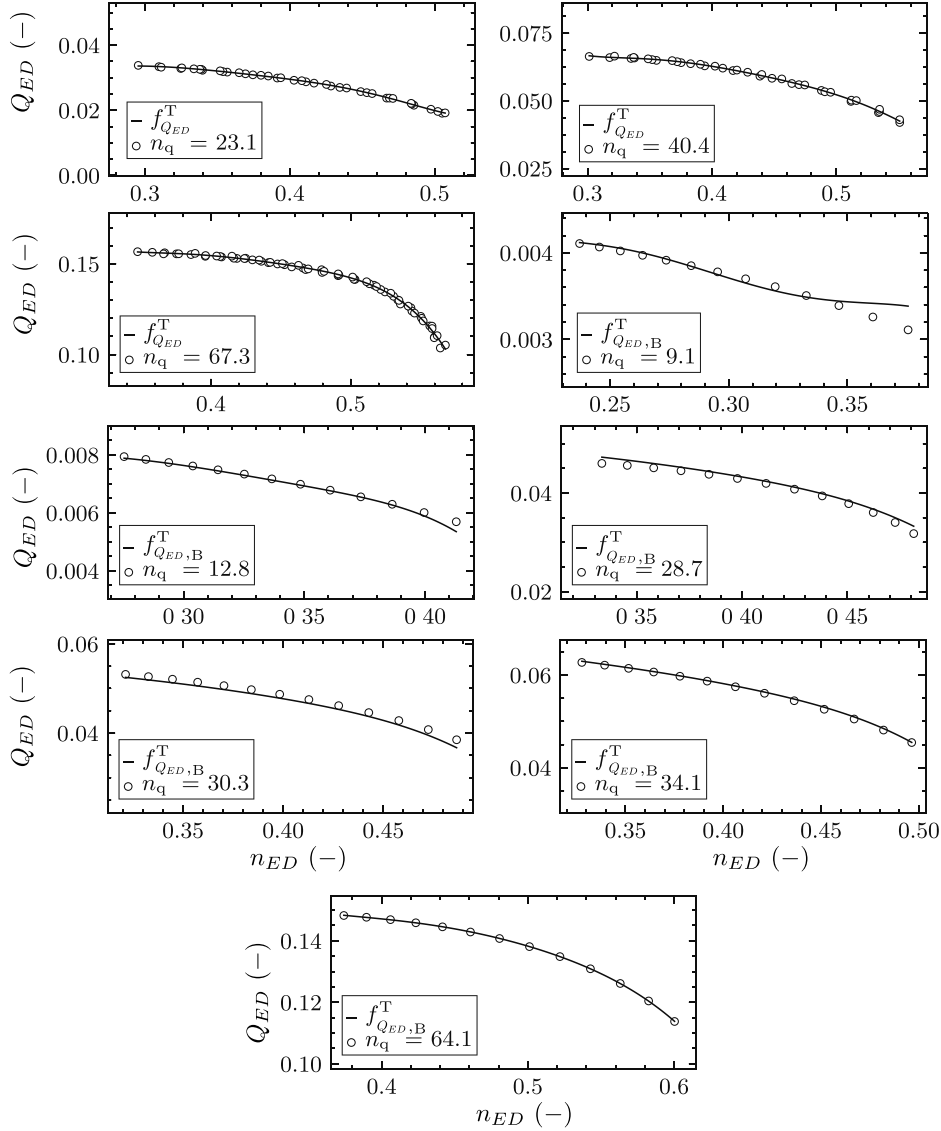


Figure 4.12 – Comparison between the experimental data, literature data and the results obtained from implementing the hydraulic surrogate functions regarding the turbine mode $f_{Q_{ED}}^T$ and $f_{Q_{ED,B}}^T$ (see Table 4.3 for the nomenclature of the surrogate functions). PATs are identified by the n_q values (see Table 4.2). The scatter points refer to the experimental data and to the literature data for each PAT. The lines refer to the results obtained by the identified hydraulic surrogate functions.

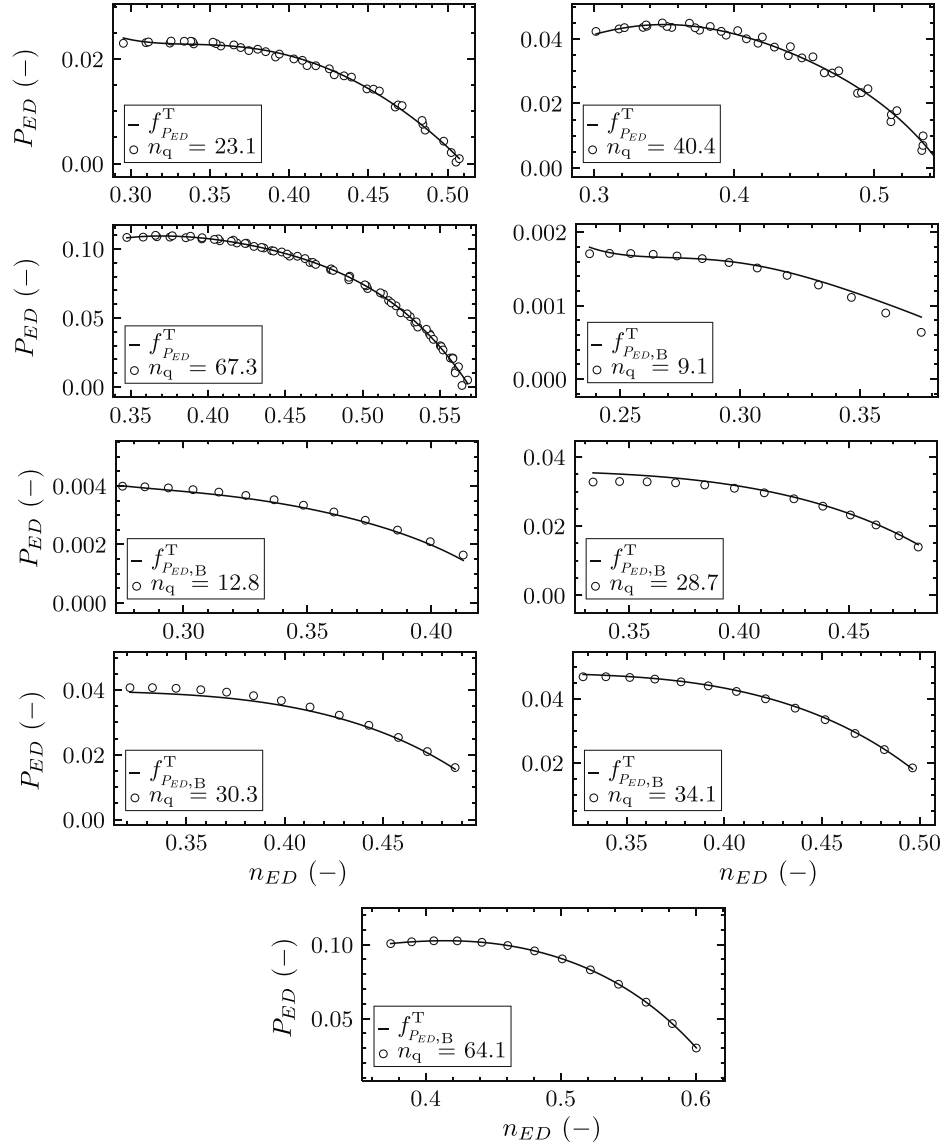


Figure 4.13 – Comparison between the experimental data, literature data and the results obtained from implementing the mechanical surrogate functions regarding the turbine mode f_{PED}^T and $f_{PED,B}^T$ (see Table 4.3 for the nomenclature of the surrogate functions). PATs are identified by the n_q values (see Table 4.2). The scatter points refer to the experimental data and to the literature data for each PAT. The lines refer to the results obtained by the identified mechanical surrogate functions.

The computation of the evaluation of the identified surrogate functions of the turbine, for a given value of unit specific speed of interest, like illustrated in the Figures 4.12 and 4.13 provide the $n_{ED} - Q_{ED}$ and $n_{ED} - T_{ED}$ characteristic curves. Equation (4.22) should now be applied to compute the parameters E , Q and η^T for a given constant value of N for obtaining the stationary performance of the PAT in the turbine mode.

4.4.3 Extended operation surrogate functions

The same procedure is applied for defining the surrogate functions to the extended operation characteristic curves with respect to the experimental data collected. The truncated basis and the values of the metrics for the propagation of the hydraulic and mechanical characteristic curves are presented in Table 4.5. The corresponding identified surrogate functions are illustrated in Figure 4.14. Results show that the Hermite PCE is also able to provide propagation of the characteristic curves inside the interval of tested unit specific speed values. The comparison of the metrics values obtained for the turbine mode (Table 4.4) and for the extended operation (Table 4.5) show that the errors regarding the latter are higher. This is an expected result, as the interpolation referent to the extended operation is more complex compared to the turbine mode, namely because of the higher curvature associated with the turbine break and reverse pump areas (the s-curve).

Table 4.5 – Characteristics and metrics values of the identified surrogate functions for modelling the propagation of the hydraulic and mechanical characteristic curves in the extended operation. Note that Q_{ED} and T_{ED} are dimensionless.

Parameter	f_{QED}^{EO}	f_{TED}^{EO}
p_{max}	32	19
Max. AE $\times 10^{-3}$ (-)	9.20	21.18
Mean. AE $\times 10^{-3}$ (-)	2.58	4.64
$\sigma_e \times 10^{-3}$ (-)	3.26	5.96
R^2 (-)	0.994	0.998

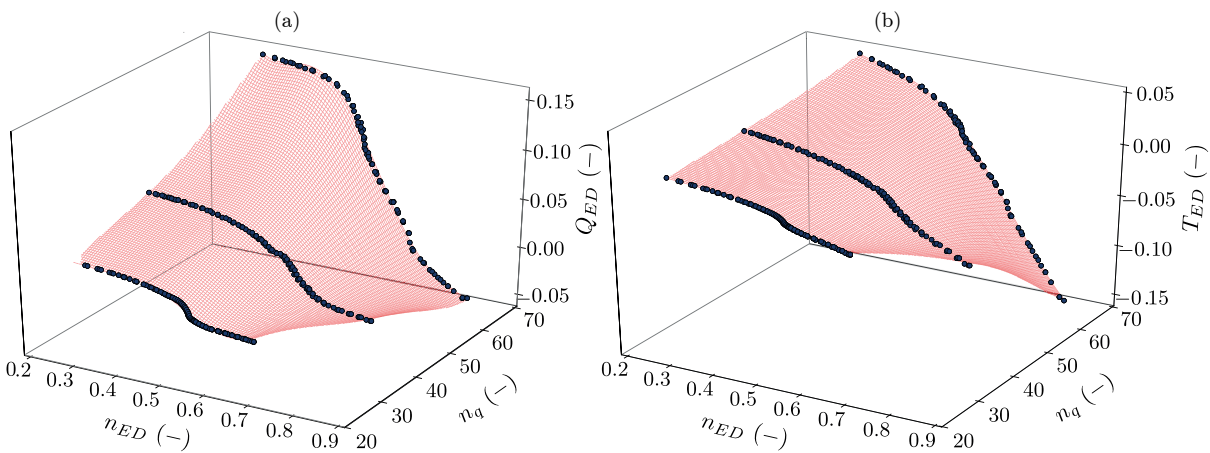


Figure 4.14 – 3D view of the identified surrogate functions for the propagation of the (a) hydraulic and the (b) mechanical characteristic curves referent to the extended operation. The red mesh refers to the surrogate functions found for the experimental data f_{QED}^{EO} and f_{TED}^{EO} .

The adjustment of the identified surrogate functions to the experimental data collected are shown in Figures 4.15 for the hydraulic and mechanical characteristic curves.

Data presented in this figure show that the model is capable of describing the average properties of the characteristic curves of Q_{ED} and P_{ED} , with respect to n_{ED} . The larger deviation between model results and the true performance of the PAT are observed for the pump with $n_q = 23.1$. This larger deviation is similar to the results obtained for the surrogate functions of the turbine mode for the literature data (see PAT with $n_q = 9.1$ in Figures 4.12 and 4.13), regarding the PAT with $n_q = 9.1$.

This larger deviation for the PATs with lower values of unit specific speed is explained by the computation of the weighting coefficients λ_k , which minimises the mean-squared error $1/N_s \sum_{i=1}^{N_s} (y - y^*)^2$. As PATs with lower n_q values have lower values of both the Q_{ED} and the P_{ED} , the identification of the λ_k values favours, in fact, the fitting of the surrogate function in the areas with higher Q_{ED} and P_{ED} values (i.e., higher values of unit specific speed). This higher deviation for lower n_q values is a limitation of the methodology, which may compromise the accuracy of the surrogate functions in the domain of lower n_q values. Nevertheless, good fittings are observed for the remaining two PATs.

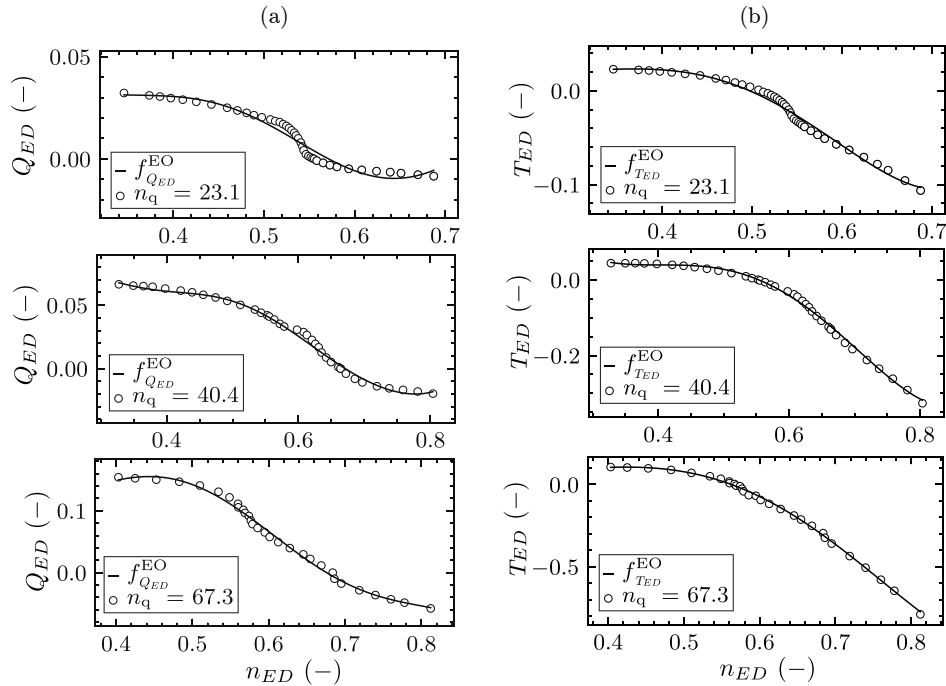


Figure 4.15 – Comparison between the experimental data and the results obtained from implementing the surrogate functions in the extended operation: (a) hydraulic surrogate function $f_{Q_{ED}}^{EO}$; (b) mechanical surrogate function $f_{T_{ED}}^{EO}$. PATs are identified by the n_q values (see Table 4.2). The scatter points refer to the experimental data for each PAT. The lines refer to the results obtained by the identified surrogate functions.

Note that the computation of the evaluation of the identified surrogate functions of the extended operation, for a given value of the unit specific speed of interest, already

provide the $n_{ED} - Q_{ED}$ and $n_{ED} - T_{ED}$ characteristic curves required for modelling the hydraulic transients in a PAT power plant.

4.5 Hill chart modelling

The variable speed hill chart of the PAT performance can be modelled by using the estimated characteristic curves obtained from the identified surrogate functions for the turbine mode, or by using data obtained by experimental tests or supplied by the PAT manufacturers (if available). Despite the Hermite PCE methodology having proven efficient for modelling the propagation of the characteristic curves, it should only be used during preliminary engineering designs. The final design of the micro hydropower plant should be performed using accurate experimental data for the PAT characteristic curves. This accurate data is obtained either by performing experimental tests prior to onsite installation (as in [38, 56]) or by using data provided by PAT manufacturers.

The procedures presented in the flow charts of Figures 4.5 and 4.6 are used to model the variable speed hill chart performance of the PATs experimentally tested, using as operating domain $\mathbf{x} = (N, Q)$ and using the variables of interest E and η^T . Note that this procedure can be replicated for any variable of interest. The experimental data used consist of the measurements performed for values of rotational speed between $1'200 \text{ min}^{-1}$ and $3'000 \text{ min}^{-1}$. The identified truncated basis and the respective values computed for the fitting metrics of the surrogate functions found for modelling the variable speed hill chart performance of the PATs experimentally tested are presented in Table 4.6.

Table 4.6 – Characteristics and metrics values of the surrogate functions for modelling the variable speed hill chart performance of the PATs experimentally tested. Results of the metrics of the surrogate functions referring to E are in $\text{J} \cdot \text{kg}^{-1}$, while the ones referring to η^T are in %.

Pump ID Parameter	$n_q = 23.1$		$n_q = 41.0$		$n_q = 67.3$	
	f_E^{HC}	f_η^{HC}	f_E^{HC}	f_η^{HC}	f_E^{HC}	f_η^{HC}
p_{max}	14	25	10	20	21	28
Max. AE (units)	2.7	1.30	1.86	1.57	2.9	1.82
Mean. AE (units)	0.56	0.30	0.40	0.29	0.9	0.34
σ_e (units)	0.77	0.40	0.56	0.43	0.59	0.47
R^2 score (-)	0.999	0.999	0.999	0.999	0.999	0.999

The 3D view of the identified surrogate functions for describing the specific hydraulic energy E and the PAT efficiency in turbine mode η^T , with respect to the discharge Q and rotational speed N for the PAT with unit specific speed $n_q = 23.1$ are illustrated in Figure 4.16. Results in this figure show that the identified surrogate functions can smoothly describe the variation of variables of interest E and η^T , with respect to the

discharge Q and rotational speed N , without evidence of overfitting issues.

Also, the standard deviation of the error, for the three tested PATs, is in the range of $0.56 \text{ J} \cdot \text{kg}^{-1}$ and $0.77 \text{ J} \cdot \text{kg}^{-1}$, for the specific hydraulic energy; and in the range of 0.40% to 0.47% for the efficiency (see Table 4.6). The order of magnitude of stationary measurements for the three PATs experimentally tested range from $50 \text{ J} \cdot \text{kg}^{-1}$ to $500 \text{ J} \cdot \text{kg}^{-1}$ for the specific hydraulic energy; and from 0% to 75% for the efficiency in turbine mode (see Figures 4.17, 4.18 and 4.19). Thus, The small standard deviation of the errors compared to the stationary measurements for both parameters E and η^T and the ability to represent the variation of the different variables of interest with respect to the dependent variables N and Q indicate that the Hermite PCE methodology is suitable for identifying continuous surrogate functions for describing the variable speed hill chart performance of PATs.

Finally, the obtained hill charts for the variable speed performance of the PATs with n_q values of 23.1, 41.0 and 67.3 are presented in Figures 4.17, 4.18 and 4.19, respectively. The best efficiency ridge line, which separates the operating areas of part load and of full load, are clearly identified in these figures.

The main advantage of modelling the performance hill chart of the PAT performance using the PCE methodology is the establishment of a continuous function inside the operating domain of the machine. As this continuous function is composed of the sum of polynomial terms, the computation of the derivatives with respect to the discharge or to the rotational speed is straightforward. Such fact is a major advantage for the development of optimisation algorithms for controlling the PAT power plant, for instance, the Maximum Power Point Tracking [174], aiming at maximising the power based on the available specific energy and discharge at the inlet of the PAT power plant.

4.6 Conclusions and future perspectives

This research paper presents the application of the bivariate Hermite polynomial chaos expansion (PCE) for modelling the performance of pumps running as turbines (PATs). The PCE allows defining empirical continuous surrogate functions in a closed-bounded interval, which are used in the scope of this research for two purposes: (i) the identification of an empirical model for predicting the PAT performance in the turbine mode and in the extended operation in the generating mode (Quadrants III and IV of the four-quadrants operation of a pump - see Figure 4.1); and (ii) the modelling the variable speed hill chart performance of a given PAT of interest.

The empirical model for predicting the PAT characteristic curves, both in the turbine mode and in the extended operation, uses the PCE to define two surrogate functions

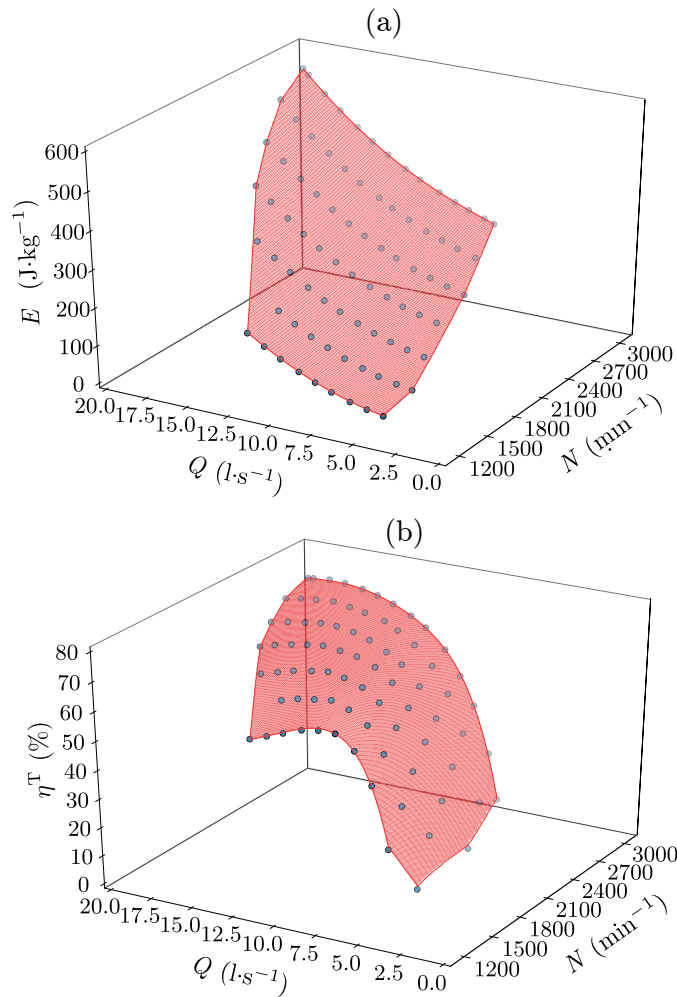


Figure 4.16 – 3D view of the adjustment of the surrogate functions for modelling the variable speed hill chart performance of the $n_q = 23.1$ PAT: (a) f_E^{HC} ; (b) f_η^{HC} . The red mesh surface indicate the identified surrogate functions, while the scatter dots indicate the experimental data collected.

aiming at propagating the hydraulic and the mechanical characteristic curves in-between of unit specific speed values of the tested PATs. These identified surrogate functions can be used to predict the characteristic curves of a given PAT of interest, using as input its value of the unit specific speed. The methodology is applied separately for two datasets of single-stage end-suction centrifugal PATs from two different manufacturers. The surrogate functions are capable of efficiently propagating the characteristic curves data, while maintaining reduced interpolation errors (see Figures 4.10, 4.12 and 4.13). The methodology should ideally be applied for predicting the performance of PATs of the same manufacturer and only for pumps of the same type aiming at reducing the prediction errors. The hypotheses of two PATs from different manufacturers and with the same rated values having the same performance is un-

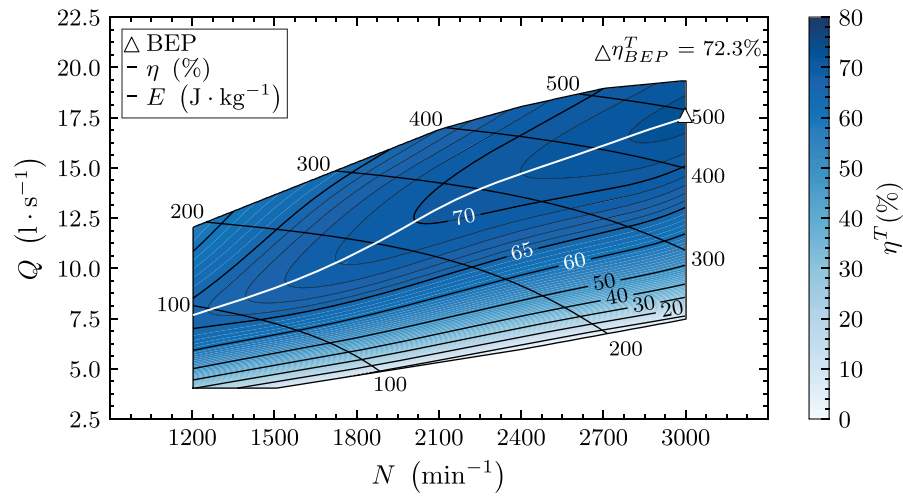


Figure 4.17 – Hill chart of the turbine mode performance of the PAT with $n_q = 23.1$. Specific hydraulic energy E and efficiency η variation as a function of the discharge Q and rotational speed N . The white line indicates the best efficiency ridge line.

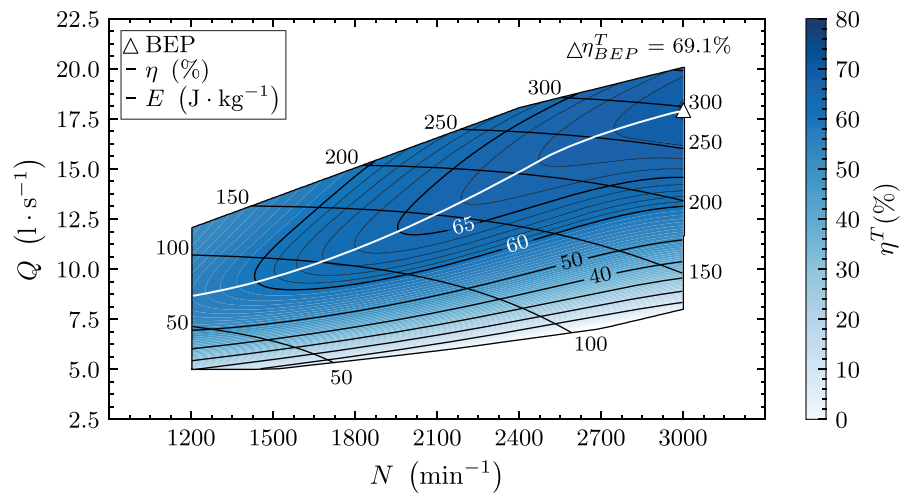


Figure 4.18 – Hill chart of the turbine mode performance of the PAT with $n_q = 41.0$. Specific hydraulic energy E and efficiency η variation as a function of the discharge Q and rotational speed N . The white line indicates the best efficiency ridge line.

likely, as manufacturers may use different components designs and materials. The developed methodology could be applied, in the future, to datasets of different types of pumps for defining surrogate functions used for predicting the characteristic curves of different types of PATs and with different ranges of unit specific speed values.

The application of the PCE for modelling the surrogate function for the prediction of the extended operation despite successful, provided results with lower accuracy compared to the turbine mode. This lower accuracy is explained by the higher complexity

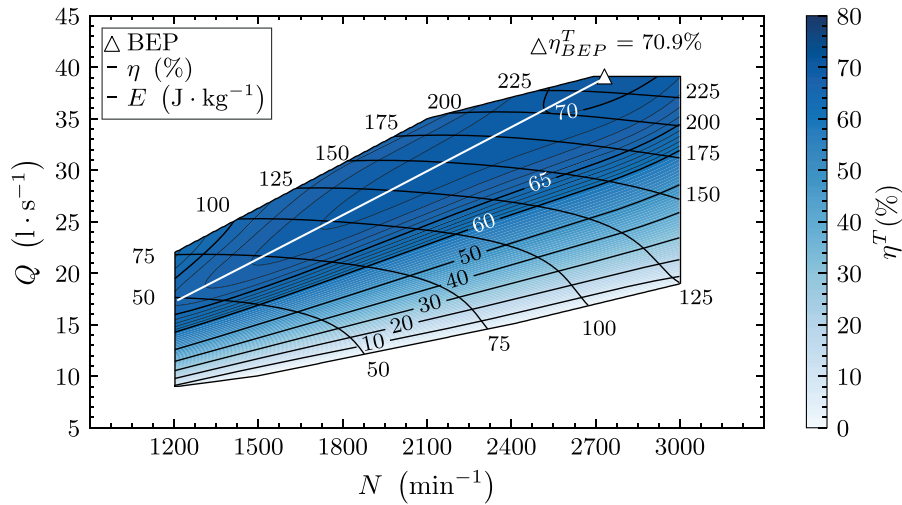


Figure 4.19 – Hill chart of the turbine mode performance of the PAT with $n_q = 67.3$. Specific hydraulic energy E and efficiency η variation as a function of the discharge Q and rotational speed N . The white line indicates the best efficiency ridge line.

of the characteristic curves. Nevertheless, the identified surrogate functions clearly propagate the characteristic curves in-between of the unit specific speed values. The use of these surrogate functions for predicting the extended operation characteristic curves provides more reliable performance data of a given PAT, compared to using the available data from a PAT with the closest unit specific speed value. The latter case may introduce errors in the hydraulic transient analysis of the power plant, and results should be used with caution. As future perspectives, more data should be added to the available dataset, aiming at increasing the prediction accuracy.

As a final note, methodologies for predicting the PAT performance (this methodology or the ones available in literature) should be only used during preliminary stages of the design of PAT power plants. Results provided in this research show that the methodologies should be applied to datasets of pumps from the same manufacturer to reduce the prediction error. However, the final design of the PAT power plants, this is, the design of the power plant layout and control settings, should be performed with reliable data, either acquired from model testing in test-rigs or by data provided by PAT manufacturers.

Finally, the PCE is used to model the variable speed hill chart of a given PAT. The obtained hill chart allows at identifying the best efficiency ridge and the operating areas of part load and full load. As the hill chart is described by a continuous function composed of the sum of polynomial terms, the computation of the derivatives of the hill chart is straightforward. This straightforward computation is a major advantage as it allows using the hill chart model for optimising the power plant layout and control settings that maximise the energy produced by the PAT power plant.

5 Guidelines for modelling the PAT performance

5.1 Introduction

This Chapter provides the stepwise guidelines for the implementation of the methodology developed for predicting and modelling the PAT performance presented in Chapter 4. For technical details about the methodology please refer to Chapter 4. Depending on the stage of the development of the PAT micro hydropower plant, this is, for the preliminary design stage or the final design stage, the modelling of the PAT performance is carried out according to the flow chart given in Figure 5.1. This thesis only takes into account the hydraulic power and the mechanical power in the shaft. The efficiency of the electrical equipment is not considered.

The ultimate goal of these guidelines is to provide the model of the variable speed hill chart for a given PAT of interest. The available data for modelling the hill chart usually depends on the design stage of the power plant. The considered design stages are: (i) preliminary design stage; and (ii) final design stage. In a preliminary design stage, the accurate data about a given PAT performance is usually not available. The characteristic curves of the PAT can be predicted using the surrogate functions identified in Chapter 4. These surrogate functions are only valid for the PATs with unit specific speed values inside the range of the tested pumps.

The prediction of the PAT characteristic curves, for both the turbine mode and the extended operation, is the reverse of the methodology carried out for identifying the surrogate functions in Chapter 4. While Chapter 4 is to identify the empirical surrogate functions for predicting the PAT characteristic curves, in this Chapter the prediction of the PAT performance uses the already identified surrogate functions to predict characteristic curves inside the valid domain of interpolation of the surrogate functions. This prediction of the PAT performance is illustrated in Figure 5.2, where the characteristic curves are obtained, by computing the evaluation of the surrogate function for a target value of unit specific speed n_q inside a valid interval of n_{ED} .

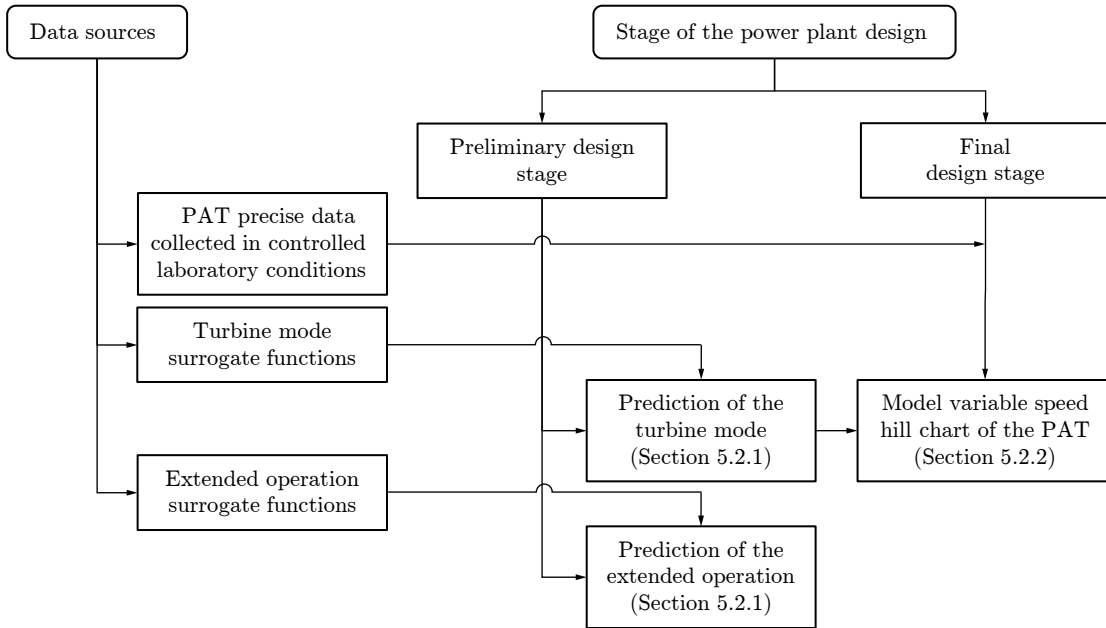


Figure 5.1 – Flow chart diagram for modelling the PAT variable speed hill chart performance depending on the design stage of the power plant.

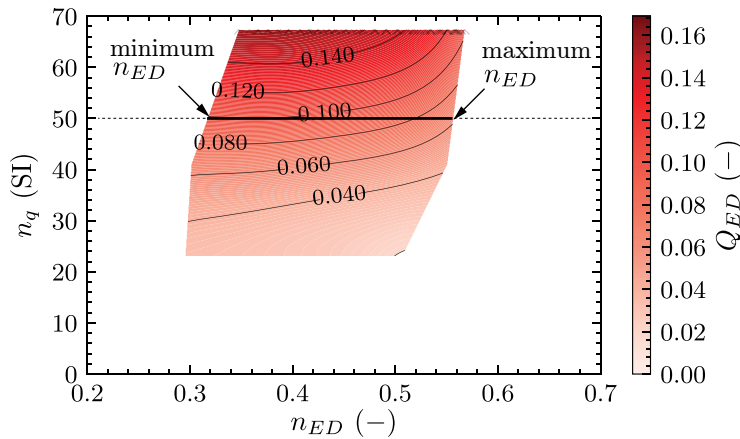


Figure 5.2 – Illustration of the PAT performance prediction methodology for the case of a pump with $n_q^P = 50$ using the hydraulic surrogate function for the experimental data collected in Chapter 2.

The surrogate functions identified in Chapter 4 allow predicting: (i) the turbine mode characteristic curves; and (ii) the extended operation in the generating mode characteristic curves. Both modes of operation are predicted using the same methodology. However, the surrogate functions used to estimate a given PAT performance are different for the turbine mode and for the extended operation in the generating mode.

Then, the characteristic curves obtained from empirical surrogate functions are used to model the variable speed hill chart of the PAT. During the final design stage, the modelling of the variable speed hill chart is carried out with accurate data of the PAT characteristic curves. These data are obtained either from the PAT manufacturers or by testing the PAT in laboratory conditions. Thus, the prediction of the PAT performance stage is ignored.

The guidelines for using the empirical surrogate functions to predict the PAT characteristic curves in the turbine mode and in the extended operation are presented in Section 5.2.1; and the guidelines for modelling the variable speed hill chart performance are presented in Section 5.2.2.

5.2 Guidelines

5.2.1 Performance prediction

The prediction of the turbine mode performance aims at obtaining the characteristic curves given by the variation of the specific hydraulic energy E , the torque T , the power P and the efficiency η^T , with respect to the discharge Q . The characteristic curves are retrieved for several constant values of the impeller rotational speed N aiming at modelling, in a further stage, the variable speed hill chart of the PAT. The prediction of the extended operation in the generating mode aims at estimating the variation of IEC discharge factor Q_{ED} and the IEC torque factor T_{ED} with respect to the IEC speed factor n_{ED} .

The prediction of both the turbine mode and the extended operation are based on the hydraulic and mechanical surrogate functions identified in Chapter 4. The prediction of the turbine mode can be performed either based on data collected during this thesis (see Chapter 2) or using literature data [98] (referred herein as experimental data and literature data for nomenclature simplicity). The prediction of the extended operation is performed only based on the experimental data collected. The values for the parameters used to build and compute the identified surrogate functions are provided in Section 5.3.

The input data from the user for predicting the PAT performance with respect to the PAT of interest for which the performance is to be estimated: (i) the rated values in the pump mode, namely the impeller rotational speed N_R^P , discharge Q_R^P , head H_R^P ; and (ii) the impeller diameter D .

The input data for modelling the surrogate functions identified in Chapter 4 are: (i) the hydraulic and mechanical surrogate functions required for the type of prediction, which are provided in Table 5.1; (ii) the coefficients a , b , c , μ_1 and μ_2 , which are

Chapter 5. Guidelines for modelling the PAT performance

provided in Table 5.2; the truncated basis for each surrogate function, which are provided in Table 5.3; and (iv) the weighting coefficients λ_k , which are given in Table 5.4.

The application of the prediction methodology for determining the performance of a given PAT of interest is given by the following steps. These steps are summarised in the flow chart of Figure 5.3.

Step 1: Choose the surrogate functions based on the type of operating mode for the prediction and the data set used according to the items below. See Table 5.1 for the details of the surrogate functions.

For the prediction of the turbine mode performance using the experimental data of Chapter 2 use data referent to the f_{QED}^T and f_{PED}^T for the hydraulic and the mechanical characteristic curves, respectively.

For the prediction of the turbine mode performance using the literature data [98] use data referent to the $f_{QED,B}^T$ and $f_{PED,B}^T$ for the hydraulic and the mechanical characteristic curves, respectively.

For the prediction of the extended operation in the generating mode performance using the experimental data of Chapter 2: use data referent to the f_{QED}^{EO} and f_{TED}^{EO} for the hydraulic and the mechanical characteristic curves, respectively.

Step 2: Compute the unit specific speed in the pumping mode n_q^P of the pump using Equation 5.1.

$$n_q^P = N_R^P \frac{Q_R^{P \frac{1}{2}}}{H_R^{P \frac{3}{4}}} \quad (5.1)$$

Step 3: Create the input data vector $\mathbf{x} = (x_1, x_2)$. The input data vector is required for computing the hydraulic and mechanical characteristic curves from the surrogate functions.

x_1 is an array evenly sampled from the minimum and the maximum n_{ED} values, which can be retrieved from Figures 5.5, 5.6 and 5.7, depending on the surrogate function used. An illustration of the identification of the minimum and maximum n_{ED} values is presented in Figure 5.2 for the hydraulic surrogate function of the experimental data f_{QED}^T . The number of samples of the array is chosen by the user (e.g., 100 points). x_2 is an array with constant values computed by Equation 5.1 and with the same number

of samples as x_1 . x_1 and x_2 are, thus, defined by Equation 5.2.

$$\begin{aligned} x_1 &= \left[{}^{(1)}n_{ED_{\min}} \quad {}^{(2)}n_{ED} \quad \dots \quad {}^{(N_s)}n_{ED_{\max}} \right]^T \\ x_2 &= \left[{}^{(1)}n_q^P \quad {}^{(2)}n_q^P \quad \dots \quad {}^{(N_s)}n_q^P \right]^T \end{aligned} \quad (5.2)$$

where the superscript $^{(k)} \in \mathbb{N}$ refer to the number of the sample and $N_s \in \mathbb{N}$ is the total number of samples. \mathbb{N} is the set of natural numbers.

Step 4: Compute the standardised data vector $\mathbf{X} = (X_1, X_2)$ using the standardisation function $g(\mathbf{x})$ defined below. The original input data needs to be standardised so that the modelling using the Hermite polynomial chaos expansion is valid (see Page 85 for technical details).

$$g: \begin{cases} \mathbb{R}^2 & \mapsto \mathbb{R}^2 \\ \mathbf{x} & \mapsto \mathbf{X} = \begin{pmatrix} a & 0 \\ b & c \end{pmatrix} \cdot (\mathbf{x} - \boldsymbol{\mu}) \end{cases} \quad (5.3)$$

where a, b, c and $\boldsymbol{\mu} = (\mu_1, \mu_2)$ are the coefficients of the standardisation function $g(\mathbf{x})$, which are indicated in Table 5.2 for all surrogate functions available.

Step 5: Generate the Hermite polynomials family He_p for the p indexes of the truncated basis Ψ of the hydraulic characteristic curve using the Equations 5.4, 5.5 and 5.6. The truncated basis Ψ of the identified surrogate functions for the prediction of the PAT performance are given in Table 5.3. Also, take into account the transformation of index given by Equation 5.7 for changing between indexes n, m to index p .

$$\begin{cases} \text{He}_{n+1,1} = a_n \cdot X_1 \cdot \text{He}_{n,1} + c_n \cdot \text{He}_{n-1,1} \\ \text{He}_{n+1,m} = \text{He}_{m-1,m} \cdot \text{He}_{n-m+2,1} \\ \text{He}_{n+1,n+2} = a_n \cdot X_2 \cdot \text{He}_{n,n+1} + c_n \cdot \text{He}_{n-1,n} \end{cases} \quad (5.4)$$

$$\begin{cases} \text{He}_{0,1} = 1 \\ \text{He}_{1,1} = X_1 \\ \text{He}_{1,2} = X_2 \end{cases} \quad (5.5)$$

$$\begin{cases} a_n = \sqrt{\frac{1}{n+1}} \\ c_n = -\sqrt{\frac{n}{n+1}} \end{cases} \quad (5.6)$$

$$p = \frac{n(n+1)}{2} + m - 1 \quad (5.7)$$

where indexes $n, m \in \mathbb{N}$ with $m \in [[2, n+1]]$ are indexes for the definition of the Hermite polynomials corresponding to the bivariate notation, $p \in \mathbb{N}$ is the univariate index used for simplicity of notation, where a_n and c_n are coefficients computed for each polynomial, which depend on the index n .

Step 6: Build the general form of the hydraulic surrogate function f with respect to $\mathbf{X} = (X_1, X_2)$ using Equation 5.8.

$$f = \sum_{k \in \Psi} \lambda_k \cdot \text{He}_k(g(\mathbf{x})) \quad (5.8)$$

where λ_k are the weighting coefficients found for the identified surrogate functions that are indicated in Table 5.4.

Step 7: Build the matrix of the Hermite polynomials $\mathbf{He}(\mathbf{X})$ evaluated for every value \mathbf{X} as in Equation 5.9.

$$\mathbf{He}(\mathbf{X}) = \begin{bmatrix} \text{He}_0^{(1)}(\mathbf{X}) & \text{He}_1^{(1)}(\mathbf{X}) & \cdots & \text{He}_{p_{\max}}^{(1)}(\mathbf{X}) \\ \text{He}_0^{(2)}(\mathbf{X}) & \text{He}_1^{(2)}(\mathbf{X}) & \cdots & \text{He}_{p_{\max}}^{(2)}(\mathbf{X}) \\ \vdots & \vdots & \ddots & \vdots \\ \text{He}_0^{(N_s)}(\mathbf{X}) & \text{He}_1^{(N_s)}(\mathbf{X}) & \cdots & \text{He}_{p_{\max}}^{(N_s)}(\mathbf{X}) \end{bmatrix} \quad (5.9)$$

Step 8: Compute the values of Q_{ED} by evaluating the hydraulic surrogate function using the Equation 5.10. The hydraulic characteristic curve is defined by the variation

of the IEC discharge factor Q_{ED} with respect to the IEC speed factor n_{ED} .

$$\begin{bmatrix} {}^{(1)}Q_{ED} \\ {}^{(2)}Q_{ED} \\ \vdots \\ {}^{(N_s)}Q_{ED} \end{bmatrix} = \begin{bmatrix} \text{He}_0({}^{(1)}\mathbf{X}) & \text{He}_1({}^{(1)}\mathbf{X}) & \cdots & \text{He}_{p_{\max}}({}^{(1)}\mathbf{X}) \\ \text{He}_0({}^{(2)}\mathbf{X}) & \text{He}_1({}^{(2)}\mathbf{X}) & \cdots & \text{He}_{p_{\max}}({}^{(2)}\mathbf{X}) \\ \vdots & \vdots & \ddots & \vdots \\ \text{He}_0({}^{(N_s)}\mathbf{X}) & \text{He}_1({}^{(N_s)}\mathbf{X}) & \cdots & \text{He}_{p_{\max}}({}^{(N_s)}\mathbf{X}) \end{bmatrix} \begin{bmatrix} \lambda_0 \\ \lambda_1 \\ \vdots \\ \lambda_{p_{\max}} \end{bmatrix} \quad (5.10)$$

Step 9: Repeat Steps 5, 6, 7 and 8 for predicting the mechanical characteristic curve. Note that if predicting the turbine mode, the mechanical characteristic curve obtained is given by the variation of the IEC power factor P_{ED} with respect to the IEC speed factor n_{ED} , while if predicting the extended operation, the obtained mechanical characteristic curve is given by variation of the IEC discharge factor T_{ED} with respect to the IEC speed factor n_{ED} .

Step 10 - Only for Turbine mode: Compute the parameters E , Q , T , P and η^T , for each constant value of N of interest using the Equation 5.11. These parameters will serve as the basis for modelling the variable speed hill chart performance of the PAT, where the guidelines for obtaining this hill chart are provided in the following Section 5.2.2.

$$\begin{aligned} n &= \frac{N}{60} \\ E &= \frac{n^2 D^2}{n_{ED}^2} \\ Q &= n D^3 \frac{Q_{ED}}{n_{ED}} \\ P &= P_{ED} \rho D^2 \sqrt{E^3} \\ T &= \frac{P}{2\pi n} \\ \eta^T &= \frac{P_{ED}}{Q_{ED}} \end{aligned} \quad (5.11)$$

where ρ is the water density, which depends on the water temperature and pressure. A table with the variation of ρ with respect to the water temperature and pressure is provided in [99].

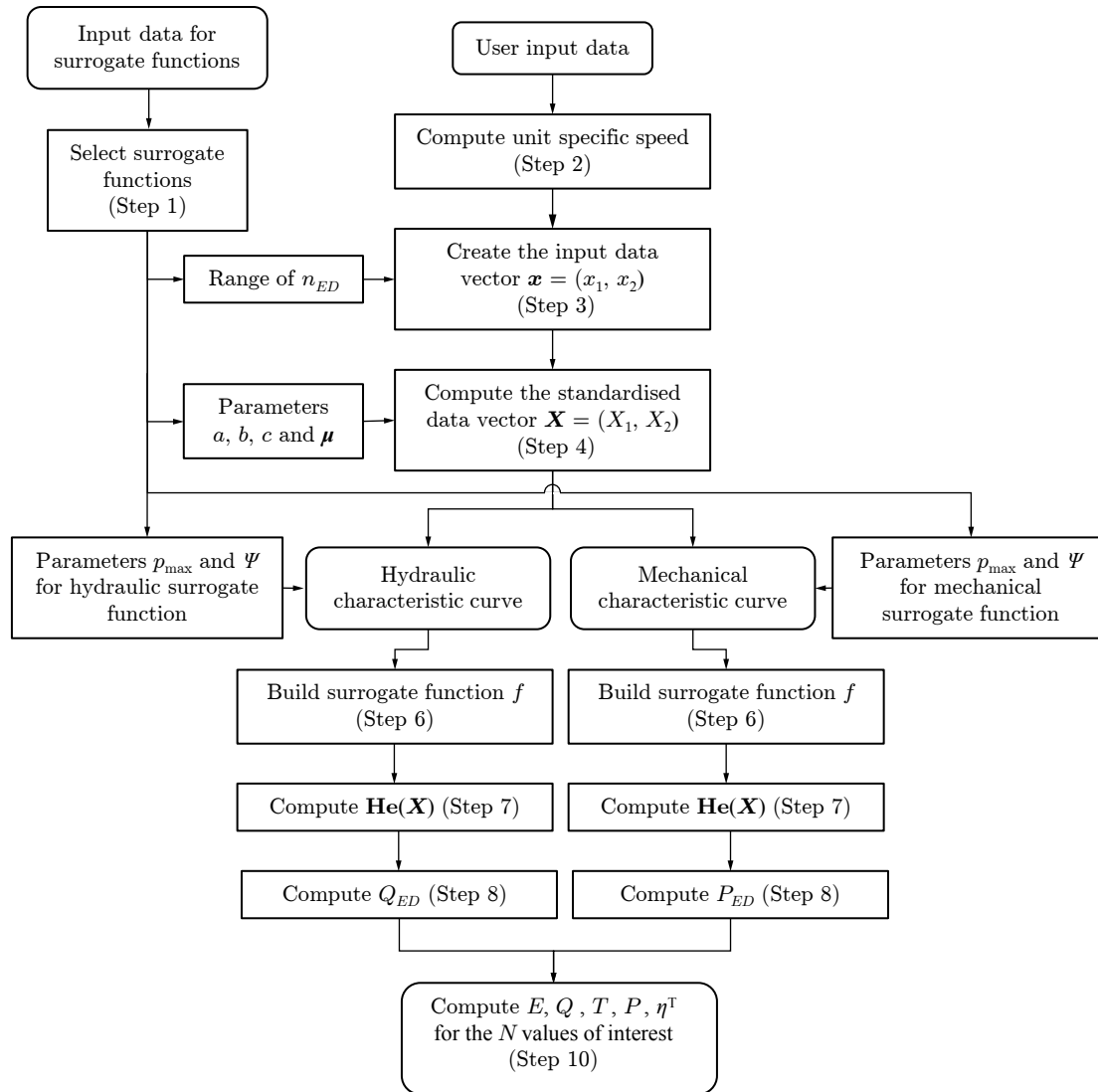


Figure 5.3 – Flow chart diagram for predicting the PAT characteristic curves. If predicting the extended operation, the computed value for the mechanical characteristic curve in Step 8 corresponds to T_{ED} and Step 10 is not performed.

5.2.2 Hill chart modelling

The modelling of the variable speed hill chart aims at determining the surrogate functions that better describe the variables of interest of the specific hydraulic energy E and the efficiency η^T , with respect to the input dependent variables of the rotational speed N and the discharge Q . Other variables of interest can be modelled such as the shaft torque T and the shaft power P . The modelling of the variable speed performance hill chart consists of the identification of the most suitable truncated basis, followed by the computation of the final surrogate functions. This procedure is similar to the one used for identifying the surrogate functions discussed in Chapter 4, though presented with higher detail.

The input data for modelling the variable speed hill chart performance are given below. Note that this data can be estimated using the guidelines described in the previous Section 5.2.1, for the preliminary design stages, or by using accurate data acquired in laboratory conditions or supplied by PAT manufacturers.

- Array with the sampled data of N such that $x_1 = [^{(1)}N \ ^{(2)}N \ \dots \ ^{(N_s)}N]^T$. This array should contain the data for all values of interest of N (e.g., $1'500 \text{ min}^{-1}$, $1'800 \text{ min}^{-1}$, $2'100 \text{ min}^{-1}$, $2'400 \text{ min}^{-1}$, $2'700 \text{ min}^{-1}$, $3'000 \text{ min}^{-1}$).
- Array with the sampled data of Q such that $x_2 = [^{(1)}Q \ ^{(2)}Q \ \dots \ ^{(N_s)}Q]^T$.
- Arrays with the sampled data for each independent variable of interest y such that $\mathbf{y} = [^{(1)}y \ ^{(2)}y \ \dots \ ^{(N_s)}y]^T$.

The methodology for modelling the variable speed hill chart performance of a given PAT is provided by the following steps. The summary of the following steps is provided in Figure 5.4.

Step 1: Compute the average values of the dependent variables $\boldsymbol{\mu}$ and the coefficients a , b and c of the standardisation function $g(\mathbf{x})$ using Equations 5.12, 5.13 and 5.14.

$$\boldsymbol{\mu} = \frac{1}{N} \sum_{j=1}^N {}^{(j)}\mathbf{x} \quad (5.12)$$

$$a = \sqrt{\frac{1}{\frac{1}{N-1} \sum_{j=1}^N ({}^{(j)}x_1 - \mu_1)^2}} \quad (5.13)$$

$$\begin{cases} \frac{1}{N-1} \sum_{j=1}^N \left[b \left({}^{(j)}x_1 - \mu_1 \right) + c \left({}^{(j)}x_2 - \mu_2 \right) \right]^2 = 1 \\ \sum_{j=1}^N \left({}^{(j)}X_1 \cdot \left[b \left({}^{(j)}x_1 - \mu_1 \right) + c \left({}^{(j)}x_2 - \mu_2 \right) \right] \right) = 0 \end{cases} \quad (5.14)$$

Step 2: Compute the standardised input data $\mathbf{X} = (X_1, X_2)$ using Equation 5.3.

For each variable of interest y repeat the following steps:

Step 3: Evaluate the adjustment of several candidate models defined by the truncated basis $\Psi = \{0, 1, \dots, p_{\max}\}$ by repeating Steps 3.1 to 3.6 for each candidate model. It is suggested to start with $p_{\max} = 2$ to account all Hermite polynomials in the boundary condition (see Equation 5.5) up to $p_{\max} = 60$. The identified surrogate functions found in Chapter 4, featured a maximum value of $p_{\max} = 35$. So, the limit of $p_{\max} = 60$ should be acceptable for the surrogate functions discussed in this work.

Step 3.1: Generate the Hermite polynomials He_p which belong to the candidate truncated basis Ψ Equations 5.4, 5.5, 5.6 and 5.7.

Step 3.2: Build the matrix $\mathbf{He}(\mathbf{X})$ using Equation 5.9.

Step 3.3: Compute the weighting coefficient $\boldsymbol{\lambda}$ by using the least-square solution given by Equation 5.15.

$$\boldsymbol{\lambda} = [\lambda_0 \ \lambda_1 \ \dots \ \lambda_{p_{\max}}]^\top = \left(\mathbf{He}(\mathbf{X})^\top \mathbf{He}(\mathbf{X}) \right)^{-1} \mathbf{He}(\mathbf{X})^\top \mathbf{y} \quad (5.15)$$

where the subscript indicates the index $p \in \mathbb{N}$. The $\boldsymbol{\lambda}$ are the weighting coefficients that minimise the mean-squared error $1/N_s \sum_{i=1}^{N_s} (y - y^*)^2$.

Step 3.4: Define the general form of the surrogate function f_y using Equation 5.8.

Step 3.5: Compute the evaluation of the surrogate function \mathbf{y}^* by using Equation 5.16.

$$\begin{bmatrix} {}^{(1)}y^* \\ {}^{(2)}y^* \\ \vdots \\ {}^{(N_s)}y^* \end{bmatrix} = \begin{bmatrix} \text{He}_0({}^{(1)}\mathbf{X}) & \text{He}_1({}^{(1)}\mathbf{X}) & \dots & \text{He}_{p_{\max}}({}^{(1)}\mathbf{X}) \\ \text{He}_0({}^{(2)}\mathbf{X}) & \text{He}_1({}^{(2)}\mathbf{X}) & \dots & \text{He}_{p_{\max}}({}^{(2)}\mathbf{X}) \\ \vdots & \vdots & \ddots & \vdots \\ \text{He}_0({}^{(N_s)}\mathbf{X}) & \text{He}_1({}^{(N_s)}\mathbf{X}) & \dots & \text{He}_{p_{\max}}({}^{(N_s)}\mathbf{X}) \end{bmatrix} \begin{bmatrix} \lambda_0 \\ \lambda_1 \\ \vdots \\ \lambda_{p_{\max}} \end{bmatrix} \quad (5.16)$$

Step 3.6: Compute the evaluation metrics corresponding to the maximum absolute error (Max AE), the mean absolute error (Mean AE), the standard deviation of the error σ_e , the determination coefficient R^2 and the corrected Akaike Information Criterion (AIC) using the Equations 5.17 to 5.22. The comparison of the values of these metrics allows comparing the suitability of the different candidate models.

$$\text{Max AE}(y, y^*) = \max(y_i - y_i^*), \quad (5.17)$$

$$\text{Mean.AE}(y, y^*) = \frac{1}{N_s} \sum_{i=1}^{N_s} |y_i - y_i^*| \quad (5.18)$$

$$\sigma_e(y, y^*) = \sqrt{\frac{1}{N_s} \sum_{i=1}^{N_s} (y_i - y_i^*)^2} \quad (5.19)$$

$$R^2(y, y^*) = 1 - \frac{\sum_{i=1}^{N_s} (y_i - y_i^*)^2}{\sum_{i=1}^{N_s} (y_i - \bar{y})^2} \quad (5.20)$$

$$\text{AIC}(y, y^*) = N_s (\log \sigma_e^2) + 2p_{\max} \quad (5.21)$$

$$\text{AIC}_c(y, y^*) = \text{AIC} + \frac{2p_{\max}(p_{\max} + 1)}{N_s - p_{\max} - 1} \quad (5.22)$$

Step 4: Compute the scaled AIC criteria $\text{AIC}_{c,s}$ using the following equation:

$$\text{AIC}_{c,s} = \text{AIC}_c - \text{AIC}_{c,\min} \quad (5.23)$$

where $\text{AIC}_{c,\min}$ is the minimum value obtained for the metric AIC_c . Since the absolute value of the AIC_c depends on the data samples, the values are scaled to a minimum of 0 for relative comparison between the candidate models.

Step 5: Select the most appropriate truncated basis by plotting the variation of the evaluation metrics with respect to p_{\max} . The most appropriate basis should be found for a p_{\max} value near the minimum value of $AIC_{c,s}$. If overfitting occurs, select a truncated basis defined by a lower p_{\max} value, by making a trade-off between the maximum and mean absolute errors and the non-occurrence of overfitting. Store the identified surrogate function f_y determined in Step 3.4. Save the values found for a , b , c and $\boldsymbol{\mu}$ for rebuilding the identified surrogate function for the variable of interest y .

Step 6: Refine the domain of the dependent variables by creating a mesh-grid from the new input data vector such that $\mathbf{x}_{\text{new}} = (x_{1,\text{new}}, x_{2,\text{new}})$, where $x_{1,\text{new}}$ and $x_{2,\text{new}}$ are defined below.

$$\begin{aligned} x_{1,\text{new}} &= [{}^{(1)}N \ {}^{(2)}N \ \dots \ {}^{(N_s)}N]^T \\ x_{2,\text{new}} &= [{}^{(1)}Q \ {}^{(2)}Q \ \dots \ {}^{(N_s)}Q]^T \end{aligned} \quad (5.24)$$

where ${}^{(1)}N$ and ${}^{(1)}Q$ are the minimum values of the original dependent variable samples of N and Q ; and ${}^{(N_s)}N$ and ${}^{(N_s)}Q$ are the maximum values of the original dependent variable samples of N and Q , respectively. Note that the new size of $\mathbf{x} \in \mathbb{R}^{N_s \times N_s}$. Consider, for instance $N_s = 500$.

Step 7: Compute the new standardised data vector $\mathbf{X}_{\text{new}} = (X_{1,\text{new}}, X_{2,\text{new}})$ the standardisation function $g(\mathbf{x}_{\text{new}})$ Equation 5.3. Use the coefficients $\boldsymbol{\mu}$, a , b and c computed in Step 1.

Step 8: Build the matrix $\mathbf{He}(\mathbf{X}_{\text{new}})$ using Equation 5.9 for the new domain of dependent variables.

Step 9: Compute the evaluation of the surrogate function for the new domain of dependent variables \mathbf{x}_{new} using the Equation 5.16. This new vector y_{new}^* corresponds to the evaluation of the identified surrogate function that better represents the original data of the variable of interest y .

Step 10: Plot the variable speed hill chart performance of y^* with respect to the dependent variables N and Q .

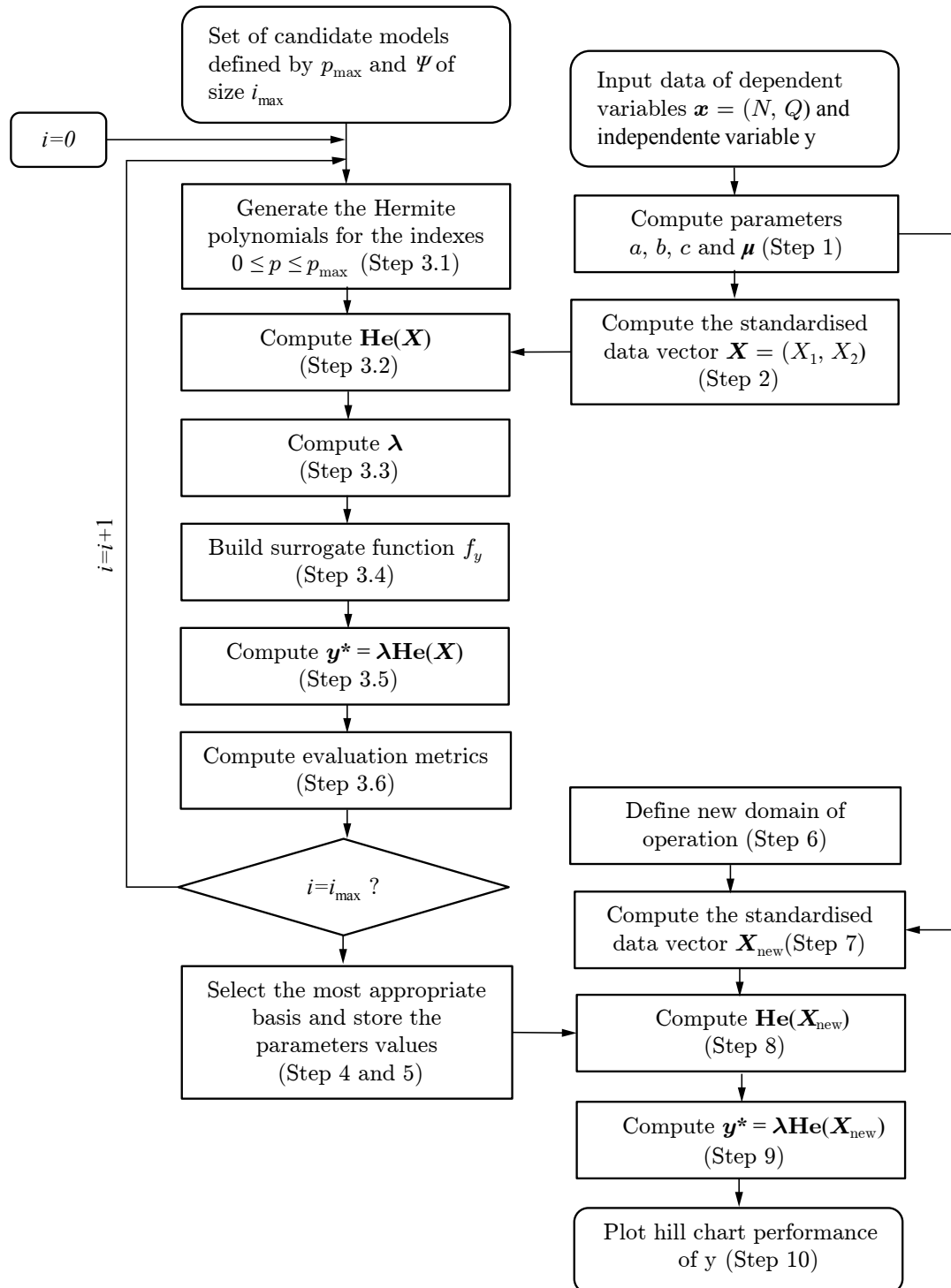


Figure 5.4 – Flow chart diagram for modelling the variable speed hill chart performance of the PAT. This flow chart is valid for one variable of interest y . Repeat the flow chart if more than one variable of interest is to be modelled.

5.3 Surrogate functions parameters

This Section provides the values of the parameters for modelling the surrogate functions used in Section 5.2.1. The available surrogate functions, which correspond to the identified surrogate functions in Chapter 4 are presented in Table 5.1. Note that the turbine mode can be computed based on the data of the PATs tested during this thesis work (see Chapter 2) or based on data published in literature [98].

Table 5.1 – Surrogate functions identified for the prediction PAT performance. The experimental data can be found in Chapter 2 and the literature data in [98].

Operating mode	Characteristic curve	Surrogate function	Dataset	Operating domain	Variable of interest
Turbine mode	f_{QED}^T	hydraulic	Exp. data	$\mathbf{x} = (n_{ED}, n_q)$	$y = Q_{ED}$
Turbine mode	f_{PED}^T	mechanical	Exp. data	$\mathbf{x} = (n_{ED}, n_q)$	$y = P_{ED}$
Turbine mode	$f_{QED,B}^T$	hydraulic	Lit. data	$\mathbf{x} = (n_{ED}, n_q)$	$y = Q_{ED}$
Turbine mode	$f_{PED,B}^T$	mechanical	Lit. data	$\mathbf{x} = (n_{ED}, n_q)$	$y = P_{ED}$
Extended operation	f_{QED}^{EO}	hydraulic	Exp. data	$\mathbf{x} = (n_{ED}, n_q)$	$y = Q_{ED}$
Extended operation	f_{TED}^{EO}	mechanical	Ex. data	$\mathbf{x} = (n_{ED}, n_q)$	$y = T_{ED}$

The values of the coefficients a , b , c , μ_1 and μ_2 of the standardisation function $g(\mathbf{x})$ corresponding the datasets used to define the surrogate functions are given in Table 5.2.

Table 5.2 – Values of the coefficient a , b and c and the average values μ_1 and μ_2 for the definition of the standardisation function $g(\mathbf{x})$.

index p	f_{QED}^T	f_{PED}^T	$f_{QED,B}^T$	$f_{PED,B}^T$	f_{QED}^{EO}	f_{TED}^{EO}
a	13.737585	13.737585	12.627483	12.627483	9.685223	9.685223
b	-6.407309	-6.407309	-12.815770	-12.815770	2.427048	2.427048
c	0.058099	0.058099	0.079298	0.079298	0.058308	0.058308
μ_1	0.444116	0.444116	0.390415	0.390415	0.570777	0.570777
μ_2	47.923611	47.923611	29.851115	29.851115	39.628333	39.628333

The truncated basis and the corresponding λ_k values found that define the identified surrogate functions are given in Tables 5.3 and 5.4, respectively. The contour view of the hydraulic and mechanical surrogate functions identified are given in Figures 5.5, 5.6 and 5.7, respectively for the turbine mode using the experimental data collected, the turbine mode for the literature data and the extended operation in the generating mode using the experimental data collected.

Table 5.3 – Values of the index p_{\max} and the corresponding truncated basis Ψ .

Surrogate function	p_{\max}	Truncated basis Ψ
f_{QED}^T	23	$\{0, 1, \dots, 22, 23\}$
f_{PED}^T	17	$\{0, 1, \dots, 16, 17\}$
$f_{QED,B}^T$	18	$\{0, 1, \dots, 17, 18\}$
$f_{PED,B}^T$	18	$\{0, 1, \dots, 17, 18\}$
f_{QED}^{EO}	32	$\{0, 1, \dots, 31, 32\}$
f_{PED}^{EO}	19	$\{0, 1, \dots, 18, 19\}$

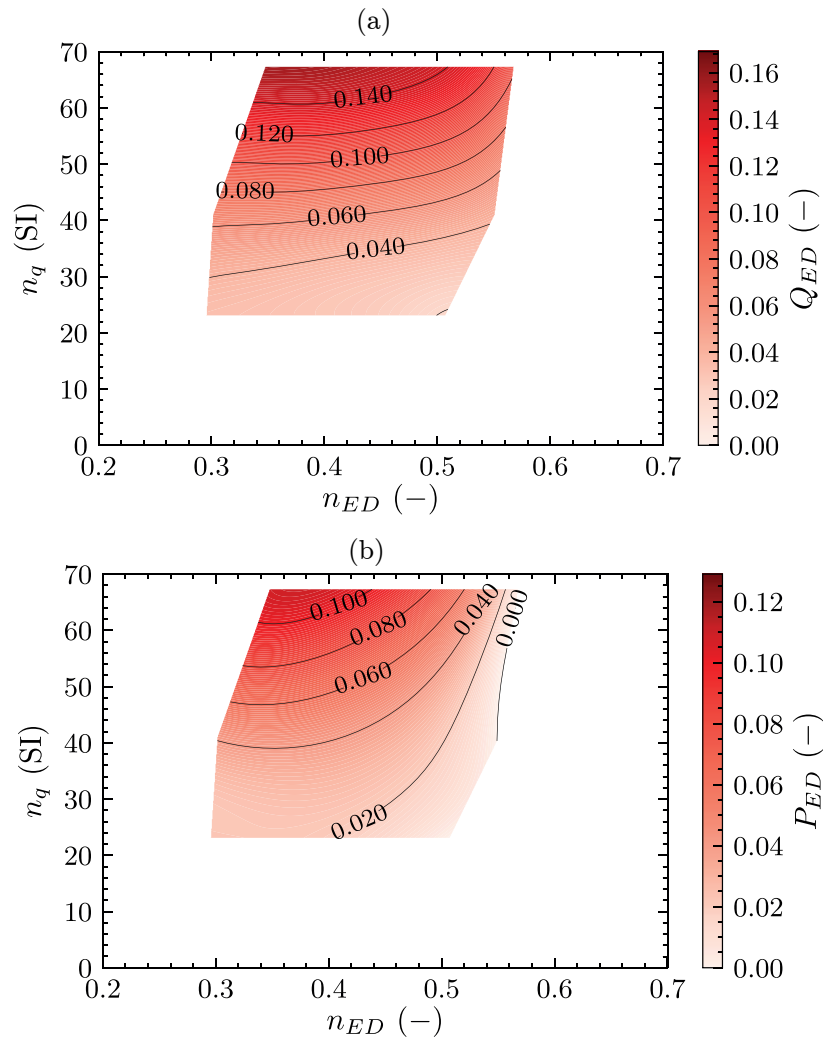


Figure 5.5 – Contour view of the identified surrogate functions for the propagation of the hydraulic and mechanical characteristic curves referent to the turbine mode using the experimental data collected (see Chapter 2). (a) f_{QED}^T ; (b) f_{PED}^T .

Chapter 5. Guidelines for modelling the PAT performance

Table 5.4 – Values of the weighting coefficients λ for the computation of the surrogate functions defined in Table 5.1.

$\lambda_k \times 10^2$	f_{QED}^T	f_{PED}^T	$f_{QED,B}^T$	$f_{PED,B}^T$	f_{QED}^{EO}	f_{PED}^{EO}
λ_0	8.026348	4.222391	5.358148	3.633139	2.755743	-1.258733
λ_1	0.075937	-1.629177	1.981003	0.823728	-2.139060	-2.385415
λ_2	3.215638	2.456607	2.615821	1.915424	2.321880	-0.209275
λ_3	-1.274995	-2.064414	0.956514	0.389293	-0.741688	-0.713907
λ_4	-0.840851	-0.003428	1.907796	1.838324	-1.531595	-1.164728
λ_5	-0.976707	-0.371670	1.313797	1.215356	0.388980	0.230062
λ_6	-1.080323	-1.756434	-0.426506	-0.367891	0.604251	0.205592
λ_7	-0.398440	-1.048006	-0.473767	-0.158689	-0.663631	-0.545424
λ_8	-1.002425	-0.222277	-0.666379	-0.491557	-0.086770	0.220850
λ_9	-1.701051	-0.748802	-0.403609	-0.459888	-0.440266	0.073293
λ_{10}	-0.573811	-0.693389	0.443152	0.455655	0.114449	0.234402
λ_{11}	-0.403443	0.015823	0.890994	1.047941	0.321130	-0.091214
λ_{12}	0.544880	0.544867	0.915919	1.076401	0.063767	0.386616
λ_{13}	-0.770350	0.099392	0.787887	0.715741	0.261330	0.269957
λ_{14}	-1.059076	-1.386887	0.357276	0.286360	-0.270550	0.265738
λ_{15}	-0.429896	-0.544406	0.018941	0.312602	-0.070378	0.026934
λ_{16}	0.213200	-0.466817	0.089323	0.387014	0.219109	0.271824
λ_{17}	1.004561	-0.029509	0.093540	0.185153	0.104989	0.441821
λ_{18}	0.553509		0.101283	0.049950	0.294024	0.219406
λ_{19}	0.124498				0.014993	0.335520
λ_{20}	0.622978				-0.518972	
λ_{21}	-0.066880				-0.150569	
λ_{22}	-0.256445				-0.166590	
λ_{23}	0.405462				-0.299231	
λ_{24}					0.446124	
λ_{25}					0.044401	
λ_{26}					0.273745	
λ_{27}					-0.494365	
λ_{28}					0.136691	
λ_{29}					-0.548858	
λ_{30}					-0.454044	
λ_{31}					0.197474	
λ_{32}					-0.092182	

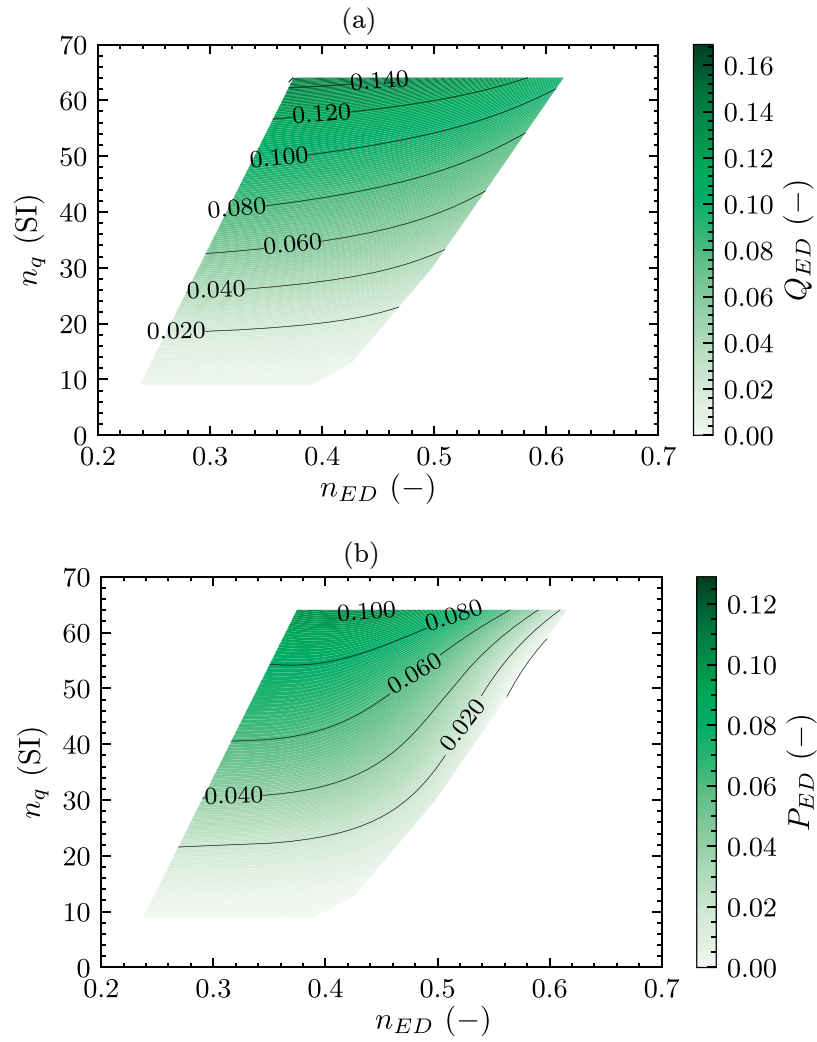


Figure 5.6 – Contour view of the identified surrogate functions for the propagation of the hydraulic and mechanical characteristic curves referent to the turbine mode using the literature data [98]. (a) $f_{QED,B}^T$; and (b) $f_{PED,B}^T$.

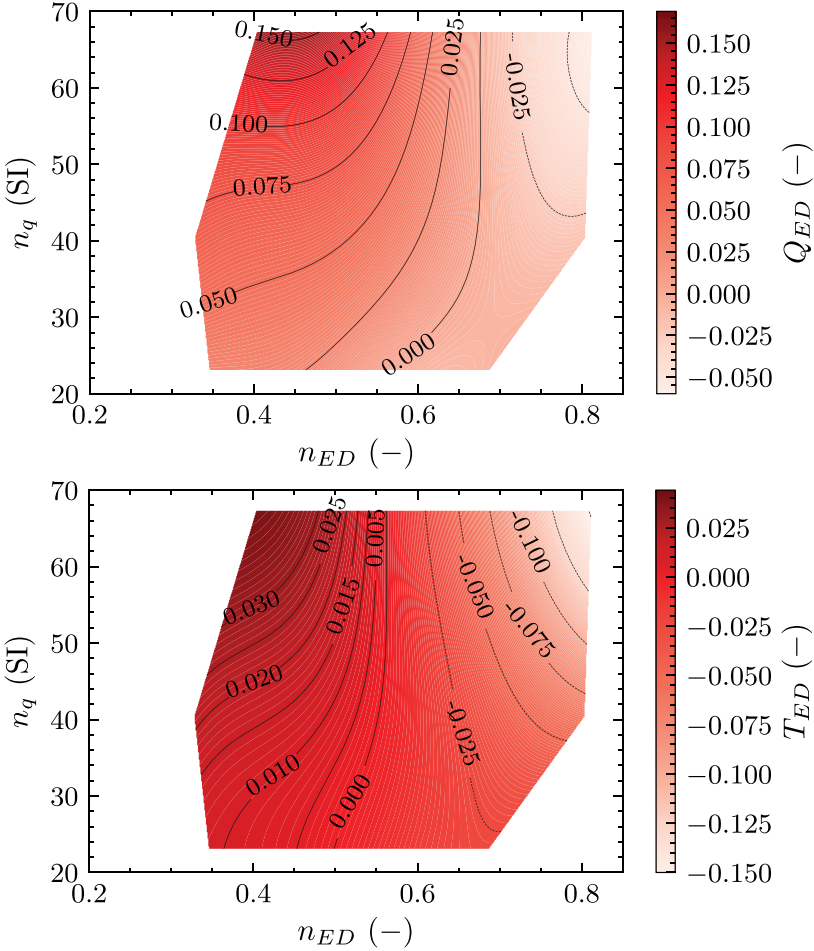


Figure 5.7 – Contour view of the identified surrogate functions for the propagation of the hydraulic and mechanical characteristic curves referent to the extended operation using the experimental data collected (see Chapter 2). (a) f_{QED}^{EO} ; (b) f_{TED}^{EO} .

6 Conclusion and outlook

6.1 Conclusion

The present research work focuses on the variable speed operation of single-stage centrifugal pumps running as turbines. The rotational speed control allows improving the operating efficiency of PAT micro hydropower plants installed in water supply systems for simultaneously controlling the pressure while recovering the excessive energy. Firstly, an extensive experimental investigation is carried out for: (i) measuring the stationary characteristic curves of the turbine mode and of the extended operation in the generating mode; and (ii) analysing the pressure fluctuations developed during the off-design operation. Secondly, a new methodology based on the Hermite polynomial chaos expansion (PCE) is proposed for predicting the PAT characteristic curves in both the turbine mode and in the extended operation in the generating mode. The PCE is also, afterwards, used for modelling the variable speed efficiency hill chart of a PAT.

In **Chapter 2**, the collected experimental data of the stationary performance of three PATs with different unit specific speed values are reported. The variable speed operation has proven to be a suitable solution for controlling the discharge at the PAT inlet and, thus, maximising the efficiency when operating under variable discharge conditions. Also, the variable speed operation allows increasing the operating head-discharge range of the PAT, providing higher flexibility to the power plant operation. This increase is a major advantage if the power plant is simultaneously used to dynamically control the pressure for minimising water leakage volumes in the WSS. For each PAT, the maximum efficiency is achieved for a constant value of the IEC discharge factor Q_{ED} , independently of the rotational speed N value. Such feature is useful for establishing the rotational speed set-point, which maximises the PAT efficiency depending on the real-time head and discharge values at the power plant inlet. The characteristic curves of the tested PATs in the extended operation in the generating mode do not have the unstable feature characterised by $\partial Q_{ED}/\partial n_{ED} \geq 0$,

which is frequently observed in Francis reversible pump-turbines. The non-existence of this unstable feature is especially relevant for the stability of the start-up and the shut-down operations of the PAT power plant.

In **Chapter 3**, the pressure fluctuations developed during the off-design operation are investigated. A cavitation vortex rope with a precessing motion develops during the part load operation if the stationary pressure in the PAT draft tube is too small. Consequently, significant pressure fluctuations are measured at both sides of the PAT. These pressure fluctuations, which are of synchronous nature, may propagate through the entire hydraulic system. The main frequency of the pressure fluctuations corresponds to the hydraulic system eigenfrequency value, which is strongly dependent on the amount of vapour generated by the cavitation flow. The major amplitudes of pressure fluctuations should be found if resonance occurs, that is when the precession frequency of the cavitation vortex rope matches the eigenfrequency of the hydraulic system. Further investigation is required about the resonance occurrence at part load conditions. The amplitude of the pressure fluctuations is hardly affected by the value of the back-pressure of the PAT. During the full load operation, despite no cavitation vortex rope is observed, strong pressure fluctuations are measured at both sides of the PAT. Both the amplitude and the frequency are significantly affected by the value of the back-pressure. Collected data do not allow drawing clear conclusions about the physical mechanisms underlying these pressure fluctuations in the full load operation and further research is required. Obtained results for the pressure fluctuations together with the unsteady radial force acting of the PAT impeller reported in the literature (e.g., [87]) suggest that the PAT full load operation should be avoided.

In **Chapter 4**, a new methodology is proposed for predicting the PAT performance and for modelling the variable speed performance hill chart of a PAT. The prediction methodology is based on the Hermite polynomials chaos expansion (PCE), which is used to define surrogate functions for propagating the known hydraulic and mechanical characteristic curves. The methodology is validated using data from a different pump manufacturer published in literature [98], has been proven effective for propagating the characteristic curves in the turbine mode. The surrogate functions should be defined separately for each pump manufacturer, aiming to minimise the prediction error. Pump manufacturers may use different designs and materials for the pump components, which may lead to different characteristic curves in the turbine mode. The PCE methodology has been found effective for propagating the characteristic curves in the extended operation in the generating mode. The fitting errors of the surrogate functions for the extended operation are higher compared to the results obtained for the turbine mode performance, which are related with the higher complexity of the interpolation and the reduced available data. Nevertheless, the obtained results from this methodology are expected to be closer to the real performance of a given PAT of interest, compared to using the data available for the PAT with the closest

value of unit specific speed. The same PCE methodology has been proven effective for modelling the functional form of the variable speed performance hill chart of a PAT. The main advantage of using the PCE approach is the description of the PAT performance using surrogate equations composed of the sum of polynomial terms. The computation of the derivatives of such equations is straightforward, which is a major advantage for the optimisation of the performance of a PAT micro hydropower plant.

Finally, in **Chapter 5**, practical guidelines are proposed for using the methodology for predicting the PAT performance and for modelling the variable speed performance hill chart of a PAT. These guidelines provide assistance to engineers for designing PAT micro hydropower plants. The methodology for predicting the PAT performance should only be used in the preliminary stages of design. The final design should be performed using reliable PAT performance data. These data should be provided by PAT manufacturers, if available, or collected under controlled laboratory conditions.

The research motivation of this thesis work is the experimental investigation and the modelling of the variable speed operation of pumps running as turbines aiming at determining if this operating strategy is suitable for maximising the energy recovered by PAT power plants under the variable discharge conditions of water supply systems (see Section 1.3 on page 15). In light of the achieved results, the variable speed operation has been proven effective for both increasing the energy recovered, but also for avoiding the operation in off-design conditions. The rotational speed control provides, thus, a greater flexibility to the operation of a PAT power plant under the variable discharge conditions of WSS. The new developed empirical model allows estimating the hydraulic and the mechanical characteristic curves of PATs if the precise data is not made available by PAT manufacturers. Finally, the modelling of the variable speed hill chart performance allows defining the power plant layout and the optimal control settings for optimising the operation of the power plant aiming at effectively controlling the pressure in the water supply systems while maximising the recovered energy.

6.2 Outlook

This research work focuses on the investigation of the variable speed operation of pumps running as turbines in subjects related to the stationary performance, the operation instabilities caused by the off-design operation and the performance modelling, being the main scientific contributions described in the previous section. This research has highlighted new challenges that require further investigation. Also, the combination of the main scientific contributions opens new possibilities for advancing the state-of-the-art research about pumps running as turbines and energy recovery in water supply systems.

The collection of additional experimental data for different PATs from the same type and manufacturer regarding the extended operation in the generating mode is of the utmost importance, as collected data are only available for three PATs. New data allow improving the surrogate functions for predicting the extended operation performance. Additional data are expected to improve the adjustment of the surrogate function. For other types of pumps, new datasets should be collected and used independently for developing new surrogate functions aiming at defining new surrogate functions suitable for that type of PATs.

The experimental evidence of the pressure fluctuations provided new insights regarding the PAT operation far from the BEP. The flow visualisation of the cavitation vortex rope in the PAT draft tube, the pressure fluctuation measurements and the results published in the literature make evidence that the PAT experiences an unsteady load when operating in off-design conditions. The synchronous pressure fluctuations propagate to the WSS pipes, reducing the performance of the system in terms of pressure but also may create fatigue in the pipes and fittings, which may lead to increased water leakage volume and pipe ruptures. Moreover, this additional load may reduce the service life of the machine. In light of these facts, the impacts of the unsteady load in the PAT and in the WSS pipes and fittings should be investigated. The same procedure described in Chapter 3 may be replicated for PATs with different unit specific speed values, aiming at identifying if there is a correlation between the PAT unit specific speed value and the relative discharge values where the pressure fluctuations occur. If so, the Hermite PCE methodology can be used to propagate the operating conditions where the pressure fluctuations occur between the values of unit specific speed tested. Despite being a far-fetched objective, such information would be of the utmost importance for designing the control specifications of PAT power plants.

The next step to this thesis is the integration of the knowledge acquired during this research for developing an optimisation model. The optimisation model would be used to establish the layout of the power plant (i.e., the layout, size and arrangement of the PATs) and the control settings of the different components. The variable speed

hill chart based on the PCE is used to provide a model of the performance of each PAT installed in the power plant. The discharge could be controlled by both a combination of several machines running in parallel, installed in a bypass to the main pipe of the WSS and, by controlling the rotational speed of each PAT and the opening of the bypass flow control valve. The combination of both a hydraulic and an electric control will guarantee higher flexibility in the PAT power plant operation. The optimisation should aim at maximising the energy recovered, avoiding the operation in off-design conditions of each machine and guaranteeing the minimum service pressure at downstream the power plant required for the adequate water supply to the consumers and for mitigating the damage caused by operating the operating instabilities caused by the PAT operation far from the best operating point.

Bibliography

- [1] European Union. Directive 2009/28/EC of the european parliament and of the council of 23 april 2009 on the promotion of the use of energy from renewable sources and amending and subsequently repealing directives 2001/77/ec and 2003/30/ec. *Official Journal of the European Union*, 5, 2009.
- [2] World Energy Council. *World energy issues monitor: A climate of innovation - Responding to the commodity price storm*. World Energy Council 2016, 2016. URL <https://www.worldenergy.org/wp-content/uploads/2016/03/2016-World-Energy-Issues-Monitor-Full-report.pdf>.
- [3] M. R. N. Vilanova and J. A. P. Balestieri. Energy and hydraulic efficiency in conventional water supply systems. *Renewable and Sustainable Energy Reviews*, 30:701–714, 2014. doi:10.1016/j.rser.2013.11.024.
- [4] Y. R. Fillion, H. L. MacLean, and B. W. Karney. Life-cycle energy analysis of a water distribution system. *Journal of Infrastructure Systems*, 10(3):120–130, 2004. doi:10.1061/(ASCE)1076-0342(2004)10:3(119).
- [5] T. Gaius-Obaseki. Hydropower opportunities in the water industry. *International Journal of Environmental Sciences*, 1(3):392, 2010. doi:10.6088/ijessi.00103010011.
- [6] J. White. Recovering energy from an existing conduit. *International Water Power and Dam Construction*, 63(6):18–20, 2011.
- [7] R.K. Saket. Design aspects and probabilistic approach for generation reliability evaluation of mww based micro-hydro power plant. *Renewable and Sustainable Energy Reviews*, 28:917 – 929, 2013. doi:10.1016/j.rser.2013.08.033.
- [8] I. Butera and R. Balestra. Estimation of the hydropower potential of irrigation networks. *Renewable and Sustainable Energy Reviews*, 48:140 – 151, 2015. doi:10.1016/j.rser.2015.03.046.
- [9] H.M. Ramos, C. Teyssier, I. Samora, and A. J. Schleiss. Energy recovery in SUDS

Bibliography

- towards smart water grids: A case study. *Energy Policy*, 62:463 – 472, 2013. doi:10.1016/j.enpol.2013.08.014.
- [10] E. Oklejas and W. F. Pergande. Integration of advanced high-pressure pumps and energy recovery equipment yields reduced capital and operating costs of seawater ro systems. *Desalination*, 127(2):181 – 188, 2000. doi:10.1016/S0011-9164(99)00203-9.
- [11] J. Steller, A. Adamkowski, Z. Stankiewicz, A. Lojek, J. Rduch, and M. Zarzycki. Pumps as turbines for hydraulic energy recovery and small hydropower purposes in Poland. In *Proceedings of the International Conference Hidroenergia*, page 10, 2008.
- [12] H. J. Van Antwerpen and G. P. Greyvenstein. Use of turbines for simultaneous pressure regulation and recovery in secondary cooling water systems in deep mines. *Energy Conversion and Management*, 46(4):563–575, 2005. doi:10.1016/j.enconman.2004.04.006.
- [13] B. Ulanicki, P.L.M. Bounds, J.P. Rance, and L. Reynolds. Open and closed loop pressure control for leakage reduction. *Urban Water*, 2(2):105 – 114, 2000. doi:10.1016/S1462-0758(00)00048-0.
- [14] A. Choulot. Energy recovery in existing infrastructures with small hydropower plants. *FP6 Project Shapes (Work Package 5—WP5)*, 2010. URL http://www.infrawatt.ch/sites/default/files/2010_06_07_Mhylab%20&%20ESHA_Energy%20recovery%20in%20existing%20infrastructures%20with%20small%20hydropower%20plants_0.pdf.
- [15] B. Orchard and S. Klos. Pumps as turbines for water industry. *World Pumps*, 2009(8):22–23, 2009. doi:10.1016/S0262-1762(09)70283-4.
- [16] S. V. Jain and R. N. Patel. Investigations on pump running in turbine mode: A review of the state-of-the-art. *Renewable and Sustainable Energy Reviews*, 30: 841 – 868, 2014. doi:10.1016/j.rser.2013.11.030.
- [17] A. Carravetta, G. del Giudice, O. Fecarotta, and H. M. Ramos. PAT design strategy for energy recovery in water distribution networks by electrical regulation. *Energies*, 6(1):411–424, 2013. doi:10.3390/en6010411.
- [18] P.-A. Su and B. Karney. Micro hydroelectric energy recovery in municipal water systems: A case study for vancouver. *Urban Water Journal*, 12(8):678–690, 2015. doi:10.1080/1573062X.2014.923919.
- [19] J. Gallagher, I. M. Harris, A. J. Packwood, A. McNabola, and A. P. Williams. A strategic assessment of micro-hydropower in the uk and irish water industry:

- Identifying technical and economic constraints. *Renewable Energy*, 81:808–815, 2015. doi:10.1016/j.renene.2015.03.078.
- [20] P. D. Zakkour, M.R. Gaterell, P. Griffin, R. J. Gochin, and J. N. Lester. Developing a sustainable energy strategy for a water utility. part ii: a review of potential technologies and approaches. *Journal of Environmental Management*, 66(2): 115–125, 2002. doi:10.1006/jema.2002.0567.
- [21] I. Loots, M. Van Dijk, S. J. Van Vuuren, J. N. Bhagwan, and A. Kurtz. Conduit-hydropower potential in the city of tshwane water distribution system: A discussion of potential applications, financial and other benefits. *Journal of the South African Institution of Civil Engineering*, 56(3):02–13, 2014.
- [22] C. Soffia, F. Miotto, D. Poggi, and P. Claps. Hydropower potential from the drinking water systems of the piemonte region (italy). In *4th International Conference on Sustainable Energy & Environmental Protection. Bari, Italy*, 2010.
- [23] D. A. Savic and J. K. Banyard. *Water distribution systems*. Thomas Telford Limited, 2011. doi:10.1680/wds.41127.
- [24] N. Carriço, D. I. C. Covas, H. Alegre, and M. C. Almeida. How to assess the effectiveness of energy management processes in water supply systems. *Journal of Water Supply: Research and Technology-Aqua*, 63(5):342, 2014. doi:10.2166/aqua.2014.094.
- [25] Aonghus McNabola, Paul Coughlan, Lucy Corcoran, Christine Power, A. Prysor Williams, Ian Harris, John Gallagher, and David Styles. Energy recovery in the water industry using micro-hydropower: an opportunity to improve sustainability. *Water Policy*, 16(1):168, feb 2014. doi:10.2166/wp.2013.164.
- [26] J. E. van Zyl, O. Piller, and Y. le Gat. Sizing municipal storage tanks based on reliability criteria. *Journal of Water Resources Planning and Management*, 134(6):548–555, 2008. doi:10.1061/(ASCE)0733-9496(2008)134:6(548).
- [27] L. S. Vamvakeridou-Lyroudia, D. A. Savic, and G. A. Walters. Tank simulation for the optimization of water distribution networks. *Journal of Hydraulic Engineering*, 133(6):625–636, 2007. doi:10.1061/(ASCE)0733-9429(2007)133:6(625).
- [28] A. Afshar, F. B. Jemaa, and M. I. A. Mariño. Optimization of hydropower plant integration in water supply system. *Journal of Water Resources Planning and Management*, 116(5):665–675, 1990. doi:10.1061/(ASCE)0733-9496(1990)116:5(665).
- [29] S. Kucukali. Municipal water supply dams as a source of small hydropower in turkey. *Renewable Energy*, 35(9):2001–2007, 2010. doi:10.1016/j.renene.2010.01.032.

Bibliography

- [30] S. Kucukali. Water supply lines as a source of small hydropower in turkey: A case study in edremit. In *World Renewable Energy Congress-Sweden; 8-13 May; 2011; Linköping; Sweden*, number 057, pages 1400–1407. Linköping University Electronic Press, 2011.
- [31] M. Pulskamp. Site inventory and hydropower energy assessment of reclamation-owned conduits: Supplement to the hydropower resource assessment at existing reclamation facilities report. *US Department of the Interior, Bureau of Reclamation, Power Resources Office, Denver, CO*, 2012.
- [32] G. S. Allen, C. N. Fay, and E. Matys. In-Conduit Hydropower Project – Phase I Report. Technical report, Alden Research Laboratory, Inc, Holden, Massachusetts, 2013. URL <http://www.mass.gov/eea/docs/dep/service/energy/hydrop1.pdf>.
- [33] A. McNabola, P. Coughlan, and A. P. Williams. Energy recovery in the water industry: an assessment of the potential of micro-hydropower. *Water and Environment Journal*, 28(2):294–304, 2013. doi:10.1111/wej.12046.
- [34] M. Rossi, M. Righetti, and M. Renzi. Pump-as-turbine for energy recovery applications: The case study of an aqueduct. *Energy Procedia*, 101:1207 – 1214, 2016. doi:10.1016/j.egypro.2016.11.163.
- [35] A. A. Williams, N. P. A. Smith, C. Bird, and M. Howard. Pumps as turbines and induction motors as generators for energy recovery in water supply systems. *Water and Environment Journal*, 12(3), 1998. doi:10.1111/j.1747-6593.1998.tb00169.x.
- [36] J. M. Chapallaz. Petites centrales hydrauliques: Pompe fonctionnant en turbine avec réglage du débit (PAT-francis) 2ème partie: Sélection de la pompe inversée pour fonctionnement en turbine (in french). *Rapport final Ecole Polytechnique Fédérale de Lausanne*, 2007.
- [37] J. P. García, A. C. Marco, and S. N. Santos. Use of centrifugal pumps operating as turbines for energy recovery in water distribution networks. two case study. *Advanced Materials Research*, 107:87–92, apr 2010. doi:10.4028/www.scientific.net/amr.107.87.
- [38] J. Frijns, A. Monteiro, M. de Graaff, N. Carriço, D. I. C. Covas, E. C. Marcet, E. S. Lausund, N. D. Seip, S. Saegrov, and J. Hofman. Intervention concepts for energy saving, recovery and generation from the urban water system. Technical report, 2014. URL www.trust-i.net/readpublicfile.php?fl=92.
- [39] EPAL - Empresa Portuguesa das Águas Livres. Water distribution network of Lisbon. <https://www.epal.pt/EPAL/menu/%C3%A1gua/sistema-de-abastecimento/sistema-de-distribui%C3%A7%C3%A3o>. Accessed: 2018-08-10.

- [40] T. Tucciarelli, A. Criminisi, and D. Termini. Leak analysis in pipeline systems by means of optimal valve regulation. *Journal of Hydraulic Engineering*, 125(3): 277–285, 1999. doi:10.1061/(ASCE)0733-9429(1999)125:3(277).
- [41] M. Girard and R. A. Stewart. Implementation of pressure and leakage management strategies on the gold coast, australia: Case study. *Journal of Water Resources Planning and Management*, 133(3):210–217, 2007. doi:10.1061/(ASCE)0733-9496(2007)133:3(210).
- [42] J. Schwaller and J. E. van Zyl. Modeling the pressure-leakage response of water distribution systems based on individual leak behavior. *Journal of Hydraulic Engineering*, 141(5):04014089, 2015. doi:10.1061/(ASCE)HY.1943-7900.0000984.
- [43] SVGW (Swiss Gas and Water Industry Association). *W4– directive for water supply*. Swiss Gas and Water Industry Association (In French), 2013.
- [44] L. S. Araujo, H. Ramos, and S. T. Coelho. Pressure control for leakage minimisation in water distribution systems management. *Water Resources Management*, 20(1):133–149, 2006. doi:10.1007/s11269-006-4635-3.
- [45] A. Carravetta, O. Fecarotta, M. Sinagra, and T. Tucciarelli. Cost-benefit analysis for hydropower production in water distribution networks by a pump as turbine. *Journal of Water Resources Planning and Management*, 140(6):04014002, 2014. doi:10.1061/(ASCE)WR.1943-5452.0000384.
- [46] F. Arbues, M. A. Garcia-Valinas, and R. Martinez-Espineira. Estimation of residential water demand: a state-of-the-art review. *The Journal of Socio-Economics*, 32(1):81 – 102, 2003. doi:10.1016/S1053-5357(03)00005-2.
- [47] D. Loureiro, A. Mamade, M. Cabral, C. Amado, and D. I. C. Covas. A comprehensive approach for spatial and temporal water demand profiling to improve management in network areas. *Water resources management*, 30(10):3443–3457, 2016. doi:10.1007/s11269-016-1361-3.
- [48] N. Fontana, M. Giugni, and D. Portolano. Losses reduction and energy production in water-distribution networks. *Journal of Water Resources Planning and Management*, 138(3):237–244, 2012. doi:10.1061/(ASCE)WR.1943-5452.0000179.
- [49] M. Giugni, N. Fontana, and A. Ranucci. Optimal location of prvs and turbines in water distribution systems. *Journal of Water Resources Planning and Management*, 140(9):06014004, 2014. doi:10.1061/(ASCE)WR.1943-5452.0000418.
- [50] L. Corcoran, A. McNabola, and P. Coughlan. Optimization of water distribution networks for combined hydropower energy recovery and leakage reduction. *Journal of Water Resources Planning and Management*, 142(2):04015045, 2016. doi:10.1061/(ASCE)WR.1943-5452.0000566.

Bibliography

- [51] I. Samora, M. J. Franca, A. J. Schleiss, and H. M. Ramos. Simulated annealing in optimization of energy production in a water supply network. *Water Resources Management*, 30(4):1533–1547, 2016. doi:10.1007/s11269-016-1238-5.
- [52] L. A. Rossman. Epanet 2: users manual. *US Environmental Protection Agency. Office of Research and Development. National Risk Management Research Laboratory*, 2000. URL <https://nepis.epa.gov/Adobe/PDF/P1007WWU.pdf>.
- [53] M. De Marchis and G. Freni. Pump as turbine implementation in a dynamic numerical model: cost analysis for energy recovery in water distribution network. *Journal of Hydroinformatics*, 17(3):347, 2015. doi:10.2166/hydro.2015.018.
- [54] L. Corcoran, A. McNabola, and P. Coughlan. Energy recovery potential of the dublin region water supply network. In *Water Congress on Water, Climate and Energy: Dublin, Ireland*, 2012.
- [55] S. Parra, S. Krause, F. Krönlein, F. W. Günthert, and T. Klunke. Intelligent pressure management by pumps as turbines in water distribution systems: results of experimentation. *Water Science and Technology: Water Supply*, 18(3):778, 2017. doi:10.2166/ws.2017.154.
- [56] A. Muhammetoglu, I. E. Karadirek, O. Ozen, and H. Muhammetoglu. Full-scale PAT application for energy production and pressure reduction in a water distribution network. *Journal of Water Resources Planning and Management*, 143(8):04017040, 2017. doi:10.1061/(ASCE)WR.1943-5452.0000795.
- [57] J. F. Gülich. *Centrifugal pumps*. Springer, 2014. ISBN 978-3-642-40114-5.
- [58] Grundfos. Grundfos product selection database. <http://www.product-selection.grundfos.com>. Accessed: 2018-08-10.
- [59] A. A. Williams. Pumps as turbines for low cost micro hydro power. *Renewable Energy*, 9(1-4):1227–1234, 1996. doi:10.1016/0960-1481(96)88498-9.
- [60] KSB. Advantages of using pumps as turbines. *World Pumps*, 2013(10):18–20, oct 2013. doi:10.1016/s0262-1762(13)70266-9.
- [61] Y. Guan, Z.Q. Zhu, I.A.A. Afinowi, J.C. Mipo, and P. Farah. Difference in maximum torque-speed characteristics of induction machine between motor and generator operation modes for electric vehicle application. *Electric Power Systems Research*, 136:406 – 414, 2016. doi:10.1016/j.epsr.2016.03.027.
- [62] R. Adams and J. Parker. Reducing pressure - increasing efficiency. *Sulzer Tech. Rev*, pages 26–29, 2011. URL https://www.sulzer.com/-/media/files/products/pumps/power-recovery/technical-articles/str_2011_1_e_26_parker.ashx.

- [63] P. and F. Nestmann. Internal hydraulic analysis of impeller rounding in centrifugal pumps as turbines. *Experimental Thermal and Fluid Science*, 35(1):121 – 134, 2011. doi:10.1016/j.expthermflusci.2010.08.013.
- [64] A. Doshi, S. Channiwala, and P. Singh. Inlet impeller rounding in pumps as turbines: An experimental study to investigate the relative effects of blade and shroud rounding. *Experimental Thermal and Fluid Science*, 82:333 – 348, 2017. doi:10.1016/j.expthermflusci.2016.11.024.
- [65] A. J. Stepanoff. *Centrifugal and axial flow pumps: theory, design, and application*. Wiley New York, 1957. ISBN 978-0894647239.
- [66] S.M. Childs. Convert pumps to turbines and recover hp. *Hydrocarbon Processing and Petroleum Refiner*, 41(10):173–174, 1962.
- [67] J. Hancock. Centrifugal pump or water turbine. *Pipe Line News*, 6:25–27, 1963.
- [68] K. M. Grover. Conversion of pumps to turbines. *GSA Inter corp., Katonah, New York*, 1980.
- [69] P. Hergt, P. Krieger, and S. Tommes. Die strömungstechnischen eigenschaften von kreiselpumpen im turbinenbetrieb. *VDMA Pumpentagung Karlsruhe*, 1984.
- [70] K. Sharma. Small hydroelectric projects—use of centrifugal pumps as turbines. *Kirloskar Electric Co., Bangalore, India*, 1985.
- [71] E. Schmiedl. Serien-kreiselpumpen im turbinenbetrieb. *Pumpentagung: Karlsruhe, Germany*, 1988.
- [72] S. Gopalakrishnan et al. Power recovery turbines for the process industry. In *Proceedings of the 3rd International Pump Symposium*. Turbomachinery Laboratories, Department of Mechanical Engineering, Texas A&M University, 1986.
- [73] Claudio Alatorre-Frenk. *Cost minimisation in micro-hydro systems using pumps-as-turbines*. PhD thesis, University of Warwick, 1994.
- [74] R. L. Sharma. Pumps as turbines (PAT) for small hydro. *Indian journal of power and river valley development*, 49:44–48, 1999.
- [75] J. M. Chapallaz, P. Eichenberger, and G. Fischer. *Manual on pumps used as turbines*. Vieweg, 1992.
- [76] S. Derakhshan and A. Nourbakhsh. Theoretical, numerical and experimental investigation of centrifugal pumps in reverse operation. *Experimental Thermal and Fluid Science*, 32(8):1620–1627, 2008. doi:10.1016/j.expthermflusci.2008.05.004.

Bibliography

- [77] S. Huang, G. Qiu, X. Su, J. Chen, and W. Zou. Performance prediction of a centrifugal pump as turbine using rotor-volute matching principle. *Renewable Energy*, 108:64–71, 2017. doi:10.1016/j.renene.2017.02.045.
- [78] S. Barbarelli, M. Amelio, and G. Florio. Predictive model estimating the performances of centrifugal pumps used as turbines. *Energy*, 107:103–121, 2016. doi:10.1016/j.energy.2016.03.122.
- [79] S.-S. Yang, F.-Y. Kong, H. Chen, and X.-H. Su. Effects of blade wrap angle influencing a pump as turbine. *Journal of Fluids Engineering*, 134(6):061102, 2012. doi:10.1115/1.4006677.
- [80] S.-S. Yang, S. Derakhshan, and F.-Y. Kong Yang. Theoretical, numerical and experimental prediction of pump as turbine performance. *Renewable Energy*, 48:507–513, 2012. doi:10.1016/j.renene.2012.06.002.
- [81] A. Bozorgi, E. Javidpour, A. Riasi, and A. Nourbakhsh. Numerical and experimental study of using axial pump as turbine in pico hydropower plants. *Renewable Energy*, 53:258 – 264, 2013. doi:10.1016/j.renene.2012.11.016.
- [82] T. Wang, C. Wang, F. Kong, Q. Gou, and S. Yang. Theoretical, experimental, and numerical study of special impeller used in turbine mode of centrifugal pump as turbine. *Energy*, 130:473 – 485, 2017. doi:10.1016/j.energy.2017.04.156.
- [83] P. Singh, J. T. Kshirsagar, S. Caglar, F. Nestmann, et al. Experimental and computational studies of the effect of ‘casing eye rib’ on the swirl flow at the exit of a pump as turbine. In *ASME 2004 Heat Transfer/Fluids Engineering Summer Conference*, pages 85–93. American Society of Mechanical Engineers, 2004.
- [84] R. Barrio, J. Fernández, J. Parrondo, and E. Blanco. Performance prediction of a centrifugal pump working in direct and reverse mode using computational fluid dynamics. In *International Conference on Renewable Energies and Power Quality*, pages 23–25, 2010.
- [85] M. Sedlář, J. Šoukal, and M. Komárek. Cfd analysis of middle stage of multistage pump operating in turbine regime. *Engineering Mechanics*, 16(6):413–421, 2009.
- [86] C. S. Morros, J. F. Oro, and K. M. A. Díaz. Numerical modelling and flow analysis of a centrifugal pump running as a turbine: Unsteady flow structures and its effects on the global performance. *International Journal for Numerical Methods in Fluids*, 65(5):542–562, 2011. doi:10.1002/fld.2201.
- [87] J. Fernández, R. Barrio, E. Blanco, J. Parrondo, and A. Marcos. Experimental and numerical investigation of a centrifugal pump working as a turbine. In *ASME 2009 Fluids Engineering Division Summer Meeting*, pages 471–479. American Society of Mechanical Engineers, 2009.

- [88] P. Singh and F. Nestmann. An optimization routine on a prediction and selection model for the turbine operation of centrifugal pumps. *Experimental Thermal and Fluid Science*, 34(2):152–164, 2010. doi:10.1016/j.expthermflusci.2009.10.004.
- [89] P. Singh and F. Nestmann. A consolidated model for the turbine operation of centrifugal pumps. *Journal of Engineering for Gas Turbines and Power*, 133(6):063002, 2011. doi:10.1115/1.4002270.
- [90] O. E. Balje. *Turbomachines-A guide to design, selection, and theory*. Number BOOK. John Wiley & Sons, 1981. ISBN 978-0-471-06036-9.
- [91] X. Tan and A. Engeda. Performance of centrifugal pumps running in reverse as turbine: Part ii- systematic specific speed and specific diameter based performance prediction. *Renewable Energy*, 99:188 – 197, 2016. doi:10.1016/j.renene.2016.06.052.
- [92] S. Derakhshan and A. Nourbakhsh. Experimental study of characteristic curves of centrifugal pumps working as turbines in different specific speeds. *Experimental thermal and fluid science*, 32(3):800–807, 2008. doi:10.1016/j.expthermflusci.2007.10.004.
- [93] G. Naldi, A. Artina, C. Bragalli, T. Liserra, and A. Marchi. Experimental investigation of characteristics curves of centrifugal pumps working as turbines, 2010.
- [94] F. Pugliese, F. De Paola, N. Fontana, M. Giugni, and G. Marini. Experimental characterization of two pumps as turbines for hydropower generation. *Renewable energy*, 99:180–187, 2016. doi:10.1016/j.renene.2016.06.051.
- [95] F. Pugliese, F. De Paola, N. Fontana, M. Giugni, and G. Marini. Performance of vertical-axis pumps as turbines. *Journal of Hydraulic Research*, 0(0):1–12, 2018. doi:10.1080/00221686.2017.1399932.
- [96] O. Fecarotta, A. Carravetta, H. M. Ramos, and R. Martino. An improved affinity model to enhance variable operating strategy for pumps used as turbines. *Journal of Hydraulic Research*, 54(3):332–341, 2016. doi:10.1080/00221686.2016.1141804.
- [97] M. Rossi and M. Renzi. A general methodology for performance prediction of pumps-as-turbines using artificial neural networks. *Renewable Energy*, 2018. doi:10.1016/j.renene.2018.05.060.
- [98] S. Barbarelli, M. Amelio, and G. Florio. Experimental activity at test rig validating correlations to select pumps running as turbines in micro-

Bibliography

- hydro plants. *Energy conversion and Management*, 149:781–797, 2017. doi:10.1016/j.enconman.2017.03.013.
- [99] IEC 60193:1999. Hydraulic turbines, storage pumps and pump-turbines - model acceptance tests. Standard, International Electrotechnical Commission (IEC), Geneva, Switzerland, 1999.
- [100] ISO 9906:2012. ISO 9906:2012: Rotodynamic pumps - hydraulic performance acceptance tests - grades 1, 2 and 3. Standard, International Organization for Standardization (ISO), Geneva, Switzerland, 2012.
- [101] C. Nicolet. *Hydroacoustic modelling and numerical simulation of unsteady operation of hydroelectric systems*. PhD thesis, École Polytechnique Fédérale de Lausanne, Lausanne, Switzerland, 2007.
- [102] P. Suter. Representation of pump characteristics for calculation of water hammer. *Sulzer Tech. Rev*, 66(4):45–48, 1966.
- [103] M. H. Chaudhry. *Applied Hydraulic Transients*, volume 3. Springer New York, 2014. ISBN 978-1-4614-8537-7. doi:10.1007/978-1-4614-8538-4.
- [104] C. Power, P. Coughlan, and A. McNabola. Microhydropower energy recovery at wastewater-treatment plants: Turbine selection and optimization. *Journal of Energy Engineering*, 143(1):04016036, 2017. doi:10.1061/(ASCE)EY.1943-7897.0000383.
- [105] A. Carravetta, G. Del Giudice, O. Fecarotta, and H. M. Ramos. Energy production in water distribution networks: A PAT design strategy. *Water Resources Management*, 26(13):3947–3959, 2012. doi:10.1007/s11269-012-0114-1.
- [106] N. Fontana, M. Giugni, L. Glielmo, and G. Marini. Real time control of a prototype for pressure regulation and energy production in water distribution networks. *Journal of Water Resources Planning and Management*, 142(7):04016015, 2016. doi:10.1061/(ASCE)WR.1943-5452.0000651.
- [107] O. Fecarotta, H. M. Ramos, S. Derakhshan, G. Del Giudice, and A. Carravetta. Fine tuning a PAT hydropower plant in a water supply network to improve system effectiveness. *Journal of Water Resources Planning and Management*, 144(8):04018038, 2018. doi:10.1061/(ASCE)WR.1943-5452.0000961.
- [108] D. R. Giosio, A. D. Henderson, J. M. Walker, P. A. Brandner, J. E. Sargison, and P. Gautam. Design and performance evaluation of a pump-as-turbine microhydro test facility with incorporated inlet flow control. *Renewable Energy*, 78: 1–6, 2015. doi:10.1016/j.renene.2014.12.027.

- [109] S.-S. Yang, H.-L. Liu, F.-Y. Kong, and B. Xia and L. W. Tan. Effects of the radial gap between impeller tips and volute tongue influencing the performance and pressure pulsations of pump as turbine. *Journal of Fluids Engineering*, 136(5): 054501, 2014. doi:10.1115/1.4026544.
- [110] C. Chen, C. Nicolet, K. Yonezawa, M. Farhat, F. Avellan, K. Miyagawa, and Y. Tsujimoto. Experimental study and numerical simulation of cavity oscillation in a diffuser with swirling flow. *International Journal of Fluid Machinery and Systems*, 3(1):80–90, 2010. doi:10.5293/IJFMS.2010.3.1.080.
- [111] A. Favrel, A. Müller, C. Landry, K. Yamamoto, and F. Avellan. Ldv survey of cavitation and resonance effect on the precessing vortex rope dynamics in the draft tube of francis turbines. *Experiments in Fluids*, 57(11):168, 2016. doi:10.1007/s00348-016-2257-y.
- [112] A. Favrel, J. G. P. Junior, C. Landry, A. Müller, C. Nicolet, and F. Avellan. New insight in francis turbine cavitation vortex rope: role of the runner outlet flow swirl number. *Journal of Hydraulic Research*, pages 1–13, 2017. doi:10.1080/00221686.2017.1356758.
- [113] A. Müller, M. Dreyer, N. Andreini, and F. Avellan. Draft tube discharge fluctuation during self-sustained pressure surge: fluorescent particle image velocimetry in two-phase flow. *Experiments in fluids*, 54(4):1514, 2013. doi:10.1007/s00348-013-1514-6.
- [114] A. Müller, A. Favrel, C. Landry, and F. Avellan. Fluid-structure interaction mechanisms leading to dangerous power swings in francis turbines at full load. *Journal of Fluids and Structures*, 69:56–71, 2017. doi:10.1016/j.jfluidstructs.2016.11.018.
- [115] P. Marques and F. F. Carvalho. Recuperação de energia em aproveitamentos hidroagrícolas: o caso do empreendimento de fins múltiplos de alqueva (in portuguese), 2011. URL <http://www.aprh.pt/jt-out-2011/pdf/42.pdf>.
- [116] S.P. Adhau, R.M. Moharil, and P.G. Adhau. Mini-hydro power generation on existing irrigation projects: Case study of indian sites. *Renewable and Sustainable Energy Reviews*, 16(7):4785 – 4795, 2012. doi:10.1016/j.rser.2012.03.066.
- [117] T. Ueda, M. Goto, A. Namihira, and Y. Hirose. Perspectives of small-scale hydropower generation using irrigation water in japan. *Japan Agricultural Research Quarterly: JARQ*, 47(2):135–140, 2013. doi:10.6090/jarq.47.135.
- [118] C. Power, A. McNabola, and P. Coughlan. Development of an evaluation method for hydropower energy recovery in wastewater treatment plants: Case studies in ireland and the uk. *Sustainable Energy Technologies and Assessments*, 7:166 – 177, 2014. doi:10.1016/j.seta.2014.06.001.

Bibliography

- [119] K.-J. Chae, I.-S. Kim, X. Ren, and K.-H. Cheon. Reliable energy recovery in an existing municipal wastewater treatment plant with a flow-variable micro-hydropower system. *Energy Conversion and Management*, 101:681 – 688, 2015. doi:10.1016/j.enconman.2015.06.016.
- [120] A. Muhammetoglu, C. Nursen, I. Karadirek, and H. Muhammetoglu. Evaluation of performance and environmental benefits of a full-scale pump as turbine system in antalya water distribution network. *Water Science and Technology: Water Supply*, 18(1):130, 2017. doi:10.2166/ws.2017.087.
- [121] World Water Assessment Programme (Nations Unies). *The United Nations World Water Development Report 2015*. United Nations Educational, Scientific and Cultural Organization, 2015.
- [122] F. Avellan. Course of hydraulic turbomachines. *École Polytechnique Fédérale de Lausanne, Switzerland*, 2014.
- [123] H. Ramos and A. Borga. Pumps as turbines: an unconventional solution to energy production. *Urban Water*, 1(3):261–263, 1999. doi:10.1016/S1462-0758(00)00016-9.
- [124] K.V. Alexander, E.P. Giddens, and A.M. Fuller. Radial and mixed-flow turbines for low head microhydro systems. *Renewable Energy*, 34(7):1885 – 1894, 2009. doi:10.1016/j.renene.2008.12.013.
- [125] Andritz Hydro. Mini compact hydro. Dedicated solutions for small hydropower plants. Technical report, Andritz Hydro, Vienna, Austria, 2015. URL <https://www.andritz.com/resource/blob/33256/4cc3cf70a02bca500e3c8e0915b31c03/hy-mini-compact-brochure-en-data.pdf>.
- [126] M. Kramer, K. Terheiden, and S. Wieprecht. Optimized design of impulse turbines in the micro-hydro sector concerning air detrainment processes. *Energy*, 93:2604–2613, 2015. doi:10.1016/j.energy.2015.10.022.
- [127] V. Sammartano, C. Aricò, M. Sinagra, and T. Tucciarelli. Cross-flow turbine design for energy production and discharge regulation. *Journal of Hydraulic Engineering*, 141(3), 2015. doi:10.1061/(ASCE)HY.1943-7900.0000977.
- [128] I. Samora, V. Hasmatuchi, C. Münch-Alligné, M. J. Franca, A. J. Schleiss, and H. M. Ramos. Experimental characterization of a five blade tubular propeller turbine for pipe inline installation. *Renewable Energy*, 95:356 – 366, 2016. doi:10.1016/j.renene.2016.04.023.
- [129] T. Ma, H. Yang, X. Guo, C. Lou, Z. Shen, J. Chen, and J. Du. Development of inline hydroelectric generation system from municipal water pipelines. *Energy*, 144:535–548, 2018. doi:10.1016/j.energy.2017.11.113.

- [130] E. Vagnoni, L. Andolfatto, S. Richard, C. Münch-Alligné, and F. Avellan. Hydraulic performance evaluation of a micro-turbine with counter rotating runners by experimental investigation and numerical simulation. *Renewable Energy*, 126: 943–953, 2018. doi:10.1016/j.renene.2018.04.015.
- [131] S. Derakhshan, B. Mohammadi, and A. Nourbakhsh. Efficiency improvement of centrifugal reverse pumps. *Journal of Fluids Engineering*, 131(2):021103, 2009. doi:10.1115/1.3059700.
- [132] O. Fecarotta, C. Aricò, A. Carravetta, R. Martino, and H. M. Ramos. Hydropower potential in water distribution networks: Pressure control by PATs. *Water Resources Management*, 29(3):699–714, 2015. doi:10.1007/s11269-014-0836-3.
- [133] S. Abazariyan, R. Rafee, and S. Derakhshan. Experimental study of viscosity effects on a pump as turbine performance. *Renewable Energy*, 127:539 – 547, 2018. doi:10.1016/j.renene.2018.04.084.
- [134] M. Kramer, K. Terheiden, and S. Wieprecht. Pumps as turbines for efficient energy recovery in water supply networks. *Renewable Energy*, 2018. doi:10.1016/j.renene.2018.01.053.
- [135] Andritz Hydro. ANDRITZ pumps used as turbines. Energy efficient in forward and reverse mode. Technical report, Andritz Hydro, Graz, Austria, 2017. URL <https://www.andritz.com/resource/blob/238812/8eacde6d9ab0a36542138dcee5e0afa8/pumps-as-turbines-en-data.pdf>.
- [136] S. V. Jain, A. Swarnkar, K. H. Motwani, and R. N. Patel. Effects of impeller diameter and rotational speed on performance of pump running in turbine mode. *Energy Conversion and Management*, 89:808 – 824, 2015. doi:10.1016/j.enconman.2014.10.036.
- [137] V. Hasmatuchi. *Hydrodynamics of a Pump-Turbine Operating at Off-Design Conditions in Generating Mode*. PhD thesis, École Polytechnique Fédérale de Lausanne, Lausanne, Switzerland, 2012.
- [138] V. Hasmatuchi, M. Farhat, P. Maruzewski, and F. Avellan. Experimental investigation of a pump-turbine at off-design operating conditions. In *Proceedings of the 3rd International Meeting of the Workgroup on Cavitation and Dynamic Problems in Hydraulic Machinery and Systems*, pages 339–347. Brno University of Technology, 2009.
- [139] R. Wright, E. Abraham, P. Parpas, and I. Stoianov. Control of water distribution networks with dynamic dma topology using strictly feasible sequential convex programming. *Water Resources Research*, 51(12):9925–9941, 2015. doi:10.1002/2015WR017466.

Bibliography

- [140] A. Carravetta, S. Derakhshan, and H. M. Ramos. *Pumps as Turbines: Fundamentals and Applications*. Springer, 2017. ISBN 978-3-319-67507-7.
- [141] X. w. Luo, J. I. Bin, and Y. Tsujimoto. A review of cavitation in hydraulic machinery. *Journal of Hydrodynamics, Ser. B*, 28(3):335–358, 2016. doi:10.1016/S1001-6058(16)60638-8.
- [142] S. V. Jain, N. K. Patel, and R. N. Patel. Experimental investigations of cavitation characteristics of pump running in turbine mode. *Journal of Energy Engineering*, 143(1):04016034, 2016. doi:10.1061/(ASCE)EY.1943-7897.0000387.
- [143] L. Gaudard and F. Romerio. The future of hydropower in europe: Interconnecting climate, markets and policies. *Environmental Science & Policy*, 37:172–181, 2014. doi:10.1016/j.envsci.2013.09.008.
- [144] J. Dujardin, A. Kahl, B. Kruyt, S. Bartlett, and M. Lehning. Interplay between photovoltaic, wind energy and storage hydropower in a fully renewable switzerland. *Energy*, 135:513–525, 2017. doi:10.1016/j.energy.2017.06.092.
- [145] F. Avellan. Introduction to cavitation in hydraulic machinery. In *The 6th International Conference on Hydraulic Machinery and Hydrodynamics, Timisoara, Romania, 2004*.
- [146] J. Arpe, C. Nicolet, and F. Avellan. Experimental evidence of hydroacoustic pressure waves in a francis turbine elbow draft tube for low discharge conditions. *Journal of Fluids Engineering*, 131(8):081102, 2009. doi:doi:10.1115/1.3155944.
- [147] M. Nishi and S. Liu. An outlook on the draft-tube-surge study. *International Journal of Fluid Machinery and Systems*, 6(1), 2013. doi:10.5293/IJFMS.2013.6.1.033.
- [148] P Dörfler. System dynamics of the francis turbine half load surge. In *Proceedings of the 11th IAHR Symposium on Hydraulic Machinery and Systems*, pages 441–453, 1982.
- [149] C. Landry, A. Favrel, A. Müller, C. Nicolet, and F. Avellan. Local wave speed and bulk flow viscosity in francis turbines at part load operation. *Journal of Hydraulic Research*, 54(2):185–196, 2016. doi:10.1080/00221686.2015.1131204.
- [150] N. Ruchonnet, S. Alligne, C. Nicolet, and F. Avellan. Cavitation influence on hydroacoustic resonance in pipe. *Journal of Fluids and Structures*, 28:180–193, 2012. doi:10.1016/j.jfluidstructs.2011.10.001.
- [151] P. Welch. The use of fast fourier transform for the estimation of power spectra: a method based on time averaging over short, modified periodograms. *IEEE Transactions on audio and electroacoustics*, 15(2):70–73, 1967. doi:10.1109/TAU.1967.1161901.

- [152] J. S. Bendat and A. G. Piersol. *Random data: analysis and measurement procedures*, volume 729. John Wiley & Sons, 2011. ISBN 978-0-470-24877-5.
- [153] S. Van der Walt, J. L. Schönberger, J. Nunez-Iglesias, F. Boulogne, J. D. Warner, N. Yager, E. Gouillart, and T. Yu. Scikit-image: image processing in python. *PeerJ*, 2:e453, 2014.
- [154] D. B. Allan, T. A. Caswell, and N. C. Keim. Trackpy v0. 2, 2014.
- [155] A. Sauret, F. Boulogne, J. Cappello, E. Dressaire, and H. A. Stone. Damping of liquid sloshing by foams. *Physics of Fluids*, 27(2), 2015. doi:10.1063/1.4907048.
- [156] E. Vagnoni, L. Andolfatto, R. Guillaume, P. Leroy, and F. Avellan. Rotating air-water ring in the vaneless gap of a pump-turbine operating in condenser mode. *International Journal of Multiphase Flow*, 2018. doi:10.1016/j.ijmultiphaseflow.2018.03.022.
- [157] R. C. Gonzalez and R. E. Woods. *Digital image processing*. Upper Saddle River, NJ: Prentice Hall, 2012. ISBN 978-0131687288.
- [158] G. Bradski and A. Kaehler. *Learning OpenCV: Computer vision with the OpenCV library*. " O'Reilly Media, Inc.", 2008. ISBN 978-0596516130.
- [159] A. K. Gupta, D. G. Lilley, and N. Syred. Swirl flows. *Tunbridge Wells, Kent, England, Abacus Press, 1984, 488 p.*, 1984.
- [160] M. R. N. Vilanova and J. A. P. Balestieri. Hydropower recovery in water supply systems: Models and case study. *Energy Conversion and Management*, 84:414 – 426, 2014. ISSN 0196-8904. doi:10.1016/j.enconman.2014.04.057.
- [161] A. A. Williams and R. Simpson. Pico hydro—reducing technical risks for rural electrification. *Renewable Energy*, 34(8):1986–1991, 2009. doi:10.1016/j.renene.2008.12.011.
- [162] A. H. Elbatran, O. B. Yaakob, Y. M. Ahmed, and H. M. Shabara. Operation, performance and economic analysis of low head micro-hydropower turbines for rural and remote areas: a review. *Renewable and Sustainable Energy Reviews*, 43:40–50, 2015. doi:10.1016/j.rser.2014.11.045.
- [163] B. Orchard. Bringing electricity to rural locations. *World Pumps*, 2016(11):28–31, 2016. doi:10.1016/S0262-1762(16)30316-9.
- [164] D. Novara and A. McNabola. A model for the extrapolation of the characteristic curves of pumps as turbines from a datum best efficiency point. *Energy Conversion and Management*, 174:1 – 7, 2018. ISSN 0196-8904. doi:10.1016/j.enconman.2018.07.091.

Bibliography

- [165] M. Rossi and M. Renzi. Analytical prediction models for evaluating pumps-as-turbines (PaTs) performance. *Energy Procedia*, 118:238–242, 2017. doi:j.egypro.2017.07.011.
- [166] J. Delgado, J. P. Ferreira, D. I.C. Covas, and F. Avellan. New test-rig for micro hydropower turbomachines. In *CCWI 2017-Computing and Control for the Water Industry*. The University of Sheffield, 2017.
- [167] M. H. Stone. The generalized weierstrass approximation theorem. *Mathematics Magazine*, 21(5):237–254, 1948. doi:10.2307/3029750.
- [168] N. Wiener. The homogeneous chaos. *American Journal of Mathematics*, 60(4): 897–936, 1938. doi:10.2307/2371268.
- [169] L. Andolfatto, J. Delgado, E. Vagnoni, C. Münch-Alligné, and F. Avellan. Analytical hill chart towards the maximisation of energy recovery on water utility networks with counter rotating micro-turbine. In *36th IAHR World Congress*, 2015.
- [170] J. P. Gomes, L. Andolfatto, and F. Avellan. Monitoring a francis turbine operating conditions. *Flow Measurement and Instrumentation*, 2018. doi:10.1016/j.flowmeasinst.2018.07.007.
- [171] C. L. Lawson and R. J. Hanson. *Solving least squares problems*, volume 15. Society for Industrial and Applied Mathematics, 1995. ISBN 978-0-89871-356-5. doi:10.1137/1.9781611971217.
- [172] H. Akaike. A new look at the statistical model identification. *IEEE transactions on automatic control*, 19(6):716–723, 1974. doi:10.1109/TAC.1974.1100705.
- [173] K. P. Burnham and D. R. Anderson. Multimodel inference: understanding AIC and BIC in model selection. *Sociological methods & research*, 33(2):261–304, 2004. doi:10.1177/0049124104268644.
- [174] L. Andolfatto, E. Vagnoni, V. Hasmatuchi, C. Münch-Alligné, and F. Avellan. Simulation of energy recovery on water utility networks by a micro-turbine with counter-rotating runners. *IOP Conference Series: Earth and Environmental Science*, 49(10), 2016. doi:10.1088/1755-1315/49/10/102012.

JOÃO NUNO GOMES BORGA DELGADO

Born in Santarém (Portugal) on December 4th 1990.

Education

- 2014 – 2018 **PhD in Energy**
Laboratory for Hydraulic Machines at EPFL (Switzerland).
Thesis: Pumps running as turbines for energy recovery in water supply systems
- 2008 – 2013 **M.Sc. in Civil Engineering**
Instituto Superior Técnico, University of Lisbon (Portugal)
Thesis: Hydraulic Transients in pumping systems – numerical modelling and experimental analysis

Work experiences

- 2011-2014 **Research Fellow (2014)**
Junior Research Fellow (2011-2013)
Instituto Superior Técnico, University of Lisbon (Portugal)
- Development of numerical models to describe hydraulic transient flow in pressurised pipe systems
 - Experimental measurements and data acquisition
- 2013-2016 (part time) **Hydropower project consultant engineer**
Instituto Superior Técnico, University of Lisbon (Portugal)
- Rehabilitation of Calheta pumped storage power plant (Madeira). 3x5 MW pumps + 2x15 MW Pelton turbines
 - Pumped storage power plant of Lagoa das Furnas, Azores: 4x3.3 MW pumps + 2x 5.7 MW Pelton turbines
 - Field measurements of pumping stations efficiency: 1 water pumping station + 8 wastewater pumping stations

Training programs

- 2014 **Hydraulic Engineering**
- Hydraulic transients control in pipeline systems. Engineering solutions and case-studies
 - Water supply systems modelling using EPANET
 - Management of leakage losses in water supply systems
- 2015 **Programming languages**
- LabVIEW Core 1, 2 and 3
 - LabVIEW Data Acquisition and Signal Conditioning
 - Microsoft Excel Macros e VBA

Curriculum Vitae

IT Skills

- *CAD/CAE Software* : CATIA V5 / Autodesk AutoCAD
- *Hydraulic engineering software*: Hammer v8i; EPANET; HEC-RAS
- *Programing languages*: LabVIEW; Python; VBA; C++

Language

Mother tongue: PORTUGUESE

Professional proficiency: ENGLISH

Limited proficiency: FRENCH, SPANISH

Peer-reviewed publications

- [1] Martins, N. M. C., Delgado, J., Ramos, H. M., and Covas, D. I. C. (2017). "Maximum transient pressures in a rapidly filling pipeline with entrapped air using a CFD model." *Journal of Hydraulic Research*, 1–14. DOI:10.1080/00221686.2016.1275046.
- [2] Delgado, J., Martins, N. M. C., and Covas, D. I. C. (2014). "Uncertainties in Hydraulic Transient Modelling in Raising Pipe Systems: Laboratory Case Studies." *Procedia Engineering*, 70, 487– 496. DOI: 10.1016/j.proeng.2014.02.054

Conference papers

- [1] Delgado, J., Covas, D.I.C., and Avellan, F. (2017). "New test-rig for micro hydropower turbomachines", *Proc. 15th Int. Computing and Control for the Water Industry Conf.*, 5-7/11, Sheffield, England.
- [2] Monteiro, L., Delgado, J., Figueiredo, D., Alves, R., Póvoa, P. Covas, D.I.C. (2016). "Assessment of the potential for energy recovery in water trunk mains". *Proc. 14th Int. Computing and Control for the Water Industry Conf.*, 7-9/11, Amsterdam, Netherlands.
- [3] Andolfatto, L., Delgado, J., Vagnoni, E., Münch-Alligné, C., and Avellan, F. (2015). "Analytical hill chart towards the maximisation of energy recovery in water utility networks with counter rotating micro-turbine." *Proc. 36th IAHR World Congress*, 28/6-03/7, The Hague, Netherlands.
- [4] Vagnoni, E., Andolfatto, L., Delgado, J., Münch-Alligné, C., and Avellan, F. (2015). "Application of laser doppler velocimetry to the development of a counter rotating micro-turbine." *Proc. 36th IAHR World Congress*, 28/6-03/7, The Hague, Netherlands.
- [5] Delgado, J., Covas, D.I.C., and Almeida, A. B. (2014). "Hydraulic Transients in Pumping Systems with Horizontal Profiles", *Proc. 3rd IAHR Europe Congress*, 14-6/4, Porto, Portugal.

